UNIVERSITAT DE
BARCELONA

Assessing the degradation and transformation of emerging pollutants submitted to TiO_2 photocatalysis by high-resolution mass spectrometry techniques

Are we posing a new hazard to the environment?

Javier Jimenez Villarin

ADVERTIMENT. La consulta d'aquesta tesi queda condicionada a l'acceptació de les següents condicions d'ús: La difusió d'aquesta tesi per mitjà del servei TDX (**www.tdx.cat**) i a través del Dipòsit Digital de la UB (**diposit.ub.edu**) ha estat autoritzada pels titulars dels drets de propietat intel·lectual únicament per a usos privats emmarcats en activitats d'investigació i docència. No s'autoritza la seva reproducció amb finalitats de lucre ni la seva difusió i posada a disposició des d'un lloc aliè al servei TDX ni al Dipòsit Digital de la UB. No s'autoritza la presentació del seu contingut en una finestra o marc aliè a TDX o al Dipòsit Digital de la UB (framing). Aquesta reserva de drets afecta tant al resum de presentació de la tesi com als seus continguts. En la utilització o cita de parts de la tesi és obligat indicar el nom de la persona autora.

ADVERTENCIA. La consulta de esta tesis queda condicionada a la aceptación de las siguientes condiciones de uso: La difusión de esta tesis por medio del servicio TDR (**www.tdx.cat**) y a través del Repositorio Digital de la UB (**diposit.ub.edu**) ha sido autorizada por los titulares de los derechos de propiedad intelectual únicamente para usos privados enmarcados en actividades de investigación y docencia. No se autoriza su reproducción con finalidades de lucro ni su difusión y puesta a disposición desde un sitio ajeno al servicio TDR o al Repositorio Digital de la UB. No se autoriza la presentación de su contenido en una ventana o marco ajeno a TDR o al Repositorio Digital de la UB (framing). Esta reserva de derechos afecta tanto al resumen de presentación de la tesis como a sus contenidos. En la utilización o cita de partes de la tesis es obligado indicar el nombre de la persona autora.

WARNING. On having consulted this thesis you're accepting the following use conditions: Spreading this thesis by the TDX (**www.tdx.cat**) service and by the UB Digital Repository (**diposit.ub.edu**) has been authorized by the titular of the intellectual property rights only for private uses placed in investigation and teaching activities. Reproduction with lucrative aims is not authorized nor its spreading and availability from a site foreign to the TDX service or to the UB Digital Repository. Introducing its content in a window or frame foreign to the TDX service or to the UB Digital Repository is not authorized (framing). Those rights affect to the presentation summary of the thesis as well as to its contents. In the using or citation of parts of the thesis it's obliged to indicate the name of the author.

Assessing the degradation and transformation of emerging pollutants submitted to TiO_2 photocatalysis by high-resolution mass spectrometry techniques.

Are we posing a new hazard to the environment?

Javier Jimenez Villarin

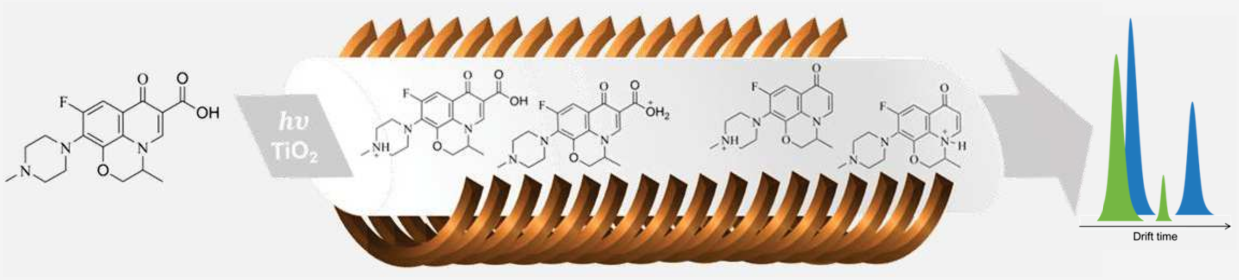

UNIVERSITAT DE BARCELONA

Barcelona 2017

Programa de Doctorat "Química Analítica del Medi Ambient i la Pol·lució"

Assessing the degradation and transformation of emerging pollutants submitted to TiO_2 photocatalysis by high-resolution mass spectrometry techniques. Are we posing a new hazard to the environment?

Memòria presentada per tal d'optar al
títol de Doctor per la Universitat de Barcelona

Javier Jimenez Villarin

Directora de la tesi:

Dra. Encarnación Moyano Morcillo
Departament d'Enginyeria Química i de Química Analítica
Secció Departamental de Química Analítica
Universitat de Barcelona

Barcelona, Juny de 2017.

La Dra. Encarnación Moyano Morcillo, professora titular del Departament d’Enginyeria Química i de Química Analítica (Secció Departamental de Química Analítica) de la Universitat de Barcelona

FA CONSTAR:

que la present memòria titulada "*Assessing the degradation and transformation of emerging pollutants submitted to* TiO_2 *photocatalysis by high-resolution mass spectrometry techniques. Are we posing a new hazard to the environment?*" ha estat realitzada sota la meva direcció pel Sr. Javier Jimenez Villarin en el Departament d’Enginyeria Química i Química Analítica (Secció Departamental de Química Analítica) de la Universitat de Barcelona, i que tots els resultats presentats són fruit de les experiències realitzades pel citat doctorand.

I perquè així es faci constar, expedeixo i firmo el present certificat.

Barcelona, 8 de Juny de 2017

Dra. Encarnación Moyano Morcillo

“*Ai las!*

Sa vida és un principi, un nus i un desenllaç.”

Joan Miquel Oliver

del disc Bombón Mallorquín.

Agraïments

Ja que la memòria d'aquesta tesi, el gruix de la meva "nena", ha estat escrita en anglès, vull utilitzar aquestes pàgines per a poder-me expressar en les meves llengües. Són moltes les persones a les que s'ha de referenciar en aquest punt de la memòria. És per això que, avui, 18 de desembre de 2015, vull començar a plasmar i a madurar sobre el paper els sentiments cap a tots aquells éssers a qui estimo i aprecio.

Primer, vull dedicar aquestes paraules al Dr. Aleix Conesa Cabeza. Crec que per més que et doni les gràcies per tot el que has fet per mi, seguiran essent poques. Gràcies per haver estat el meu *jefe* sense ser-ho, i per haver-me donat una tranquil·litat i confiança infinita. Gràcies per haver-me acompanyat al llarg del mig any de TFG, un més de màster i aquests tres anys de tesi. Gràcies per ser tan i tan generós amb aquesta tesi, doncs per una o altra raó, no has pogut constar com a director d'aquesta. Gràcies per ensenyar-me a lidiar amb diferents tipus de persones i veure-hi sempre la seva part positiva. Per aprendre a saber donar i a ser agraït, a ser pacient i no defallir en l'intent. Però crec que el que més m'emporto de tu és la meva evolució al llarg d'aquest temps. M'has fet créixer com a científic però, sobretot, i arribats a aquest punt, ho he fet com a persona. I, per damunt de tot, m'enduc les lliçons magistrals a la Mola. És allí on he pogut conèixer l'Aleix més íntim, el més personal i el més proper. Has estat tu el que ha plantat la llavor en mi d'apreciar i estimar la muntanya i, aquesta, no deixarà de créixer en tot el que li resta de vida. Espero que estiguis tan orgullós com ho estic jo del producte de tantíssim esforç i, tot i que insuficients, que aquestes paraules et paguin el teu.

A continuación quiero dar las gracias a mi directora de tesis, la Dra. Encarnación Moyano Morcillo, del departamento de Química Analítica de la Universidad de Barcelona. Gracias por las horas de dedicación que le has prestado a todos los trabajos publicados, a esta tesis y a tan buena dirección. Te estoy especialmente agradecido por los buenos consejos ofrecidos durante las correcciones de esta tesis, los cuales han mejorado significativamente la presente memoria.

My special acknowledgments to Dr. David Douce and Dr. Mike McCullagh for making real and possible my visit to Waters Corporation (Wilmslow, United Kingdom). It has been an amazing, fruitful and wonderful experience. Thanks David for making sure that everything was done in the limited time we had (3 weeks) and showing me all around the vast number of Ferraris at Waters and questions I had. Also, thanks Mike for making it real, since my visit would not have occurred if you were not behind the scenes. Unfortunately, we have not worked together, but all discussions I had with you have been invaluable master classes.

Agrair especialment a la Dra. Anna Serra Clusellas, per tots els seus bons consells científics i humans, i per cercar sempre el màxim rigor científic en la present memòria i en tots els treballs realitzats amb tu. Gràcies, per trobar forats per discutir alguns dels resultats d'aquesta tesi tot i estar a l'Argentina. I gràcies per sempre portar un somriure dibuixat a la cara i la seva rialla característica, possible d'ésser escoltada des de l'altre punta de l'oficina.

Également, je dois remercier Dr. Eng. Laurent Aubouy. C'est grâce à vous que j'ai fait mes premiers pas dans la recherche scientifique en m'acceptant au sein du groupe Nanomatériaux. Ça devait être il y a 5 ans, plus ou moins, quand j'étais un chimiste en herbe… Je souhaite aussi vous remercier pour m'avoir donné l'opportunité de faire la thèse de master et spécialement la thèse doctorale parmis vous. C'était un plaisir, mais pas facile, de vous avoir eu comme directeur de thèse. C'était un vrai challenge de ne pas vous décevoir par mon travail de ces 3 dernières années. Finalement, merci beaucoup pour tous les conseils que vous m'avez donnés depuis que l'on se connaît.

També, agrair l'esforç i dedicació a aquesta tesi per part del Dr. Albert Solé del departament de Química Física de la Universitat de Barcelona. Ja no tan sols per la col·laboració científica que hem mantingut al llarg d'aquests darrers mesos, sinó pel tracte, tan humà i tan proper, que he rebut en travessar la porta del seu despatx. Perquè encara recordo aquell primer cop que ho vaig fer, amb només 18 anys, i just acabava d'aterrar a la universitat. Moltíssimes gràcies per les seves lliçons magistrals, i no solament per les de química teòrica i computacional.

Així mateix vull donar tot l'agraïment al departament de SCT (Serveis Cientificotècnics) del centre tecnològic LEITAT, però molt especialment a la Clara, la meva "cuchufleta". Són moltes hores les que hem passat junts, tant a la feina com fora d'ella. A pesar de les friccions que puguem tindre per com de caòtic arribo a ser i per les nostres diferències, t'aprecio i t'estimo. Gràcies per haver-me deixat formar part d'un dels dies més especials de la teva vida.

Tanmateix, a la Dra. Lourdes Gombau i a la Dra. Maria Ángeles Vazquez del grup de *bioinvitro* del centre tecnològic LEITAT, per mostrar una paciència infinita quan em varen ensenyar a treballar en condicions estèrils en cabina de cultius cel·lulars i per la discussió dels resultats derivats de la recerca. Així mateix, agrair a tot el grup pel bon acolliment que vaig rebre en aterrar, Joan, Anna, Jessica, Marta i Alberto. Hem de repetir sopar i sortida... :-)

Tampoc puc oblidar tot el repertori de gent del centre tecnològic LEITAT que m'han acompanyat al llarg d'aquests anys. Perquè tots vosaltres vàreu començar com a companys de feina i la barrera amb la zona personal es va traspassar fa molt i molt de temps... Gràcies a la Laura sexy, Guillem, Silvia, Gemma, Elma, Belén, Ángel, el meu estimat químic orgànic i company de taula, Mazini, Rostoll i tantíssims altres que seria impossible nombrar-los a tots. Tanmateix, als companys de fatigues d'esport, Edu, Pedrito, Pau Serret, Pau Bosch, Cousin... Moltes hores i encara més somriures plegats. Que perdurin molts d'anys aquests moments, que són molt i molt bons.

També recordar a n'Hector el qual va aconseguir que anés a la colla castellera del Poble Sec després de 3 anys, a en Joseba i n'Ainhoa, amb els quals he compartit tants i tants bons moments fora de la feina que seria impossible nombrar-los tots. I a l'Ainhoa, pel meravellós dibuix que hi ha a la portada d'aquesta tesi. I finalment a na Silvi. La distància, l'ésser caòtic que sóc, les mil i una coses que sempre tinc al cap, fa que em preocupi relativament poc d'escriure't. Però hi ets (i sou) ben present(s) en el meu dia a dia.

Recordar-me també d'uns quants bons amics que, tot i haver-me separat físicament d'ells, hi són molt presents emocionalment: na Llucia, n'Helena, en Guillem i n'Alberto (gracias por los repasos de última hora del papeleo de la tesis). També, n'Adrián, na Lucile i na Dori. Mai oblidaré Brussel·les.

Als companys d'universitat. Dr. Oscar Nuñez, Dra. Elida Alechaga, Dr. Sergio Carneado, Juanfra, Raquel i tants altres. En trec valuoses lliçons, moltíssims i moltíssims bons moments a pesar que pràcticament la totalitat de la tesi l'he feta fora de la universitat. Elida i Sergio, heu estat un grandíssim recolzament dins i fora de la universitat, no sabeu fins a quin punt. Estic orgullosíssim d'haver compartit part de la tesi doctoral amb vosaltres. Ja no tant des del punt de vista científic, que també, sinó a

nivell personal. Hem compartit moltes penes però moltíssimes més alegries. I segur que aquí no s'acabaran.

A mis padres, Rigo y Clara. Dudo sinceramente que cojan este librillo, fruto de tantísimo esfuerzo para leer estas palabras, pero creo que llegados a este punto, las palabras escritas nadie se las llevará, salvo incendio y/o hackeo de las copias digitales. A pesar de que no os lo diga cada día y que tengamos riñas día sí, día también, os quiero con auténtica locura. Si hoy estoy aquí defendiendo esta tesis es gracias a vosotros. Gracias a ti, papá, que te levantabas cada día a las cinco y media de la mañana para coger el taxi y lo aparcabas de nuevo a las nueve de la noche. Gracias a ti, mamá, que también te pegabas el madrugón y después de plegar, te preocupabas de llevarme a básquet, que hiciera los deberes, estudiara y que todo fuera bien en casa. Después de 26 años con vosotros, no me dejo de dar cuenta de lo afortunado que he sido de teneros como padres. Suena muy típico, pero yo no podría haber sido más feliz con otros padres. Sois mis ídolos y mi ejemplo a seguir. Os quiero y espero que estéis orgullosos de este día, en el que (teóricamente y salvo susto de enorme envergadura) me otorgarán el título de doctor. Yo me lo he tenido que currar, pero este título, también os hace doctores a vosotros. Os quiero.

I a tu, batiskafo, per oferir-me cada dia un somriure, consol, tranquil·litat, serenor i comprensió en els moments que més ho he necessitat. T'estimo.

~ Index

Page

i) Summary *i*

ii) Resumen *iii*

iii) Abbreviations and acronyms *v*

Chapter 1. Introduction 1

1.1. Pharmaceuticals in the environment 8

1.2. Removal of pharmaceuticals 12

  1.2.1 Non-biological treatments 13

    1.2.1.1. Membrane technologies 13

    1.2.1.2. Adsorption materials 14

    1.2.1.3. Advanced oxidation processes 17

      1.2.1.3.1. Fenton process 18

      1.2.1.3.2. Ozone based processes 19

      1.2.1.3.3. Photocatalysis 20

      1.2.1.3.4. Advanced electrochemical oxidation processes 22

  1.2.2 Biological treatments 28

1.3. Analysis of pharmaceuticals 31

  1.3.1. Sampling and storage 32

  1.3.2. Sample preparation 33

  1.3.3. Instrumental analysis 34

    1.3.3.1. GC-MS 35

    1.3.3.2. LC-MS 37

1.4. References 41

Chapter 2. Objectives and thesis structure 49

Chapter 3. Development and characterisation of TiO_2 nanofibers for photocatalysis applications. 53

3.1. Introduction 55

  3.1.1. Physico-chemical properties of TiO_2 58

3.1.2. Toxicity of TiO_2 58
  - 3.1.2.1. Ecotoxicity of nano-TiO_2 59
  - 3.1.2.2. *In-vivo* toxicity of nano-TiO_2 60
  - 3.1.2.3. *In-vitro* toxicity of nano-TiO_2 60

3.1.3. Strategies for improving TiO_2 efficiency 61
  - 3.1.3.1. Morphological considerations 62
  - 3.1.3.2. Chemical modification 70

3.1.4. Alternative photocatalysts 73

3.2. Experimental section 75

3.2.1. Materials and methods 77
  - 3.2.1.1. Chemicals and reagents 77
  - 3.2.1.2. Synthesis of electrospun TiO_2 nanofibers 77
  - 3.2.1.3. TiO_2 fixation 78
  - 3.2.1.4. TiO_2 characterisation 78
  - 3.2.1.5. Adsorption experiments 79
  - 3.2.1.6. Photocatalytic experiments 79
  - 3.2.1.7. LC-MS/HRMS 81
  - 3.2.1.8. Other analytical determinations 81

3.2.2. Results and discussions 83
  - 3.2.2.1. TiO_2 synthesis 83
  - 3.2.2.2. TiO_2 fixation 85
  - 3.2.2.3. TiO_2 characterisation 87
  - 3.2.2.4. Chemical analysis 91
  - 3.2.2.5. Adsorption kinetics 95
  - 3.2.2.6. Degradation kinetics 101

3.3. Conclusions 107

3.4. References 109

Chapter 4. Tandem high-resolution mass spectrometry and ion mobility mass spectrometry for the characterisation of ofloxacin transformation products. 117

4.1. Introduction 119

4.1.1. Ionisation techniques and mass spectrometers 122

4.1.1.1. Ionisation techniques 122

4.1.1.2. Mass analysers 124

4.1.1.2.1. Hybrid mass analysers 126

4.1.1.2.2. Ion mobility 128

4.1.1.2.2.1. CCS calculation 129

4.1.1.2.2.2. Instrumentation 131

4.1.1.3. Targeted *versus* non-targeted analysis 133

4.1.1.4. Processing tools 136

4.1.1.4.1. Data pre-processing 136

4.1.1.4.2. Data post-processing 140

4.2. Experimental section 143

4.2.1. Materials and methods 145

4.2.1.1. Materials 145

4.2.1.2. Photocatalysis experiments 145

4.2.1.3. Sample treatment 146

4.2.1.4. High performance liquid chromatography 146

4.2.1.5. High-resolution mass spectrometry 146

4.2.1.6. Ion mobility 147

4.2.1.7. Peak extraction 148

4.2.1.8. Data analysis 148

4.2.1.9. Theoretical CCS calculation 149

4.2.2. Results and discussions 151

4.2.2.1. Chemical characterisation of ofloxacin 151

4.2.2.2. Chemical analysis of irradiated samples 151

4.2.2.3. Data processing 155

4.2.2.4. Discrimination between TPs and in-source generated ions 158

4.2.2.5. Characterisation of ofloxacin transformation products 167

4.2.2.6. Adding an extra dimension to high-resolution mass spectrometry 170

4.2.2.7. Ofloxacin degradation pathway 183

4.3. Conclusions 189

4.4. References 191

Chapter 5. Toxicological evaluation of generated transformation products 197

5.1. Introduction 199

5.1.1. Factors affecting toxicity 201

5.1.2. Bioassays 203

5.1.2.1. Invertebrates 208

5.1.2.2. Microbial techniques 208

5.1.3. Cytotoxicity tests 210

5.1.4. Toxicological endpoints 212

5.2. Experimental section 215

5.2.1. Materials and methods 217

5.2.1.1. Chemicals and reagents 217

5.2.1.2. Photocatalysis experiments 217

5.2.1.3. LC-MS/HRMS conditions 218

5.2.1.4. Sample fractionation 218

5.2.1.5. Bioluminescence inhibition test of *Vibrio fischeri* 219

5.2.1.6. Cell culture 219

5.2.1.7. MTT assay 220

5.2.1.8. Statistics 220

5.2.2. Results and discussions 221

5.2.2.1. Selection of human cell lines of choice 222

5.2.2.2. Seeding requirements 223

5.2.2.3. Selection of cell density 225

5.2.2.4. Ofloxacin IC_{50} 226

5.2.2.5. Toxicity kinetics on *Vibrio fischeri* 232

5.2.2.6. Toxicity kinetics on human cells 232

5.2.2.7. Fractionation 236

5.3.Conclusions 245

5.4.References 247

General conclusions 253

Summary

In the past 50 years there has been increasing interest and concern over pharmaceutical drugs and their presence in the environment, since they and/or their metabolites could induce toxicological effects and bacterial resistance in living organisms. Conventional sewage treatment plants are not able to efficiently remove these chemicals, reason why these compounds are being introduced into the aquatic environment at concentration levels of parts per-billion (ppb) and parts per-trillion (ppt). Although these concentrations are much lower than those used in medical applications, the related potential toxic effects are still poorly known and cannot be discarded. Heterogeneous TiO_2 photocatalysis is an advanced oxidation process that can achieve complete oxidation and mineralisation of such organic compounds. TiO_2 nanoparticles and nanofibers have been extensively investigated as the suspended semiconductors in common heterogeneous photocatalysis *set-ups*. However, the complete recovery of the semiconductor is still a major industrial challenge. That is the reason why their fixation onto an inner support represents a great alternative to overcome this problem.

The present PhD thesis has studied the degradation of four pharmaceutical drugs (ofloxacin, clofibric acid, diclofenac and ibuprofen) using two different *set-ups* (suspended and supported conditions) with three different TiO_2 catalysts: synthesised TiO_2 nanofibers and P25 nanoparticles and commercially available nanofibers, used as reference materials. Prior performing the photocatalytical process, all TiO_2 samples were submitted to physical characterisation (BET surface area, X-Ray diffraction and SEM microscopy) showing significant differences between the synthesised and reference materials. Prepared TiO_2 nanofibers, however, appeared to be the material with maximum adsorption capacity (derived from Langmuir's isotherm) and appeared to be slightly better at degrading the pharmaceuticals under study at a concentration of 10 $\mu g\ L^{-1}$. Nevertheless, when the experiments were conducted under real conditions, none of all the studied catalysts could effectively degrade the studied compounds.

Additionally, this work has studied how one of the selected pharmaceuticals (ofloxacin) was degraded along the photocatalytical process by mass spectrometry techniques: (tandem) high-resolution mass spectrometry and ion mobility mass spectrometry. Due to the vast amount of information generated by these *cutting-edge* instruments, different data treatment techniques were applied in order to achieve a fast identification of the generated transformation products (TPs). The degradation of ofloxacin led to the formation of 59 TPs. Chemical structures of these TPs were hypothesised on the basis of their accurate mass and product ion spectra. However, due to the lack of standards of these TPs, these hypothesised structures could not be confirmed until ion mobility, in combination with theoretical calculations, was used. This technique not only rendered additional separation in the gas phase for some of the identified TPs but also provided a tool to support the complete elucidation of the chemical structures hypothesised.

Having detected and identified ofloxacin TPs, the investigation of this PhD thesis was centred on the study of their toxicological impact. Toxicity was assessed by two different end-points: luminescence, using the luminescent bacteria *Vibrio-fischeri* and cytotoxicity using three different human cell lines (HK-2, HepG2 and fibroblast cells). Both end-points clearly demonstrated that, even at low concentrations, the formation of these TPs led to a toxicity increase when compared to the parent drug ofloxacin. Even though this toxicity increase, complete detoxification was achieved by ensuring enough irradiation time and promoting the complete depletion of ofloxacin TPs. The individual toxicity of these TPs was then studied by fractionating the reaction crude with a semi-preparative HPLC column which restricted the number of toxic TPs. Due to the poor chromatographic resolution achieved, the chemical synthesis of the generated TPs seems to be the only option, to date, to study their individual toxicity.

Resumen

A lo largo de los últimos 50 años ha habido un creciente interés y preocupación acerca de los fármacos y su presencia en el medio ambiente debido a que éstos y/o sus metabolitos podrían inducir efectos toxicológicos adversos y/o resistencia bacteriana en organismos vivos. Los sistemas de depuradoras de aguas, actualmente, no son capaces de eliminar estos compuestos, motivo por el cual, son introducidos y detectados en el sistema acuático en concentraciones de partes por billón (ppb) o partes por trillón (ppt). Aunque estas concentraciones reportadas son mucho menores que las usadas en aplicaciones médicas, los efectos adversos de su presencia son poco conocidos y no pueden ser descartados.

La fotocatálisis heterogénea mediante TiO_2 es un proceso de oxidación avanzado que puede conseguir la completa oxidación y mineralización de estos compuestos orgánicos presentes en el agua. El óxido de titanio (IV) en su forma de nanopartícula y nanofibra ha sido ampliamente estudiado en condiciones de catalizador suspendido. Sin embargo, la completa recuperación de este catalizador para su posterior reutilización supone actualmente un reto a escala industrial. Es por ello que, su fijación sobre un soporte inerte supone una alternativa de alto interés para solventar la mencionada limitación.

La presente tesis doctoral se ha centrado en la en la síntesis y caracterización de nanofibras de TiO_2 para la posterior degradación de cuatro fármacos modelo (ofloxacino, ácido clofíbrico, diclofenaco e ibuprofeno). Asimismo, se han utilizado dos catalizadores adicionales como materiales de referencia en la de nanopartícula (P25) y nanofibras. Previo a su uso como catalizadores, todas las muestras fueron sometidas a análisis físicos (área superficial BET, difracción de rayos X y microscopía SEM), los cuales mostraron diferencias significativas entre ellos. Sin embargo, las nanofibras de TiO_2 preparadas se caracterizaron por mostrar la mayor capacidad de adsorción (estudiado mediante la isoterma de Langmuir) y de degradación de los fármacos bajo estudio a una concentración de 10 $\mu g\ L^{-1}$. A pesar de los buenos resultados obtenidos, cuando dichos experimentos fueron realizados con una matriz de agua real, ninguno de los tres materiales estudiados fue capaz de degradar los compuestos referidos anteriormente.

Adicionalmente, en el presente trabajo se estudia como uno de los fármacos seleccionados (ofloxacino, OFX) se degradaba y se transformaba a lo largo del proceso fotocatalítico. Para ello se han utilizado técnicas basadas en la espectrometría de masas, concretamente la espectrometría de masas en tándem, la de alta resolución y la de movilidad iónica. La combinación de las tres técnicas persigue la caracterización de los diferentes productos de transformación (TPs) del OFX. Se utilizaron diferentes filtros de tratamiento de datos para conseguir su rápida y selectiva detección. El análisis de los datos permitió la identificación de 59 productos de transformación, proponiendo sus estructuras químicas asociada con el empleo combinado de las técnicas de tándem y de alta resolución. No obstante, la utilización de la técnica de movilidad iónica acompañada de los cálculos teóricos permitió la confirmación inequívoca de algunos de estos compuestos isobáricos. El estudio de la aplicabilidad de dicha técnica de análisis ha puesto de manifiesto su capacidad para la separación de diferentes productos de transformación en la fase gas a pesar de su coelución cromatográfica y de su similitud en los espectros de masas. Además ha demostrado ser una herramienta de alto valor para la confirmación de las estructuras químicas que ya habían sido propuestas.

Después de la detección y la identificación de los productos de transformación del ofloxacino, la investigación se ha centrado en el estudio de la toxicidad de estos productos generados. Dicha toxicidad ha sido evaluada mediante dos métodos (endpoints): 1) luminiscencia, mediante la bacteria luminiscente *Vibrio-fischeri* y 2) citotoxicidad usando tres líneas celulares humanas (HK-2, HepG2 y fibroblastos). Ambos endpoints claramente han demostrado que la generación de estos productos de degradación produce un incremento de la toxicidad, a pesar de encontrarse a concentraciones bajas. Aun así, la completa detoxificación se ha podido conseguir irradiando durante suficiente tiempo la solución de estudio para asegurar la eliminación de los productos de transformación. A fin de estudiar la toxicidad individual de cada uno de los TPs generados, el crudo de reacción obtenido se fraccionó mediante un HPLC semipreparativo. Sin embargo, la baja resolución cromatográfica obtenida y el gran número de analitos presentes, complicó. No obstante, se ha observado que sólo una de las fracciones experimentó un aumento de toxicidad. Actualmente, la síntesis química de cada uno de los TPs identificados, parece la vía más factible para posibilitar el estudio individual de los productos generados y así estudiar sus posibles efectos sobre el medio ambiente y organismos vivos.

Abbreviations and acronyms

ADME	Adsorption, Desorption, Metabolism and Excretion
APCI	Atmospheric Pressure Chemical Ionisation
AEOPs	Advanced Electrochemical Oxidation Process
AOP	Advanced Oxidation Process
API	Atmospheric Pressure Ionisation
APPI	Atmospheric Pressure PhotoIonisation
BDD	Boron-Doped Diamond
CI	Chemical Ionisation
COD	Chemical Oxygen Demand
C_{18}	Octadecyl stationary phase
C_8	Octyl stationary phase
CB	Conduction Band
CLOF	Clofibric acid
CCS	Collission Cross Section
CID	Collission Induced Dissociation
COD	Chemical Oxygen Demand
CYP450	Cytochrome P-450
CW	Constructed Wetland
D. Magna	*Daphnia Magna*
DAD	Diode Array Detector
DART	Direct Analysis in Real Time
DCF	Diclofenac
DDA	Data Dependant Analysis
DESI	Desorption Electrospray
DIA	Data Independent Analysis
DNA	Deoxyribonucleic acid
EC	European Commission

ECD	Electron Capture Dissociation
EHSS	Exact Hard-Sphere Scattering
EQS	Environmental Quality Standards
EQSD	Environmental Quality Standards Directive
EI	Electron Ionisation
ESI	Electrospray Ionization
ESP	Electrostatic Surface Potential
FIA	Flow Injection Analysis
FLD	Fluorescence Detector
FT-ICR	Fourier Transform Ion Cyclotron Resonance
FWHM	Full Width Half Maximum
GC	Gas Chromatography
GC-MS	Gas Chromatography coupled to Mass Spectrometry
Ha	Hartree
HAc	Acetic acid
HCD	High Collision Dissociation
HILIC	Hydrophilic Interaction Liquid Chromatography
HLB	Hydrophilic-Lipophilic Balance
HRMS	High-Resolution Mass Spectrometry
IBU	Ibuprofen
IC_{50}	Half maximal Inhibitory Concentration
ICP-MS	Inductively coupled plasma coupled to Mass Spectrometry
IM	Ion Mobility
IT	Ion Trap
LC	Liquid Chromatography
LC-MS	Liquid Chromatography coupled to Mass Spectrometry
LC-MS/HRMS	Liquid Chromatography coupled to Tandem High-Resolution Mass Spectrometry
LIT	Linear Ion Traps

LOD	Limit of Detection
LOQ	Limit of Quantification
MF	Microfiltration
MIP	Molecular Imprinted Polymer
MISPE	Molecular Imprinted Solid Phase Extraction
MRM	Multiple Reaction Monitoring
MS	Mass Spectrometry
MS/HRMS	Tandem High-Resolution Mass Spectrometry
MS^n	Multiple Stage Tandem Mass Spectrometry
MTT	3-[4,5-dimethylthiazol-2-yl]-3,5-diphenylformazan
NCE	Normalised Collision Energy
NHE	Normal Hydrogen Electrode
NMR	Nuclear Magnetic Resonance
NF	Nanofiltration
NFs	Nanofibers
NPA	Natural Population Analysis
NPs	Nanoparticles
NSAIDs	Non-Steroidal Anti-Inflammatory Drugs
OECD	Organisation for Economic Co-operation and Development
OFX	Ofloxacin
OFX-d_3	Ofloxacin-d_3
PA	Projection Approximation
PCA	Principal Component Analysis
PVP	Polyvinylpyrrolidone
Q	Quadrupole
QqQ	Triple Quadrupole
Q-ToF	Quadrupole – Time of Flight
Q-TRAP	Quadrupole – Ion Trap

QuEChERS	Quick, Easy, Cheap, Effective, Rugged, Safe
RANSAC	RANdom SAmple Consensus
RNA	Ribonucleic acid
RO	Reverse Osmosis
ROS	Reactive Oxygen Species
SEM	Scanning Electron Microscopy
SIM	Selected-Ion Monitoring
SPE	Solid Phase Extraction
SRM	Selected-Reaction Monitoring
TIP	Titanium Isopropoxide
TiO_2	Titanium (IV) oxide
TM	Trajectory Method
TPs	Transformation Products
Triton X-100	4-octylphenol polyethoxylate
TWIMS	Tavelling Wave Ion Mobility
ToF	Time of Flight
UF	Ultrafiltration
UHPLC	Ultra High Performance Liquid Chromatography
UPLC	Ultra Pressure Liquid Chromatography
V. fischeri	*Vibrio fischeri*
VB	Valence Band
XRD	X-Ray Diffraction

~ Chapter 1.

Introduction

It all starts with education. Highly developed and industrialised societies have traditionally viewed water as a plentiful, cheap and poorly considered resource if it is directly compared to gas or electricity. However, this fact has come up to a point where it is no longer valid.

With the increasing population growth and industrialisation experimented during the last decades, a noticeable interest and awareness have arisen from both public and scientific communities related to the environment and associated problems that did not exist before. These uncontrolled growing patterns, in combination with poor environmental education and the inexistence of governmental campaigns supporting water efficiency, have led to the overexploitation of aquifers and other water resources. Moreover, climate change has not helped at all to tackle this problem. Water scarcity and drought episodes have started to be common phenomena in areas of the world that used not to have such these problems. These water unavailability or restricted availability events were common in areas with low rainfall in certain seasons but have converted to a serious problem in areas with high population density, intensive irrigation and industrial activity. For instance, several studies have already pointed out the possible outcome on water availability in the European Union (**Figure 1.1**) by the year 2030.

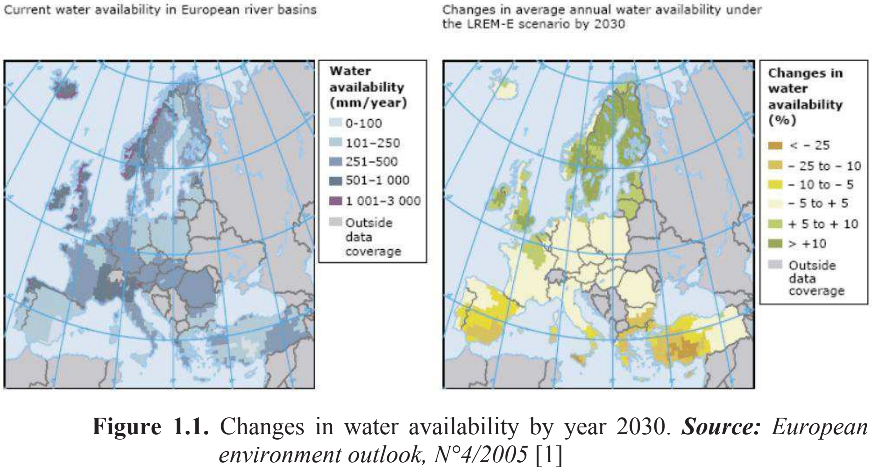
Current water availability in European river basins
Water availability (mm/year)
0-100
101-250
251-500
501-1 000
1 001-3 000
Outside data coverage
Changes in average annual water availability under the LREM-E scenario by 2030
Changes in water availability (%)
< - 25
- 25 to - 10
- 10 to - 5
- 5 to + 5
+ 5 to + 10
> +10
Outside data coverage

Figure 1.1. Changes in water availability by year 2030. ***Source:*** *European environment outlook, N°4/2005* [1]

This continuous overexploitation and uncontrolled waste of natural resources, helped with the inexistence of highly developed water treatment technologies, has been accompanied with a growing anthropogenic contamination of the water resources. If water pollution is not (partially) reduced in the years to come, this may pose a relevant and serious environmental and human health problem. The prevention of contamination was, and still is, far away from becoming a reality, especially on those developed and highly industrialised cities and countries.

A wide range of anthropogenic compounds are continuously detected in industrial and municipal wastewater. Some of these compounds (both synthetic organic and inorganic chemicals and naturally occurring substances) may pose severe problems in biological treatment systems due to their resistance to biodegradation or/and toxic effects on microbial processes. Amongst these chemicals, the discharge of heavy metals, fertilizers, pesticides, pharmaceuticals (and their metabolites) and other consuming goods meant about $6 \cdot 10^6$ tones in the year 2000 [2].

However, in the past 10 years, governmental organisations, with the help and assistance of chemists, biologists and engineers, have finally put in practice new environmental policies and legislations to achieve a higher control on the disposed water quality and use, giving emphasis on the creation of lists of chemicals to be considered, in terms of concentration, to be monitored in the coming years.

This is the case of the European Union, which, in 2000, launched a directive (directive 2000/60/EC [3]) establishing a framework for community action in the field of water policy. In this first directive, the European Commission established the bases for the monitoring of water quality: selection of monitoring sites, parameters to be monitored (oxygen content, conductivity, etc.), monitoring of long term anthropogenically trends in pollutant concentrations, etc. Hence, this first directive included a list of 45 substances consisting in heavy metals (and metal complexes) and organic compounds (specific molecules or families of chemicals). However, this directive only focused in the inclusion of these substances but did not specify the maximum allowed concentration in the monitored water.

It was in 2008, however, when the EU launched a reviewed version of that of 2000, (directive 2008/105/EC [4]; (the Environmental Quality Standards Directive, EQSD)), to ensure the identification and quantification of a reviewed list including, this time, 33 substances to be monitored (12 less than listed in directive 2000/60/EC). This directive, however, annexes 13 chemicals subject to be considered priority substances or priority hazardous substances in reviewed directives, which included α-amino-3-hydroxy-5-methyl-4-isoxazolepropionic acid (AMPA), glyphosate and dioxins, amongst others.

The Commission conducted a review of the list of priority substances in 2013, directive 2013/39/EU [5], reaching the conclusion, with the support from the scientific committee on health and environmental risks, that it was needed to modify the list of priority substances by identifying new substances for priority action at the Union level, also setting the environmental quality standards (EQS) for those newly identified substances, and submitting to revision the EQS for those substances already included in the past directive. Hence, this directive included, another time, the presence of 45 chemicals to be monitored and quantified (**Figure 1.2**). Surprisingly though, was the maximum allowed concentration of some chemicals, for instance benzo(g,h,i)-perylene, cypermethrin, dichlorvos, heptachlor and heptachlor epoxide, which ranged from $3 \cdot 10^{-5}$ to $8 \cdot 10^{-4}$ µg L^{-1}, concentrations completely out of the scope of cutting-edge analytical platforms.

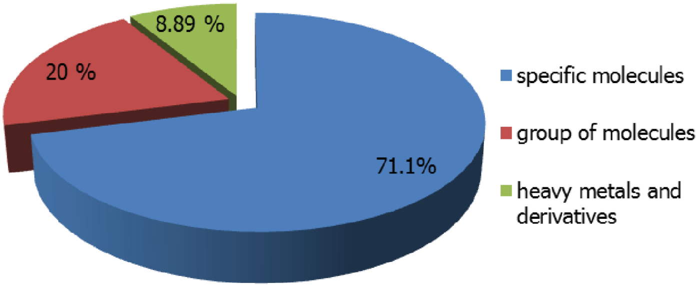

Figure 1.2. Distribution of chemicals as described by directive 2013/39/EU.

Both 2008 and 2013 directives settled up several mechanisms by which the European Commission, in the coming years after both directives were launched, should create a “watch list” that would be used as an instrument to require temporary monitoring (up to 4 years). This list would include other substances (up to a maximum of 10 substances or group of substances, not the already included priority substances) for which experimental evidences suggested a possible risk to or via the environment. The latter goal of this watch list was to inform on the selection of additional priority substances to be included in revisions of the latest EU water framework directives. These “other substances” were aimed at emerging pollutants for which the available monitoring data was either insufficient or of insufficient quality for the purpose of identifying the risk posed across the EU. This list could increase by one at each update, up to a maximum of 14 substances or groups of substances.

This came into a reality in 2015 (Decision 2015/495 [6]) when this directive included the chemicals listed in **Table 1.1**. The EU experts committee, however, had already chosen, in the 2013 Directive and before the creation of the first watch list, three chemicals that should be included in the first watch list to facilitate the determination of appropriate measures to address the risk posed by those substances: the natural hormone oestradiol (E2) and two pharmaceuticals, the anti-inflammatory diclofenac and the synthetic hormone ethinyl oestradiol (EE2), used in contraceptives.

Table 1.1. List of chemicals included in the first watch list.

Diclofenac
17-Beta-estradiol (E2), Estrone (E1)
17-Alpha-ethinylestradiol (EE2)
Oxadiazon
Methiocarb
2,6-ditert-butyl-4-methylphenol
Tri-allate
Imidacloprid, Thiacloprid, Thiamethoxam, Clothianidin, Acetamiprid
Erythromycin, Clarithromycin, Azithromycin
2-Ethylhexyl 4-methoxycinnamate

The main criteria used for inclusion in the initial list of candidate substances were:

1) The substance was suspected of posing a significant risk to, or via, the aquatic environment

2) There was not enough information: insufficient monitoring data or data of insufficient quality, nor sufficient modelled exposure data to decide whether to prioritise the substance.

Hence, an initial list of 43 substances was created, including pharmaceuticals such as ofloxacin, ciprofloxacin, ibuprofen, etc., heavy metals (zinc and its compounds) and chromium, amongst other chemicals. 16 substances were then de-selected based on availability of sufficient monitoring data. The final dataset (**Table 1.1**) was obtained after studying the substance-specific hazard data and information on exposure to the substance in or via the aquatic environment.

It is for this reason that governments have also invested large amounts of money in education campaigns supporting water efficiency and in developing or improving water treatment technologies able to handle with environmentally relevant pollutants. These technologies are not only expected to provide efficiency but also to be environmentally and health friendly (ecosystems and humans). The main processes involved in the removal of micropollutants are biological, chemical transformation (activated sludge, membrane bioreactors, advanced oxidation processes), and sorption (pollutants are removed by the adhesion to a sorbent but they are not degraded), all summarised in **Figure 1.3**. **Table 1.2** lists advanced oxidation processes (AOPs) employed for the removal of environmentally relevant organic compounds. In recent years, advanced oxidation processes (destroying organic pollutants using free radicals), has proved to be an useful degradation technique, likely to be used and installed in wastewater treatment plants. These AOPs will be further reviewed in **section 1.2.1.3**, on the removal of organic compounds from water matrices.

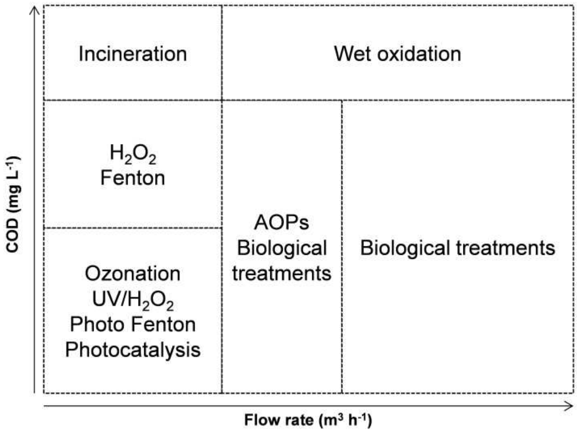

Figure 1.3. Current wastewater treatment technologies as a function of pollutant load and water flow to be treated.

The existing technology, however, lacks of flexibility and adaptability in terms of pollutants nature, concentration load of these pollutants, water volume and flow to be treated. Hence, current research is devoted to the adjustment of such flexibility in water treatment conditions, also enabling combinations of biological and/or chemical treatments in order to achieve higher degradation rates and their easy incorporation to wastewater treatment plants.

1.1. Pharmaceuticals in the environment

The advances made over the last century by the scientific and medical communities are out of question. Both communities have been the responsible for the observed increase in life expectancy in developed countries [7]. Some researches evidenced that, in combination with medical technology, the great development and investment done in the pharmaceutical industry over the past 20 years (**Figure 1.4**) has been the main reason for this increase in life expectancy all over the world.

Table 1.2. Current AOPs available for wastewater treatment.

AOP	Oxidation basis
Ozone-based	O_3/UV
	O_3/H_2O_2
	O_3/H_2O_2/UV
Heterogeneous photocatalysis	Catalyst/Uv-Vis
	Catalyst/Uv-Vis/H_2O_2
Homogeneous photocatalysis	Fenton (H_2O_2/Fe^{2+})
	Photo-Fenton (H_2O_2/Fe^{2+}/UV)
Photochemistry processes	H_2O_2/Fe^{2+}/UV
Sub-critical wet air oxidation	H_2O/Temperature/Pressure
Ultrasounds oxidation	Ultrasounds/H_2O
	Ultrasounds/H_2O_2
	Ultrasounds/O_3
Electrochemical oxidation	Pt, TiO_2,IrO_2, PbO_2, BDD/H_2O
	Pt, TiO_2,IrO_2, PbO_2, BDD/H_2O_2/Fe^{2+}

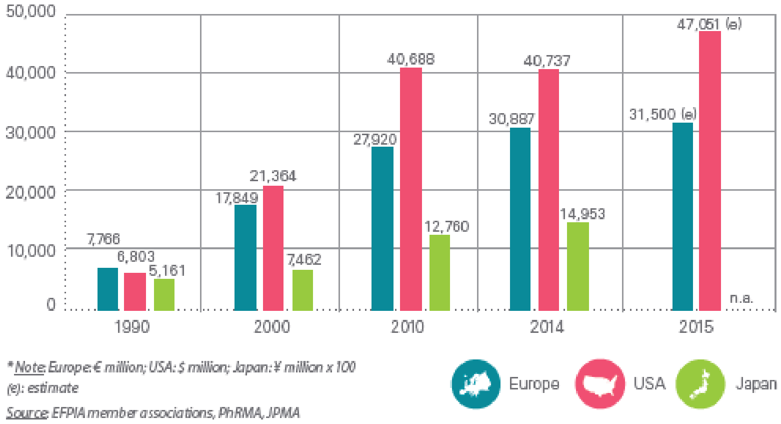

*Note: Europe: € million; USA: $ million; Japan: ¥ million x 100

(e): estimate

Source: EFPIA member associations, PhRMA, JPMA

Figure 1.4. R&D investment in pharmaceuticals in the EU, USA and Japan. Adapted from European Federation of Pharmaceutical Industries and Associations report 2016 [8]

But, what is a pharmaceutical?

According to the latest version of the Directive 2001/83/EC3 [9], Directive 2004/27/EC [10], on the Community code relating to medicinal products for human use:

"a) Any substance or combination of substances presented as having properties for treating or preventing disease in human beings; or

b) Any substance or combination of substances which may be used in or administered to human beings either with a view to restoring, correcting or modifying physiological functions by exerting a pharmacological, immunological or metabolic action, or to making a medical diagnosis."

The increasing research and efforts done in this field have led to the development and availability and authorisation of three thousands active pharmaceutical ingredients (APIs) which are currently authorised in the EU market (4000 worldwide), with an overall consumption of about 100,000 tons or more every year [11]. Moreover, recent reports published by the Organization for Economic Co-operation and Development (OECD) in 2015 [12] points out the growing demand and expenditure of pharmaceuticals to treat chronic diseases (cancer, diabetes and mental illness), population ageing, changes in clinical, etc. However, this tendency changed in years comprised from 2009 to 2014, as depicted in **Figure 1.5**. The average annual growth rate for the overall European Union experimented a 1.4% increase per year in the 2005-2009 period (pre-crisis), while dropped by 1.1% in the same period comprising the years 2009-2014. This reduction was significantly high in Greece (-8.5%), Portugal (-7.5%) and Denmark (-5.3%), mainly attributed to cutbacks done by local governments during the economic and financial crisis.

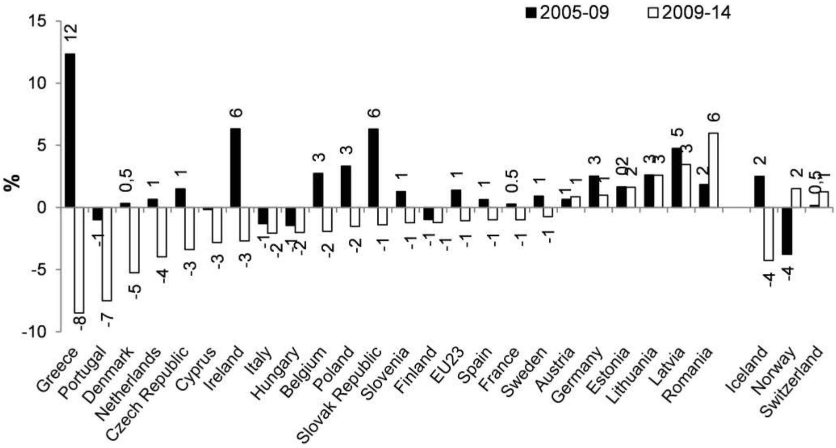

Figure 1.5. Pharmaceutical consumption in the EU (2005-2014). *Adapted from OECD report* [11].

These pharmaceuticals can be classified as: hormones, anti-cancer, antidepressants, antibiotics, etc. Pharmaceuticals and their related products (transformation products and metabolites) have been detected in such a wide variety of environmental samples such as surface water, groundwater, soil, air, biota and in wastewater [13–18] at concentrations ranging from ng L^{-1} to μg L^{-1} levels.

Pharmaceuticals and related products can enter the environment via different sources such as manufacturing facilities, hospitals, agricultural, domestic use (consumption) and improper disposal. However, it is assumed that, and mainly because the elevated price of the active ingredients, pharmaceutical disposal done by pharmaceutical industries is negligible [19,20]. Moreover, these production facilities employ good manufacturing practices (GMPs), comply with environmental legislations and try to recover active pharmaceutical ingredients [19,20].

Hence, it is therefore after consumption, and once pharmaceuticals are excreted as a mixture of parent compounds and metabolites (both biological active and inactive), that pharmaceuticals are emitted to the sewage system. These compounds may then be released to surface waters or enter terrestrial systems through sewage effluent and/or sludge, when used for irrigation or as a fertiliser to agricultural land.

Pharmaceuticals under study in this PhD thesis

The present PhD thesis has focused on the study and the removal by advanced oxidation processes of four pharmaceutical drugs belonging to three different drug families: ofloxacin (fluoroquinolones), clofibric acid (fibrates), diclofenac and ibuprofen (NSAIDs (non-steroidal anti-inflammatory drugs)).

Fluoroquinolones are a wide class of antibacterial agents used for human and veterinary applications. Fluoroquinolones are photolabile compounds that absorb photons within the range of natural sunlight, being able to generate reactive oxygen species (ROS), causing DNA damage and genotoxicity on eukaryotic cells. As a consequence, they can photosensitize red blood cells, decrease cell viability, induce lipid peroxidation and DNA strand-breaks in *in-vitro* and *in-vivo* tests [21–25]. Fluoroquinolones inhibit DNA gyrase, a type II topoisomerase, and topoisomerase IV inhibiting cell division [26]. They display high activity not only against bacterial topoisomerases [27], but also against eukaryotic topoisomerases [28]. Ofloxacin (**Figure 1.6**) is a second-generation fluoroquinolone used to treat mild to moderate bacterial infections and it is always administrated when less toxic fluoroquinolones have not been successful in treating the bacterial infection.

Clofibric acid (**Figure 1.7**) belongs to the family of fibrates which medical use is intended to lower plasma lipids, mainly triglyceride levels. In the 1980s, clofibric acid was banned or highly restricted because the high mortality rate attributed to clofibric acid and cancer enhancement. Clofibric acid was the first pharmaceutical drug to be detected in water in the 1950s by Hignite and Azarnoff [29] and has an estimated persistence in the environment of 21 years. Moreover, it is still detectable in lakes and rivers after its withdrawal from the market.

pKa$_1$ = 6.08 and pKa$_2$ = 8.25 [30];
pKa$_1$ = 6.10 and pKa$_2$ = 7.99 [31]

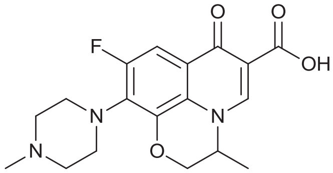

Figure 1.6. Ofloxacin chemical structure

pKa = 2.84 [32]

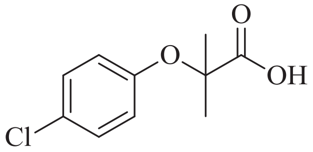

Figure 1.7. Clofibric acid chemical structure

Ibuprofen and Diclofenac (**Figures 1.8 and 1.9 respectively**) are well known pharmaceuticals commonly used for the whole society as pain killers. Both chemicals belong to the family of NSAIDs (non-steroidal anti-inflammatory drugs). Their consumption and market sales represent the 40 % of the available NSAIDs [33–36]. These pharmaceuticals have vastly demonstrated their efficacy in the management of pain and for their analgesic and anti-inflammatory properties, being used by more than 30 million people every day all over the world. NSAIDs inhibit the biosynthesis of prostaglandins by preventing the substrate arachidonic acid from binding to the COX enzyme active site [37,38].

pKa = 4.54 [39]

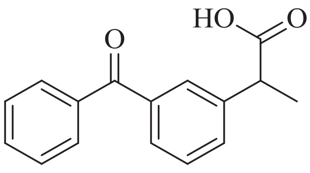

Figure 1.8. Ibuprofen chemical structure

pKa =4.19 [39]

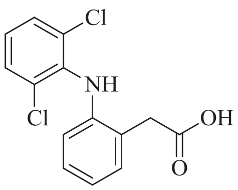

Figure 1.9. Diclofenac chemical structure

1.2. Removal of pharmaceuticals

As it has been already mentioned along the present chapter, governmental institutions have invested large amounts of money on the investigation and development (or optimisation and scale-up) of water treatment technologies capable of removing pollutants (both organic and inorganic) from industrial and urban wastewaters.

The recovery and reutilisation of urban and industrial wastewaters have been and still is one of the pillars and main topics of current investigation done in this field. These researches and projects not only focus on the removal of regulated organic and inorganic pollutants but also ensure the recovery of energy and the re-use of chemicals and nutrients. That is the reason why, the European Union, for example, has invested more than 2400 Million euros in the past nine years (**Figure 1.10**) in "Water" calls. This chart represents all the investment done under the challenge "Climate action, environment, resource efficiency and raw materials" from both FP7 framework (2007-2013) and Horizon 2020 projects (2014 to date).

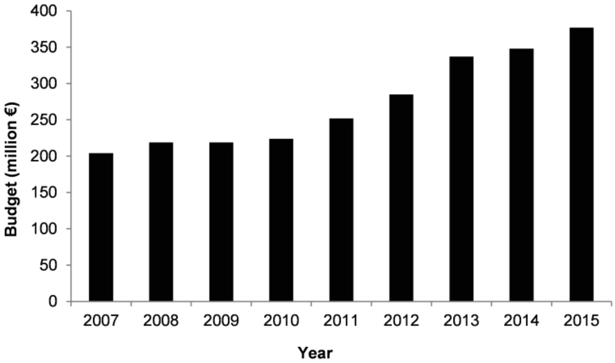

Figure 1.10. Budget for financed european projects under the FP7 and H2020 frameworks.

Along the mentioned years, EU funded projects not only have centred their investigations on basic research (new technologies, approaches, etc.) but also have had to come up with new ideas for bringing new or conventional water treatment technologies available to the market. Hence, sections 1.2.1 and 1.2.2 of this introductory chapter will review the main wastewater treatment technologies with higher TRL (Technology Readiness Level) or technologies that have demonstrated promising results at laboratory scale and that should be available in the market in the coming years.

1.2.1- Non-biological treatments

1.2.1.1- Membrane technologies

The recovery of urban and industrial wastewater has been identified as a viable way for the reutilisation of water, for the preservation of natural resources and to reduce the consumption of fresh water. In this way, water treatment technologies based on membrane processes have been vastly studied and applied in wastewater treatment plants, achieving satisfactory results in the reutilisation of industrial wastewater [40–46].

Reverse osmosis (RO) has been identified as the best technology for water purification and its later reutilisation in such a wide variety of applications where the complete removal of total dissolved solids (TDS) and pollutants is required [40–48], such as drinking water, military uses, food industry, etc.

Fouling, however, is the worst enemy of reverse osmosis membranes [49–53]. The accumulation of particulate matter in the membrane surface reduces their lifespan, making the whole treatment process unviable due to the high costs associated. In order to prevent (or reduce) this phenomenon, low-pressure filtration membranes such as those used in microfiltration (MF), ultrafiltration (UF) and nanofiltration (NF) are used as pre-filters of reverse osmosis. In comparison to conventional water pre-treatments, based on the use of chemicals, these MF and UF treatments not only provide a water of higher quality but also reduce energy consumption and costs (both operation and maintenance).

RO fouling is mainly controlled by the cited pre-treatments and the wastewater treatment plant design. Amongst all parameters that can be changed to prevent fouling, pH, temperature and water flow rate have the deepest weight on the lifespan of RO membranes. Moreover, these membranes can be treated with chemicals such as ammonia and sodium hypochlorite to prevent biological contamination, as stated by De la Torre *et al.* [54] , which attributed the formation of chloroamines to the enlargement of RO's membranes life.

However, with the increasing needs of water purification by means of reverse osmosis, it has been vastly demonstrated in industrial applications the extended lifespan of RO membranes when used in combination with MF or UF membranes as pre-filters. In addition to fouling reduction, these pre-filters decrease the cleaning, disinfection and substitution needs of RO membranes, thus, making the whole process more efficient and economically viable. UF is particularly interesting as a previous step of RO in order to reduce turbidity

(<0.1 NTU), the total content of suspended solids (TSS), pathogen organisms (virus, coliform bacteria, amongst others) and particles (algae, bacteria, microorganisms, etc.).

Several strategies [55–63] have been investigated and adopted to improve the lifespan of these membranes, which include:

- The use of acids and bases to clean UF membranes. For instance, sodium hydroxide is commonly employed to remove organic matter, colloids and silicates and hydrochloric and sulfuric acid are commonly employed for the removal of inorganic chemicals. The combination of alkali-acid-alkali has been reported to favour and improve the reuse of these membranes through a high number of cycles.
- The introduction of oxidising agents such as hydrogen peroxide and sodium hypochlorite have been used to remove organic matter and bio-fouling. Amongst them, sodium hypochlorite offers better results and it is more efficient at higher pH.
- The application of air scour. This method has been widely employed since it does not require the use of chemicals for the removal of the fouling deposited onto UF membranes. This technique consists in the injection of air to the filter so the filter bed expands, forcing accumulated particles to be into suspension.
- Backwashing refers to pumping water backwards, during a certain amount of time, so the filter or membrane in operation can be successfully cleaned, thus improving its filtering and cleaning capacities. Backwash water is then collected and stored for its latter treatment, since its discharge is highly regulated and discouraged.
- The application of ultrasounds. In a similar way as occurred with the Air Scour technique, the use of high frequency pulses forces particulate matter adsorbed onto membranes to desorb.

1.2.1.2- Adsorption materials

Amongst all water treatment technologies, adsorption phenomena based on materials with high-adsorption capabilities are the most used in industrial applications due to its simplicity, easy manipulation and low price. This technique is especially interesting for the separation, extraction and valorisation of heavy metals in industrial and urban wastewaters.

Several materials have been studied and widely employed as industrial solid adsorbents for this kind of applications, such as activated carbon (both mineral and vegetal origins), zeolites, metallic oxides and resins [64–72]. Even though these materials have high adsorbent capacities (1000-3000 $m^2 g^{-1}$), these are usually expensive and non-selective, thus, disabling the possibility of recovering compounds of interest such as heavy metals, rare earths and precious metals.

Activated carbon

Activated carbon is, by far, the adsorption material mostly employed for the removal of chemical substances (both organic and inorganic) contained in water and air [69–73]. Its installation and implementation in wastewater treatment plants is rather new and dates back to 1920-1940 in Europe and the United States. At the very beginning, this material was used as a purification and separation technology, mainly used as filters. It was in the late 60s – early 70s when activated carbon was found to be efficient at removing a broad spectrum of chemicals.

The manufacturing process of activated carbon consists of two phases: carbonization and activation. The first step involves the pyrolysis, up to 600-900 ºC, of the carbon-rich material (coal, peat, or any other rich-carbonaceous material) in an inner atmosphere. Once the material is thermally treated, the material undergoes activation through different methods: gas or chemical treatment. Gas activation consists in the oxidation of the material under a heated oxygen stream (900-1200 ºC) so the oxygen can bond to carbon. If the chemical treatment is to be done, carbonization and activation occur at the same time. The rich-carbonaceous material is submerged into a bath of acid or base. The whole bath is then heated up to 450-900 ºC, obtaining the final product in this one-step synthesis.

Activated carbon is applied in two forms; powdered (PAC) and granular (GAC) in packed bed filters. Several authors have largely demonstrated the removal efficiency. For instance, Katsigiannis *et al.* [70] mostly achieved the complete removal of bisphenol A, triclosan, ibuprofen, naproxen and ketoprofen using bed depths ranging between 4 and 16 cm of GAC. On the other hand, Margot *et al.* [72] compared the efficiency of PAC beds to conventional wastewater treatment plants and ozone for 70 micropollutants at $\mu g\ L^{-1}$ concentration levels. Their results showed enhanced removal rates compared to WWTPs and equivalent removal rates in respect to ozone-based technologies.

Molecularly imprinted polymers

Contrary to activated carbon, which is a general and non-specific sorbent, molecularly imprinted polymers (MIPs) represent an alternative and interesting material for the selective recovery of both organic and inorganic compounds.

Molecularly imprinting is not new and the first publication dates back to 1931, when Polyakov *et al.* [74] carried out the first investigations using silicones for their latter use in chromatography applications. Research continued while in 1972, two independent groups, Klotz *et al.* and Wulff *et al.* [75] used this technology on synthesised organic polymers. In both studies, molecular recognition was done by covalent interactions. It was not until 1994, when Mosbach *et al.* [76] established a new methodology to obtain MIPs whose molecular recognition was based on electrostatic interactions or hydrogen bonding. Nowadays, most of the published records on MIPs are based on this synthesis method and molecular recognition.

MIPs are obtained in a cost-effective and easy way and starts by the polymerisation of a monomer (2-vinylpyridine, 4-vinylpyridine, m-divinylbenzene, p-divinylbenzene, methacrylic acid, etc.) in the presence of the template (the target molecule or complex to be recognised by the synthesised polymer). It is this step where the electrostatic and hydrogen bonding interactions start to occur. In this reaction, a cross-linker is usually used to give the polymer more stiffness and porosity. Finally, this template is removed from the polymer matrix leaving available specific sites for the latter recognition of the imprinted molecule or complex (**Figure 1.11**).

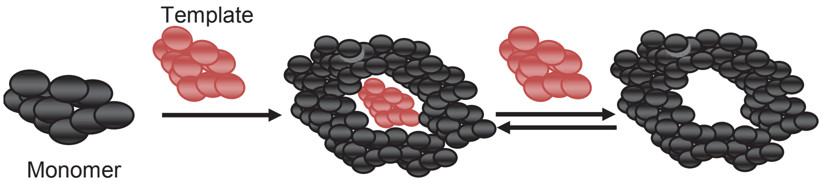

Figure 1.11. Scheme on MIPs molecular recognition.

Even though MIPs have not extensively been used for industrial applications, some researches have conducted the selective recovery of heavy metals in water [77–79], but more efforts have to be driven towards their implementation for the selective recovery of more than two elements simultaneously. Moreover, their extensive applicability has already been demonstrated in such a wide variety of investigation fields, such as aminoacid detection [77–79], explosives [80], pesticides [81], etc. as well as on-line sensors [82]. Even though they have not been designed for wastewater treatment plants, an alternative application is devoted to chromatography, electrophoresis and solid phase extraction (SPE) [83–87]. This last possible use has led to a wide number of scientific publications due to the high interest of separating, recovering and concentrating target molecules of interest.

1.2.1.3- Advanced oxidation processes

Advanced oxidation processes (AOPs) are chemical treatments designed to non-selectively remove organic and inorganic pollutants in water. They are all characterised by the *in-situ* generation or radical species of high oxidising power, mainly the radical hydroxyl (•OH), E^o_{NHE} (•OH/H_2O) = 2.80 V *versus* NHE (normal hydrogen electrode). This kind of processes have been of special interest for those pollutants that, with conventional water treatments such as membranes or biological treatments, have been found to present a high chemical stability and/or strong difficulty to be completely mineralized.

Most of the studied AOPs operate at, or near operate, at room temperature and atmospheric pressure. AOPs can be classified according to the reaction phase (homogeneous or heterogeneous) or on the way the hydroxyl radical is generated (chemical, electrochemical, photochemical, etc.). Some of the most developed AOPs include: heterogeneous photocatalysis with TiO_2 (it can also be assisted with the addition of H_2O_2; (TiO_2/H_2O_2)), ozone based technologies (also assisted with the addition of H_2O_2 (O_3/ H_2O_2) with or without UV with the irradiation of UV light (O_3/H_2O_2/UV), H_2O_2/UV, and Fenton like reactions, such as Fenton, photo-Fenton and electro-Fenton. The way on which each of these mentioned techniques remove organic pollutants is based on the non-selective attack of the radical hydroxyl, but differing in how this *in-situ* generation of the •OH is performed (explained in detail in the coming sections), giving an intrinsic versatility to advanced oxidation processes. **Table 1.3** shows some examples on the AOPs technologies employed for the degradation of the chemicals under study.

In order to increase the purification efficiency, the integration of biological treatments as a previous or post AOP step has been explored and successfully applied [88–90], exploiting the individual potentialities offered by both treatments. However, the main goal should be focused towards the minimisation of the AOP in front of the biological stage, while being able to reduce at maximum the use of chemicals and energy consumption. Another issue concerning AOPs applicability is that referring to the organic load, expressed as COD (chemical oxygen demand). Only wastewater with small COD contents ($\leq$5.0 g L^{-1}) can be suitably treated by means of these oxidation techniques. Higher COD contents would require the consumption of higher amounts of chemicals and energy consumption.

1.2.1.3.1. Fenton process

The water treatment process based on the Fenton reagent is nowadays one of the most used technologies for the purification of industrial wastewaters [91–99]. The oxidative properties of hydrogen peroxide with Fe^{2+} salts were first discovered by John Horstman Fenton in 1894 [100].

This oxidative method is carried out at pH 3 and consists in the addition of hydrogen peroxide with catalytic amounts of a Fe^{2+} salt (this mixture is known as the Fenton reagent) generating the radical hydroxyl. This process can be carried out in the absence of light (Fenton process) or light-assisted (photo-Fenton). Hence, the Fenton reaction is described as **Equation 1.1**. Fe (II) is oxidised to Fe (III) while H_2O_2 is reduced to the hydroxide ion and hydroxyl radical [101]:

$$Fe^{2+} + H_2O_2 \rightarrow Fe^{3+} + OH^{-} + {}^{\bullet}OH \qquad \textbf{Eq. 1.1}$$

Moreover, the ferric ion, Fe^{3+}, can be reduced back to the ferrous ion, Fe^{2+}, by a second molecule of H_2O_2 (**Equations 1.2** and **1.3**). This reduction step, however, is much slower than the initial step. Different ways of accelerating the auto-catalytical process include the irradiation of the overall solution with UV light (photo-Fenton, depicted in **Equations 1.4** and **1.5**)) or the application of a voltage to promote the electrochemical reaction, also known as the electro-Fenton reaction [101–103].

$$Fe^{3+} + \rightarrow Fe^{2+} + H^{+} + HO_2^{\bullet} \qquad \textbf{Eq. 1.2}$$

$$Fe^{3+} + HO_2^{\bullet} \rightarrow Fe^{2+} + H^{+} + O_2 \qquad \textbf{Eq. 1.3}$$

$$Fe(OH)^{2+} \overset{h\upsilon}{\rightarrow} Fe^{2+} + {}^{\bullet}OH \qquad \textbf{Eq. 1.4}$$

$$H_2O_2 \overset{h\upsilon}{\rightarrow} 2\ {}^{\bullet}OH \qquad \textbf{Eq. 1.5}$$

Hence, the overall Fenton process is considered to be a catalytical process, requiring an excess of hydrogen peroxide to generate the ferrous ion. Moreover, any residual hydrogen peroxide that is not consumed in the process will decompose into water and molecular oxygen, thus, being a "clean” reagent by itself.

The Fenton process major drawbacks reside in its inhibition by dissolved salts that may be present in the water to be treated. For instance, the presence of the chloride or sulfate ions has been extensively reported to drastically reduce the degradation rates of organic compounds in the water matrices of study [97,104,105]. This has been mainly attributed to the complexation of the ferrous ion inhibiting the generation of the hydroxyl radical. Moreover, the degradation rates can also be affected by the presence of ions inhibiting the radical chain, also known as *scavengers*, mainly carbonate and bicarbonate ions. These ions react with the radical hydroxyl (**Equations 1.6** to **1.9**) generating non-oxidising chemicals, terminating the overall oxidative process [106–110].

$$^{\bullet}OH + HCO_3^- \rightarrow H_2O + CO_3^{\bullet-}$$ **Eq. 1.6**

$$^{\bullet}OH + CO_3^{2-} \rightarrow {}^{-}OH + CO_3^{\bullet-}$$ **Eq. 1.7**

$$^{\bullet}OH + Cl^- \rightarrow [ClOH]^{\bullet-}$$ **Eq. 1.8**

$$^{\bullet}OH + HSO_4^- \rightarrow H_2O + SO_4^{\bullet-}$$ **Eq. 1.9**

1.2.1.3.2. Ozone based processes

Due to the high oxidising power of ozone ($E^0 = 2.07$ V *versus* the NHE), ozone-based technologies have been widely employed for the treatment of industrial and urban wastewaters [111–114]. Ozone is usually produced *in-situ* by the application of a high-voltage electrical discharge in the presence of air or pure oxygen at atmospheric pressure.

Ozone based processes oxidises organic compounds in two different mechanisms: direct and indirect oxidation. Via direct oxidation, dissolved ozone molecules selectively react with unsaturated bonds of organic compounds. The reaction rate depends on the type of compound, but generally, degradation rates fall in the range of 1 to 10^3 $M^{-1}s^{-1}$ [115,116]. These degradation rates, however, are much lower than those found in other AOPs processes governed by the hydroxyl radical with degradation rates ranging 10^6 to 10^9 $M^{-1}s^{-1}$ [115,116]. This direct oxidation can be accelerated if the organic compounds to be treated contain electron-supplying substituents, like hydroxyl or amine groups, as reported by Gottschalk [117]. Indirect oxidation involves the generation of the hydroxyl radical and the latter attack to organic molecules present in the water to be treated. It can be generated through three different mechanisms: ozonation, the peroxone process (O_3/H_2O_2) and light-assisted ozonation (O_3/UV).

The overall reaction, summarising the complex mechanism, by which the hydroxyl radical is generated in direct ozonation can be depicted by **Equation 1.10**:

$$3O_3 + H_2O \rightarrow 2\ ^{\bullet}OH + 4O_2$$ **Eq. 1.10**

The presence of other oxidants or irradiation, can significantly improve the •OH yield. For instance, the so-called peroxone process (O_3/H_2O_2) takes advantage on the utilisation of hydrogen peroxide for enhancing the production of the radical hydroxyl, (**Equations 1.11** and **1.12**) [115,118,119]. In this process, the radical hydroxyl formation is mainly promoted by the hydroperoxide (HO_2^-) ion produced from the decomposition of H_2O_2.

$H_2O_2 \rightarrow HO_2^- + H^+$ **Eq. 1.11**

$HO_2^- + O_3 \rightarrow {}^{\bullet}OH + O_2^- + O_2$ **Eq. 1.12**

In light-assisted ozonation (O_3/UV), hydrogen peroxide is produced through the photolysis of ozone (**Equation 1.13**). Then, the reaction mechanism follows the steps described in **Equations 1.11** and **1.12**. Moreover, the radical hydroxyl can also be generated by the photolysis of hydrogen peroxide (**Equation 1.5**)

$O_3 + H_2O + hv \rightarrow H_2O_2 + O_2$ **Eq. 1.13**

1.2.1.3.3. Photocatalysis

The first step of any photocatalytic process is the excitation of the semiconductor with a photon of energy equal or greater than the band gap energy. If that happens, an electron, e^-, is promoted from the valence band (VB) into the conduction band (CB) generating a hole (h^+) behind. A brief scheme of all reactions taking place is shown in **Figure 1.12**. Briefly, both electron and hole can follow different steps: surface recombination (step a), bulk recombination (step b), migration to the semiconductor surface (steps c and d), and trapping by (adsorbed) substrate molecules. After the absorption of the photon by the catalyst's, the formation of the hole – electron (h^+ - e^-) pair occurs in 10^{-15} seconds. Once charge separation is done, some of them migrate to the catalyst's surface (steps a, c and d) and others migrate to the inner of the catalyst's structure (step b). Independently whether these charges have migrated to the inner of the catalyst or to its surface, charge recombination (steps a and b) is a phenomenon that occurs in the nanosecond time scale with heat dissipation.

If a suitable surface defect is available to trap charge carriers, charge recombination may be prevented and redox reactions may take place. It is for this reason that the presence of electron scavengers is of great importance for prolonging their recombination and successful functioning of the photocatalysis process.

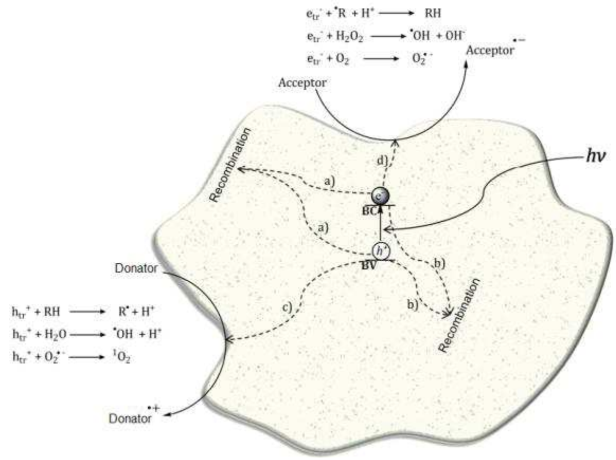
$e_{tr}^- + {}^\bullet R + H^+ \longrightarrow RH$
$e_{tr}^- + H_2O_2 \longrightarrow {}^\bullet OH + OH^-$
$e_{tr}^- + O_2 \longrightarrow O_2^{\bullet -}$
Acceptor
Acceptor$^{\bullet -}$
hv
Recombination
a)
a)
d)
e^-
BC
h^+
BV
b)
b)
c)
Recombination
Donator
$h_{tr}^+ + RH \longrightarrow R^\bullet + H^+$
$h_{tr}^+ + H_2O \longrightarrow {}^\bullet OH + H^+$
$h_{tr}^+ + O_2^{\bullet -} \longrightarrow {}^1O_2$
Donator$^{\bullet +}$

Figure 1.12. Reactions and processes occurring in TiO_2 photocatalysis.
Reprinted with permission from Clusellas *et al.* [120].

For instance, the hole may react with a donor molecule (step c) like organic molecules or OH groups while conduction band electrons can reduce electron acceptors (step d), like oxygen molecules or protons. It is for this reason that photogenerated holes are powerful oxidising agents (+1.0 to 3.5 V *versus* the normal hydrogen electrode (NHE) depending on the semiconductor and pH), while the electrons are good reductants (+0.5 to -1.5 V *versus* NHE). Hence, the reactions mostly accepted for the generation of reactive oxygen species (ROS) are summarised in **Equations 1.14** to **1.18**.

$$O_{2\,(ads)} + e_{tr}^- \rightarrow\ O_{2\,(ads)}^{\bullet -} \qquad \textbf{Eq. 1.14}$$

$$O_{2\,(ads)} + e_{tr}^- \rightarrow\ O_{2\,(ads)}^{-} \qquad \textbf{Eq. 1.15}$$

$$O_{2\,(ads)}^{\bullet -} + h_{tr}^+ \rightarrow O_{2\,(ads)}\ (Ec.) \qquad \textbf{Eq. 1.16}$$

$$H_2O_2 + e_{tr}^+ \rightarrow\ {}^\bullet OH_{(ads)} + OH_{(ads)}^-\ (Ec.) \qquad \textbf{Eq. 1.17}$$

$$H_2O_2 + h_{tr}^+ \rightarrow\ {}^\bullet OH_{(ads)} + H_{(ads)}^+\ (Ec.) \qquad \textbf{Eq. 1.18}$$

Bearing in mind the generation of the electron-hole pair after the photocatalyst excitation and the later formation of reactive oxygen species, it is of sum interest to know how organic matter can be treated by means of the mentioned processes. The first mechanism involves the adsorption of the organic matter onto the catalyst's surface and consecutive oxidation or reduction of the superficial holes or electrons (**Equations 1.19** and **1.20**).

$$RH_{(ads)} + h_{tr}^+ \rightarrow\ {}^\bullet R_{(ads)} + H_{(ads)}^+ \qquad \textbf{Eq. 1.19}$$

$${}^\bullet R_{(ads)} + H^+ + e_{tr}^- \rightarrow RH_{(ads)}\ (Ec.) \qquad \textbf{Eq. 1.20}$$

The second mechanism refers to the indirect oxidation of the organic molecules in dissolution via the attack of the reactive oxidising species generated in **Equations (1.21** to **1.23**). Amongst all the oxidising chemical species produced in **Equations 1.14** to **1.18**, the radical hydroxyl is the most oxidising one, thus, being the most important for the later degradation of the organic chemicals dissolved in water. The main mechanism by which the hydroxyl radical attacks organic matter is the abstraction of a hydrogen atom leaving behind organic radical species (**Equation 1.21**). Other pathways include the electronic transference from the organic matter to the hydroxyl radical **(Equation 1.22)** or the electrophilic addition of the •OH to unsaturated bonds **(Equation 1.23)**, in the same way as it would happen in an electrophilic aromatic substitution.

$$^{\bullet}OH + RH \rightarrow R^{\bullet} + H_2O$$ **Eq. 1.21**

$$^{\bullet}OH + RX \rightarrow RX^{\bullet} + OH^{-}$$ **Eq. 1.22**

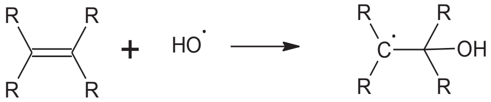

Eq. 1.23

When reaching high concentrations of the radical hydroxyl, this can evolve into the generation of hydrogen peroxide (H_2O_2), **Equation 1.24**, radical hydroperoxide ($HO_2^{\bullet}$), depicted in **Equation 1.25**. This last radical, however, shows little oxidising power compared to radical hydroxyl, thus, representing an insignificant contribution to the degradation of the organic pollutant.

$$^{\bullet}OH + {}^{\bullet}OH \rightarrow H_2O_2$$ **Eq. 1.24**

$$^{\bullet}OH + H_2O_2 \rightarrow H_2O + HO_2^{\bullet}$$ **Eq. 1.25**

The reactions, rates and extent of reactions shown will strongly depend on the nature of the photocatalyst because of the absolute energy levels of both valence and conduction bands *versus* the oxidation and reduction potential of the redox half-reaction.

1.2.1.3.4. Advanced electrochemical oxidation processes (AEOPs)

Advanced electrochemical oxidation processes, such as electro-oxidation (EO), electrochemical coagulation (EC) and electrochemical flotation (EF) have received an increasing interest by the scientific community in recent years, since they have been applied to treat wastewaters, disinfect drinking water or enhance the remediation of polluted soils. Amongst them, electrochemical oxidation (EO) is the AEOP technique receiving the greatest attention and interest in wastewater treatment from the scientific community. Hence, this technique will be the only AEOP deeply reviewed in the present chapter.

- However, all these technologies offer several benefits and advantages against the already reviewed AOPs [121–125].
- *Versatility:* several techniques can be applied such as direct and indirect oxidations and reductions, phase separations, biocide functions, etc. Moreover, contrary to what has been reported to AOPs, AEOPs can be submitted to wastewater containing a pollution load, expressed as COD, ranging 0.1 to 25 g L^{-1} COD.
- *Green technologies*: since the principal reagent is the electron (green reagent), there is little or no need of using chemicals to facilitate water treatment.
- *Cost-effectiveness*: are energetically favourable, since they can operate at room temperature and pressure conditions.
- *Simple operation*: the electrical variables used in the electrochemical processes (current density and voltage) are particularly suited for facilitating data acquisition, process automation and control

Electrochemical oxidation

EO of pollutants can occur directly at anodes as a result of the *in-situ* generation of the radical hydroxyl (or other oxidising species) through electrochemical oxidation of adsorbed water (**Equations 1.26 – 1.28**). Due to the fact of using anodes with oxygen overpotential, **reaction 1.28** is significantly lower than **reaction 1.26**, favouring the generation of the radical hydroxyl (equation a, **Figure 1.13**). However, most of the generated •OH is adsorbed onto the anode’s surface, therefore, its reactivity will strongly depend on the nature of this material. In this way, two classes of anodes can be distinguished: “active’’ and ‘‘non-active’’ anodes. **Figure 1.13** shows the mechanistic scheme of the oxidation of an organic compound using anodes with oxygen overpotential.

$$H_2O\ (ads) \rightarrow {}^{\bullet}OH\ (ads) + H^{+}(ads) + e^{-} \qquad \textbf{Eq. 1.26}$$

$${}^{\bullet}OH\ (ads) \rightarrow 1/2\ O_2(ads) + H^{+}(ads) + e^{-} \qquad \textbf{Eq. 1.27}$$

$$H_2O\ (ads) \rightarrow 1/2\ O_2(ads) + 2H^{+}(ads) + 2e^{-} \qquad \textbf{Eq. 1.28}$$

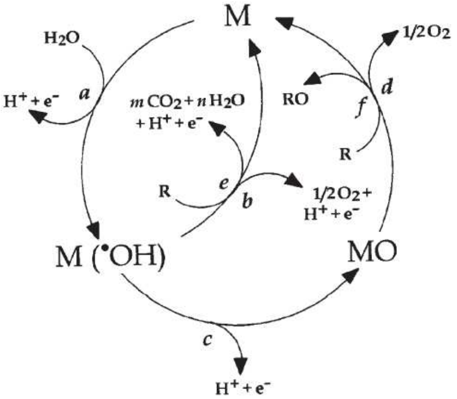

Figure 1.13. Reactions and processes occuring under indirect oxidation of organic compounds. *Adapted from* Marselli *et al.* [126].

Active electrodes such as Pt, IrO_2, and RuO_2 are characterised by their strong interaction between the electrode (M) and the hydroxyl radical. This kind of anodes favours the evolution of the radical hydroxyl to oxygen. Adsorbed hydroxyl radicals interact with the anode, forming the so-called higher oxide MO (equation c). Hence, the redox couple MO/M acts as the mediator in the oxidation of the organic molecule (equation f), being in competence with the decomposition of MO to O_2 (equation d).

Non-active electrodes (SnO_2, PbO_2, Boron-Doped Diamond) are characterised by the weak interactions between the OH and the anode's surface. In this case, the oxidation of organic molecules is mediated by the non-selective attack of hydroxyl radicals, achieving in most of the cases, the complete oxidation of the organic molecules present in solution.

Other indirect oxidation can occurs when oxidants like chlorine Cl_2, HClO, ClO^-, H_2O_2 or O_3 are formed at the electrode as depicted by **Equations 1.29 to 1.35**.

$2\,Cl^- \rightarrow Cl_2 + 2\,e^-$ **Eq. 1.29**

$Cl_2 + H_2O \rightarrow HOCl + H^+ + Cl^-$ **Eq. 1.30**

$HOCl \rightarrow H^+ + ClO^-$ **Eq. 1.31**

$H_2O \rightarrow {}^{\bullet}OH + H^+ + e^-$ **Eq. 1.32**

$2\,{}^{\bullet}OH \rightarrow H_2O_2$ **Eq. 1.33**

$H_2O_2 \rightarrow O_2 + 2H^+ + 2e^-$ **Eq. 1.34**

$O_2 + {}^{\bullet}O \rightarrow O_3$ **Eq. 1.35**

Table 1.3. AOPs technologies employed for the degradation of the chemicals under study.

Compound	Technology	Drug conc.	Water matrix	Exp. conditions	Main results	Refs.
Ofloxacin	Fenton	10 mg L^{-1}	Demineralised water Simulated natural freshwater Simulated municipal wastewater Pre-treated real effluent	V =44 L; T=37 ºC λ=solar irradiation pH 2.8–2.9 $[Fe^{2+}]_0 = 2$ mg L^{-1} $[H_2O_2]_0 = 2.5$ mg L^{-1}	78 % of the initial ofloxacin was mineralised after 500 min of solar-Fenton treatment using demineralised water. In all other cases, inorganic ions scavenged the reaction, achieving <58 % ofloxacin degradation.	[127]
Ofloxacin	Ozone-based	22 mg L^{-1}	Synthetic water Sewage treatment plant effluent	V= 1.44L; T=r.t. $[O_3]$=4.2-145 mg L^{-1} pH = n.s.*	The complete abatement of ofloxacin was achieved in both synthetic and real water matrices. The degradation of ofloxacin in the real matrix not only was scavenged by inorganic ions but also by organic compounds dissolved in the sample.	[128]
Ofloxacin	Electrochemical oxidation	10-50 mg L^{-1}	Synthetic water	V= 0.3 L; T=r. t. pH = n.s.* TiO_2-based SnO_2-Sb/FR-PbO_2electrode Current density=5-50 mA cm^{-2} Voltage= 3.5-8.6 V	The complete depletion of ofloxacin was achieved in 60 minutes. Current density, initial ofloxacin concentration and pH drastically influenced ofloxacin depletion, achieving the best results with 50 mA cm^{-2}, 10 mg L^{-1} ofloxacin and pH 11.	[129]
Clofibric acid	Fenton	25-100 mg L^{-1}	Synthetic water	V= 0.25L; T=25 ºC pH=3.3 $[Fe^{2+}]_0 = 1$-3 g L^{-1} (Synthesised FeOOH catalysts) $[H_2O_2]_0 = 0.25$ -5 g L^{-1}	The degradation of clofibric acid using Fenton-like was completely achieved after 6 hours of treatment. Different variables (pH, T, H_2O_2 concentration, catalyst load) highly influenced the degradation rates observed.	[130]

Table 1.3 *(continued)*. AOPs technologies employed for the degradation of the chemicals under study.

Compound	Technology	Drug conc.	Water matrix	Exp. conditions	Main results	Refs.
Clofibric acid	Ozone-based	25-100 mg L^{-1}	Synthetic water	V= 0.5L; T = 25 ºC $[O_3]$=1.2 g/h O_2 flow rate 40 L h^{-1}	The ozonation of clofibric acid resulted in its fast disappearance (less than 15 min) and was improved by catalytic ozonation using FeOOH catalysts.	[131]
Clofibric acid	Electrochemical oxidation	179 mg L^{-1}	Synthetic water	V=0.1 L; T = 25 to 45 ºC Current density = 33, 100 150 mA cm^{-2} BDD thin-film deposited on conductive single crystal p-type Si (1 0 0) pH = 2 to 12	Clofibric acid was completely mineralized in the pH range 2–12 (pH independent) by anodic oxidation with BDD. The degradation becomes faster as current density increases and so does with temperature.	[124]
Diclofenac	Fenton	5 mg L^{-1}	Synthetic water	V= 0.1L; T=25ºC pH = 4 Fe source=Pyrite (FeS_2) 4-29 mg $L^{-1}$$Fe^{2+}$ $[H_2O_2]_0$ = 4 - 81 mg L^{-1}	The complete abatement of diclofenac was observed in 2 minutes with the pyrite Fenton system, while only 65% of diclofenac was removed by classic Fenton system in 3 minutes. The increasing additions of H_2O_2 enhanced diclofenac degradation (up to a maximum of 56 mg·L^{-1}).	[132]
Diclofenac	Ozone-based	50 mg L^{-1}	Synthetic water	V = 0.5 L; T=r.t. $[O_3]$=130 ± 5 mg L^{-1}; Power=30W O_2 flow rate 10 L h^{-1}	Diclofenac is completely depleted only after four min of ozonation treatment, slightly enhanced by the combination with photocatalysis (photocatalytical ozonation).	[133]
Diclofenac	Electrochemical oxidation	30 mg L^{-1}	Synthetic water	V=0.1 L; T = r.t. pH = 6.7 Current density = 1.2 mA cm^{-2} BDD thin-film deposited on conductive single crystal p-type Si (1 0 0)	Nearly complete abatement of diclofenac was observed within 4 h using electrochemical oxidation. The contribution of direct oxidation was found to be insignificant, mainly attributing its degradation to indirect oxidation mediated reactive organic species.	[125]

Table 1.3 *(continued)*. AOPs technologies employed for the degradation of the chemicals under study.

Compound	Technology	Drug conc.	Water matrix	Exp. conditions	Main results	Refs.
Ibuprofen	Fenton	205 mg L^{-1}	Synthetic water	V=1 L; T=30 ºC pH = 3 $[Fe^{2+}]_0$ = 8-67 mg L^{-1} $[H_2O_2]_0$ = 11 mg L^{-1}	50% of initial ibuprofen was degraded after 2 hours of Fenton treatment. As $[Fe^{2+}]$ and $[H_2O_2]$ increased, so did the degradation rate. The assistance of UV light (photo-Fenton) also accelerated the degradation of ibuprofen	[134]
Ibuprofen	Ozone-based	50 mg L^{-1}	Synthetic water	V = 0.5 L; T = r.t. $[O_3]$=130 ± 5 mg L^{-1}; power of 30W O_2 flow rate 10 L h^{-1}	Diclofenac is completely depleted after 30 min of ozonation treatment, highly enhanced by the combination with photocatalysis (photocatalytical ozonation).	[135]
Ibuprofen	Electrochemical oxidation	20-50 mg L^{-1}	Synthetic water	V=0.1 L; T = r.t. pH = 3 and 8 Current density = 10-70 mA cm^{-2} Three anodes tested: PtRu-FTO[1] Pt/MWCNT-FTO[2] Pt-FTO[3]	The present research highlighted that the degradation efficiency of ibuprofen increased as increased its initial concentrations for all anodes used. Acidic pH led to enhanced ibuprofen degradation. Moreover, The higher applied current density, the higher mineralization efficiency of ibuprofen was observed.	[136]

r.t: room temperature

*not specified

[1] Platinum Ruthenium fluorine-doped tin oxide

[2] Platinum nanoparticles/multi-walled carbon nanotube-Fluorine-doped tin oxide conductive glass

[3] Platinum Ruthenium fluorine-doped tin oxide

1.2.2- Biological treatments

Biological treatment processes have been traditionally used for the treatment of organic waste, but nowadays, they are being used for the treatment of hazardous waste. Apart from oxidising organic matter, these processes can also be useful to reduce the inorganic concentration or to transform or remove nutrients such as nitrogen and phosphorous. Biological treatments are now commonly found as secondary treatments in wastewater treatment plants due to their moderated low cost and their efficiency in processing large amounts of wastewaters with high organic matter content.

Depending on whether organisms obtain carbon, they can be classified as heterotrophs or autotrophs. The first group uses organic carbon for growth and represents the most important class of organisms used in biological treatments. They can be further divided based on how they obtain energy; if the heterotroph uses light, it is considered a photoheterotroph, whereas if it uses chemical energy, it is called chemoheterotroph. The second class of organisms, autotrophs, use inorganic carbon for their growth and energy is generally obtained from light (photosynthesis) or inorganic chemical reactions (chemosynthesis). The population of microorganisms used in biological treatments are usually constituted by bacteria, fungi, algae and protozoa.

Biological treatments occur when these microorganisms are mixed together with pre-treated wastewater and, by means of biochemical reactions, use carbon (organic and/or inorganic) to obtain energy for their synthesis, growth and maintenance, as depicted by **Equation 1.36**.

$$C_{18}H_{19}O_9N_{(aq)} + 12O_{2(g)} + 2H^+_{(aq)} \xrightarrow{\substack{microoganisms\\ nutrients}} 13CO_{2(g)} + NH^+_{4(aq)} + 5H_2O + C_5H_7O_2N_{(s)} + E \qquad \textbf{Eq.1.36}$$

Where $C_{18}H_{19}O_9N$ is the influent organic matter; $C_5H_7O_2N$ the synthesised organism (new cells) and E is the energy produced from the consumption of carbon [137]. This activated sludge can only mineralise the biodegradable and non-toxic organic matter. It is for this reason that several environmental conditions (pH, temperature, oxygen, availability of nutrients, etc.) must be taken into account for their selection. However, Suarez-Ojeda *et al.* [138] demonstrated that, after repeated conditioning to a certain kind of wastewater or matrix, this activated sludge can get used to it and fully oxidise persistent and/or toxic organic matter contained in water.

Biological treatments can be classified into four categories: aerobic treatment (in the presence of oxygen); anaerobic treatment (in the absence of oxygen); anoxic treatment (in the presence of nitrate or nitrite ions); and combinations of the last three mentioned. Constructed wetlands is a kind of biological treatment where these three categories can be successfully combined in order to achieve the complete depletion of chemicals (inorganic and organic) present in the influent water. Moreover, it can be further classified depending on the location of these microorganisms: suspended in the media (batch or continuous flow reactors) or fixed on solid supports (fixed beds). In the first group, microorganisms grow in suspension in the wastewater under treatment. Once the biodegradation is completed, these microorganisms are removed by clarification. In the latter group, microorganisms are allowed to attach to the surface of an inner medium filling the whole reactor. Once the biodegradation is finished, the treated wastewater is drained and the biomass is left fixed to the solid.

Constructed wetlands

Constructed wetlands (CW) are water treatment systems that use natural processes to remove (or partially treat) undesired contamination contained in the receiving water effluents [139–141]. These systems use vegetation, invertebrates (insect larvae and worms), substrates used for their construction (oil, sand, gravel, rock, and organic materials such as compost) and microorganisms (mainly bacteria but also yeasts, algae, protozoa, etc.) to improve water quality. These systems are especially interesting for the treatment of water due to their simplicity, their cost-effective operation and maintenance, no need of using chemicals, no residues are generated, they can be built to fit harmoniously into the landscape etc.

Wetlands improve water quality by different mechanisms [139–143]:

- Filtrating particulate matter.
- Adsorption of chemicals (both organic and inorganic) on the surface of plants and substrates.
- Chemical transformation of pollutants by microorganisms and plants.

Several types of constructed wetlands can be distinguished: surface flow wetlands (**Figure 1.14 A**), subsurface flow wetlands (**Figures 1.14 B and 1.14 C**), and hybrid systems (**Figure 1.15**) composed of both types of wetlands.

- Surface flow wetlands: water circulation occurs at the surface of the constructed wetland, through plant stems and leafs. The water layer in contact with the wetland is always lesser than one meter height.
- Subsurface flow wetlands can be further classified in horizontal and vertical flow:
    - Horizontal flow: water flows horizontally through the substrate by gravity and parallel to the surface. Anoxic and anaerobic processes are predominant in these kind of constructed wetlands such as denitrification and fermentation.
    - Vertical flow: Water moves from the planted layer down through the substrate and out. Aerobic processes, such as nitrification and oxidation of organic matter are the most favourable to occur.

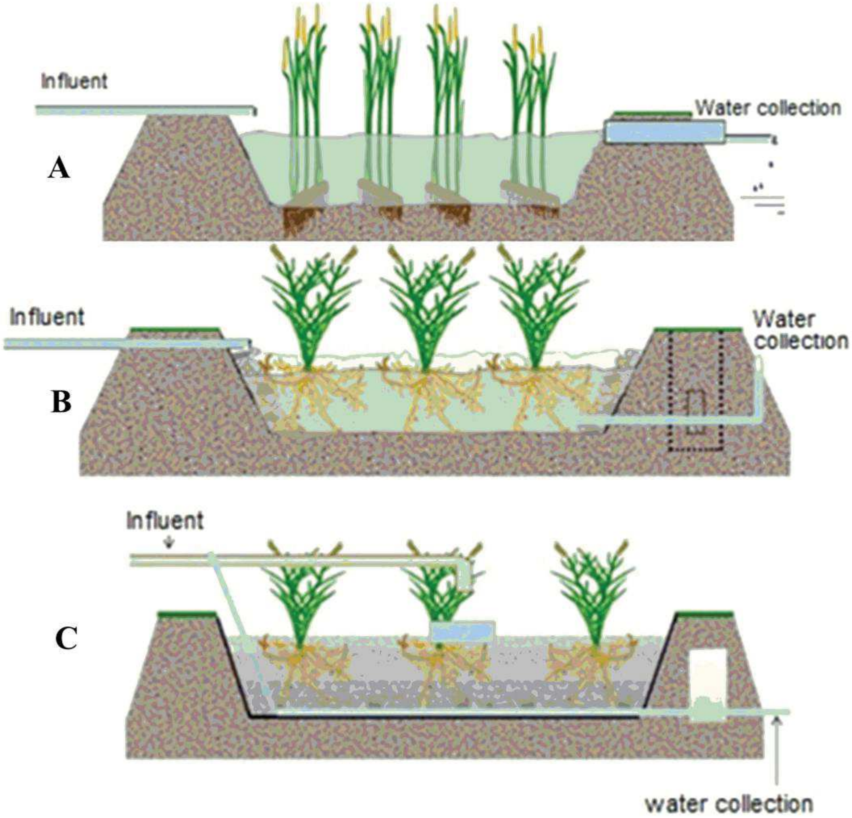

Figure 1.14. Schematic design of: **A)** a surface flow constructed wetland. **B)** a subsurface horizontal flow constructed wetland **C)** a subsurface vertical flow constructed wetland. *Adapted from Garcia and Corzo* [144].

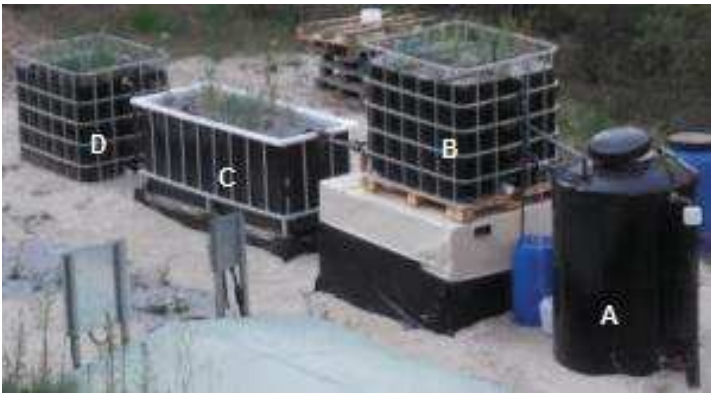

Figure 1.15. Hybrid constructed wetland. A) Influent mixer; B) vertical subsurface flow CW; C) horizontal subsurface flow CW; D) surface flow CW.

There have been numerous investigations proving the efficiency of these systems in depurating heavy metals [145,146] and organic pollutants [147–152]. Tromp *et al.* [146] investigated the removal efficiency of PAHs, Cu, Zn, Pb, Cd and Ni by a vertical subsurface constructed wetland. While PAHs were mostly removed from the system (up to 95%), this investigation found relatively small removal rates for Cd, Cr and Cu (40, 39 and 13% respectively). Ni, Pb and Zn were found to be more retained for the overall system, achieving removal percentages of 48, 76 and 60 respectively. Amongst the numerous authors working in the removal of emerging pollutants by constructed wetlands, Chen *et al.* [149] studied the removal of several antibiotics (erythromycin monensin, clarithromycin, leucomycin, sulfamethoxazole, trimethoprim, sulfamethazine and sulfapyridine) at ng L^{-1} concentration levels. In their study, horizontal and vertical subsurface constructed wetlands showed up to 98% degradation of the contaminants under study. Moreover, Ávila *et al.* [152] carried out a similar study with ibuprofen, naproxen, diclofenac, tonalide and bisphenol A at μg L^{-1} concentration. This investigation found that the degradation and sorption behaviour of these chemicals highly differed through the stages of the constructed wetland. Degradation rates found for all these pharmaceuticals ranged between 50-80 % of the initial concentration.

1.3. Analysis of pharmaceuticals

Investigations dealing with the occurrence and fate of pharmaceuticals in the environment, as well as their removal by wastewater treatment techniques have always been accompanied with the development of complex and sophisticated analytical methodologies published in the literature. Such methods are usually composed of five steps: sampling, sample preparation, separation, detection, and data analysis.

Given the different nature and physic-chemical properties of available pharmaceutical drugs, most of the published analytical methods were focused on specific therapeutic families (NSAIDs, antibiotics, beta-blockers, etc.), while only a few were devoted to multi-residue analysis. However, with the irruption of new and simpler sample treatment techniques such as QuEChERS and the availability of high-resolution mass spectrometry systems in environmental and routine laboratories, the number of publications dealing with environmental multi-residue analysis has exponentially grown over the past 20 years.

1.3.1. Sampling and storage

Opposite to the pharmaceutical analysis, sampling and storage of environmental samples regarding their latter analysis has not been object of numerous scientific publications. Moreover, it is vastly known that these steps are the major sources of inaccuracies throughout the analytical methodology [153–157].

Obtaining representative environmental samples may be, at a time, a difficult and tedious task given several factors and conditions: sample homogeneity, (limited) accessibility to collection sites, seasonal fluctuations in weather (temperature, rainfall, humidity, etc.), anthropogenic actions, etc. It is for this reason that additional information is commonly obtained while conduction wastewater sampling: pH, dissolved oxygen, total residual conductivity, temperature, photographs, flow, etc.

Two sampling techniques may be used when dealing with wastewater samples: grab and composite.

- *Grab sampling*: This technique consists in the collection of a single discrete sample over a period of time no longer than 15 minutes [153–157].
- *Composite sampling*: Composite samples are obtained by continuous sampling or by mixing collected single samples. Composite sampling can further be divided into time composite and flow proportional sampling. The first one consists in the mix of equal volumes of different aliquot samples while the second varies the sample volume of each sample as a function of the wastewater flow [153–157].

Since composite sampling represents the average wastewater characteristics during the sampling period, it is commonly accepted to provide more representative samples with the exception of those chemicals degrading over the collection time.

Once collected, samples must be stored and perfectly preserved until their analysis, up to a maximum of 28 days. Common strategies for *in-field* sample storage may involve the use of plastic or glass amber bottles (depending on the nature of the analytes to be analysed) at a temperature of 4 ºC. Chemical preservation may be used too only when it is shown not to interfere with the method of analysis. This may involve pH control and/or addition of chemicals. For instance, sulfuric and hydrochloric acids and sodium azide have been previously employed as chemical preservatives. Moreover, the addition of quenching agents such as ascorbic acid, sodium thiosulfate or sodium sulfite have also been implemented in sample preservation in environmental studies [158].

1.3.2. Sample preparation

Despite the enormous advances achieved in the analytical instrumentation over the past twenty years, achieving higher sensitivity, sensibility, accuracy and precision, the analysis of pharmaceuticals, pesticides and related compounds have always been accompanied with pre-treatment and *clean-up* methods to extract and isolate the target analytes from the matrix under study.

Whereas the pre-treatment of the sample usually comprises simple tasks such as homogenization, pH adjustment, etc. the *clean-up* aims to isolate the compounds of interest from the sample and preparing both the sample and analytes to the latter detection and quantification by means of an instrumental technique. Such *clean-up* methods may involve liquid-liquid extraction (LLE), solid-liquid extraction (SLE), accelerated solvent extraction (ASE) QuEChERS (Quick, Easy, Cheap, Effective, Rugged, Safe) pressurized-liquid extraction (PLE), solid-phase extraction (SPE), solid-phase microextraction (SPME), molecularly imprinted polymers (MIPs), etc. Even though the wide diversity of *clean-up* procedures and analytical methodologies currently available for sample pre-treatment, solid-phase extraction is the most frequently used one due to its flexibility in stationary phases, possibility of automation, improved recoveries, etc.

In SPE, the separation is based on the partitioning of the target analytes between the stationary phase (solid) and solvent (liquid). Typical SPE procedures involve four steps that need to be optimised to obtain high recovery rates and reproducible results: conditioning of the stationary phase; sample loading; sorbent washing to remove interfering compounds and elution of the target analytes. Mixed-mode sorbents such as those manufactured by Waters Corporation (Oasis HLB), Phenomenex (Strata-X), Agilent (Bond Elut Plexa), etc. have been the most employed cartridges for the extraction of the studied compounds and for multi-residue analysis comprising a wide diversity of organic compounds (neutral, basic and acidic) from water matrices over a wide range of working pH. These sorbents offer good and highly reproducible recoveries for groups of compounds of similar physic-chemical properties. Other sorbent chemistries are also available for the selective extraction of basic and acidic compounds. For instance, those based in ion exchange mechanisms such as the Oasis MCX cartridges (Mixed mode Cation eXchange) are employed for the specific retention of basic compounds while Oasis MAX cartridges (Mixed mode Anion eXchange) are suitable for acidic compounds. Even though the use of on-line SPE with LC dates back to 30 years ago [159], it has been in the past 10 years that on-line SPE has grown in commercial availability and use. The basis and principle of this technique is the same as that described for off-line SPE but differing on the instrumental system used. Common on-line SPE systems are composed of two pumps: loading and “analytical” pumps and two columns: SPE and analytical columns. The loading pump transfers the injected sample on to the SPE column while the analytical pump, after switching loop valves, elutes the analytes to the LC column using a proper hydro-organic solvent composition. These systems are automatable, reducing manual preparation steps and risk of human errors [160–162].

Finally, solid phase extraction has been one of the most investigated fields for molecularly imprinted polymers [81,83–86]. Molecularly imprinted solid phase extraction (MISPE) makes use of its molecular recognition capabilities to selectively extract the compounds of interest and lowering matrix interferences. Due to their high selective behaviour, MISPE cartridges are to be custom-made since few MISPE cartridges are commercially available (Sigma-Aldrich: patulin, aminoglycosides and bisphenol A; Biotage: custom designed).

1.3.3. Instrumental analysis

After sample extraction, concentration and *clean-up*, pharmaceutical drugs and related compounds are commonly analysed by means of a separation technique with a selective detection system. For instance, LC-DAD (diode array detector) has been one of the systems most frequently used due to its ease of use, low cost and robustness. However, in order to achieve more selectivity for the analysis compounds such as fluoroquinolones, tetracyclines, photosensitizers, etc., LC-FLD (fluorescence detection) has proven to be especially useful. In contrast, the unequivocal identification and confirmation of the presence of pharmaceuticals in complex environmental water samples is compromised. This is one of the main reasons to choose chromatography coupled to mass spectrometry as the technique of choice, with the additional advantage of providing a great sensitivity and selectivity to achieve detection and quantitation limits within the lower range (ng L^{-1} and µg L^{-1}) in environmental matrices. Nowadays, advanced analytical techniques such as GC/MS, GC-MS(/MS) and LC-MS(/MS) have become essential in analytical laboratories. Moreover, due to the increasing demand of detection and discovery capabilities, high-resolution mass spectrometers have gradually been acquired and incorporated to environmental laboratories. These instruments not only offer enhanced detection but are highly suitable for avoiding false positives (already reported by LC/GC-tandem mass spectrometry) and the discovery of natural occurring drug metabolites or transformation products.

1.3.3.1. GC-MS

Gas chromatography coupled to mass spectrometry has traditionally been the analytical technique of choice for the analysis of persistent organic pollutants due to the high sensibility and sensitivity offered for non-polar and volatile compounds (dioxins, pesticides, organochloride compounds, etc.). Nevertheless, one disadvantage when dealing with polar compounds is the need for a derivatisation step prior the GC-MS analysis. By derivatising, the polarity of the molecule can be decreased and its volatility and thermal stability increases, making these compounds suitable for GC-MS analysis. Common derivatisation reagents include BSTFA (N,O-Bis(trimethylsilyl) trifluoroacetamide), BSA (N,O-Bis(trimethylsilyl)-acetamide), BF_3 (boron trifluoride), MSTFA (N-methyltrimethylsilyltrifluoroacetamide), MTBSTFA (Nmethyl-N-t-butyldimethylsilyltrifluoroacetamide), etc.

Generally, ionisation in GC-MS takes place under vacuum conditions via electron ionisation (EI) or chemical ionisation (CI). The first one generates highly fragmented mass spectra (70 eV ionisation energy) and so does when used at lower ionisation energies (~35 eV). Chemical ionisation produces less fragment ions by using low ionisation energies (5 eV) and a reagent gas filling the source. Moreover, recent instrumental developments have successfully coupled and launched to the market GC-APCI (Atmospheric Pressure Chemical Ionisation)-MS systems that is gaining increased interest and popularity amongst analytical chemists. These systems make use of the so-called "*soft*" ionisation techniques to generate mass spectra rich in molecular or protonated molecular ions nut requiring tandem mass spectrometry to obtain structural information. **Table 1.4** shows published literature related to the analysis of the studied pharmaceutical drugs carried out by GC-MS.

Table 1.4. Literature review on GC-MS methods employed for the analysis of the pharmaceuticals under study.

Analytes	Sample	Sample treatment Derivatisation	Column	Instrument; mass analyser Ionisation; Acquisition mode	LOD (ppb)	LOQ (ppb)	Ref.
Clofibric acid Diclofenac Ibuprofen	Wastewater	SPE (Oasis HLB) BSTFA silylation	Agilent HP-5MS	GC-MS; (Q) EI; Full scan and SIM	0.025 0.022 0.012	0.083 0.075 0.040	[163]
Diclofenac Ibuprofen Ketoprofen	Wastewater	SPME (polydimethylsiloxane (PDMS) fibers (100 µm film thickness)) BSTFA silylation	Agilent DB-5MS	GC-MS; (Q) EI; Full scan and SIM	0.006 0.020 0.022	0.030 0.070 0.080	[164]
Clofibric acid Diclofenac Ibuprofen	Wastewater	SPE (Strata X) Pentafluorobenzylation with Pentafluorobenzyl bromide (PFBBr)	Agilent DB-5MS	GC-MS; (Q) EI; Full scan and SIM	0.001 0.002 0.001	0.003 0.006 0.003	[165]
Clofibric acid Diclofenac Ibuprofen	Wastewater	SPE (Oasis HLB) MSTFA silylation	Agilent DB-5MS	GC-MS; (Q) EI; Full scan and SIM	0.001 0.002 0.001	0.003 0.006 0.003	[166]
Clofibric acid Diclofenac Ibuprofen	Wastewater	SPE (Oasis HLB) BSA+TMCS silylation	Supelco DB-5	GC-MS; (Q) EI; Full scan and SIM	30 20 10	n.s.	[167]
Clofibric acid Diclofenac Ibuprofen	Wastewater	Liquid-liquid extraction MTBSTFA silylation	Phenomenex ZB5	GC-MS; (Q) EI; Full scan and SIM	0.1-1.9	0.4-6.3	[168]

* All columns were (5%-phenyl)-methylpolysiloxane 30 m length, 0.25 mm I.D. and 0.25 µm film thickness.
n.s.: Not specified

As explained in the introduction of GC-MS instrumental analysis and depicted in Table 1.4, the studied pharmaceutical drugs studied in this PhD thesis need to be derivatised prior their analysis by this instrumental technique. Even though different derivatising procedures have been used, it is generally accepted that sylilation is the most widely employed for the analysis of pharmaceuticals [167]. BSTFA, the mixture containing BSTFA, TMCS, MTBSTFA and MSTFA are the most common derivatising agents for the analysis of the studied NSAIDs. For instance, Azzouz *et al.*[167] compared the derivatising performance of BSA, BSTFA, TMCS and mixtures of them for the analysis of ibuprofen, diclofenac, clofibric acid, fibrate, ketoporfen and 8 additional chemicals of environmental interest. This research found that the best derivatising agent was the mixture containing BSA+TMCS, achieving an instrumental linearity of 0.1 – 400 ng L^{-1} and method detection limits within 0.01 and 0.04 ng L^{-1}. On the other side, the researches conducted by Molina-Fernandez *et al.* [168] and Togola *et al.* [169] found that the best derivatising agent was MTBSTFA for the analysis of the same NSAIDs studied by Azzouz *et al*. Their instrumental LODs, however, were much higher than those claimed for Azzouz *et al.* (100 – 1900 ng L^{-1}). Despite the numerous derivatising agents commercially available, ofloxacin has not been reported to date to be analysed by GC-MS.

1.3.3.2. LC-MS

Despite the fact all the advantages GC-MS may offer, HPLC-MS(/MS) has become the analytical technique of choice for the analysis of pharmaceuticals and related compounds in environmental samples, since it does not require the laborious and time-consuming sample preparation needed when performing the analysis by gas chromatography. Moreover, the coupling of liquid chromatography to mass spectrometry using of atmospheric pressure ionisation (API) techniques has led to enhanced sensibility and sensitivity analysis (both quantitative and qualitative) of more polar pharmaceuticals in different kind of samples. **Table 1.5** shows some of the published methods dealing with the development of analytical methods based on LC-MS analysis of a wide diversity of organic compounds and matrices.

LC-MS chromatographic methods are usually carried out using reversed-phase octyl C_8–bonded or octadecyl C_{18}–bonded column chemistries with different hydro-organic solvent combinations, mainly acetonitrile/methanol in combination with water as aqueous phase. These column chemistries, in combination with mass spectrometry, offer an interesting flexibility for the analysis of the studied drugs and related compounds (for instance, metabolites or transformation products). However, other column chemistries have been successfully used in the literature such as phenyl-hexyl based columns [170,171] and HILIC (hydrophilic liquid chromatography) [172,173], amongst others. For instance, Rossmann *et al.* carried out the analysis of different fluoroquinolones and different antibiotic classes (up to 18 chemicals) using an HILIC column achieving satisfactory separation conditions for all of them. The same column used Nemoto *et al.* for the study of diclofenac, ibuprofen and 13 additional NSAIDs. Both researches achieved instrumental detection limits ranging from 50 – 100 μg L^{-1}. For instance, conventional HPLC methods used to be developed with 5 micron particle size, but, the development and incorporation for routine analysis of <2 μm LC columns, totally and superficially porous, have been accompanied with an enormous development of LC systems capable of handling column backpressures of more than 10,000 psi. The use of such columns have led to several advantages in comparison to conventional HPLC methods: more efficient chromatographic peaks, higher chromatographic resolution and higher sensibility and sensitivity, with the additional advantages of shorter analysis time and less matrix effects.

Volatile solvents and additives (compatible with Atmospheric Pressure Ionisation (API) sources) are commonly added to mobile phases in order to improve chromatographic peak shape, chromatographic retention and resolution. Hence, formic acid/formate, acetic acid/acetate and ammonia are frequently used solvent additives for the LC-MS analysis of the analytes under study. This increase in LC performance has been especially attractive for its coupling to mass spectrometry. Electrospray (ESI) is, by far, the most used ionisation technique for the coupling of liquid chromatography to mass spectrometry for the analysis of the analytes under study. Other API sources such as APCI and Atmospheric Pressure PhotoIonisation (APPI) have also been used for the analysis of the studied compounds [174–177].

Once the sample and the analytes contained in it have been ionised, detection is the last step of the analytical methodology. For this purpose, single quadrupoles (Q) have been widely employed for the identification and quantification of organic compounds in environmental samples. However, due to the limited sensibility and sensitivity that simple quadrupoles offer, triple quadrupoles (QqQ) have been, by far, the instrument of choice for the identification and quantification of environmentally-relevant compounds at ultra-trace levels, thus, obtaining higher confidence in complex matrices. Ion Traps (IT) and Lineal Ion traps (LIT) have also attracted special attention to analytical chemists due to their tandem in-time capabilities, making them highly suitable for identification and quantitation purposes.

Table 1.5. Literature review on LC-MS methods employed for the analysis of the pharmaceuticals under study.

Analytes	Matrix	Sample treatment	Column Dimensions	Instrument; Ionisation Acquisition method	LOD* (ppb)	LOQ* (ppb)	Ref.
Clofibric acid Ibuprofen Diclofenac	Wastewater drinking water	SPE (Oasis HLB)	Zorbax C18; 150×2.1 mm; 5 µm	HPLC-MS/MS (QqQ) ESI (+/-); MRM	0.001 0.006 0.004	0.003 0.020 0.012	[178]
Ibuprofen Diclofenac Clofibric acid Ofloxacin	Drinking water	SPE (Oasis HLB)	Purospher Star RP-18 endcapped C18; 125×2.1 mm;5 µm	HPLC-MS/MS (QqLIT) ESI (-); MRM	0.0004 0.001 0.0001 0.0004	0.002 0.007 0.0003 0.002	[179]
Ibuprofen Diclofenac	Wastewater	SPE (Oasis HLB and C18 sorbent)	Nucleodur C18; C18; 125×2 mm; 3 µm	HPLC-MS/MS (QqQ) ESI (+/-); MRM	0.003 0.003	0.01 0.01	[180]
Clofibric acid Diclofenac Ibuprofen	Wastewater	SPE (Oasis HLB, MAX and WAX)	Ascentis Express C18; 100×4.6 mm;2.7 µm	HPLC-MS/MS (QqQ) ESI (-); MRM	0.001 0.001 0.015	0.005 0.02 0.01	[181]
Ibuprofen Clofibric acid	Drinking water	SPE (C18 sorbent)	Waters BEH C18,C18; 50×2.1 mm;1.7 µm	UHPLC-MS/MS (Orbitrap) ESI(-); Full scan	-	-	[182]
Ofloxacin	Wastewater	On-line SPE (Oasis HLB)	BetaBasic C18; 150×2.1 mm; 3 µm	HPLC-MS/MS (IT) ESI (+); MRM	0.012	0.040	[183]
Multi residue	Drinking water Sediments	SPE (Oasis HLB) ASE*	Waters BEH C18;C18; 50×2.1 mm; 1.7 µm	UHPLC-MS/MS (QqToF) ESI (-); Full scan	-	-	[184]
Fluoroquinolone antibiotics	Wastewater	MISPE Ciprofloxacin as template	Hypersil Gold; C18; 30× 2.1mm; 5.0 µm	HPLC-MS/MS (QqQ) ESI (+); SIM	0.005	0.003	[185]
Fluoroquinolone antibiotics	Wastewater	MISPE Enrofloxacin as template	LUNA C18 (2); C18; 150×4.6 mm; 5 µm	HPLC-MS/MS (QqQ) ESI (+); SIM	0.005	0.002	[186]

* Values presented in this table refer to method LOD and LOQ.

Nevertheless, other hybrid instruments such as quadrupole-linear ion trap (QqLIT) that can perform both tandem in-time and in-space in the same instrument are also widely used.

In recent years, however, with the growing demand of higher complex analysis and samples (detection and identification of unknown chemicals at ultra-trace levels), tandem mass spectrometry combined with high-resolution mass spectrometry has exponentially gained attention and use by the scientific community for the analysis of environmental samples. Recent developments of electronics and related hardware, moreover, has conferred high resolution mass spectrometers improved sensibility and sensitivity, as well as enhanced dynamic range for quantitation purposes.

Both ionisation and instrumentation paragraphs will deeply be revised and extended in **Chapter 4** of the present manuscript, since liquid chromatography coupled to (tandem)-high resolution mass spectrometry will be the main analytical technique for the analysis of the pharmaceutical ofloxacin and its transformation products after having submitted it to TiO_2 photocatalysis.

1.4. References

1. (EEA), E. E. A. *European Environment Outlook* (2005).
2. Schwarzenbach, R.; Escher, B.; Fenner, K.; Hofstetter, T.; Johnson, C.; Von Gunten, U.; Wehrli, B. *Science (80-.)*. **313,** 1072–1077 (2006).
3. EC (European Commission). *Off. J. Eur. Communities* **L 269,** 1–93 (2000).
4. The European Parliament and the Council of the European Union. *Off. J. Eur. Union* **L348,** 84–97 (2008).
5. The European Parlament and the Council of the European Union. *Off. J. Eur. Union* **2013,** 1–17 (2013).
6. 2015/495, C. I. D. (Eu); 2015, of 20 M. *Off. J. Eur. Union* **L78/40,** 20–30 (2015).
7. Paul Grootendorst, E. P. & M. S. *Expert Rev. Pharmacoecon. Outcomes Res.* **9,** 353–364 (2009).
8. Associations, E. F. of P. I. and. (2016).
9. European Community. *Off. J. Eur. Union* 67–128 (2004).
10. The European Parliament and the Council of the European Union. *Off. J. Eur. Union* **L,** 34–57 (2004).
11. Touraud, E.; Roig, B. *KNAPPE - Knowl. Need Assess. Pharm. Prod. Environ. Waters* 41 (2008).
12. OECD. *OECD Publishing* (2013). doi:10.1787/health_glance-2013-en
13. Ebele, A. J.; Abou-Elwafa Abdallah, M.; Harrad, S. *Emerg. Contam.* (2017). doi:10.1016/j.emcon.2016.12.004
14. Geissen, V.; Mol, H.; Klumpp, E.; Umlauf, G.; Nadal, M.; Van der Ploeg, M.; Van de Zee, S. E. a. T. M.; Ritsema, C. J. *Int. Soil Water Conserv. Res.* **3,** 57–65 (2015).
15. Zuccato, E.; Calamari, D.; Natangelo, M.; Fanelli, R. *Lancet* **355,** 1789–1790 (2000).
16. Andreu, V.; Gimeno-García, E.; Pascual, J. A.; Vazquez-Roig, P.; Picó, Y. *Sci. Total Environ.* **540,** 278–286 (2016).
17. Archer, E.; Petrie, B.; Kasprzyk-Hordern, B.; Wolfaardt, G. M. *Chemosphere* **174,** 437–446 (2017).
18. Sangion, A.; Gramatica, P. *Environ. Int.* **95,** 131–143 (2016).
19. Kümmerer, K. *Chemosphere* **75,** 435–441 (2009).
20. Kümmerer, K. *Chemosphere* **75,** 417–434 (2009).
21. Trisciuoglio, D.; Krasnowska, E.; Maggi, A.; Pozzi, R.; Parasassi, T.; Sapora, O. in *Toxicology in Vitro* 449–456 (2002).
22. Umezawa, N.; Arakane, K.; Ryu, A.; Mashiko, S.; Hirobe, M.; Nagano, T. *Arch. Biochem. Biophys.* **342,** 275–281 (1997).
23. Marrot, L.; Belaidi, J. P.; Chaubo, C.; Meunier, J. R.; Perez, P.; Agapakis-Causse, C. *Toxicol. Vitr.* **15,** 131–142 (2001).

24. Yamamoto, T.; Tsurumaki, Y.; Takei, M.; Hosaka, M.; Oomori, Y. *Toxicol. Vitr.* **15,** 721–727 (2001).
25. Miolo, G.; Viola, G.; Vedaldi, D.; Dall'Acqua, F.; Fravolini, A.; Tabarrini, O.; Cecchetti, V. *Toxicol. Vitr.* **16,** 683–693 (2002).
26. Drlica, K. *Current Opinion in Microbiology* 504–508 (1999).
27. Chételat, A.; Albertini, S.; Gocke, E. *Mutagenesis* **11,** 497–504 (1996).
28. Hussy, P.; Maass, G.; Tummler, B.; Grosse, F.; Schomburg, U. *Antimicrob. Agents Chemother.* **29,** 1073–1078 (1986).
29. Hignite., C.; Azarnoff., D. L. *Life Sci.* **20,** 337–341 (1977).
30. Okeri, H. a; Arhewoh, I. M. *African J. Biotechnol.* **7,** 670–680 (2008).
31. Sanz-Nebot, V.; Toro, I.; Barbosa, J. *J. Chromatogr. A* **933,** 45–56 (2001).
32. Matamoros, V.; Bajona, J. M. *Environ. Sci. Technol.* **39,** 5449–5454 (2005).
33. IMS Health. 2013 (2013).
34. IMS Health. 2013 (2013).
35. McGettigan, P.; Henry, D. *PLoS Med.* **10,** (2013).
36. Awodele, O.; Fadipe, A. O.; Adekoya, M.; Adeyemi, O. O. *Ghana Med. J.* **49,** 25–9 (2015).
37. Lichtenberger, L.; Wang, Z.; Romero, J.; Ulloa, C.; Perez, J.; Giraud, M.; Barreto, J. *Nat. Med.* **1,** 154–158 (1995).
38. Vane, J. R.; Botting, R. M. *Am. J. Med.* **104,** 2–8 (1998).
39. Meloun, M.; Bordovská, S.; Galla, L. *J. Pharm. Biomed. Anal.* **45,** 552–564 (2007).
40. Acero, J. L.; Benitez, F. J.; Real, F. J.; Teva, F. *Sep. Purif. Technol.* **181,** 123–131 (2017).
41. Prado, M.; Borea, L.; Cesaro, A.; Liu, H.; Naddeo, V.; Belgiorno, V.; Ballesteros, F. *Int. Biodeterior. Biodegradation* **119,** 577–586 (2016).
42. Ahmed, M. B.; Zhou, J. L.; Ngo, H. H.; Guo, W.; Thomaidis, N. S.; Xu, J. *J. Hazard. Mater.* **323,** 274–298 (2017).
43. Besha, A. T.; Gebreyohannes, A. Y.; Tufa, R. A.; Bekele, D. N.; Curcio, E.; Giorno, L. *J. Environ. Chem. Eng.* (2017). doi:10.1016/j.jece.2017.04.027
44. Al-Obaidi, M. A.; Li, J.-P.; Kara-Zaïtri, C.; Mujtaba, I. M. *Chem. Eng. J.* **316,** 91–100 (2017).
45. Lee, H.; Jin, Y.; Hong, S. *Desalination* **399,** 185–197 (2016).
46. Cui, Y.; Liu, X. Y.; Chung, T. S.; Weber, M.; Staudt, C.; Maletzko, C. *Water Res.* **91,** 104–114 (2016).
47. Jiang, S.; Li, Y.; Ladewig, B. P. *Sci. Total Environ.* **595,** 567–583 (2017).
48. Joo, S. H.; Tansel, B. *J. Environ. Manage.* **150,** 322–335 (2015).
49. Tang, F.; Hu, H. Y.; Sun, L. J.; Sun, Y. X.; Shi, N.; Crittenden, J. C. *Water Res.* **90,** 329–336 (2016).
50. Fujioka, T.; Kodamatani, H.; Aizawa, H.; Gray, S.; Ishida, K. P.; Nghiem, L. D. *Water Res.* **118,** 187–195 (2017).

51. Sari, M. A.; Chellam, S. *J. Memb. Sci.* **520,** 231–239 (2016).
52. Bell, E. A.; Poynor, T. E.; Newhart, K. B.; Regnery, J.; Coday, B. D.; Cath, T. Y. *J. Memb. Sci.* **525,** 77–88 (2016).
53. Shafi, H. Z.; Matin, A.; Akhtar, S.; Gleason, K. K.; Zubair, S. M.; Khan, Z. *J. Memb. Sci.* **527,** 152–163 (2017).
54. De la Torre, T. .; Rodŕiguez, C. .; Gómez, M. A. .; Alonso, E. .; Malfeito, J. J. .; De la Torre, T.; Rodríguez, C.; Gómez, M. A. .; Alonso, E. .; Malfeito, J. J. . *Desalin. Water Treat.* **51,** 1063–1069 (2013).
55. Madaeni, S. S.; Mansourpanah, Y. *Desalination* **161,** 13–24 (2004).
56. Fujioka, T.; Khan, S. J.; McDonald, J. A.; Roux, A.; Poussade, Y.; Drewes, J. E.; Nghiem, L. D. *Desalination* **343,** 60–66 (2014).
57. Linares, R. V.; Li, Z.; Yangali-Quintanilla, V.; Li, Q.; Vrouwenvelder, J. S.; Amy, G. L.; Ghaffour, N. *Desalination* **393,** 31–38 (2015).
58. Li, Y. S.; Shi, L. C.; Gao, X. F.; Huang, J. G. *Desalination* **390,** 62–71 (2016).
59. Lee, S.; Shon, H. K.; Hong, S. *Desalination* (2017). doi:10.1016/j.desal.2017.02.010
60. You, M.; Wang, P.; Xu, M.; Yuan, T.; Meng, J. *Polym. (United Kingdom)* **103,** 457–467 (2016).
61. Yu, T.; Meng, L.; Zhao, Q.-B.; Shi, Y.; Hu, H.-Y.; Lu, Y. *Water Res.* **113,** 1–10 (2017).
62. Wang, Z.; Tang, J.; Zhu, C.; Dong, Y.; Wang, Q.; Wu, Z. *J. Memb. Sci.* **475,** 184–192 (2015).
63. Li, X.; Cai, T.; Amy, G. L.; Chung, T. S. *J. Memb. Sci.* **522,** 116–123 (2017).
64. Wang, Z.; Wang, C.; Yuan, J.; Zhang, C. *J. Chromatogr. B* **1040,** 38–46 (2017).
65. Herzog, T. H.; Jänchen, J. *Energy Procedia* **91,** 155–160 (2016).
66. Seliem, M. K.; Komarneni, S. *Microporous Mesoporous Mater.* **228,** 266–274 (2016).
67. Wei, H.; Teo, B.; Chakraborty, A.; Fan, W. *Microporous Mesoporous Mater.* **242,** 109–117 (2017).
68. Lyu, J.; Zeng, Z.; Zhang, N.; Liu, H.; Bai, P.; Guo, X. *React. Funct. Polym.* **112,** 1–8 (2017).
69. Mailler, R.; Gasperi, J.; Coquet, Y.; Buleté, A.; Vulliet, E.; Deshayes, S.; Zedek, S.; Mirande-Bret, C.; Eudes, V.; Bressy, A.; *et al. Sci. Total Environ.* **542,** 983–996 (2016).
70. Katsigiannis, A.; Noutsopoulos, C.; Mantziaras, J.; Gioldasi, M. *Chem. Eng. J.* **280,** 49–57 (2015).
71. Beijer, K.; Björlenius, B.; Shaik, S.; Lindberg, R. H.; Brunström, B.; Brandt, I. *Chemosphere* **176,** 342–351 (2017).
72. Margot, J.; Kienle, C.; Magnet, A.; Weil, M.; Rossi, L.; de Alencastro, L. F.; Abegglen, C.; Thonney, D.; Chèvre, N.; Schärer, M.; *et al. Sci. Total Environ.* **461–462,** 480–498 (2013).
73. Yagmur, E.; Turkoglu, S.; Banford, A.; Aktas, Z. *J. Clean. Prod.* **149,** 1109–1117 (2017).
74. Polyakov, M. V. *Zhur. Fiz. Khim* **2,** 799–805 (1931).
75. G., Wulff; A., S. *Angew. Chemie* **11,** (1972).

76. K, M. *Trends Biochem. Sci.* **19,** 9–14 (1994).
77. Liu, Y.; Liu, Z.; Gao, J.; Dai, J.; Han, J.; Wang, Y.; Xie, J.; Yan, Y. *J. Hazard. Mater.* **186,** 197–205 (2011).
78. Ersöz, A.; Say, R.; Denizli, A. *Anal. Chim. Acta* **502,** 91–97 (2004).
79. Li, F.; Du, P.; Chen, W.; Zhang, S. *Anal. Chim. Acta* **585,** 211–218 (2007).
80. Xu, S.; Lu, H. *Biosens. Bioelectron.* **85,** 950–956 (2016).
81. Li, J. W.; Wang, Y. L.; Yan, S.; Li, X. J.; Pan, S. Y. *Food Chem.* **192,** 260–267 (2016).
82. Kotova, K.; Hussain, M.; Mustafa, G.; Lieberzeit, P. A. *Sensors Actuators, B Chem.* **189,** 199–202 (2013).
83. Villar-Navarro, M.; Martín-Valero, M. J.; Fernández-Torres, R. M.; Callejón-Mochón, M.; Bello-López, M. Á. *J. Chromatogr. B Anal. Technol. Biomed. Life Sci.* **1044–1045,** 63–69 (2017).
84. Hanna Leijoto de Oliveira, Sara da Silva Anacleto, Anny Talita Maria da Silva, Arnaldo César Pereira, Warley de Souza Borges, Eduardo Costa Figueiredo, K. B. B. *J. Chromatogr. B* **1033–1034,** 27–39 (2016).
85. Qi, J.; Li, X.; Li, Y.; Zhu, J.; Qiang, L. *Front. Chem. Eng. China* **2,** 109–114 (2008).
86. Dai, C. M.; Zhou, X. F.; Zhang, Y. L.; Liu, S. G.; Zhang, J. *J. Hazard. Mater.* **198,** 175–181 (2011).
87. Guo, X.; Xia, Z.; Wang, H.; Kang, W.; Lin, L.; Cao, W. *Talanta* **166,** 101–108 (2017).
88. Del Moro, G.; Mancini, A.; Mascolo, G.; Di Iaconi, C. *Chem. Eng. J.* **218,** 133–137 (2013).
89. Moreira, F. C.; Vilar, V. J. P.; Ferreira, A. C. C.; dos Santos, F. R. A.; Dezotti, M.; Sousa, M. A.; Gonçalves, C.; Boaventura, R. A. R.; Alpendurada, M. F. *Chem. Eng. J.* **209,** 429–441 (2012).
90. Cassano, D.; Zapata, A.; Brunetti, G.; Del Moro, G.; Di Iaconi, C.; Oller, I.; Malato, S.; Mascolo, G. *Chem. Eng. J.* **172,** 250–257 (2011).
91. González, O.; Sans, C.; Esplugas, S. *J. Hazard. Mater.* **146,** 459–464 (2007).
92. Molkenthin, M.; Olmez-Hanci, T.; Jekel, M. R.; Arslan-Alaton, I. *Water Res.* **47,** 5052–5064 (2013).
93. Trovó, A. G.; Nogueira, R. F. P.; Agüera, A.; Fernandez-Alba, A. R.; Sirtori, C.; Malato, S. *Water Res.* **43,** 3922–3931 (2009).
94. Trovó, A. G.; de Paiva, V. A. B.; Machado, A. E. H.; de Oliveira, C. A.; Santos, R. O. *Sol. Energy* **97,** 596–604 (2013).
95. Trovó, A. G.; Pupo Nogueira, R. F.; Agüera, A.; Fernandez-Alba, A. R.; Malato, S. *Water Res.* **45,** 1394–1402 (2011).
96. Poerschmann, J.; Trommler, U.; Górecki, T. *Chemosphere* **79,** 975–986 (2010).
97. Bacardit, J.; Stötzner, J.; Chamarro, E.; Esplugas, S. *Ind. Eng. Chem. Res.* **46,** 7615–7619 (2007).

98. De Luna, L.; Da Silva, T.; Nogueira, R.; Kummrow, F.; Umbuzeiro, G. *J. Hazard. Mater.* **276,** 332–338 (2014).

99. Punzi, M.; Anbalagan, A.; Aragão Börner, R.; Svensson, B. M.; Jonstrup, M.; Mattiasson, B. *Chem. Eng. J.* **270,** 290–299 (2015).

100. Fenton, J. *J. Chem. Soc.* **65,** 899–911 (1984).

101. A. Sychev, V. I. *Russ. Chem. Rev.* **65,** 1105–1129. (1995).

102. Nidheesh, P. V.; Gandhimathi, R. *Desalination* **299,** 1–15 (2012).

103. Babuponnusami, A.; Muthukumar, K. *J. Environ. Chem. Eng.* **2,** 557–572 (2014).

104. Kiwi, J.; Lopez, A.; Nadtochenko, V. *Environ. Sci. Technol.* **34,** 2162–2168 (2000).

105. Teel, A. L.; Watts, R. J. *Carbon N. Y.* **94,** 179–189 (2002).

106. Liao, C. H.; Kang, S. F.; Wu, F. A. *Chemosphere* **44,** 1193–1200 (2001).

107. Balachandran, R.; Zhao, M.; Dong, B.; Brown, I.; Raghavan, S.; Keswani, M. *Microelectron. Eng.* **130,** 82–86 (2014).

108. Ghazi, N. M.; Lastra, A. A.; Watts, M. J. *Water Res.* **56,** 148–155 (2014).

109. Souza, B. S.; Dantas, R. F.; Cruz, A.; Sans, C.; Esplugas, S.; Dezotti, M. *Chem. Eng. J.* **237,** 268–276 (2014).

110. Crittenden, J. C.; Hu, S.; Hand, D. W.; Green, S. A. *Water Res.* **33,** 2315–2328 (1999).

111. Mehrjouei, M.; Müller, S.; Müller, D. *Chem. Eng. J.* **263,** 209–219 (2015).

112. Nawrocki, J.; Kasprzyk-Hordern, B. *Appl. Catal. B Environ.* **99,** 27–42 (2010).

113. Cheng, M.; Zeng, G.; Huang, D.; Lai, C.; Xu, P.; Zhang, C.; Liu, Y. *Chem. Eng. J.* **284,** 582–598 (2016).

114. Andreozzi, R.; Caprio, V.; Insola, A.; C, R. M. **53,** 51–59 (1999).

115. Meshref, M. N. A.; Klamerth, N.; Islam, M. S.; McPhedran, K. N.; Gamal El-Din, M. *Chemosphere* **180,** 149–159 (2017).

116. Suzuki, H.; Araki, S.; Yamamoto, H. *J. Water Process Eng.* **7,** 54–60 (2015).

117. Christiane Gottschalk, Judy Ann Libra, A. S. (Wiley, 2009).

118. De Witte, B.; Dewulf, J.; Demeestere, K.; Van Langenhove, H. *J. Hazard. Mater.* **161,** 701–708 (2009).

119. Li, X.; Wang, Y.; Yuan, S.; Li, Z.; Wang, B.; Huang, J.; Deng, S.; Yu, G. *Water Res.* 81–93 (2014).

120. Clusellas, A. S. (Universitat Autònoma de Barcelona, 2010).

121. Division, M. S.; Campus, O. R. (2018).

122. Jojoa-Sierra, S. D.; Silva-Agredo, J.; Herrera-Calderon, E.; Torres-Palma, R. A. *Sci. Total Environ.* **575,** 1228–1238 (2016).

123. Moreira, F. C.; Boaventura, R. A. R.; Brillas, E.; Vilar, V. J. P. *Appl. Catal. B Environ.* **202,** 217–261 (2017).

124. Sirés, I.; Cabot, P. L.; Centellas, F.; Garrido, J. A.; Rodríguez, R. M.; Arias, C.; Brillas, E.

Electrochim. Acta **52,** 75–85 (2006).

125. Zhao, X.; Hou, Y.; Liu, H.; Qiang, Z.; Qu, J. *Electrochim. Acta* **54,** 4172–4179 (2009).
126. Marselli, B.; Garcia-Gomez, J.; Michaud, P. -a.; Rodrigo, M. a.; Comninellis, C. *J. Electrochem. Soc.* **150,** D79 (2003).
127. Michael, I.; Hapeshi, E.; Aceña, J.; Perez, S.; Petrović, M.; Zapata, A.; Barceló, D.; Malato, S.; Fatta-Kassinos, D. *Sci. Total Environ.* **461–462,** 39–48 (2013).
128. Carbajo, J. B.; Petre, A. L.; Rosal, R.; Herrera, S.; Letón, P.; García-Calvo, E.; Fernández-Alba, A. R.; Perdigón-Melón, J. A. *J. Hazard. Mater.* **292,** 34–43 (2015).
129. Xie, R.; Meng, X.; Sun, P.; Niu, J.; Jiang, W.; Bottomley, L.; Li, D.; Chen, Y.; Crittenden, J. *Appl. Catal. B Environ.* **203,** 515–525 (2017).
130. Sable, S. S.; Ghute, P. P.; Álvarez, P.; Beltrán, F. J.; Medina, F.; Contreras, S. *Catal. Today* **240,** 46–54 (2015).
131. Sun, Q.; Wang, Y.; Li, L.; Bing, J.; Wang, Y.; Yan, H. *J. Hazard. Mater.* **286,** 276–284 (2015).
132. Bae, S.; Kim, D.; Lee, W. *Appl. Catal. B Environ.* **134–135,** 93–102 (2013).
133. Beltrán, F. J.; Pocostales, P.; Alvarez, P.; Oropesa, A. *J. Hazard. Mater.* **163,** 768–776 (2009).
134. Méndez-Arriaga, F.; Esplugas, S.; Giménez, J. *Water Res.* **44,** 589–595 (2010).
135. Quero-Pastor, M. J.; Garrido-Perez, M. C.; Acevedo, A.; Quiroga, J. M. *Sci. Total Environ.* **466–467,** 957–964 (2014).
136. Chang, C.-F.; Chen, T.-Y.; Chin, C.-J. M.; Kuo, Y.-T. *Chemosphere* **175,** 76–84 (2017).
137. George Tchobanoglous, Hilary Theisen, S. V. (McGraw-Hill, 1993).
138. Suarez-Ojeda, M. E.; Guisasola, A.; Baeza, J. A.; Fabregat, A.; Stüber, F.; Fortuny, A.; Font, J.; Carrera, J. *Chemosphere* **66,** 2096–2105 (2007).
139. Scholz, M.; Lee, B. *Int. J. Environ. Stud.* **62,** 421–447 (2005).
140. Sultana, M. Y.; Akratos, C. S.; Pavlou, S.; Vayenas, D. V. *Int. Biodeterior. Biodegrad.* **96,** 181–190 (2014).
141. Wu, H.; Zhang, J.; Ngo, H. H.; Guo, W.; Hu, Z.; Liang, S.; Fan, J.; Liu, H. *Bioresour. Technol.* **175,** 594–601 (2015).
142. Vymazal, J. *Ecol. Eng.* **73,** 724–751 (2014).
143. Zhang, D. Q.; Jinadasa, K. B. S. N.; Gersberg, R. M.; Liu, Y.; Ng, W. J.; Tan, S. K. *J. Environ. Manage.* **141,** 116–131 (2014).
144. Joan Garcia Serrano, A. C. H. *Univ. Politec. Cataluña* 1–96 (2008).
145. A, D.; Oka, M.; Fujii, Y.; Soda, S.; Ishigaki, T.; Machimura, T.; Ike, M. *Sci. Total Environ.* **584–585,** 742–750 (2017).
146. Tromp, K.; Lima, A. T.; Barendregt, A.; Verhoeven, J. T. A. *J. Hazard. Mater.* **203–204,** 290–298 (2012).
147. Lv, T.; Carvalho, P. N.; Zhang, L.; Zhang, Y.; Button, M.; Arias, C. A.; Weber, K. P.; Brix, H.

Water Res. **110,** 241–251 (2017).

148. Matamoros, V.; Rodríguez, Y.; Bayona, J. M. *Ecol. Eng.* **99,** 222–227 (2017).
149. Chen, J.; Ying, G. G.; Wei, X. D.; Liu, Y. S.; Liu, S. S.; Hu, L. X.; He, L. Y.; Chen, Z. F.; Chen, F. R.; Yang, Y. Q. *Sci. Total Environ.* **571,** 974–982 (2016).
150. Zhang, J.; Sun, H.; Wang, W.; Hu, Z.; Yin, X.; Ngo, H. H.; Guo, W.; Fan, J. *Bioresour. Technol.* **224,** 222–228 (2016).
151. Guittonny-Philippe, A.; Masotti, V.; Claeys-Bruno, M.; Malleret, L.; Coulomb, B.; Prudent, P.; Höhener, P.; Petit, M. É.; Sergent, M.; Laffont-Schwob, I. *Water Res.* **68,** 328–341 (2015).
152. Ávila, C.; Pedescoll, A.; Matamoros, V.; Bayona, J. M.; García, J. *Chemosphere* **81,** 1137–1142 (2010).
153. Clark, I. D. (2015).
154. Crompton, T. R. in *Determination of Metals in Natural Waters, Sediments and Soils; Chapter 6* 191–201 (2015).
155. Crompton, T. R. in *Determination of Metals in Natural Waters, Sediments, and Soils.* 1–8 (2015).
156. Holmes, R. J. *Advances in Gold Ore Processing* **15,** (Elsevier B.V., 2005).
157. Minkkinen, P. O.; Esbensen, K. H. *Anal. Chim. Acta* **653,** 59–70 (2009).
158. Vanderford, B. J.; Mawhinney, D. B.; Trenholm, R. A.; Zeigler-Holady, J. C.; Snyder, S. A. *Anal. Bioanal. Chem.* **399,** 2227–2234 (2011).
159. Mills, R. J. D. F. W. W. A. D. *J. Chromatogr. A* **7,** 259–268 (1976).
160. Wang, X.; Li, X.; Li, Z.; Zhang, Y.; Bai, Y.; Liu, H. *Anal. Chem.* **86,** 4739–4747 (2014).
161. Willenberg, I.; Meschede, A. K.; Schebb, N. H. *J. Chromatogr. A* **1391,** 40–48 (2015).
162. Khoeini Sharifabadi, M.; Saber-Tehrani, M.; Waqif Husain, S.; Mehdinia, A.; Aberoomand-Azar, P. *Sci. World J.* **2014,** (2014).
163. Yu, Y.; Wu, L. *J. Chromatogr. A* **1218,** 2483–2489 (2011).
164. Guo, L.; Lee, H. K. *J. Chromatogr. A* **1235,** 26–33 (2012).
165. Yu, J. T.; Bisceglia, K. J.; Bouwer, E. J.; Roberts, A. L.; Coelhan, M. *Anal. Bioanal. Chem.* **403,** 583–591 (2012).
166. Salgado, R.; Marques, R.; Noronha, J. P.; Carvalho, G.; Oehmen, A.; Reis, M. A. M. *Environ. Sci. Pollut. Res.* **19,** 1818–1827 (2012).
167. Azzouz, A.; Souhail, B.; Ballesteros, E. *J. Chromatogr. A* **1217,** 2956–2963 (2010).
168. Molina-Fernandez, N.; Perez-Conde, C.; Rainieri, S.; Sanz-Landaluze, J. *Environ. Sci. Pollut. Res.* **24,** 1–12 (2017).
169. Togola, A.; Budzinski, H. *Anal. Bioanal. Chem.* **388,** 627–635 (2007).
170. He, Y.; Sutton, N. B.; Rijnaarts, H. H. H.; Langenhoff, A. A. M. *Appl. Catal. B Environ.* **182,** 132–141 (2016).
171. López-Serna, R.; Petrović, M.; Barceló, D. *Sci. Total Environ.* **440,** 280–289 (2012).

172. Gu, L.; Hou, P.; Zhang, R.; Liu, Z.; Bi, K.; Chen, X. *J. Chromatogr. B Anal. Technol. Biomed. Life Sci.* **1033–1034,** 157–165 (2016).
173. Petersson, P.; Haselmann, K.; Buckenmaier, S. *J. Chromatogr. A* **1468,** 95–101 (2016).
174. Kwon, M.; Kim, S.; Yoon, Y.; Jung, Y.; Hwang, T. M.; Lee, J.; Kang, J. W. *Chem. Eng. J.* **269,** 379–390 (2015).
175. Ghauch, A.; Abou Assi, H.; Bdeir, S. *J. Hazard. Mater.* **182,** 64–74 (2010).
176. Lonappan, L.; Pulicharla, R.; Rouissi, T.; Brar, S. K.; Verma, M.; Surampalli, R. Y.; Valero, J. R. *J. Chromatogr. A* **1433,** 106–113 (2016).
177. Cristina, T.; Santos, R.; Cesar, J. *J. Chromatogr. A* **879,** 3–12 (2000).
178. Chen, H. C.; Wang, P. L.; Ding, W. H. *Chemosphere* **72,** 863–869 (2008).
179. Gros, M.; Petrović, M.; Barceló, D. *Anal. Chem.* **81,** 898–912 (2009).
180. Pailler, J. Y.; Krein, A.; Pfister, L.; Hoffmann, L.; Guignard, C. *Sci. Total Environ.* **407,** 4736–4743 (2009).
181. Gilart, N.; Marcé, R. M.; Borrull, F.; Fontanals, N. *J. Sep. Sci.* **35,** 875–882 (2012).
182. Pinhancos, R.; Maass, S.; Ramanathan, D. M. *J. Mass Spectrom.* **46,** 1175–1181 (2011).
183. Feitosa-Felizzola, J.; Temime, B.; Chiron, S. *J. Chromatogr. A* **1164,** 95–104 (2007).
184. Smital, T.; Terzić, S.; Lončar, J.; Senta, I.; Žaja, R.; Popović, M.; Mikac, I.; Tollefsen, K. E.; Thomas, K. V.; Ahel, M. *Environ. Sci. Pollut. Res.* **20,** 1384–1395 (2013).
185. Prieto, A.; Schrader, S.; Bauer, C.; Möder, M. *Anal. Chim. Acta* **685,** 146–152 (2011).
186. Benito-Peña, E.; Martins, S.; Orellana, G.; Moreno-Bondi, M. C. *Anal. Bioanal. Chem.* **393,** 235–245 (2009).

~ Chapter 2.

Objectives and thesis structure

With the development of such new and sophisticated analytical techniques, able to detect up to ng L^{-1} concentration levels of organic and inorganic pollutants present in ground and surface waters, high concern has arisen from the scientific community from its presence and the way to get rid of them. However, it has been vastly demonstrated that conventional sewage treatment plants are not able to efficiently remove these chemicals from polluted waters. The main focus of the research conducted to date is to use advanced oxidation processes (AOP) and/or biological treatments to reduce these concentration levels, up to their non-detection. TiO_2 photocatalysis is a well-known AOP which has resulted in promising results for its possible inclusion in wastewater treatment plants.

The main objectives and goals of the present thesis are:

- To develop *easy to support* TiO_2 nanofibers for its inclusion on industrial applications.
- To study the degradation, upon TiO_2 photocatalysis, of 4 environmentally relevant pharmaceutical drugs: ofloxacin, clofibric acid, diclofenac and ibuprofen.
- Demonstrate if this oxidative treatment, TiO_2 photocatalysis, generates and introduces potential hazards to the aquatic environment and humans after removing these pharmaceutical drugs from water.

These main objectives can be then sub-divided into more specific objectives:

- To develop novel materials, based on TiO_2, to be used as new catalysts in industrial applications.
- The development of analytical techniques, mainly based on HPLC coupled to tandem high-resolution mass spectrometry, to identify and quantify low trace amounts of these pharmaceuticals in real water samples.
- The application of tandem high-resolution mass spectrometry to assess the degradation of these pharmaceutical drugs after photocatalytic degradation in order to propose the degradation pathway.
- To study the toxicity evolution of the degradation kinetics in order to know which phases of the photocatalytical process are of higher concern.

These mentioned points will be presented and discussed along the three chapters proposed for this thesis:

- Chapter 1 has introduced a brief overview on the challenges that both society and scientific community have to face for a better reutilisation of the water resources and the removal of environmentally relevant pollutants from the aquatic system. Moreover, this chapter has reviewed the most important wastewater treatment technologies available today for the removal of these pollutants of high concern. Finally, a revision on the analytical methodologies available for the analysis of the compounds under study is also included.
- Chapter 3 will introduce the history of titanium (IV) oxide as a photo-catalyst and how different research groups have addressed their investigations to achieve better removal efficiencies of this material. This chapter includes the experimental section where it is described the development of titanium (IV) oxide nanofibers used in this PhD thesis, their physico-chemical characterisation and their performance degrading the four pharmaceuticals selected.
- Chapter 4 is devoted to the analysis of transformation products coming from oxidative treatments. A brief revision will be given to the present target and non-target mass spectrometry strategies to detect and identify all these unknown chemicals. This chapter includes the experimental section devoted to the detection and characterisation of ofloxacin transformation products after being submitted to TiO_2 nanoparticles and nanofibers. High-resolution mass spectrometry, tandem mass spectrometry and ion mobility mass spectrometry have been used to characterize the transformation products detected.
- Chapter 5 deals with the toxicological implications these transformation products may pose to the aquatic and human toxicity. First of all, it will be introduced how different research groups have addressed this issue and which are the main organisms and endpoints to estimate aquatic and human toxicity. The experimental section includes the toxicological studies in order to provide information for, both aquatic and human, implications of ofloxacin after being submitted to TiO_2 photocatalysis.
- Although each Chapter includes their own conclusions, overall conclusions of all the research carried out are included in the last section of this manuscript as well as the references cited and used along the thesis.

~ Chapter 3.

Development and characterisation of TiO_2 nanofibers for photocatalysis applications.

In the past four decades, the detection and quantification of environmentally relevant chemicals (emergent or prior pollutants) such as surfactants, antibiotics, drugs, pesticides and their metabolites or by-products, etc. has been the premise and the major goal of thousands of analytical research laboratories established around the world. The major source of such pollutants is the continuous disposal of urban and industrial wastewaters. Conventional sewage treatment plants do not completely remove these chemicals, and as a result, they are being introduced into the aquatic environment at parts per-billion ($\mu g\ L^{-1}$) and parts per-trillion ($ng\ L^{-1}$) concentration levels. Although these concentrations are much lower than those used in medical applications, the related potentially toxic effects in the aquatic environment are still poorly known and cannot be discarded.

Hence, the concern about the above context entailed some researchers to investigate about the use of advanced oxidation processes (AOPs) to achieve the complete removal of a wide diversity of organic compounds. Amongst the technologies dealing with such oxidative treatments, heterogeneous photocatalysis, photo-Fenton and ozonation are the most representative ones, as already discussed in **Chapter 1**.

This chapter is divided in four sections: the introduction, the experimental methods, the results and discussions from the present research and all conclusions derived from the whole chapter. Having discussed TiO_2 photocatalysis and the main mechanism in **Chapter 1**, this introduction will be mainly focused on the TiO_2 structure and properties and recent developments done in this research area and results derived from past research done in this field. The experimental section will be devoted to settle the experimental bases by which **Chapter 4** and **Chapter 5** will be then build up. This will be centred on the development of TiO_2 nanofibers, its characterisation and the description of experimental *set-up* and operational conditions. The section that compiles the results will be focused on the application of synthesised nanofibers to removal of four target contaminants presented in **Chapter 1**. The activity of commercially available TiO_2 nanoparticles and nanofibers will also be tested along the present research. Once their performance is studied in MilliQ water (synthetic samples), raw water coming from a real wastewater treatment plant will be used as a real test sample in order to study the performance of TiO_2 photocatalysis under real conditions.

3.1. Introduction

Titanium is the ninth most abundant element (the seventh metal) in the earth's crust [1,2] and can be found in practically all rocks and sediments, and is present in plants, animals and natural waters. Even though pure TiO_2 can be found in nature [3] from rutile, anatase and brookite it is from the mineral ilmenite, $FeTiO_3$, by which TiO_2 is mostly produced and obtained nowadays, up to 6.1 million tonnes in 2016 [4]. Hence, ilmenite can be treated in two ways to obtain titanium (IV) oxide: the chloride and the sulphate processes, representing the 60 and 40 % of the production respectively. The main advantages of the chloride process over the sulphate process are: less energy is required; less waste disposal, the possibility to recover most of the reactants used and it is usually conducted in continuous while the sulphate process is run in batch mode. Even though these advantages the chloride process offers, it requires high grade ore, namely rutile TiO_2, which may finally increase the final production cost.

The chloride process

This process was first introduced by Du Pont in the 1950s [5–7] and begins by mixing the raw material with coke (900-1000 ºC) in order to reduce rutile TiO_2 to elemental Ti (**Equation 3.1**). Then, a stream of chlorine gas oxidises Ti to $TiCl_4$ (**Equation 3.2** and **3.3**). Finally, $TiCl_4$ is converted to pure TiO_2 by its oxidation in a pure oxygen flame at 1500 ºC, recovering, at the same time, the vast majority of chlorine gas.

$$TiO_2 + C \rightarrow Ti + CO_2 \qquad \textbf{Eq. 3.1}$$

$$Ti + 2Cl_2 \rightarrow TiCl_4 \qquad \textbf{Eq. 3.2}$$

$$TiCl_4 + O_2 \rightarrow TiO_2 + 2Cl_2 \qquad \textbf{Eq. 3.3}$$

The sulphate process

In the sulphate process, ilmenite is digested with concentrated sulphuric acid, generating a mixture of sulphate salts (**Eq. 3.4**). The resulting solution contains titanylsulphate ($TiOSO_4$) and iron sulphate ($FeSO_4$). Before obtaining titanium (IV) oxide, a reduction step is needed, in which remaining ferric ions (Fe^{3+}) are converted to ferrous ions (Fe^{2+}). Titanyl sulphate is hydrolysed to titanium dioxide hydrated, which precipitates and consequently is separated from ferrous sulphate and sulphuric acid (**Eq. 3.5**). Finally, hydrated titanium is calcinated at a temperature over 1000º C (**Eq. 3.5**).

$$FeTiO_3 + 2\,H_2SO_4 \rightarrow TiOSO_4 + FeSO_4 + 2H_2O \qquad \textbf{Eq. 3.4}$$

$$TiOSO_4 + 2\,H_2O \rightarrow TiO_2 \cdot nH_2O + H_2SO_4 \qquad \textbf{Eq. 3.5}$$

$$TiO_2 \cdot nH_2O \rightarrow TiO_2 + nH_2O \qquad \textbf{Eq. 3.6}$$

3.1.1. Physicochemical properties of TiO_2

Titanium (IV) oxide, TiO_2, has three crystalline polymorphs: rutile (tetragonal, space group $P4_2$/mnm;); anatase (tetragonal, space group /4_1/amd); and brookite (orthorhombic, space group Pbca). Rutile has the highest density and refractive index and is the most thermally stable polymorph. Anatase and brookite can be transformed to the rutile polymorph by thermal treatment.

Amongst the three crystalline phases, only anatase and rutile have been used in photocatalytical applications. Whereas rutile presents a lower *band-gap* energy than anatase (3.0 and 3.2 eV respectively), properties such as crystallographic orientation, surface properties, electron transfer, amongst other properties, directly affects the photocatalytical properties of TiO_2. However, anatase is generally considered to be more active than the rutile phase. Despite the intensive investigation carried out on TiO_2 for photocatalytical applications, there is not a general consensus rationalising these experimental evidences, mainly attributed to the difficulties in studying individual factors affecting its photocatalytical properties [8].

Nevertheless, it has been widely demonstrated and accepted that the *co-existence* of the anatase and rutile phases leads to a synergic effect resulting in greater photocatalytical properties that when compared these phases alone. That is the case of *Degussa* P25 nanoparticles, a mixture 80:20 anatase:rutile.

3.1.2. Toxicity

The toxicity of TiO_2 is low and was approved as a food colorant (E-171 in the European legislation) [9]. TiO_2 can be encountered in toothpastes, pill coatings and chewing gums [9,10]. Even though its low toxicity, new concerns and awareness have arisen due to its use in its nanometric size. This question and concern is not only related to this catalyst but also to other metal oxides such as ZnO, CuO which will be further discussed in the following lines. It is for this reason that further research into the properties of bulk (non-nano) and nano materials is required to efficiently evaluate their eco-toxicity and possible adverse effects on animals and humans health.

3.1.2.1. Ecotoxicity of nano-TiO_2

Xiong *et al.* [11] studied the toxicity of nanoTiO_2 and ZnO on zebrafish, showing that TiO_2 nanoparticles were slightly more toxic than bulk TiO_2 while no differences were observed between nano and bulk (non-nano) ZnO. Another important conclusion derived from this study was that nanoTiO_2 could render toxic effects even though if these nanoparticles were not inside the cell: TiO_2 promoted the formation of radical oxidative species (ROS), which had a strong effect on membrane integrity. In the same line of research, Cherchi *et al.* [12] observed that cyanobacteria cells suffered severe stress responses when they were exposed to TiO_2. These responses included membrane disruption, membrane crystalline inclusions and formation of ROS species [12].

Daphnia Magna has been the main focus of several investigations dealing with the ecotoxicity of nano-metal oxides. For instance, Wiench *et al.* [13] studied several factors that could influence on the toxic response (acute toxicity) of nanometric and bulk TiO_2 and ZnO: coatings of the materials tested, the medium used for the dispersion of the catalyst, etc. This investigation showed no differences between nano and bulk TiO_2. In the same line of research worked Zhu *et al.* [14], who gave a deeper insight on possible adverse effects of nano TiO_2 (nanoTiO_2) at prolonged exposures. These researchers studied the consequences of chronic exposure to this catalyst using *D. Magna* too. This study demonstrated that while acute toxicity (up to 48 h) did not show remarkable toxic adverse effects, 72 h of exposure did. When this administration was prolonged up to 21 days, inhibition of growth and reproduction and mortality was observed. Even though it was not possible to establish a direct relationship, these authors also revealed that *D. Magna* exposed to nTiO_2 displayed abnormal food intake which could be the cause of growth and reproduction inhibition.

Heinlaan *et al.* [15] used a test battery of ecotoxicity assays, *Vibrio fischeri*, *Daphnia magna* and *Thamnocephalus platyurus* for the toxicity assessment of different metal oxide nanoparticles: ZnO, CuO and TiO_2. The most remarkable conclusion of this study, in the same line as other researchers did before and discussed above, was that the intimate contact particle – cell wall was the most notorious phenomena rendering toxic adverse effects on the studied organisms. They stated that this contact could favour the solubilisation of metals and generate extracellular ROS (in accordance with previous studies mentioned above).

3.1.2.2. *In-vivo* toxicity of nano-TiO_2.

To date, several research groups have addressed *in-vivo* toxicity using mice and rats as *in-vivo* models. Most of these researches have focused their point of attention to study the Adsorption, Desorption, Metabolism and Excretion (ADME studies) of these particles. As a brief summary of the ADME behaviour of this catalyst, once administrated to mice, its concentration was still high after 14 days after administration in different organs studied: spleen, lung, kidney, and liver. These results could be also extended up to testicles, brain, heart and other organs depending on how TiO_2 was administrated, for instance, intravenous, abdominal injection etc. [16,17]. All these researches, in accordance to the ecotoxicological evaluation, pointed out to the enhancement of the reactive species generated as the main cause of the potential hazard of TiO_2 nanoparticles. Wang *et al.* [18] investigated the acute toxicity of 25, 80 nm and fine TiO_2 particles on mice. No acute toxicity was observed after a single oral exposure to 5 g kg^{-1} of TiO_2 nanoparticles. However, these researchers observed liver injury after the exposure of nano-sized TiO_2 (25 and 80 nm) compared to that of bulk TiO_2 ADME studies, performed by ICP-MS, revealed that TiO_2 was mainly retained in livers, kidneys, spleen, and lung. Finally, the histopathological examination revealed hepatic injury and renal lesion on those animals submitted to nanometric TiO_2, compared to those which had been administrated bulk TiO_2. Wen *et al.* [19] also submitted mice to oral exposure of TiO_2 nanoparticles. They demonstrated that its administration at a concentration of 500 mg kg^{-1} caused DNA strand breaks and chromosomal damage which could explain the mechanisms of TiO_2 nanoparticles carcinogenicity. Moreover, they finally stated that TiO_2 nanoparticles induced genotoxicity in organs, such as blood, bone marrow and embryos. Finally, Shrivastava *et al.* [20] investigated the toxic effects of three metal oxide nanoparticles, TiO_2, ZnO and Al_2O_3 on mouse erythrocytes, brain and liver. Mices were administered a single oral dose of 500 mg kg^{-1} of each nanoparticle for 21 consecutive days. Their results not only showed that nanoTiO_2 was responsible for enhanced levels of ROS species but also their neurotoxic potential due to the high levels of dopamine and norepinephrine present in the brain.

3.1.2.3. *In-vitro* toxicity of nano-TiO_2.

Opposite to those mentioned researchers, which addressed the main issue of study in the comparison of bulk and nanoTiO_2, Sayes *et al.* [21] focused on nanoscale TiO_2 but investigated its adverse effects as function of the crystalline phase in human dermal fibroblasts and human lung epithelial cells. This study revealed that rutile was two orders of magnitude less cytotoxic than similarly sized anatase nanoparticles. This fact could be directly linked to their structure-activity relationship. Hence, anatase, the most active crystalline phase in generating ROS under UV illumination was also the most active in generating ROS without UV irradiation, thus, causing disruptive cellular functioning and oxidative damage to the cells of study. In the same line of investigation, Petkovi *et al.* [22] investigated the genotoxic responses to two types of anatase and rutile in human hepatoma HepG2 cells. Anatase not only was found to generate more reactive species but also was found to cause persistent DNA strand breaks. None of both kinds of TiO_2 affected the viability of HepG2 cells, thus, not being cytotoxic, but this research demonstrated that both crystalline structures induced changes in the mRNA expression, thus, showing their potential to be considered as genotoxic agents. Human embryonic kidney (HEK-293) cells were the main focus of attention of Meena *et al.* [23] since this organ plays a critical role on the excretion of these nanoparticles. This research found TiO_2 nanoparticles to be cytotoxic using both the MTT and LDH assays. This study attributed the oxidative stress as the main reason by which nanoTiO_2 was toxic: elevated ROS levels, reduced levels of glutathione and increased lipid peroxidation. Mouse fibroblasts were the main object of study of Jin *et al.* [24]. The exposition of TiO_2 to these cells led to a reduction of cell viability (MTT assay), en enhancement of ROS levels whereas a decrease on the glutathione GSH was observed. These evidences led to the unequivocal conclusion, in agreement with past researches, that TiO_2 nanoparticles enhanced cell mortality and altered ADME processes.

3.1.3. Strategies for improving TiO_2 efficiency

In recent years, thousands of publications have devoted their lines of research into the modification of titanium (IV) oxide to improve its photocatalytic activity. All these modifications consist of either morphological or chemical modification. Amongst the morphological considerations, the interest basically resides in synthetizing TiO_2 nanomaterials with controlled particle sizes, which directly affects its surface area and its optical properties. On the other hand, the chemical modification consists in the incorporation of additional metals, non-metals or other semiconductors. Even though the tremendous effort done and the improvements achieved, all literature agrees that seems to be difficult and a laborious task to control, one by one, all parameters and factors involved in the improvement of the catalyst [8].

3.1.3.1. Morphological considerations

The surface morphology (particle and agglomerate size) of a photocatalyst is a key factor to determine its photoactivity. The morphological modification of bulk TiO_2 has been vastly investigated in their form of nanoparticles [25–30], nanofibers [31–35], nanotubes [36–38] and other morphological phases [39–43]. These has been possible due to the great variety of synthetic routes to obtain them, for instance, sol-gel [25,44,45], hydrothermal [34,36,43] and solvothermal [27,46,47], amongst others. These TiO_2 controlled shapes and structures have already demonstrated excellent results in terms of photoactivity and photodegradation of organic compounds in respect to bulk TiO_2 (non-nanometric). Moreover, several improvements have been made in respect to commercial TiO_2 nanoparticles, mainly P25 Degussa (Evonik), obtained by the Aerosil® (or flame hydrolysis) synthesis method. Since the present research has devoted all the efforts on TiO_2 nanoparticles and nanofibers, this introduction will be centred in all the achievements, to date, of both kinds of particles. A little introduction of the most promising researches on nanotubes, nanorods and arrays will be also revised in this section.

TiO_2 nanoparticles

Apart from the mentioned reasons for such TiO_2 popularity among the scientific community (low-cost, moderate toxicity, ease of synthesis, availability of commercial TiO_2 nanoparticles, etc.) the possibility to improve TiO_2 photoactivity have deeply attracted numerous investigations. As cited before, particle size drastically determines the efficiency of the catalyst to be used in photocatalysis applications. By decreasing particle size, the specific surface area of the catalyst increases, thus, also increasing the number of available active sites to promote the generation of oxidative species and the adsorption phenomena. At the same time, the recombination of photogenerated charges (electron (e^-) and hole (h^+)). By decreasing the catalyst's particle size, this phenomenon becomes less significant, thus, improving the catalyst's efficiency. However, this strategy works up to the point where the optical properties of a material start to change. For instance, bulk TiO_2, more concretely, anatase and rutile, have been widely found to present a band-gap of 3.2 and 3.0 respectively. Nevertheless, by decreasing TiO_2's (or other semiconductor) particle size, its band's gap energy increases, as stated by Brus *et al.* [48] who stated that the valence band energy is shifted to lower energies while the conduction band is shifted to higher energies. In the same way, numerous research groups have reported quantum confinement of nanometric TiO_2 (< 10 nm) observing a clear shift on the band-gap position. This is the case of Satoh *et al.*

[49] who synthesised 1.5 – 2.8 nm TiO_2 nanoparticles by the sol-gel method. From the optical absorption spectra of the synthesised nanoparticles they derived a difference in 1 eV in the band-gap energies for particles differing only in 1 nm size. For these reasons cited before, several groups have evaluated the effect of particle size on the photodegradation efficiency of TiO_2 nanoparticles (**Table 3.1**), being the optimum particle size for photocatalytic applications between 14 and 60 nanometers.

TiO_2 nanofibers

TiO_2 nanoparticles have a large surface to volume ratio which facilitates photocatalytic reactions. However, when they are suspended in a solution, these particles tend to agglomerate with the consequent efficacy reduction, the charge recombination rate increases and are difficult to separate from the matrix where they are suspended. However, if these particles are supported to avoid the separation step, the major advantage of using this nanomaterial is lost (decrease of surface to volume ratio). In recent years, however, one-dimensional (1-D) nanomaterials have attracted the attention of research groups pursuing higher photocatalytical properties. In this way, nanofibers have already shown and demonstrated properties with significant relevance for its application in photocatalysis and other research areas (in comparison to TiO_2 in its nanoparticle form): high electron mobility, improved charge-separation ability, large surface to volume ratio, high porosity, interconnected pores along the dimension and strong light scattering.

TiO_2 nanofibers are easily fabricated by the electrospinning technique [32,33,50,51]. A scheme of the electrospinning process is depicted in **Figure 3.1** and **3.2**. TiO_2 nanofibers are fabricated by electrospinning a TiO_2 precursor, usually tetrabutyl titanate or titanium (IV) isopropoxide, with a suitable polymer. The major effects affecting the synthesis process are: materials (polymer nature, concentration, viscosity, etc.) and operational conditions (electric current, spinning distance, temperature, humidity, etc.) [52–55]. Amongst all variables, polymer concentration and solvent used are the main factors affecting the formation of uniform nanofibers. At low polymer concentrations, nanofibers are not formed due to their low viscosity whereas at high concentrations, nanofibers with different undesired morphological defects are usually obtained [52–55]. Solvent affects the surface tension of the prepared polymer solution, affecting the electrospinning process and the fibers obtained [52–55]. Once finished, the resulting product is burned to remove the polymer at high temperature sintering process.

Table 3.1. Influence of particle size on the degradation efficiency of TiO_2.

TiO_2 characteristics	Synthesis	Targets	TiO_2 concentration [Target] Other conditions	Main results	Ref.
Particles size ranging from 4.5 to 29 nm 100 % crystalline anatase 3.11 eV band-gap and 170 $m^2 g^{-1}$ (4.5 nm particles) 3.09 eV band-gap and 58 $m^2 g^{-1}$ (29 nm particles)	Sol-gel method from titanium (IV) alkoxide	CO_2 reduction	1mg mL^{-1} TiO_2 1 ppm CO_2 8W Hg lamp (254 nm)	The photocatalytical reduction of CO_2 was found to be greatest with 14 nm size particles, thus, clearly showing that the photocatalytical performance not only depends in TiO_2's band gap or specific surface area but also on the synergic effect between all crystallite properties and characteristics.	[25]
Particles size of 6, 11 and 21 nm 253, 146, and 70 $m^2 g^{-1}$ BET surface area respectively 100 % crystalline anatase Doping with Fe^{3+}, Nb^{5+} and Pt/Nb^{5+} No information on band-gap.	Sol-gel hydrolysis precipitation of titanium isopropoxide followed by hydrothermal treatment or post-calcination.	Chloroform	0.5 g L^{-1} TiO_2 1.2 10^{-2} M $CHCl_3$ 1000 W Xe arc lamp	The oxidation of $CHCl_3$ in pure TiO_2 increased when particle size was reduced from 21 to 11 nm, but decreased when it was further reduced to 6 nm. The optimal dopant [Fe^{3+}] was investigated and was found to decrease by increasing particle size. Nb^{5+} doped particles showed better removal yields than pure TiO_2 and Fe^{3+} doped nanoparticles. Pt/Nb^{5+} loaded onto unmodified particles, however, did not result in significant $CHCl_3$ removal yields.	[26]
Synthesised particles ranged 2.3 and 30 nm and BET surface area between 268 and 28 $m^2 g^{-1}$ respectively. 100 % anatase No information on band-gap.	Sol-gel synthesis from titanium tetraisopropoxide and calcinations.	Trichloroethylene	6 mg TiO_2 coated on a glass plate UV lamp (no details given)	The prepared particles enhanced their activity when particle size decreased from 27 to 7 nm. The efficiency dropped when this particle size was further decreased, in accordance to previous investigations carried out.	[29]

Table 3.1 ***(continued).*** Influence of particle size on the degradation efficiency of TiO_2.

TiO_2 characteristics	**Synthesis**	**Targets**	**TiO_2 concentration [Target] Other conditions**	**Main results**	**Ref.**
Particles ranged from 10 to 35 nm depending on the acetic acid and tetrabutyl titanate ratio used in each synthesis. 100 % crystalline anatase 83 to 120 m^2g^{-1} surface area No information on band-gap.	Solvothermal treatment of tetrabutyl titanate and calcinations	Benzene	0.4 g TiO_2 UV lamp 250 W (365 nm) 0.1 – 0.5 mg L^{-1} benzene	The acetic acid/tetrabutyl titanate (HAc/TBT) ratio had a significant influence on the morphology of synthesised TiO_2. The authors found that by decreasing the HAc/TBT ratio particle size also decreased (up to 12nm). However, in terms of photocatalytical degradation of benzene, the authors found the optimal particle size was 15 nm, achieving a 75 % conversion of benzene in 120 minutes.	[27]
Particles ranged from 5 to 60 nm with BET surface areas ranging from 300 to 25 m^2 g^{-1}. 100 % anatase obtained. No information on band-gap.	Flame synthesis from titanium tetraisopropoxide	Phenol	2.5 g L^{-1} TiO_2 450 W Xe lamp 1.4 mM phenol	The photoactivity of synthesised TiO_2 in degrading phenol increased as particle size increased too (up to 30 nm). When increased up to 60 nm, the rate of phenol's degradation significantly decreased.	[28]
Particle size of 8, 14 and 19 nm were prepared by sol-gel synthesis and post-calcination. Their BET areas were 80, 41 and 30 m^2 g^{-1} respectively. 100 % anatase No information on band-gap.	Sol-gel synthesis from titanium tetraisopropoxide and calcinations.	Methylbutynol	No details are given	The photocatalytical decomposition rate of 8 nm size TiO_2 nanoparticles was much higher than 14 nm nanoparticles (up to 7 times) and up 16 times when compared to 19 nm nanoparticles.	[30]

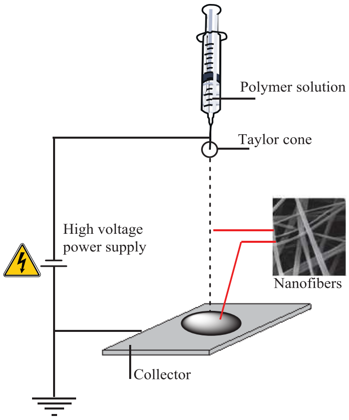

Figure 3.1. Scheme of the electrospinning process.

Figure 3.2. Electrospinning instrument.

Researches on the application of nanofibers to photocatalysis have already shown promising results [32,33], especially in dispersed (suspended) conditions. In comparison to nanoparticles, this 1D material can be separated easier than spherical nanomaterials. Their fixation onto an inner support considerably reduces the photocatalytical activity (due to lowering of the surface-to-volume ratio and partial loss of the active surface sites of photocatalysts) [56–59], a phenomenon also observed when immobilising TiO_2 nanoparticles. **Table 3.2** shows a collection of research papers dealing with the synthesis of TiO_2 nanofibers, its applicability to the degradation of organic compounds and their comparison to commercially available TiO_2 nanoparticles (P25 Degussa).

For instance, Maeng *et al.* [59] prepared TiO_2 nanofibers from titanium (IV) isopropoxide for the photocatalytic degradation of pharmaceuticals three pharmaceuticals: cimetidine, propranolol and carbamazepine. This research tuned the anatase-rutile content by changing the annealing temperature to which NFs were submitted concluding that the optimum anatase-rutile content was 70:30 respectively (as P25 NPs). Whereas the synthesised NF completely removed the studied pharmaceuticals in MilliQ water, a significant drop was observed (20 times) when the same experiments were conducted with a secondary wastewater effluent matrix. Zabar *et al.* [58] used the same TiO_2 precursor and the synthesised NFs were immobilised on glass slides of 262 cm^2 area by a sol-gel method. This research was focused in the removal of three neonicotinoid insecticides: imidacliprid, thiamethoxam and clothianidin. Despite the high initial concentration used in the present study (100 mg L^{-1}), the complete degradation of the three selected compounds was achieved in less than 2 hours (MilliQ water). Their degradation performance, however, was not tested under real conditions.

Table 3.2. TiO_2's nanofibers for photocatalytical applications

TiO_2 NF characteristics	Synthesis	Targets	Experimental conditions	Main results	Ref.
BET surface area 49 to 59 $m^2\ g^{-1}$ 100 % anatase (10 nm crystallite size)	Electrospinning of tetrabutyl titanate + calcination	CO_2 reduction	1000 mg mL^{-1} TiO_2 in MilliQ water 300 W Xe arc lamp CO_2 was produced by reaction of $NaHCO_3$ with HCl	P25 nanoparticles are used as reference material. Prepared TiO_2 nanofibers show much more photocatalytical activity than reference P25 nanoparticles (25 fold higher).	[31]
No BET information Calcinated in air: 100 % anatase (10 nm crystallite size) Fibers annealed under NH_3 flow: 99% anatase, 1% rutile (10 nm crystallite size)	Electrospinning and sol-gel preparation with tetrabutyl titanate Calcination in air (undoped) Calcination under NH_3 flow (N-doped)	Rhodamine B	1000 mg L^{-1} TiO_2 8 W UV lamp (254 nm) [target] = 12 mg L^{-1}	Nitrited TiO_2 nanofibers possessed enhanced visible-light photocatalytic activity compared with TiO_2 nanofibers and their photocatalytical activity was 12 times greater than undoped nanofibers.	[32]
BET surface area ranged from 370 to 579 $m^2\ g^{-1}$ TiO_2: anatase and rutile (not % included in reference) Band gap: 2.2 to 2.8 eV	Electrospinning and hydrothermal synthesis.	Congo red, methylene blue, methyl orange, eosin red	0.25 mg mL^{-1} TiO_2 in MilliQ water [target] = 10 mg L^{-1}	Prepared carbon TiO_2 composites show relevant visible-light photoactivity. The prepared composites easily degraded 10 mg L^{-1} of the target compounds (up to 6 times) and were able to degrade higher concentrations as well (up to 120 mg L^{-1}).	[33]

Table 3.2 *(continued).* TiO_2's nanofibers for photocatalytical applications

TiO_2 NF characteristics	Synthesis	Targets	Conditions	Main results	Ref.
BET surface area: 19.79 $m^2\ g^{-1}$ Band gap: 3.21 eV for anatase nanofibers and decreased to 3 eV by increasing rutile TiO_2 nanorods	Electrospinning of titanium(IV) isopropoxide and annealed in air ; TiO_2 nanorods on TiO_2 NFs surface	Rhodamine 6G	1 mg mL^{-1} TiO_2 in MilliQ water [target] = 8 mg L^{-1}	The photocatalytical activity of the 3D nanostructure (nanorod + nanofibers) showed a significant enhancement of Rhodamine 6G removal yield. (up to 20 %).	[34]
16.8 $m^2\ g^{-1}$ BET surface area 100% anatase	$K_2Ti_2O_5$ was converted to TiO_2 anatase by calcination at 810 ºC	Phenol	1 mg mL^{-1} TiO_2 in Methanol [target] = 20 mg L^{-1} 300 W Hg lamp	Single crystalline {001} anatase facets exposed. Nanofibers showed higher degradation rates (up to 3 times) than TiO_2 P25 nanoparticles (reference material). Nanofibers were recycled up to 20 times with no appreciable lose in degradation rate and were easier to recover by sedimentation than P25 nanoparticles.	[35]
No BET information Different samples were synthesised, obtaining TiO_2 phases from 0 to 100% rutile TiO_2. For photocatalysis tests, 70% anatase and 30% rutile NFs were used.	Electrospinning of titanium(IV) isopropoxide	Furfuryl alcohol (FFA) Cimetidine (CMT) Propranolol (PRP) Carbamazepine (CBZ)	Six 4W lamps (350 to 400 nm) with a light intensity of $3x10^4$ E $min^{-1}\ L^{-1}$. TiO_2 NFs were immobilised onto 2 quartz pieces of 4 cm^2. [target] = 1 mg L^{-1}	The optimum % of anatase:rutile was found 70:30. The degradation achieved was 80 % depletion. Lower pH led to faster degradation kinetics whereas when a secondary wastewater effluent was used, a drastic reduction of pharmaceutical removal was observed.	[59]

Table 3.2 (*continued*). TiO_2's nanofibers for photocatalytical applications

TiO_2 NF characteristics	**Synthesis**	**Targets**	**Conditions**	**Main results**	**Ref.**
BET surface area of 69.5 m^2 g^{-1} and pore volume of 0.13 m^3 g^{-1} 100 % anatase (crystal size of 8.62 nm)	Electrospinning of titanium(IV) isopropoxide	1,4-dioxane	5 NFs films with a total coated area of 75cm^2. 1 Xe lamp (1000W m^{-2}) Light intensity 80 mW cm^{-2} (315–400 nm) [target] = 25–200 mg L^{-1}	No adsorption was found between 1,4-dioxane and the prepared TiO_2 films. The photocatalytic treatment of 1,4-dioxane resulted in the linear removal of TOC whereas the removal of 1,4-dioxane was concentration dependent. The prepared TiO_2-NF films appeared to have an equivalent photocatalytic activity compared to P25 nanoparticles.	[60]

Other engineered nanostructures

As cited before, TiO_2 nanoparticles have a high surface to volume ratio but suffers from high scattering of free electron (reduced mobility) due to its structural disorder when these particles are placed together in solution or supported. Apart from nanofibers, another way of solving electron scattering are nanotubes. Nano-TiO_2 have been synthesised in the past 20 years by a wide diversity of methods such as sol-gel, anodization, hydrothermal, solvothermal, etc. Nanotubes [36–38] are highly ordered architectures with a high number of contact points which enables the good electrical conductivity. As well as occurred with TiO_2 nanoparticles or nanofibers, nanotubes have also been tuned in order to achieve better electrical and optical properties. For instance, some of the modifications carried out on this catalyst are: annealing, doping, conversion to titanates (for piezoelectric or ferroelectric properties), the filling (or decoration) of the nanotube with other nanoparticles and their conversion to monolayers.

These mentioned solutions (fibers and tubes) cited before are one-dimension structures which aim was to overcome the major drawbacks of zero-dimensional material (particles). An alternative engineered solution are TiO_2 nanosheets [41,61] (two-dimensional) and interconnected architectures (three dimensional). Nanosheets have a small thickness (1-10 nm) and a lateral size ranging from the submicrometer to 10 micrometers. However, these structures have not given remarkable results due to their electronic insulation (few of the electron–hole pairs produced after TiO_2 irradiation can diffuse to the surface), thus, not being possible the degradation of the organic compound and the generation of oxidative species.

3.1.3.2. Chemical modification

Even though nanometric TiO_2, in whatever of the mentioned forms, has been successfully applied as a photocatalyst in environmental applications, there is still a gap for improving its photo-efficiency, that is, enhancing the quantum yield of TiO_2 (number of degraded pollutant *versus* absorbed photons). In order to overcome this limitation, several strategies have been published, in which TiO_2 was chemically modified. Amongst them, the most employed ones are: doping [32,33,62–64], dye sensitization [65–68] and noble metal deposition [69–71]. Other researches carried out to date are: polymer conjugation [72–74] and coupling TiO_2 with a p-conjugated structure [75–77].

Doping

The main objective of TiO_2 doping is to dope (or incorporate) trace impurities of metal and non-metal species into the TiO_2 structure. The scope of TiO_2 doping is to: extend the range in which TiO_2 can absorb, always with the willing to make TiO_2 absorb at higher wavelengths and favour photo-induced charge separation. Moreover, this impurity needs to be introduced at low concentrations in order to not produce changes in TiO_2's crystalline phase. The way in which TiO_2 is modified comprises the following methodologies: ion-assisted sputtering, plasma, ion-implantation, chemical vapour deposition (CVD) and sol-gel.

TiO_2 metal doping (cationic doping) refers to the incorporation of manganese, molybdenum, vanadium, chromium, cerium, selenium, iron, nickel, copper, tin, aluminium, lead, silver, zirconium, zinc, cobalt, etc. [55–62]. Despite that metal doping has resulted in great results, its efficiency strongly depends on the concentration of dopant used and the *d*-level electronic configuration. However, the cons of metal doping relate to the possibility of these metal impurities to act as recombinant centres of the photo-generated charges.

On the other side, non-metal doping refers to the introduction of B, C, P, S, Cl, As, Se, Br, Sb, Te, or I [63–75]. Non-metal doping has gained much attention in recent years as a way to enhance the photocatalytical activity of TiO_2 in the visible region. This was firstly demonstrated by the novel study conducted by Asahi *et al.* [95]. They prepared TiO_2-N_x films by sputtering TiO_2 in an N_2 (40%)/Ar gas mixture for 4 hours at 550º C. The optical properties of the obtained N-doped TiO_2 clearly demonstrated that could absorb incident light below 380 nm, thus, significantly narrowing TiO_2's band gap.

They attributed this phenomenon to the overlapping of N p states with O 2p states. In the same line of research, Wang *et al.* [96] prepared N-doped TiO_2 from commercial P25 TiO_2 by submitting it under a NH_3 gas flow. The results indicated that N-doped TiO_2 possessed visible light absorption in the wavelength range of 400–520 nm, mainly attributed to the formation of single-electron-trapped oxygen vacancies, in accordance with the study of Asahi *et al.* [95]. Other strategies such as C doping have been explored with consideration due to its low cost and its potential for band-gap narrowing [97]. It has been demonstrated, by comparing it to untreated TiO_2, that this alternative made this new catalyst to absorb in the visible wavelength range. Contrary to N doping, C did not seem to be incorporated into the TiO_2's structure but to be located on the surface of the catalyst, being the C-C bond the responsible for visible light absorption. Carbon doping has been explored with consideration of its low cost and its potential for band-gap narrowing, which can help to achieve significant improvements in visible light absorption capabilities. Chen *et al.* [98] synthesized pure anatase C-doped TiO_2 by a low-pressure flat-flame metal organic chemical vapour condensation method by eliminating the nitrogen doping possibility. They demonstrated that visible light absorption was attributed to the carbon doping, but that the carbon did not incorporate into the TiO_2 crystal, and instead located on the surface. They also claimed that the C–C bond was the responsible for the light absorption.

Dye sensitization

Dye sensitization [99–103] is one of the main and most promising alternatives to date to extend TiO_2's absorption response in the visible region. The reaction mechanism is proposed from **Equations 3.7** to **3.10**. Here, the dye, adsorbed on TiO_2's surface, absorbs light and passes from the ground state (D) to the excited state (D*). Then, the excited electrons are directly injected into the conduction band of the TiO_2 material, also resulting in the oxidation of the dye (D^+). Shang et al. [103] demonstrated that the enhanced photocatalytic activity of dye-sensitized TiO_2 could be attributed to the wider absorption spectrum range and the electron transferred from the excited state of the dye molecule directly to the CB of TiO_2, which results in a greater number of electrons in the CB of TiO_2.

$Dye\ (D) + hv \rightarrow dye^*(D^*)$ **Eq. 3.7**

$TiO_2 + D^* \rightarrow D^+ + TiO_2(e^-)$ **Eq. 3.8**

$TiO_2(e^-) + O_2 \rightarrow TiO_2 + {}^{\bullet}O_2^-$ **Eq. 3.9**

$e^- + {}^{\bullet}D^+ \rightarrow D$ **Eq. 3.10**

${}^{\bullet}O_2^- + 2H^+ \rightarrow {}^{\bullet}O_2 + H_2O_2$ **Eq. 3.11**

$H_2O_2 + {}^{\bullet}O_2^- \rightarrow {}^{\bullet}OH + OH^- + O_2$ **Eq. 3.12**

$pollutant + ({}^{\bullet}OH,\ {}^{\bullet}OOH\ or\ O_2^-) \rightarrow pollutant\ degradation$ **Eq. 3.13**

Noble metal deposition

The incorporation of noble metals and metals such as Pt, Au, Ag, Cu, V, Ni, and Sn to the TiO_2's structure has demonstrated to extend the spectral response of the photocatalyst [69–71,104–106]. This is because Fermi's level of deposited metals is lower than that of the TiO_2, making possible the transference of the photo-generated electrons from TiO_2's conduction band to the metallic particle. However, several studies claim that these metallic species, especially transition metals, act as recombination sites for the photo-induced charge carriers, thereby lowering the quantum efficiency. Due to this fact, the main challenge of this strategy is to fully optimize the concentration of the metallic species and optimize the stability between the metallic particle and TiO_2. Moreover, co-doping with two or more suitable heteroatoms (non-metal–non-metal, metal–non-metal, and metal–metal) has also demonstrated its applicability to change the band structures of the TiO_2-metal system to obtain the desired photo-activity response.

3.1.4. Alternative photocatalysis

As it has been discussed along the document, TiO_2 is the semiconductor mostly employed for photocatalytic applications due to its high efficiency, photochemical stability, low toxicity and low cost. However, several semiconductors have also been tested as alternative materials for photocalysis applications. This is the case of ZnO [107–111], CdS [44,112–114], CeO_2 [115–118], WO_3 [119–122], Fe_2O_3 [47,123–125], and other metal oxides. By far, ZnO represents nowadays the major alternative to TiO_2 photocatalysis.

ZnO has been considered as the main alternative to TiO_2 for photocatalytic applications. In the same line as TiO_2, this material has been prepared by several groups in different nano-shapes: nanofibers [45,126–128], nanoarrays [66,129–131], nanorods [123,132–134], nanotubes [135–138], etc. Contrary to TiO_2, its solubility in strong acids and alkalis limits the pH range in which it can be used.

Comparisons between TiO_2 and ZnO have yielded variable results. For instance, Poulios *et al.* [107] compared the photocatalytic activities of ZnO (Merck) and TiO_2 (Degussa P25) for the degradation of aqueous solutions of the herbicide triclopyr with higher degradation rates for ZnO. Kansal *et al.* [139] reported the photocatalytic decolorization of Reactive Blue 19 (RB-19) in aqueous solutions containing TiO_2 or ZnO as catalysts and concluded that ZnO is a more efficient catalyst than TiO_2 in the color removal of RB-19. Daneshvar *et al.* [111], in the same line as Kansal *et al.* reported a similar degradation mechanism of Acid Red 14 over ZnO nanoparticles when compared to TiO_2 nanoparticles, also observing a higher degradation rate that the reference material (TiO_2). On the other hand, Poulios *et al.* [107] showed that ZnO, in terms of CO_2 formation as a function of time, was slower than Degussa P25 TiO_2 in decolorisating Reactive Black 5.

In the same line as discussed with TiO_2, several approaches have been employed to tune the photocatalytic properties of ZnO and overcome its drawbacks. For instance, ZnO has been coupled to different metals such as Cd [140–142], Mn [143–145], Ni [146–150] , Co [151,152], etc. obtaining significant reduction in the ZnO's band gap (up to 1 eV). Similar to

TiO_2, another limitation of ZnO is its wide band gap (3.2 eV), which restricts light absorption to the UV region. A possible strategy to extend ZnO absorption to visible light may be the modification of its valence band position by anionic doping, as has been achieved for TiO_2. In this line of research, C [153,154], N [155–157], S [158,159], amongst others, have been the most widely used ZnO dopants, achieving reductions in the ZnO band's gap between 0.2 and 0.7 eV.

Experimental work

As discussed in the general introduction of **Chapter 1**, several water treatment methods may be applied in order to achieve the complete degradation and mineralisation of environmentally relevant organic pollutants contained in natural water matrices. The research undergone during the present thesis, however, has only focused its point of attention in one technology, TiO_2 photocatalysis, and four pharmaceutical drugs: ofloxacin, clofibric acid, diclofenac and ibuprofen.

The experimental work of the present chapter deals with the synthesis and characterisation of 1D TiO_2 nanofibers for their latter use in adsorption and degradation studies of the mentioned drugs. Due to the fact that the vast majority of published applications dealing with TiO_2 photocatalysis are carried out in suspended conditions, to date, one limitation of this technology is the complete recovery (or fixation onto an inner support) of the material for its reutilisation in industrial applications. Hence, an added value of the present research is the development of fixation methods to avoid the recovery step of the catalyst in industrial applications.

TiO_2 nanoparticles (P25 *Degussa*) and commercially available TiO_2 nanofibers (PARDAM Nanotechnologies) were used along the present study so as to compare the morphological characteristics and photocatalytical performance to that synthesised material. Morphological analysis consisted in the evaluation of surface characteristics (SEM) and BET surface area and structural composition, determined by X-Ray Diffraction (crystallite phase and size).

The adsorption and photocatalytical performance of the tested materials were evaluated and were the main point of the present study. The maximum adsorption capacity of the tested materials was derived by fitting concentration *versus* time kinetics to Langmuir-Hinshelwood and Freundlich adsorption isotherms. The photocatalytical performance of the the tested materials was finally evaluated by carrying out these photocatalytical processes at an environmentally realistic concentration of the four model drugs under study (10 $\mu g\ L^{-1}$) in MilliQ water. Prior scaling the lab conditions set-up, the photocatalytical degradation of these four model drugs was conducted in a real water matrix coming from an urban wastewater treatment plant.

3.2.1. Materials and methods

3.2.1.1. Chemicals and reagents

Polyvinylpyrrolidone (PVP), ethanol, acetic acid (HAc) and titanium isopropoxide (TIP) used for the synthesis of TiO_2 nanofibers were purchased from Sigma-Aldrich. Ethyl cellulose, 4-octylphenol polyethoxylate (Triton X-100), acetylacetone, and α-terpineol, used for the fixation of the studied catalysts were obtained from Sigma-Aldrich. TiO_2 P25-Degussa nanoparticles were purchased from Fluka (Sigma-Aldrich) whereas commercial TiO_2 nanofibers were obtained from PARDAM Nanotechnologies (Czech Republic). The studied pharmaceutical drugs ofloxacin (OFX), clofibric acid (CLOF), diclofenac (DCF) and ibuprofen (IBU) were purchased from Sigma-Aldrich (Steinheim, Germany). LC/MS grade acetonitrile and water were obtained from Fluka (Steinheim, Germany), while formic acid (98– 100%) was purchased from Merck (Darmstadt, Germany). Nitrogen (99.995% pure) used as collision induced dissociation (CID) gas was supplied by Air Liquide (Barcelona, Spain).

3.2.1.2. Synthesis of electrospun TiO_2 Nanofibers

The procedure used in this doctoral research to synthesize the TiO_2 nanofibers consisted in three steps: (I) preparation of the TiO_2 precursor solution to be used in the electrospinning process; (II) fabrication of electrospun polymeric nanofibers and (III) thermal treatment to obtain the crystalline inorganic nanofibers.

The precursor solution for the electrospinning process was prepared by dissolving polyvinylpyrrolidone (PVP, 6.0 g) in 50 g ethanol. Then, acetic acid (4.0 g, HAc) and titanium isopropoxide (TIP, 20 g) were added into the above prepared solution. All polymeric solutions were mixed by magnetic stirring for 2 hours in order to yield a homogeneous solution. Once mixed together, the obtained solution was electrospun onto an aluminum foil by using commercially available electrospinning equipment (MECC Co. LTD., model NF-103). Plastic syringes fitted with metal needles were used as electrospinning nozzles. The operating conditions were: flow rates of 2 mL h^{-1}, applied voltage 30 kV, and working distance of 10 cm.

Finally, TiO_2 nanofibers were obtained by thermal treatment in a pyrolysis furnace of the resulting polymeric precursor nanofibers. The fibers were heated at 500 °C in air with a ramp of 5 ºC min^{-1}. This temperature was finally held for 3 hours.

3.2.1.3. TiO_2 fixation

Synthesised TiO_2 nanofibers, ethyl cellulose (EC) with 48.0-49.5% ethoxyl content, 4-octylphenol polyethoxylate (Triton X-100), acetylacetone, acetic acid and α-terpineol were used as received for the preparation of the TiO_2 paste. An ethyl cellulose gel was prepared to be used as a binder in the TiO_2 paste formulation. The pure EC content was 15% in the EC gel whereas the rest of the 85% was α-terpineol. Triton X-100, acetylacetone and acetic acid were mixed together before the addition of the TiO_2 nanopowder (20% *w/w*). Then, α-terpineol was added and the whole mixture was mixed until the TiO_2 catalysts were completely wetted. Finally, the previously prepared ethyl cellulose gel was added and the whole mixture was thoroughly mixed. The resulting TiO_2 paste deposition was performed by conventional casting knife process over a glass fiber filter (Glass Filter GF-52, Hahnemuehle). This method homogeneously distributed the paste over the support with a thickness of 50 μm. Finally, sintering treatment was carried out in order to remove all additives containing TiO_2 paste. The sintering heat treatment consisted on: I) an isotherm at 80 ºC held for 20 min, II) a 12.3º C min^{-1} ramp until 450 °C III) an isotherm at 450 ºC held for 30 min in order to avoid any change in the TiO_2 structure.

3.2.1.4. TiO_2 Characterization

For XRD analysis, samples were prepared by manual pressing in cylindrical standard sample holders of 16 millimetres of diameter and 2.5 millimetres of height. XRD measurements were performed by means of a PANalytical X′Pert PRO MPD alpha1 powder diffractometer (Almelo, Netherlands). Current was set at 45 kV and 40 mA. A Bragg-Brentano θ/2θ geometry was used and a Cu Kα1 radiation (λ=1.5406 Å) was selected by means of a Johanson type Ge (111) focusing primary monochromator. An X′Celerator silicon strip 1D detector (active length of 2.113°). 2θ scans were obtained from 4 to 120° 2θ with step size of 0.033° and measuring time of 150 s per step. An automatic divergence slit system and a mask enabled a constant irradiated surface of 120 mm^2 over the analysed sample. The nitrogen adsorption and desorption isotherms were measured using a TriStar 3000 gas adsorption analyser (Micromeritics, Georgia, United States). All samples were degassed at 150° C prior to nitrogen adsorption measurements. The Brunauer–Emmett–Teller (BET) specific surface area (SBET) was determined by a multipoint BET method using the adsorption data in the relative pressure (P/P_0) range of 0.05–0.3. The pore size distribution was determined using adsorption data via the Barret–Joyner–Halender (BJH) method. The average pore size was obtained from the nitrogen adsorption volume at P/P_0 of 0.97. A

Scanning Electron Microscope (SEM, JSM-6010LV-Touchscope, Jeol Instruments) was used to study the surface morphology of the synthesised nanofibers. SEM samples were coated with a 4 nm gold layer using a sputter coater (Sputter Coater 108 auto, Cressington Scientific Instruments).

3.2.1.5. Adsorption experiments

All batch adsorption experiments were conducted in the dark over a 30 min period under magnetic stirring. The analytical measurements were made on suspensions prepared by mixing 350 mL solution containing different drug (ofloxacin, clofibric acid, diclofenac and/or ibuprofen) under several concentrations, ranging from 10 μg L^{-1} to 10 mg L^{-1}, at a fixed TiO_2 concentration (250 mg L^{-1}) and fixed pH (7). The prepared solution was sonicated for 30 min in darkness. Sample aliquots (1500 μL) were withdrawn at 1, 2.5, 5, 10, 15, 20 and 25 and 30 minutes, centrifuged at 20000 g (15000 rpm) and diluted with water when necessary. Preliminary experiments were performed until 24 h under constant magnetic stirring confirmed that equilibrium was reached after 30 min.

Derived concentration *versus* time results were then fitted to Langmuir and Freundlich isotherms to study and compare the performance and adsorption characteristics of the studied catalysts.

3.2.1.6. Photocatalytic experiments

Photocatalytic experiments with artificial irradiation were performed in a 600 mL Borosilicate 3.3 cylindrical photochemical reactor (Trallero&Schlee, Barcelona, Spain). Photocatalytic experiments with suspended TiO_2 NPs or NFs (nanoparticles and nanofibers respectively) were carried out as follows: 350 mL of an aqueous solution containing 10 μg L^{-1} of each individual drug and the appropriate amount of TiO_2 NPs was added so as to have the desirable catalyst loading (250 mg L^{-1}). The resulting suspension was loaded into the photochemical reactor (**Figure 3.3**) and sonicated for 30 min in darkness to ensure the homogenization of the TiO_2 suspension and the complete equilibration of adsorption/desorption of the substrate on the catalyst surface. The solution was then irradiated using 4 UVA lamps of 25W (Radium Ralutec, 9W/78, 315–400 nm, λmax = 365 nm) placed around the reactor, providing a total UV irradiation at the center of the solution in the 0.8-1.1 mW cm^{-2} range. UV irradiation was measured with an UV light meter YK-35UV from Lutron (Barcelona, Spain).

Supported TiO_2 experiments (**Figure 3.4**) were conducted as follows: a disc of 15 cm^2 containing the photocatalyst (10 mg) was laid on the bottom centre of the photochemical reactor. 50 mL of solution containing the tested pollutants was then placed in it and left for 30 min in darkness while stirring at 200 rpm to ensure the complete equilibration of adsorption/desorption of the pollutant on the catalyst surface In this case, 1 UVA lamps was then placed 3 cm above the solution surface in order to achieve the same UV irradiation than when TiO_2 was suspended. The height from the UVA lamp to the surface of the solution was adjusted in order to have the same irradiance as those cited in the suspended conditions set-up.

The treatment in both suspended and supported conditions was conducted up to 240 minutes. Temperature was always kept at 25 ± 2º C and pH to 7. To follow the kinetic evolution of the intact drugs and photoproducts, 15 samples were periodically withdrawn (1500 and 250 µL in suspended and supported conditions respectively) from the reactor: 0.5, 1, 2.5, 5, 10, 15, 20, 25, 30, 60, 90, 120, 150, 180, and 210 min. Prior analysis, the solution was centrifuged at 20,000 g (15,000 rpm) in both set-up experiments

First of all, the set of trials were conducted by MilliQ water to elucidate the type of by-products generated through the treatment and its toxicity. Therefore, every target drug was evaluated separately with a relatively high concentration (10 mg L^{-1}). Afterwards, concentration was diminished to 10 µg L^{-1} (final conditions) in order to simulate those concentrations found on real waters. Finally, photocatalytic activity of these semi-conductors was evaluated under a real water matrix coming from an urban wastewater treatment plant (UWWTP) located in Terrassa, Barcelona, Spain.

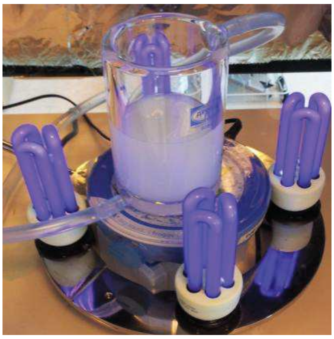

Figure 3.3. Suspended conditions set-up.

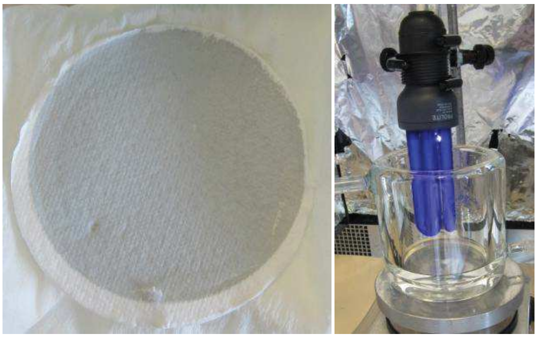

Figure 3.4. “Supported” conditions set-up.

3.2.1.7. LC-MS/HRMS

Ultra high performance liquid chromatography (UHPLC) was performed on an Accela HPLC system (Thermo Fisher Scientific, San José, CA, USA) equipped with a quaternary pump, an autosampler and a column oven. A BEH C18 column (100 x 2.1 mm and 1.7 µm particle size; Waters, Milford, CA, USA) was used with a flow rate of 400 µL min^{-1} and held at 40 ºC. Solvents used in the gradient elution program were H_2O (solvent A), acidified with a 0.05% formic acid and CH_3CN (solvent B) (*v/v*). The gradient elution program was as follows: 10% B isocratic for 1 min as initial conditions, then in 5 min solvent B was risen up to a 90% B and this mobile phase composition was held for 1 min; finally the system went back to initial condition in 1 min. HRMS analysis was performed in a Q-Exactive Orbitrap (Thermo Fisher Scientific, San José, CA, USA) equipped with a thermally assisted electrospray ionization source (H-ESI II).The operating parameters in the positive ion mode were as follows: ESI voltage was 3.5 kV; capillary and vaporizer temperatures were 320º C; sheath gas, auxiliary gas and sweep gas flow rate were 40, 10 and 2 au (arbitrary units) respectively, and the tube lens was held at 50 V. In the negative mode, the ESI voltage was set at −2.5 kV and the rest of tune parameters were the same as in positive mode. For targeted tandem MS experiments (MS/HRMS), nitrogen was used as collision gas (1.5mTorr), and the normalized collision energy (NCE) ranged from 10 to 30% depending on the compound. The mass spectrometer was operated in profile mode (scan range, *m/z* 100–1000) with a resolving power of 70,000 FWHM (full width half maximum) (at *m/z* 200) and an automatic gain control setting of 3×10^6 with a maximum injection time of 200 ms.

3.2.1.8. Other analytical determinations

Ionic chromatography

Ionic chromatography was performed on a Dionex ICS 3000 (Thermo Fischer Scientific, San José, CA, USA) equipped with a binary pump, an autosampler and a column oven. Conductivity detection was used to detect and quantify the analytes of interest. An precolumn AG19 and IonPac Anion Exchange column AS19 (250 x 4.0 mm and 7.5 µm particle size) were used at a flow rate of 1 mL min^{-1} held at room temperature. Solvents used in the gradient elution program were H_2O as solvent A and H_2O (100 mM NaOH) as solvent B. The gradient elution program was as follows: 10% B isocratic for 10 min (as initial conditions); then in 25 min solvent B was risen up to a 50% B. The system went back to initial conditions in 5 min and stabilised for 10 minutes.

Inductive coupled plasma coupled to mass spectrometry

Inductive Coupled Plasma coupled to Mass Spectrometry (ICP-MS) was performed on an Agilent ICP-MS 7500 (Agilent, Santa Clara, CA, USA) and an analytical microwave (CEM, Mars, NC, USA). 10 mL of water sample is digested with 10 mL of ultrapure concentrated nitric acid (70%, Sigma-Aldrich). The analytical microwave digestion program consisted in a temperature ramp of 15 minutes to reach 190 ºC and held for 10 minutes. Digested samples were then diluted with a 2% HCl aqueous solution to obtain the desired concentration for ICP-MS analysis.

Surfactants

The analysis of cationic, anionic and non-ionic surfactants was carried out using the commercially available Hach-Lange kits. Cationic surfactants (LCK 331, Dr. Lange) were measured as complexes of bromophenol blue extracted in chloroform and later photometrically evaluated at 410 nm. Anionic surfactants (LCK 332, Dr. Lange) were determined as methylene blue complexes, extracted in chloroform and later measured by UV-Vis detection at an absorbance of 610 nm. Finally, non-ionic surfactants (LCK 333, Dr. Lange) were analysed by the reaction of these compounds with tetrabromophenolphthalein ethyl ester (TBPE) to yield complexes which are extracted in dichloromethane and later photometrically analysed at an absorbance of 610 nm.

3.2.2. Results and discussions

3.2.2.1. TiO_2 synthesis

At the beginning of the experimental section of the present chapter has been described the optimised conditions of TiO_2 synthesis and its fixation over a glass fiber support for its latter use in immobilised applications. The detailed description of the sol-gel synthesis method used for the preparation of the investigated TiO_2 nanofibers will be discussed all along this section, as well as the methodology used for its immobilisation.

Electrospinning precursor solution

Different solutions consisting in polyvinylpyrrolidone (PVP, polymer acting as viscosity increaser), titanium isopropoxide (TIP, TiO_2 precursor), ethanol (Et, solvent) and acetic acid (HAc, catalyst agent of the sol-gel reaction) were prepared in order to test the stability and the reaction rate of the resulting solution prior submitting it to the electrospinning process, as depicted in **Table 3.3**. Fixing the amount of polymer, ethanol and acetic acid to 6, 50 and 4 g respectively, the TIP content was varied from 2 to 20 grams. As the TIP/PVP ratio increased, the inorganic content of the solution also raised and so did the final weight of the obtained nanofibers after being submitted to the electrospinning process and calcination.

Table 3.3. Composition and properties of the prepared precursor electrospinning solutions

Test	PVP (g)	Et (g)	TIP(g)	HAc (g)	TIP / HAc	Viscosity (cP)	Conductivity (µS/cm)	Stability
0	6	50	2	4	0.5	162	12	Low
1	6	50	4	4	1	173	23	Low
2	6	50	8	4	2	158	41	High
3	6	50	12	4	3	149	88	High
4	6	50	16	4	4	144	146	High
5	6	50	20	4	5	142	401	High

Moreover, as the TIP/HAc increased, so did the stability of the precursor solution (before the electrospinning process). In fact, a white precipitate of TiO_2 was observed in solutions of tests 1 and 2 after a brief period of time (up to 3 hours), thus, disabling the option of controlling the whole synthesis process. The stability of those prepared solutions significantly increased for TIP/HAc ratios greater than 2. The conductivity and viscosity of the resulting solution were also measured in order to achieve a greater control of the electrospinning process, since both of them play a key role on the final results obtained. Conductivity can tune the width of the final nanofibers obtained, thus, obtaining thinner nanofibers as conductivity increases. On the other side, viscosity directly affects the electrospinning performance, hence, not being possible to obtain smooth fibers in very low viscosity solution, whereas very high viscosity solutions results in the hard ejection of jets from solution. Therefore, the chosen test solution for the latter electrospinning process was number 5, containing a TIP/HAc ratio of 5.

Electrospinning

Even though test solutions 0 and 1 were initially discarded for further nanofibers fabrication due to the impossibility of controlling the whole reaction, these solutions were also submitted to the electrospinning process. As expected, this process resulted to be less stable for these solutions but still was possible to obtain homogeneous nanofibers as can be seen in the SEM images of **Figure 3.5** and high resolution SEM (**Figure 3.6**). The remaining solutions tested also presented large and homogeneous TiO_2-precursor nanofibers having a diameter size ranging between 200 and 600 nm width. The diameter width could be tuned by changing the TIP/PVP ratio. By increasing it, the diameter width of the obtained solution decreased. This change, however, also affected to the final product, leading to a brittlerer (more breakable) final product (**Figure 3.7**).

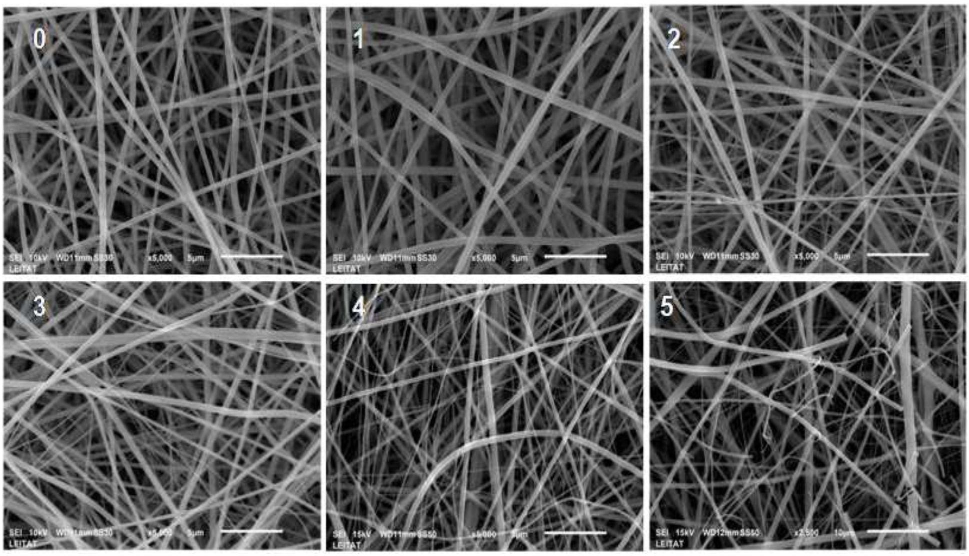

Figure 3.5. SEM images obtained for the prepared precursor solutions (as referred in **Table 3.6**).

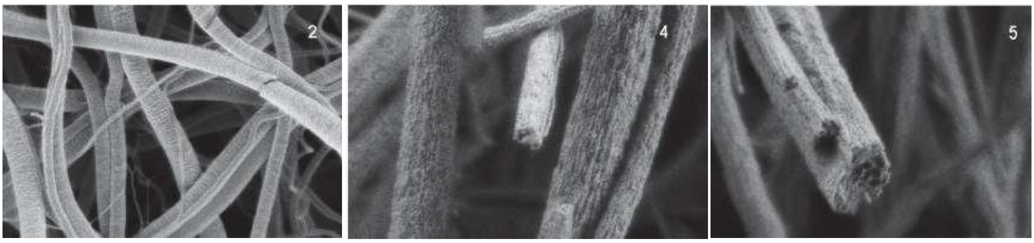

Figure 3.6. High resolution SEM images obtained for the prepared precursor solutions.

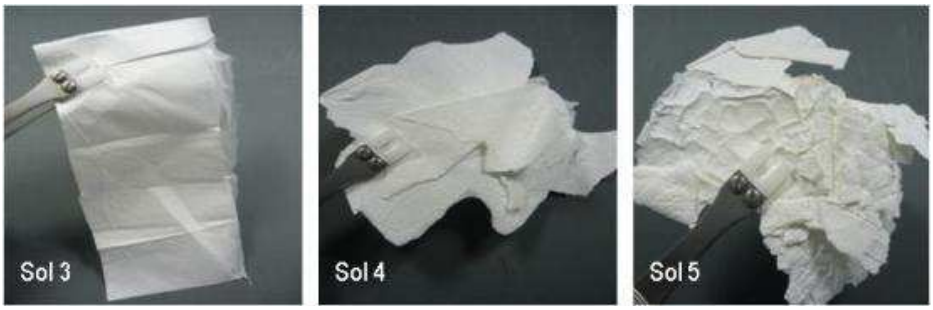

Figure 3.7. TiO_2 nanofibers appearance.

Once submitted to the electrospinning process, these TiO_2 precursor nanofibers were calcinated in order to obtain the final resulting TiO_2 nanofibers.

3.2.2.2. TiO_2 fixation

As it has been already cited along the present chapter, one of the main challenges of TiO_2 photocatalysis for industrial applications is the recovery of the catalyst. It is for this reason that the present research was devoted to find a fixation method by which this separation could be ignored when testing solutions containing the organic chemicals to be removed. Two methods were proposed:

(A)- TiO_2 dispersion + vacuum deposition + fixation by heat and pressure treatment.

100 mg of the catalyst was suspended in water with a 0.05% dispersing agent (Pluronic F-127) and sonicated twice at 30 kJ for 30 minutes. The resulting suspension was filtered three times under vacuum (**Figure 3.8**) on the selected support. Finally, the obtained support with the deposited catalyst was submitted twice to pressure and heat treatment (140º C for 45 s) in order to assure TiO_2 fixation.

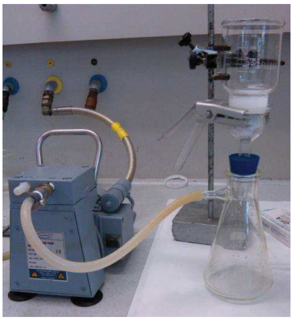

Figure 3.8. Experimental set-up for TiO_2 fixation by heat and pressure treatment.

(B)- Preparation of a precursor TiO_2 paste + fixation via casting knife + heat treatment.

First, an ethylcellulose gel is prepared consisting in 25% *w/w* ethylcellulose (ligand agent) and 85% of α-terpineol (viscosity and porosity adjusting solvent) is prepared and reserved for further use. Then, a solution containing Triton X-100 (dispersing agent), acetylketone (provides more surface adherence) and acetic acid (chelating agent) are mixed prior the addition of the TiO_2 catalyst (20% *w/w*). α-terpineol is then added to ensure the complete mixing and homogenization of the solution. Finally, the ethylcellulose gel is added and stirred until complete homogeneisation (2 hours). The obtained paste containing the catalyst is submitted to the casting knife procedure. This methodology ensures complete fixation and homogeneisation of the TiO_2 paste onto the selected support at 50 µm. height (see **Figure 3.9** for more details on the casting-knife procedure). In order to remove all undesired organic additives, the fixed catalyst is submitted to a 450 ºC heat treatment for 2 h.

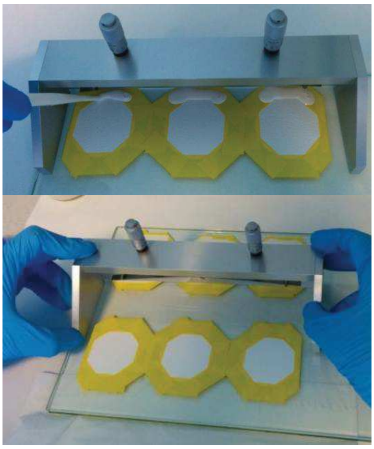

Figure 3.9. Casting-knife procedure

Both methods resulted in good TiO_2 fixation onto the selected support. However, SEM images reveal treats in common and differences between the fixation methodologies described above as depicted in **Figure 3.10** and **3.11**, for the methodology (A) and (B) respectively. Both figures clearly show that the TiO_2 fixation was homogeneous all along the support's surface. However, it is clear from **Figure 3.10** that the methodology (A) lead to the appearance of cracks on the surface while the second did not. The appearance of such cracks would presumably result in TiO_2 leaching and a drop on the photocatalytical performance of the tested material. On the basis of the obtained SEM images, the methodology based on the preparation of the TiO_2 paste was selected for TiO_2 fixation.

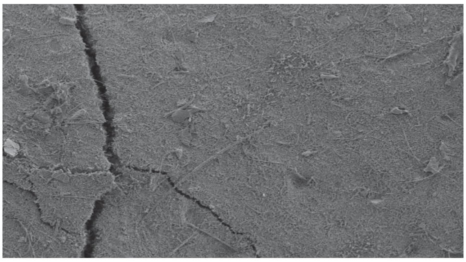

Figure 3.10. SEM image from method (A)

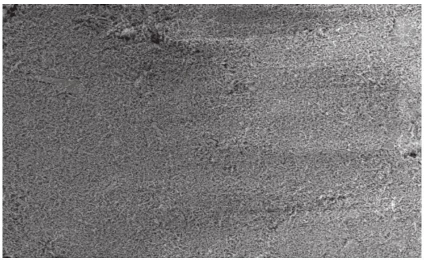

Figure 3.11. SEM image from fixation method (B)

3.2.2.3. TiO_2 characterisation

XRD characterisation

Figure 3.12 shows the XRD reference patterns of pure TiO_2 polymorphs: anatase (in blue), rutile (in red) and brookite (in green), all obtained from the Crystallography Open Database (COD) contained in the processing crystallographic software Match! [160]. The quantitative analysis of all samples was performed by the Rietveld Method. Crystallite size of individual TiO_2 phase was calculated by means of Scherrer's equation (**Equation 3.14**) from the characteristic XRD diffraction peak (**Table 3.4**).

Eq. 3.14 $$\tau = \frac{K\,\lambda}{\beta \cos\theta}$$

Scherrer's equation

Table 3.4. Characteristic diffraction peaks for the estimation of TiO_2 crystallite size.

Phase	Diffraction peak; Miller index (hkl)
Anatase	$2\theta = 25.3°$; (101)
Rutile	$2\theta = 27.4°$; (110)
Brookite	$2\theta = 30.8°$; (101)

Scherrer's equation relates the crystallite size (τ) of any solid to the peak broadening experimentally obtained in a diffraction pattern. This equation is defined by: K, a dimensionless factor, which its typical value is 0.9; λ is the wavelength of the filament used in the XRD instrument, β is the peak's width at the half maximum intensity and θ is the Bragg angle (in degrees).

Figures 3.13, 3.14 and **3.15** show the XRD spectra for the reference materials, TiO_2 P25 nanoparticles, commercially available nanofibers and synthesised TiO_2 nanofibers respectively. The crystallographic characteristics, crystallite phase and size, are included in **Table 3.5**. In agreement to what has been vastly published about the crystalline structure of TiO_2 P25 nanoparticles [8], the anatase and rutile content was found to be of 87.3% and 12.7% respectively with crystallite sizes of 232 Å and 369 Å for anatase and rutile respectively. Contrary to P25 nanoparticles, commercially available and synthesised TiO_2 nanofibers presented the third TiO_2's crystallite phase, brookite. Its quantitative analysis in both samples resulted to have a percentage of 32 and 13 % respectively. In addition to the brookite content, what especially differed in the crystallographic analysis of these three samples was the peak broadening found in the diphractograms obtained for the nanofibers samples.

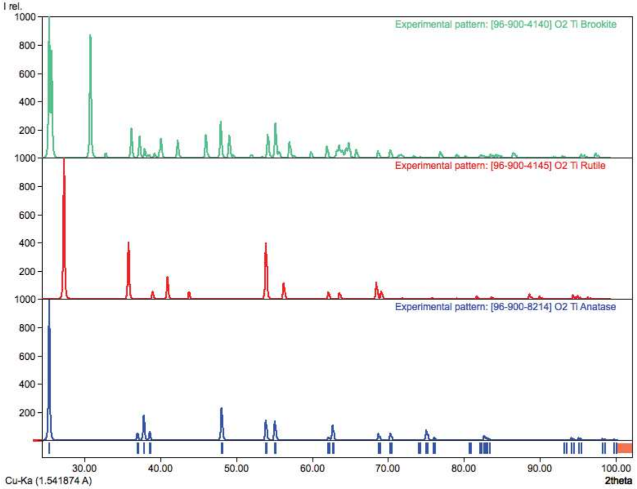

Figure 3. 12. XRD patterns of TiO_2; anatase (blue), rutile (red) and brookite (green)

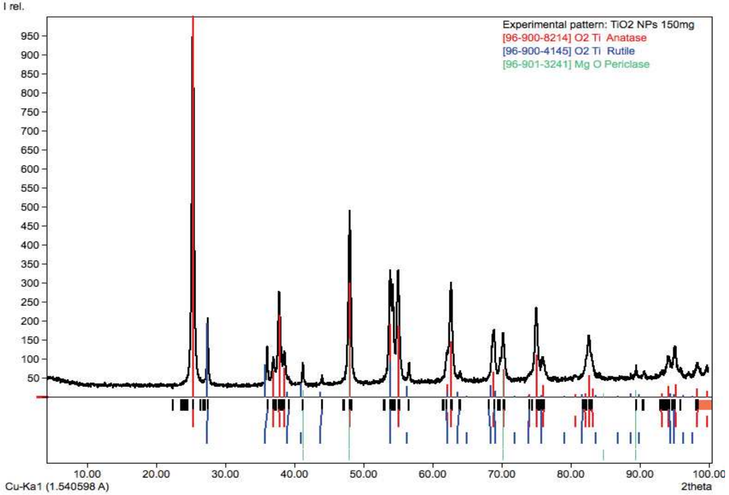

Figure 3.13. Obtained XRD spectrum of P25 nanoparticles.

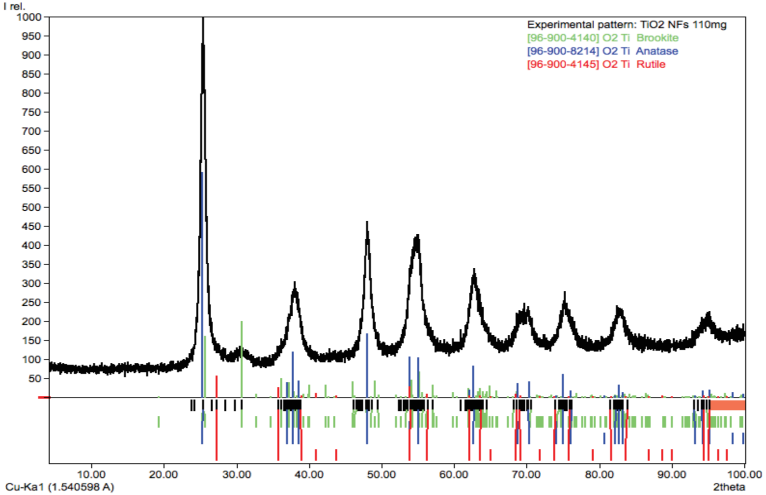

Figure 3.14. Obtained XRD spectrum of commercially available nanofibers.

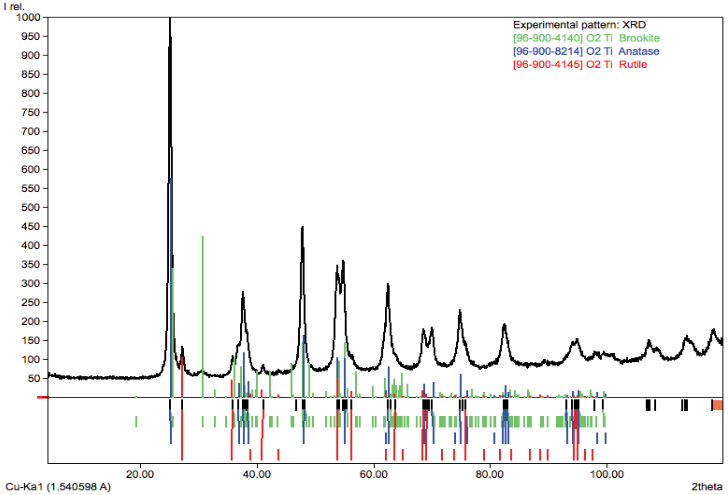

Figure 3. 15. Obtained XRD spectrum of synthesised nanofibers.

The examination of the acquired XRD spectra of TiO_2 commercial nanofibers clearly shows broad anatase and brookite peaks at 25° and 31° respectively. In this sample, however, the observation of the characteristic rutile peak at 27.4° remained a challenging task due to its crystallite size (4 nm) and the overlapping with the anatase peak.

Table 3.5. Crystallite phase content and crystallite size for TiO_2 samples examined

XRD	Crystallite phase (%)			Crystallite size (Å)		
	Anatase	**Rutile**	**Brookite**	**Anatase**	**Rutile**	**Brookite**
TiO_2 NPs	79.1	20.9	-	232	369	-
Comm. TiO_2 NFs	49.1	6.1	44.8	117	56	41
Leitat TiO_2 NFs	80	7	13	208	44	119

BET surface area

The method developed by Brunauer, Emmet and Teller in 1938 [161] for the determination of surface characteristics of a solid (surface area, pore, etc.) consists in the adsorption of an inert gas at low temperature, usually nitrogen at 77 K, over the solid of study. As discussed in the introduction of **Chapter 1** and the present chapter, the photocatalytical efficiency of a semiconductor is mainly governed by its surface area, pore width and volume, crystallite phase, crystallite size, etc. Having examined the catalyst surface and the crystal characteristics of the catalysts used in this study, the specific surface areas and the microporosity of the TiO_2 samples were examined by nitrogen sorption (**Figures 3.16** to **3.18**). For all tested materials, the N_2-adsorption-desorption isotherms are of type II, according to the Brunauer-Deming-Deming-Teller (BDDT) classification [162]. Type II isotherms are characteristic of non-porous or macroporous materials and are characterised by unrestricted monolayer-multilayer adsorption. These kind of isotherms are characterised by the point where multilayer adsorption starts. However, the obtained representations at $p/p_0 < 0.2$ indicated the overlap of monolayer and multilayer adsorption coverage. Moreover, a hysteresis loop of type 3 (H3) can be observed when reaching the upper limit of relative pressures. These hysteresis loops are characteristic from materials forming aggregates or mesoporous adsorbents. All these facts were confirmed by the results obtained from the Barrett-Joyner-Halenda (BJH) method by which was determined pore sizes distribution of all materials used **(Table 3.6).**

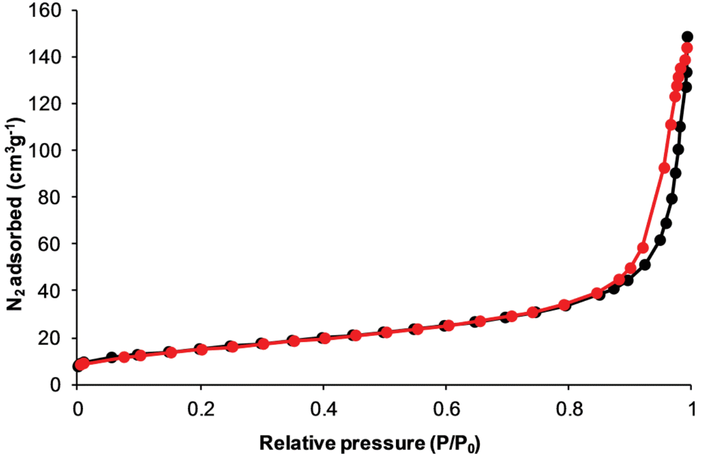

Figure 3.16. Adsorption isotherm obtained for P25 nanoparticles.

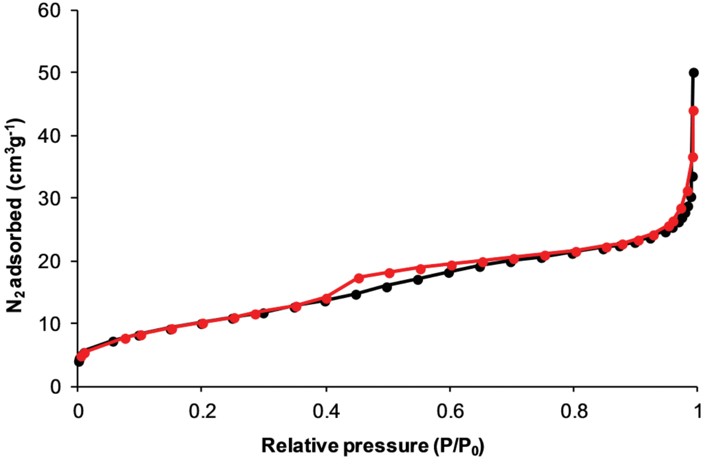

Figure 3.17. Adsorption isotherm obtained for commercial TiO_2 nanofibers.

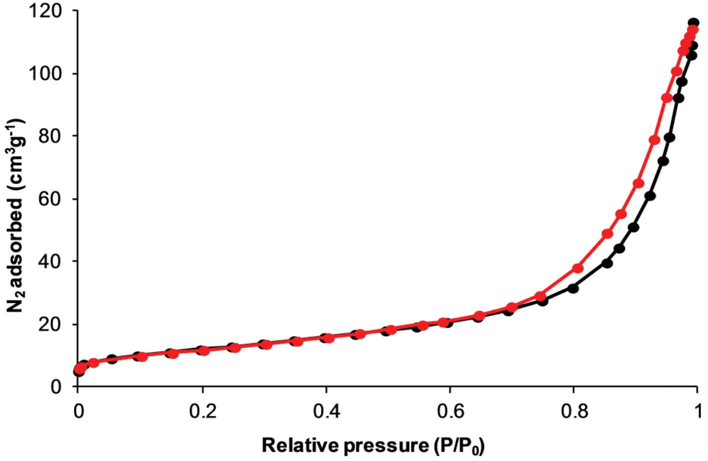

Figure 3.18. Adsorption isotherm obtained for synthesised TiO_2 nanofibers.

Table 3.6. Crystallite phase content and crystallite size for TiO_2 samples examined

BET	**TiO_2 NPs**	**Comm. TiO_2**	**Leitat TiO_2 NFs**
Single point surface area ($m^2\ g^{-1}$)	53.55	36.30	42.07
BET surface area ($m^2\ g^{-1}$)	55.12	37.75	43.27
Desorption average pore width (Å)	155.54	60.27	166.39
Adsorption average pore diameter (Å)	168.19	83.40	154.36
Desorption average pore diameter (Å)	155.50	66.70	135.99

3.2.2.4. Chemical analysis

Prior evaluating the adsorption and the photocatalytic activity of the synthesised and commercial catalysts over the target compounds, an UHPLC-(MS)/HRMS method was developed and optimised in order to detect and quantify the four drugs (ofloxacin, clofibric acid, diclofenac and ibuprofen). at low concentration levels (< μg L^{-1}).

Before optimising the chromatographic methodology, stock solutions of 100 μg L^{-1} of the four analytes were infused into the MS system in order to optimise source and MS/HRMS conditions. All analytes could ionise in the negative ion mode, *via* deprotonation of the carboxylic acid contained in their structures while ofloxacin and diclofenac could also ionise in the positive ion mode *via* the protonation of the amino group(s) contained in the piperazine ring of ofloxacin and the secondary amine of diclofenac respectively. Once the source parameters were optimised in order to maximise the signal of the protonated or deprotonated $[M+H]^+$ or $[M-H]^-$ ions and avoid *in-source* fragmentation, the collision energy for tandem mass experiments was then optimised. **Table 3.7** shows both precursor and product ions, collision energies and accurate mass measurements together with the detection and quantification limits (LOD and LOQ respectively) and precision of accurate mass measurements. Briefly, the fragmentation patterns of the tested drugs can be described as:

- Ofloxacin, **Fig. 3.19**: the ESI + of OFX leads to *m/z* 362.1510 and its MS/HRMS shows characteristic fragment ions: *m/z* at 318.1612 attributed to the loss of CO_2 and *m/z* 261.1034 due to the loss simultaneous loss of CO_2 and the piperazine group.

- Clofibric acid, **Fig. 3.20**: the ESI – of this compounds shows the isotopic pattern attributed to a molecule containing one chlorine atom in its structure. Clofibric acid fragments by the ether group, giving rise to only one product ion (*m/z* 126.9961).

- Diclofenac, **Fig. 3.21**: Since the signal obtained for the same standard solution was up to 20 times higher in the negative ion mode rather than its positive form, the tandem MS conditions were only optimised in the negative ion mode. Deprotonated diclofenac showed the characteristic isotopic cluster corresponding to two chlorine atoms in its molecular structure. Its characteristic product ions resulted from the loss of CO_2 (*m/z* 250.0185) and *m/z* 214.0418, from the simultaneous loss of CO_2 and one chlorine atom.

- Ibuprofen, **Fig. 3.22**: the fragmentation of ibuprofen was performed, two product ions were observed: *m/z* 159.1170 and *m/z* 161.1336.

Table 3.7. High-resolution and tandem high-resolution mass spectra of the four model drugs.

Compound **Accurate mass *m/z*;** **mass error (ppm; mDa)**	**Product ions (*m/z*),** **mass error (ppm; mDa)**	**Product ion assignment**	**LOD (µg L^{-1})**	**LOQ (µg L^{-1})**	**Precision (%)**	
					Intra-day	**Inter-day**
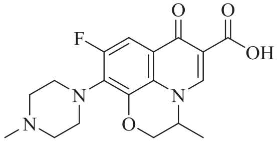 **Ofloxacin** 362.1510; (-0.1; 0.5)	318.1612; (-0.1; -0.03) 261.1034; (0.1; 0.02)	$[M+H-CO_2]^+$ $[M+H-C_3H_7N]^+$	0.05	0.18	1.5	2.0
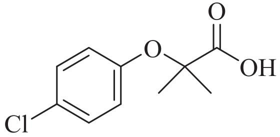 **Clofibric Acid** 213.0310; (-1.1; -1.4)	126.9961; (12.5; 1.5) 85.0294; (11.6; 1.0)	$[M-H-C_4H_6O_2]^-$ $[M-H-C_6H_5ClO]^-$	0.09	0.59	0.5	0.89
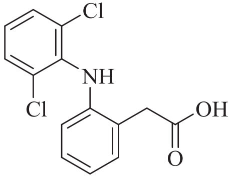 **Diclofenac** 294.0084; (0.31; 1)	250.0185; (0.1; 0.02) 214.0418; (-0.02; -0.004)	$[M-H-CO_2]^-$ $[M-H-CO_2-Cl]^-$	0.08	0.67	0.6	0.9
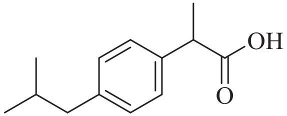 **Ibuprofen** 205.1228; (2.4; 1)	161.1339; (6.9; 1.4) 159.1170; (1.1; 0.2)	$[M-H-CO_2]^-$ $[M-H-CO_2-H_2]^-$	3	10	2.1	3.5

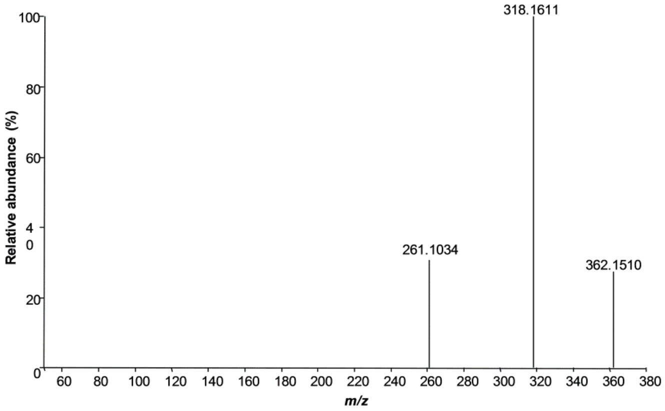

Figure 3.19. Tandem MS spectrum of ofloxacin (NCE = 30V)

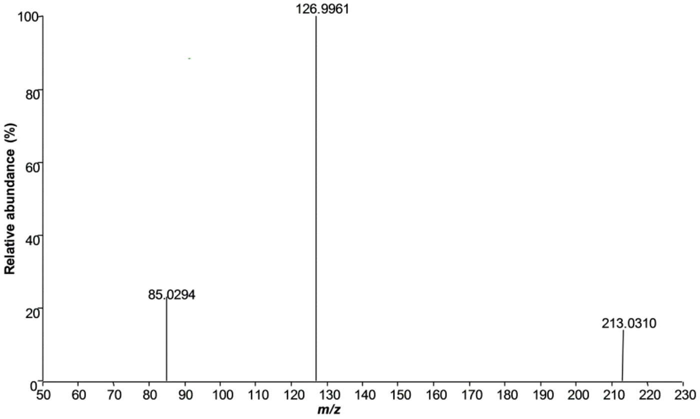

Figure 3.20. Tandem MS spectrum of clofibric acid (NCE = 30V)

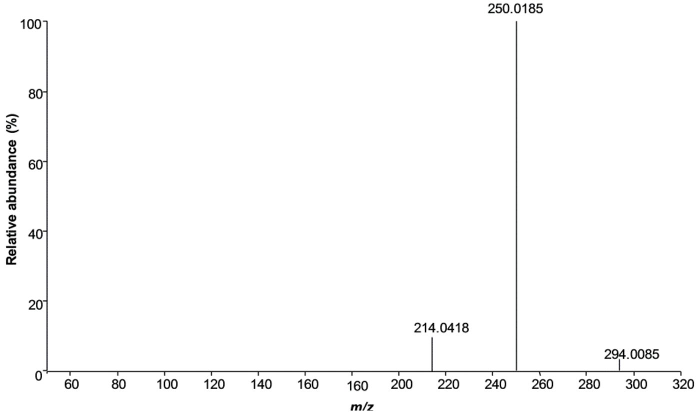

Figure 3.21. Tandem MS spectrum of diclofenac (NCE = 30V)

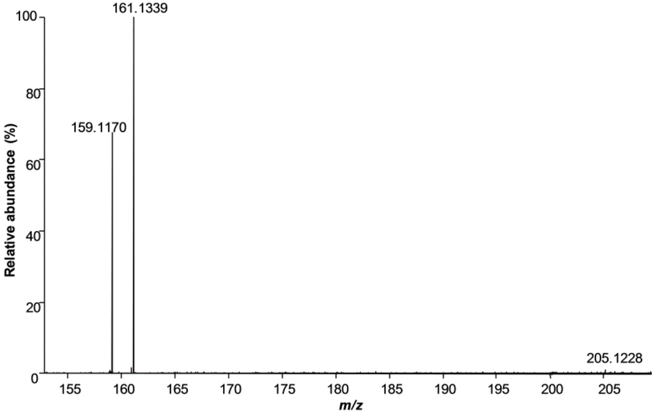

Figure 3.22. Tandem MS spectrum of ibuprofen (NCE = 30V)

Both ions have been reported to be the product ions of ibuprofen. Whereas the ion at *m/z* 161.1336 is obtained in triple quadrupole instruments, the ion at *m/z* 159.1179 can be generated as an *in-time* oxidation of product ion *m/z* 195 **(Figure 3.23)**. As stated by Boleda *et al.* [163], this process only occurs when ion at m/z 161 is stored in the instrument long enough to allow the loss consecutive loss of CO_2 and 2H.

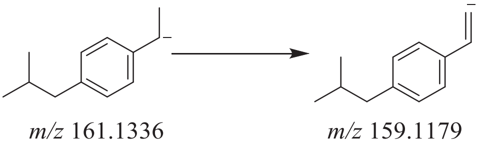

Figure 3.23. I*n-time* oxidation of *m/z* 159.1170

Once the mass spectrometry conditions were fixed, the chromatographic separation was studied and optimised. This consisted on a water:acetonitrile gradient (**section 3.1.2.7**) on a 100 mm length C_{18} column (**section 3.2.1.7**). Different solvent compositions were studied in order to achieve the best separation and response of the four analytes under study: H_2O:CH_3CN (without additives) and H_2O:CH_3CN with 0.01 % to 0.1 % *v/v* formic acid in the aqueous phase. In comparison to the mixture consisting in H_2O:CH_3CN, the increasing additions of formic acid lead to sharper chromatographic peaks but resulted in slightly intensity drops for those ions ionising in the negative ion mode. Ibuprofen was the analyte under study which suffered most from ion suppression by increasing concentrations of formic acid. When its concentration ranged from 0.07 to 0.1 % the disappearance of ibuprofen's signal was observed. Opposite to this behaviour was ofloxacin's signal, whose maximum intensity reached when 0.1% *v/v* formic acid was added. In order to analyse all the analytes in a single LC-MS run, an intermediate formic acid concentration was chosen, thus, fixing it at a concentration of 0.05 % *v/v* only in the aqueous solution. As illustrated in **Figure 3.24**, these four analytes were perfectly separated under the final conditions established, also obtaining exceptional quantification and detection limits, as depicted in **Table 3.7**.

Even though the instrumentation used in this analysis, a QExactive Orbitap, offered great sensitivity even if working in the full scan mode, the instrument was ran in the product ion-scan, isolating the precursor ion in the quadrupole mass filter and post-processing the obtained data by only considering the fragment ions depicted in **Table 3.7**. This operation mode lead to detection and quantification limits up to 3 and 5 times lower than if the instrument was operated in the full scan mode.

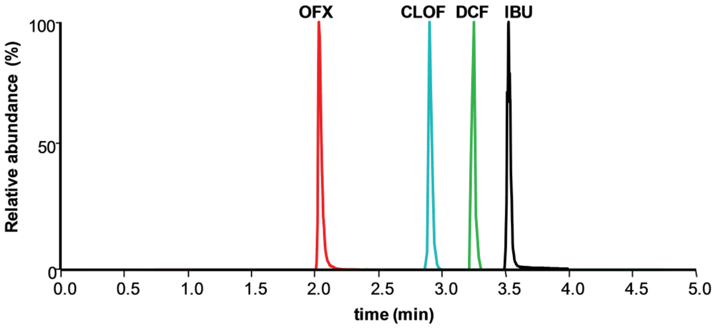

Figure 3.24. Chromatographic separation of all compounds under study

3.2.2.5. Adsorption kinetics

Many experimental results of undergone researches indicates that the adsorption and photocatalysis degradation rate of inorganic and organic chemicals by TiO_2 follows the Langmuir–Hinshelwood kinetics model described by **Equation 3.14**,

$$q_e = \frac{q_m k_L C_e}{1 + k_L \cdot C_e} \qquad \textbf{Eq. 3.14}$$

where C_e is the concentration of the tested compound once the adsorption equilibrium has been established (mg L^{-1}); q_e the equilibrium adsorption capacity (mg·g^{-1}); q_m the maximum adsorption capacity (mg g^{-1}) and k_L the Langmuir–Hinshelwood constant for the adsorption process (mg L^{-1}). The L-H isotherm is an empirical model which assumes that adsorption can only occur at a finite number of definite localized sites, and the adsorbed layer is one molecule in thickness or monolayer adsorption. At low concentrations of drug ($1>>KC_e$) the coverage is proportional to the drug concentration, with a proportionality constant of k_{ads}, whereas, at high concentrations (saturation, $1<< KC_e$), the coverage is the unity, independent of the drug concentration. The amount of drug(s) adsorbed when the equilibrium was reached, (qe, mg drug/g), was calculated by **Equation 3.15**, being C_0 and C_e the initial and the equilibrium concentration respectively (mg drug·L^{-1}), V, the volume of the solution (L) and m the amount of catalyst (g).

$$q_e = \frac{(C_0 - C_e) \cdot V}{m} \qquad \textbf{Eq. 3.15}$$

In addition to the described isotherm, the Freundlich isotherm describes the non-ideal and reversible adsorption, which can be applied to multilayer adsorption, on the basis of an assumption concerning the energetic surface heterogeneity (characterized by the 1/n factor). Hence, the non-linear expression of Freundlich isotherm model can be illustrated as **Equation 3.16**:

$q_e = K_F \cdot C_e^{1/n}$ **Eq. 3.16**

where C_e is the concentration of the drug in solution at equilibrium (mg drug·L^{-1}); k_F is the Freundlich adsorption constant ($mg^{1-(1/n)}$ $L^{1/n}$ g^{-1}) and n the heterogeneity factor of adsorption sites (dimensionless).

Both Langmuir-Hinshelwood and Freundlich isotherms can then be rewritten in their linear expression (**Table 3.8**) form so as to fit the obtained experimental data and find the characteristic parameters of both expressions: q_m, $K_{L\text{-}H}$, K_F and n (**Equations 3.17** to **3.21**). The Langmuir-Hinshelwood isotherm, however, can be linearised into four different types, each of them, resulting in different parameters estimation.

Table 3.8. Linear forms of the isotherm models

Isotherm	Lineal form	
Langmuir	$\frac{C_e}{q_e} = \frac{1}{q_m K_L} + \frac{C_e}{q_m}$	**Eq. 3.17**
	$\frac{1}{q_e} = \frac{1}{q_m K_L} \cdot \frac{1}{C_e} + \frac{1}{q_m}$	**Eq. 3.18**
	$q_e = q_m - \frac{1}{K_L} \cdot \frac{q_e}{C_e}$	**Eq. 3.19**
	$\frac{q_e}{C_e} = q_m K_L - K_L q_e$	**Eq. 3.20**
Freundlich	$\ln q_e = \ln K_F + \frac{1}{n} \ln C_e$	**Eq. 3.21**

Amongst the four linear forms of the Langmuir-Hinshelwood isotherm, the first one is the most used in the literature [164] due to the minimal deviations from the fitted equation. In the present thesis, the experimental data was fitted to the non-linear and linear forms of both Langmuir-Hinshelwood and Freundlich isotherms.

Non-linear fitting of the isotherm models

Figures 3.25 and **3.27** shows the Langmuir and Freundlich adsorption isotherms (experimental and non-linear fitted) of the four drugs under study onto the prepared TiO_2 nanofibers. Moreover, **Table 3.9** shows the non-linear regression parameters for both isotherms of the obtained kinetic data for the four drugs under study onto the three catalysts used. Even though Langmuir's isotherm produced better fitting data than Freundlich's one, the results depicted in **Figures 3.25** and **3.27** and **Table 3.9** clearly suggest that both isotherms models can generate satisfactory fits to the experimental data obtained. This would suggest that, the concentration ranges used in the present experimental section was small enough in comparison to the maximum adsorption capacity of all the tested photocatalysts under study.

In terms of Langmuir's isotherm, the values of maximum adsorption capacity, q_m, determined ranged between 0.6 to 4 mg g^{-1}, 0.12 to 150 mg g^{-1} and 0.8 to 5 mg g^{-1} for P25 nanoparticles, commercially available nanofibers and in-home nanofibers respectively. By comparison, the studied catalysts appeared to have a similar trend to the adsorption of the studied drugs onto their surface, being ofloxacin the most sensible to adsorption, followed by diclofenac and ending with ibuprofen and clofibric acid. Under the studied conditions, this fact could be directly linked to the electrostatic interactions between the catalyst and the tested compounds (under study by *z-potential*). Ranking the adsorption performance of the studied catalysts, prepared TiO_2 nanofibers appeared to be the catalyst with maximum adsorption capacities followed by TiO_2 P25 nanoparticles while commercially available nanofibers resulted to be the catalyst with poorest adsorption capacities under the studied conditions. With the exception of OFX (commercial NFs), the maximum adsorption capacities derived from data fitting to Langmuir's isotherm were close to the experimental adsorption isotherm plateau indicating that the model was acceptable.

Linear Fitting of the Isotherm Models

In the same line as it has been described with the non-linear fitting of the obtained data, **Figures 3.26** and **3.28** shows the Langmuir and Freundlich linear fitting of the four tested drugs onto the prepared TiO_2 nanofibers and **Table 3.10** shows the characteristic adsorption parameters once data was fitted as described by **Equations 3.17** and **3.21** (Langmuir and Freundlich respectively) for the four drugs under study and the three catalysts used. In the same way as the non-linear fitting, both studied isotherms fitted the experimental adsorption data. However, the linear fitting of Freundlich's isotherm resulted in slightly better fit scores than Langmuir's model, as suggested by the correlation coefficient (r^2) obtained. As indicated in the non-linear regression of both isotherms, the experimental conditions used in the present research (concentration of the solutes and maximum adsorption capacities of the sorbents) could lead to the satisfactory fitting of both isotherms.

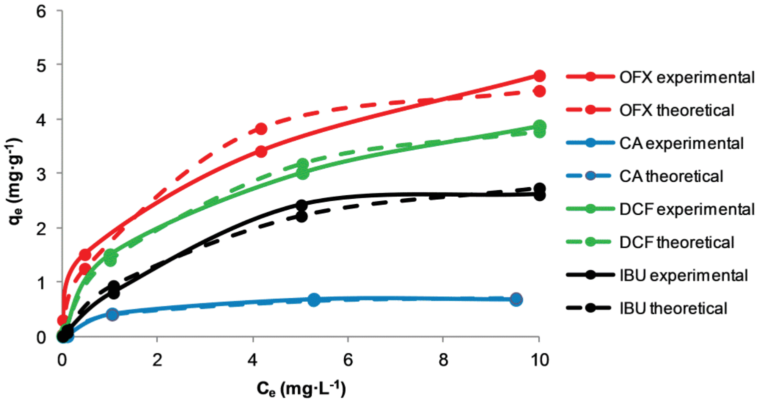

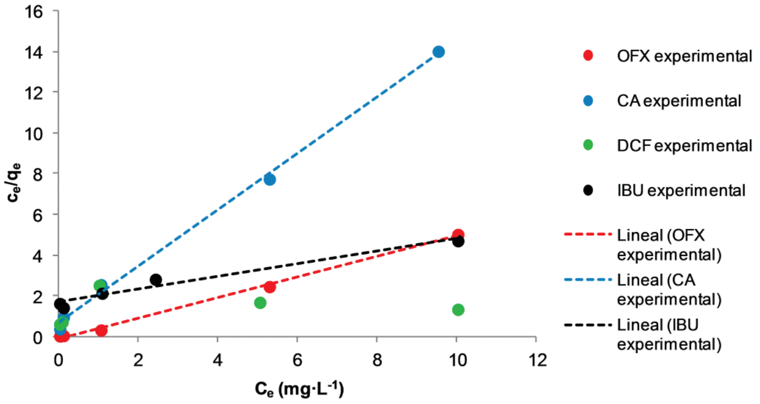

Figure 3.25. Experimental (straight lines) and Langmuir's non-linear fitting (dashed lines) of the tested drugs onto in-home nanofibers.

Figure 3.26. Experimental (straight lines) and Langmuir's linear fitting (dashed lines) of the tested drugs onto in-home nanofibers.

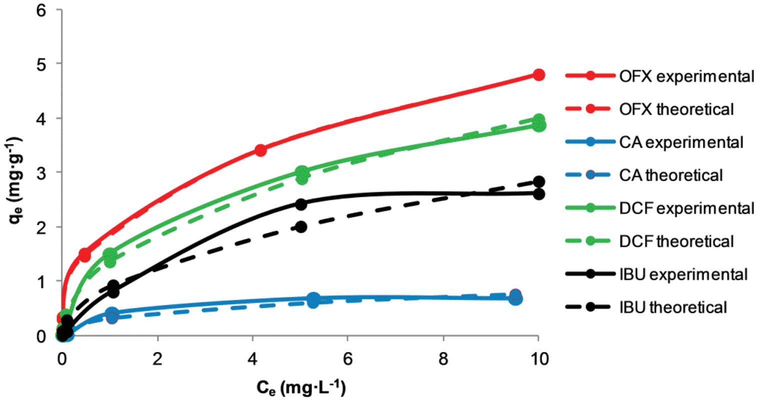

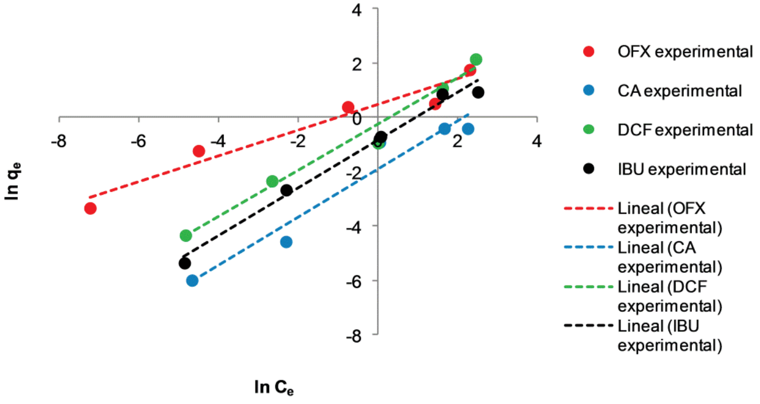

Figure 3.27. Experimental (straight lines) and Freundlich's non-linear fitting (dashed lines) of the tested drugs onto in-home nanofibers.

Figure 3.28. Experimental (straight lines) and Freundlich's linear fitting (dashed lines) of the tested drugs onto in-home nanofibers.

Table 3.9. Langmuir and Freundlich isotherm parameters obtained by non-linear fitting.

Material	Model	Parameter	Ofloxacin	Diclofenac	Clofibic Acid	Ibuprofen
TiO_2 NPs	Langmuir	K_L	0.80	0.0045	*	4.01
		q_m	3.51	4.14	*	0.58
		r^2	-	-	-	-
	Freundlich	K_F	1.51	0.080	0.020	0.32
		n	1.63	0.80	0.45	4.44
		r^2	-	-	-	-
Commercial TiO_2 NFs	Langmuir	K_L	0.0069	1.05	0.039	0.25
		q_m	150.45**	0.85	0.12	0.53
		r^2	-	-	-	-
	Freundlich	K_F	0.64	0.33	0.56	0.15
		n	0.96	0.76	0.86	0.99
		r^2	-	-	-	-
Leitat TiO_2 NFs	Langmuir	K_L	0.67	0.43	0.98	0.33
		q_m	5.18	4.63	0.78	3.53
		r^2	-	-	-	-
	Freundlich	K_F	1.96	1.36	2.60	0.89
		n	2.57	2.14	0.31	1.99
		r^2	-	-	-	-

* No fitting was possible

** Theoretical values derived from data fitting. The set did not reach the plateau-like shape of Langmuir's isotherm.

Table 3.10. Langmuir and Freundlich isotherm parameters obtained by linear fitting.

Material	Model	Parameter	Ofloxacin	Diclofenac	Clofibic Acid	Ibuprofen
TiO_2 NPs	Langmuir	K_L	3.90	*	5.18	0.20
		q_m	1.20	*	0.14	2.27
		r^2	0.99	0.99	0.99	0.99
	Freundlich	K_F	1.72	1.99	0.15	0.28
		n	1.25	0.75	1.12	1.46
		r^2	0.99	0.99	0.99	0.99
Commercial TiO_2 NFs	Langmuir	K_L	0.36	0.96	2.55	0.11
		q_m	2.38	1.1	0.03	1.5
		r^2	0.99	0.99	0.99	0.99
	Freundlich	K_F	0.76	0.225	0.15	0.1
		n	1.03	0.85	1.06	1.27
		r^2	0.99	0.99	0.99	0.99
Leitat TiO_2 NFs	Langmuir	K_L	6.4	1.6	3.84	0.15
		q_m	1.4	1.1	0.7	3.94
		r^2	0.99	0.99	0.99	0.99
	Freundlich	K_F	1.59	0.76	0.15	0.43
		n	2.11	1.17	1.12	1.13
		r^2	0.99	0.99	0.99	0.99

* no fitting was possible

** theoretical values derived from data fitting. The set did not reach the plateau-like shape of Langmuir's isotherm.

In terms of Langmuir's isotherm, the maximum adsorption capacity obtained by linear fitting ranged 0.14 to 2 mg g^{-1}, 0.03 to 2.4 mg g^{-1} and 0.7 to 4 mg g^{-1} for P25 nanoparticles, commercially available nanofibers and in-home nanofibers respectively, thus, having the same adsorption capacities rank of that obtained with the non-linear fitting: home-made TiO_2 NFs > P25 NPs > commercially available TiO_2 NFs. In terms of ranking compounds as a function of their adsorption behaviour onto the catalysts surface, the most sensitive compound appeared to be ibuprofen followed by ofloxacin. Even though diclofenac could not be fitted into the linear form of Langmuir's isotherm for P25 nanoparticles, it presented high adsorption capacities for both prepared and commercially available TiO_2 nanofibers. Clofibric acid was the tested drug with lowest adsorption capacity, being the synthesised TiO_2 nanofibers the catalyst with maximum adsorption capacity for the tested drug (0.7 mg L^{-1}).

The comparison of both linear and non-linear fitting indicated a discrepancy on the behaviour of the studied drugs onto the catalyst's surface. Nevertheless, these results indicated a low adsorption capacity if these materials are compared to cutting-edge sorbents commercially available in the market with high adsorption capacities such as active carbon. Since the overall goal of the research was to study the photocatalytical activity of the studied materials, without any physic-chemical change of the final testing water (real water), no further tuning of the experimental conditions was carried out in order to achieve the maximum adsorption capacity of the materials tested.

3.2.2.6. Degradation kinetics

Once the adsorption-desorption kinetics was studied with the different materials under investigation with the four model drugs, their photocatalytic activity was studied using P25 Degussa nanoparticles as the reference material. Since the presence of salts, surfactants, dissolved organic matter, etc. has been vastly proved to affect the photocatalytical performance of titanium (IV) oxide, before carrying out the degradation of the tested drugs in real water, MilliQ water was first used to study their performance without quenching agents in solution.

Having fixed the initial concentration of each drug to 10 μg L^{-1}, and TiO_2 amount up to 250 mg L^{-1}, the degradation kinetics were adjusted to a *pseudo-first* order reaction kinetics, assuming that 1>>k Ce from Langmuir's equation isotherm,

$$r = -\frac{dC}{dt} = \frac{KC_e}{1 + K \cdot C_e} \rightarrow r = -\frac{dC}{dt} = KC_e \qquad \textbf{Eq. 3.22}$$

hence, **Equation 3.22** can be integrated as **Equation 3.23** and linear plotted using **Equation 3.24**, concentration *versus* time:

$[C] = [C]_0 e^{-kt}$ **Eq. 3.23**

$ln[C] = ln[C]_0 - kt$ **Eq. 3.24**

where C and C_0 are the concentration of the analyte (mg L^{-1}) in the solution at time t (minutes) and before being irradiated respectively. k makes reference to the pseudo-first order kinetics followed by the analyte on the studied conditions (min^{-1}). As cited before, two *set-ups* were used in order to carry out the present investigation: slurry (or suspended) and supported conditions, as refereed in **section 3.2.5**.

The *pseudo-first* order rate constants for the photocatalytic degradation of the pharmaceutical drugs in MilliQ water and real water respectively are shown in **Figures** from **3.29** to **3.32**. Moreover, **Table 3.12** resumes the main physic-chemical parameters obtained for the tested real water obtained from an urban wastewater treatment plant located in Terrassa, Barcelona, Spain.

Abatement of organic pollutants from synthetic water

The results obtained in MilliQ water showed that the four pharmaceutical drugs were completely removed from the solution in less than 30 min during the experiments performed with TiO_2 NPs and synthesised TiO_2 NFs, as can be seen in **Figures 3.29** and **3.30**. The *pseudo-first* order kinetic constants derived from the linear fitting of concentration *versus* time kinetics are presented in **Table 3.11**. Commercial nanofibers did not show appreciable photocatalytical activity, needing up to 4 h to completely remove the chemicals from the tested solution.

In general terms, both tables clearly show that batch experiments carried out with the suspended nanomaterials led to higher degradation rates for the four pharmaceuticals in comparison to supported experiments. As it has been previously reported [60,165–167], these results are mainly attributed to the reduction of TiO_2 specific sites capable of undergoing direct oxidation or reduction of adsorbed analytes onto their surface or via the generation of reactive organic species (ROS) capable of degrading the target compounds. In this later case, an appreciable diminution of such reactive was expected, leading to the consequent reduction of the degradation rates of the chemicals under study.

Table 3.11. Linear fitting of degradation kinetics on MiliQ water.

Drug	TiO_2 NPs; *k* (min^{-1})		Comm. TiO_2 NFs; *k* (min^{-1})		Leitat TiO_2 NFs; *k* (min^{-1})	
	Suspension. (r^2)	Supported. (r^2)	Suspension. (r^2)	Supported. (r^2)	Suspension. (r^2)	Supported. (r^2)
Ofloxacin	5.1 (0.99)	0.11 (0.99)	0.05 (0.98)	0.03 (0.99)	4.3 (0.99)	0.09 (0.99)
Diclofenac	3.6 (0.99)	0.03 (0.96)	0.03 (0.95)	0.03 (0.99)	3.3 (0.91)	0.05 (0.96)
Clofibric acid	0.72 (0.99)	0.05 (0.96)	0.02 (0.98)	0.01 (0.95)	0.6 (0.98)	0.05 (0.98)
Ibuprofen	0.5 (0.99)	0.12 (0.97)	0.01 (0.99)	0.007 (0.99)	1.5 (0.97)	0.03 (0.98)

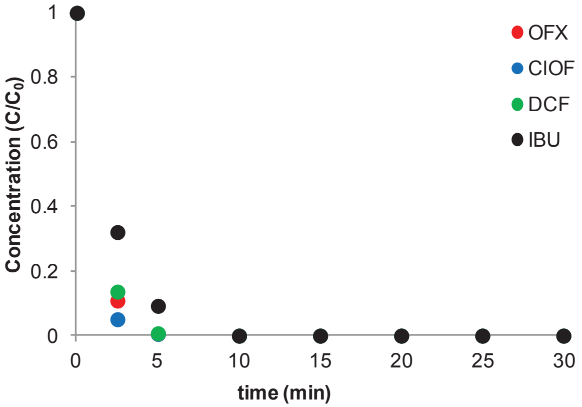

Figure 3.29. Degradation kinetics under synthesised NF (suspended *set-up* in MilliQ water).

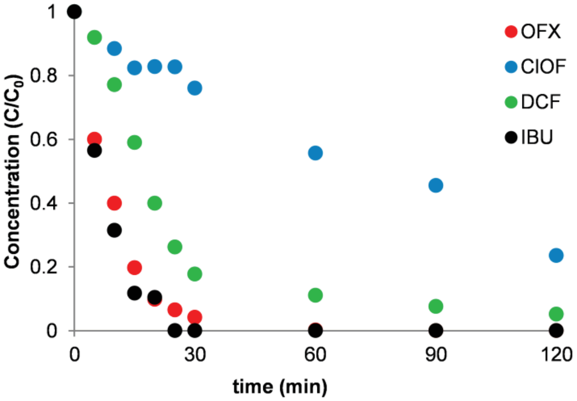

Figure 3.30. Degradation kinetics under synthesised NF (supported *set-up* in MilliQ water).

Going into detail into both tables and comparing the performance of the tested catalysts, it was quite clear that the ranking, in terms of degradation rates, was: P25 TiO_2 nanoparticles ≈ in-home TiO_2 nanofibers >> commercially available TiO_2 nanofibers.

Despite the slightly difference in phase composition and surface area of the most active catalyst under study, these results suggest comparable degradation rates between in-home nanofibers *versus* P25 nanoparticles for all the tested drugs, with the exception of ibuprofen, whose degradation was three times faster using TiO_2 home-made NF than the reference catalystTiO_2 NPs. This could be associated to the presence of brookite in the TiO_2 home-made NFs.

As stated by Kaplan *et al.* [168], the presence of this third crystalline phase may pose a benefit on the photocatalytical activity of TiO_2 rather than the two-phase material by which is composed P25 nanoparticles, attributed to a more efficient charge separation in the material and an increased resistance to the deposit of carbonaceous materials onto the TiO_2 surface. By ranking compounds, ofloxacin was the easiest drug to mineralise and completely degrade, followed by diclofenac, ibuprofen and finishing with clofibric acid. A deeper insight into the mineralization and degradation process of ofloxacin will be presented in the **Chapter 4** by studying their transformation products with high-resolution and ion mobility mass spectrometry.

Abatement of organic pollutants from real water

Already reported in past publications and one of the most challenging tasks to overcome in future investigations concerned to TiO_2 photocatalysis is the observed effect when comparing **Table 3.11** and **3.13**. Both tables clearly show the significant drop in the photocatalytical performance of the catalysts under study when changing the reaction solvent from MilliQ water to raw water in both suspended and supported *set-ups*.

This photocatalytical drop was mainly attributed to the scavenger effect that dissolved salts and organic matter, such as anionic, cationic and non-ionic surfactants pose onto the efficiency of the oxidation process. These salts, such as Cl^-, SO_4^{2-}, NO_3^-, etc. can react with the hydroxyl radical leading to intermediate species with a smaller oxidizing power than that of the hydroxyl radical [169–171], already mentioned in **Chapter 1**. In degradation terms, this lead to a time increase, up to four hours, to completely (or partially) remove the pollutants under study (both suspended and supported set-ups) as depicted in **Figures 3.31** and **3.32**. pH and the rest of chemical parameters remained constant along the photocatalytic process. As observed when performing the reaction in MilliQ water, P25 nanoparticles and in-home TiO_2 nanofibers appeared to have the same photocatalytical performance, only showing little differences in respect to ofloxacin's degradation rate under supported conditions. Clofibric acid was partially removed, up to a 15 and 20%, when using the synthesised and commercial nanofibers respectively. Opposite to the observed results under MilliQ water, this chemical showed no degradation when the photocatalysis was carried out using P25 nanoparticles. Surprisingly and despite the good results obtained when the experiments were carried out under MilliQ water, ibuprofen did not have any symptom of partial oxidation neither under P25 nanoparticles, commercial nanofibers or prepared TiO_2 nanofibers.

Table 3.12. Chemical quality parameters of the real water employed.

Parameter	**Method**	**Result**
pH		6.8
SST (mg L^{-1})	UNE-EN 872:2006	8
DBO_5 (mg O_2 L^{-1})	SM 5210D	< 30
COD (mg O_2 L^{-1})	UNE 77004:2002	< 30
Phosphorous (mg L^{-1})	Acid digestion and ICP/MS	< 2
Total nitrogen (mg L^{-1})	UNE-EN 25663:1994	16.8
Anionic surfactant (mg LLS L^{-1})	Hach Lange Kit (UV-Vis)	1.2
Cationic surfactant (mg LLS L^{-1})		0.25
Non-ionic surfactant (mg LLS L^{-1})		0.14
Anions		
Fluoride (F^-) (mg L^{-1})	Ionic chromatography	<1
Chloride (Cl^-) (mg L^{-1})		318.5
Nitrite (NO_2^-) (mg L^{-1})		<1
Bromide (Br^-) (mg L^{-1})		<1
Nitrate (NO_3^-) (mg L^{-1})		3.35
Sulfate ($SO_4^{2-)}$		106.7
Phosphate (PO_4^{3-})		<1

Table 3.13. Linear fitting of degradation kinetics on real water.

Drug	TiO_2 NPs; *k* (min^{-1})		Comm. TiO_2 NFs; *k* (min^{-1})		Leitat TiO_2 NFs; *k* (min^{-1})	
	Suspension. (r^2)	Supported. (r^2)	Suspension. (r^2)	Supported. (r^2)	Suspension. (r^2)	Supported. (r^2)
Ofloxacin	0.01(0.99)	0.01 (0.99)	0.01 (0.97)	0.01 (0.98)	0.01 (0.99)	0.026 (0.95)
Diclofenac	0.02 (0.99)	0.01 (0.96)	Max. 15% deg	0.01 (0.99)	Max. 24% deg	0.01 (0.88)
Clofibric acid	- (-)	- (-)	Max. 20% deg	- (-)	Max 15% deg	0.005 (0.99)
Ibuprofen	- (-)	- (-)	- (-)	- (-)	- (-)	- (-)

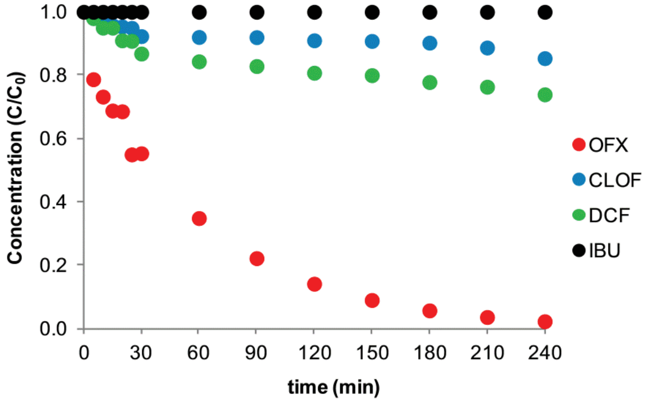

Figure 3.31. Degradation kinetics under synthesised NF (suspended *set-up* in real water).

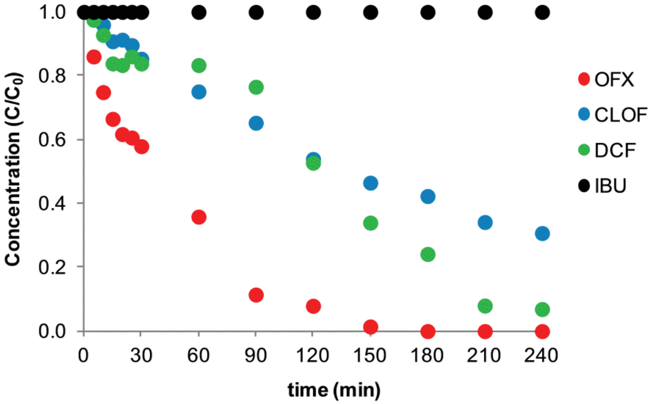

Figure 3.32. Degradation kinetics under synthesised NF (supported *set-up* in real water).

3.3. Conclusions

The experimental section of this chapter has been devoted to the development and characterisation of 1D TiO_2 nanofibers and their latter application to the photocatalysis of four model pharmaceutical drugs (ofloxacin, clofibric acid, diclofenac and ibuprofen).

- TiO_2 nanofibers have been synthesised and characterised with several physical techniques (SEM, BET, XRD) and compared to the reference material (*Degussa* P25 nanoparticles) and commercially available TiO_2 nanofibers. Moreover, a simple method to fix the catalyst onto an inner support has been adapted and successfully applied for the latter use of this catalyst on industrial application.
- The physical characterisation of the synthesised material has shown different similarities and differences to that compared to the reference TiO_2 NPs and commercially available NFs. Contrary to P25 NPs, prepared and commercial NFs presented the three crystallite TiO_2 phases but those synthesised NFs had the same anatase content than the reference material. Moreover, the prepared catalyst has 20% less surface area compared to the reference material, property that could drastically affect onto their photocatalytical properties.
- Even though not having the same physical characteristics, synthesised nanofibers resulted to be the catalyst with the maximum adsorption capacity (derived from Langmuir isotherms) and to have equivalent degradation performance as the reference P25 nanoparticles for ofloxacin, clofibric acid and diclofenac while appeared to degrade 3 times faster ibuprofen (under suspended conditions).
- The latter support of these catalysts led to a significant reduction in the photocatalytical performance in batch experiments (up to 100 times) due to the drop of available surface TiO_2 sites capable of undergoing direct oxidation or reduction onto the molecules of interest or promoting the production of reactive oxygen species for indirect oxidation. This point could be easily improved by performing *in-flow* experiments, permitting enough residence time to promote the photocatalytical reaction.

Moreover, TiO_2 photocatalysis might not be the best degradation technique to be used in order to directly treat wastewater containing high concentration of dissolved salts and COD values due to the scavenger effect TiO_2 suffers. However, it might be useful when coupled to other water treatment technique in order to completely ensure the removal of chemicals contained in it.

3.4. References

1. McDonough, W. F.; Sun, S. s. *Chem. Geol.* **120,** 223–253 (1995).

2. Wedepohl, K. H. *Geochim. Cosmochim. Acta* **59,** 1217–1232 (1995).

3. Imam, M. A., Froes, F. H. and Housley, K. L. in *Kirk-Othmer Encyclopedia of Chemical Technology* 1–41 (John Wiley & Sons, Inc., 1983).

4. ResearchandMarkets. (2016).

5. Du Pont. (1951).

6. Du Pont. (1949).

7. Du Pont. (1949).

8. Luttrell, T.; Halpegamage, S.; Tao, J.; Kramer, A.; Sutter, E.; Batzill, M. *Sci. Rep.* **4,** 4043 (2014).

9. Efsa. *EFSA J.* **415,** 1–10 (2006).

10. Carp, O.; Huisman, C. L.; Reller, A. *Prog. Solid State Chem.* **32,** 33–177 (2004).

11. Xiong, D.; Fang, T.; Yu, L.; Sima, X.; Zhu, W. *Sci. Total Environ.* **409,** 1444–1452 (2011).

12. Cherchi, C.; Chernenko, T.; Diem, M.; Gu, A. Z. *Environ. Toxicol. Chem.* **30,** 861–869 (2011).

13. Wiench, K.; Wohlleben, W.; Hisgen, V.; Radke, K.; Salinas, E.; Zok, S.; Landsiedel, R. *Chemosphere* **76,** 1356–1365 (2009).

14. Zhu, X.; Chang, Y.; Chen, Y. *Chemosphere* **78,** 209–215 (2010).

15. Heinlaan, M.; Ivask, A.; Blinova, I.; Dubourguier, H. C.; Kahru, A. *Chemosphere* **71,** 1308–1316 (2008).

16. Chen, J.; Dong, X.; Zhao, J.; Tang, G. *J. Appl. Toxicol.* **29,** 330–337 (2009).

17. Elgrabli, D.; Beaudouin, R.; Jbilou, N.; Floriani, M.; Pery, A.; Rogerieux, F.; Lacroix, G. *PLoS One* **10,** 1–13 (2015).

18. Wang, J.; Zhou, G.; Chen, C.; Yu, H.; Wang, T.; Ma, Y.; Jia, G.; Gao, Y.; Li, B.; Sun, J.; *et al. Toxicol. Lett.* **168,** 176–185 (2007).

19. Wen, B.; Lampe, J. N.; Roberts, A. G.; Atkins, W. M.; Rodrigues, A. D.; Nelson, S. D. *Cancer Resesearch* **454,** 42–54 (2007).

20. Shrivastava, R.; Raza, S.; Yadav, A.; Kushwaha, P.; Flora, S. J. S. **545,** (2014).

21. Sayes, C. M.; Wahi, R.; Kurian, P. A.; Liu, Y.; West, J. L.; Ausman, K. D.; Warheit, D. B.; Colvin, V. L. *Toxicol. Sci.* **92,** 174–185 (2006).

22. Petkovi C, J.; Žegura, B.; Stevanovi C, M.; Drnovšek, N.; Uskokovi C, D.; Novak, S.; Filipi, M. *Nanotoxicology* **5,** 341–353 (2011).

23. Meena, R.; Rani, M.; Pal, R.; Rajamani, P. *Appl. Biochem. Biotechnol.* **167,** 791–808 (2012).

24. Jin, C. Y.; Zhu, B. S.; Wang, X. F.; Lu, Q. H. *Chem. Res. Toxicol.* **21,** 1871–1877 (2008).

25. Kočí, K.; Obalová, L.; Matějová, L.; Plachá, D.; Lacný, Z.; Jirkovský, J.; Šolcová, O. *Appl. Catal. B Environ.* **89,** 494–502 (2009).

26. Zhang, Z.; Wang, C.-C.; Zakaria, R.; Ying, J. Y. *J. Phys. Chem. B* **102,** 10871–10878 (1998).

27. He, F.; Li, J.; Li, T.; Li, G. *Chem. Eng. J.* **237,** 312–321 (2014).

28. Almquist, C. B.; Biswas, P. *J. Catal.* **212,** 145–156 (2002).

29. Maira, A. J.; Yeung, K. L.; Lee, C. Y.; Yue, P. L.; Chan, C. K. *J. Catal.* **192,** 185–196 (2000).

30. Zaki, M. I.; Fouad, N. E.; Mekhemer, G. A. H.; Jagadale, T. C.; Ogale, S. B. *Colloids Surfaces A Physicochem. Eng. Asp.* **385,** 195–200 (2011).

31. Fu, J.; Cao, S.; Yu, J.; Low, J.; Lei, Y. *Dalt. Trans.* **43,** 9158–65 (2014).

32. Li, H.; Zhang, W.; Huang, S.; Pan, W. *Nanoscale* **4,** 801–806 (2012).

33. Li, X.; Lin, H.; Chen, X.; Niu, H.; Zhang, T.; Liu, J.; Qu, F. *New J. Chem.* **39,** 7863–7872 (2015).

34. Meng, X.; Shin, D.-W.; Yu, S. M.; Jung, J. H.; Kim, H. I.; Lee, H. M.; Han, Y.-H.; Bhoraskar, V.; Yoo, J.-B. *CrystEngComm* **13,** 3021–3029 (2011).

35. Li, W.; Bai, Y.; Liu, W.; Liu, C.; Yang, Z.; Feng, X.; Lu, X.; Chan, K.-Y. *J. Mater. Chem.* **21,** 6718 (2011).

36. Zhang, H.; Lv, X.; Li, Y.; Wang, Y.; Li, J. *ACS Nano* **4,** 380–386 (2010).

37. Yu, Y.; Yu, J. C.; Chan, C. Y.; Che, Y. K.; Zhao, J. C.; Ding, L.; Ge, W. K.; Wong, P. K. *Appl. Catal. B Environ.* **61,** 1–11 (2005).

38. Leary, R.; Westwood, A. *Carbon N. Y.* **49,** 741–772 (2011).

39. Chouchene, B.; Chaabane, T. Ben; Balan, L.; Girot, E.; Mozet, K.; Medjahdi, G.; Schneider, R. *Beilstein J. Nanotechnol.* **7,** 1338–1349 (2016).

40. Jia, H.; Xu, H.; Hu, Y.; Tang, Y.; Zhang, L. *Electrochem. commun.* **9,** 354–360 (2007).

41. Ren, L.; Mao, M.; Li, Y.; Lan, L.; Zhang, Z.; Zhao, X. *Appl. Catal. B Environ.* **198,** 303–310 (2016).

42. Wang, X.; Ni, Q.; Zeng, D.; Liao, G.; Xie, C. *Appl. Surf. Sci.* **389,** 165–172 (2016).

43. Yu, Y.; Xu, D. *Appl. Catal. B Environ.* **73,** 166–171 (2007).

44. Sun, G.; Zhu, C.; Zheng, J.; Jiang, B.; Yin, H.; Wang, H.; Qiu, S.; Yuan, J.; Wu, M.; Wu, W.; *et al. Mater. Lett.* **166,** 113–115 (2016).

45. Li, B.; Yuan, H.; Yang, P.; Yi, B.; Zhang, Y. *Ceram. Int.* **42,** 17405–17409 (2016).

46. Wang, T.; Yang, G.; Liu, J.; Yang, B.; Ding, S.; Yan, Z.; Xiao, T. *Appl. Surf. Sci.* **311,** 314–323 (2014).

47. Cheng, X. L.; Jiang, J. Sen; Jin, C. Y.; Lin, C. C.; Zeng, Y.; Zhang, Q. H. *Chem. Eng. J.* **236,** 139–148 (2014).

48. Brus, L. *J. Phys. Chem.* **90,** 2555–2560 (1986).

49. Satoh, N.; Nakashima, T.; Yamamoto, K. *Sci. Rep.* **3,** 1959 (2013).

50. Lu, B.; Zhu, C.; Zhang, Z.; Lan, W.; Xie, E. *J. Mater. Chem.* **22,** 1375 (2012).

51. Chacko, D. K.; Madhavan, A. A.; Arun, T. a.; Thomas, S.; Anjusree, G. S.; Deepak, T. G.; Balakrishnan, A.; Subramanian, K. R. V.; Sivakumar, N.; Nair, S. V.; *et al. RSC Adv.* **3,** 24858 (2013).

52. Nayak, R.; Padhye, R.; Arnold, L. *Electrospun Nanofibers* (Elsevier Ltd., 2017).

53. Srivastava, R. K.; Delhi, N. *Electrospun Nanofibers* (Elsevier Ltd., 2017).

54. Salas, C. *Electrospun Nanofibers* (Elsevier Ltd., 2017).

55. Moheman, A.; Alam, M. S.; Mohammad, A. *Adv. Colloid Interface Sci.* **229,** 1–24 (2015).

56. Chaúque, E. F. C.; Adelodun, A. A.; Dlamini, L. N.; Greyling, C. J.; Ray, S. C.; Ngila, J. C. *Mater. Chem. Phys.* **192,** 108–124 (2017).

57. Avila, M.; Burks, T.; Akhtar, F.; Göthelid, M.; Lansåker, P. C.; Toprak, M. S.; Muhammed, M.; Uheida, A. *Chem. Eng. J.* **245,** 201–209 (2014).

58. Žabar, R.; Komel, T.; Fabjan, J.; Kralj, M. B.; Trebše, P. *Chemosphere* **89,** 293–301 (2012).

59. Maeng, S. K.; Cho, K.; Jeong, B.; Lee, J.; Lee, Y.; Lee, C.; Choi, K. J.; Hong, S. W. *Water Res.* **86,** 25–34 (2015).

60. Barndõk, H.; Hermosilla, D.; Han, C.; Dionysiou, D. D.; Negro, C.; Blanco, Á. *Appl. Catal. B Environ.* **180,** 44–52 (2016).

61. Tian, F.; Li, Y.; Xing, J.; Tian, H.; Whitmore, L.; Yang, H.; Yang, X. *Mater. Lett.* **123,** 254–257 (2014).

62. Zhang, Y.; Xing, Z.; Liu, X.; Li, Z.; Wu, X.; Jiang, J.; Li, M.; Zhu, Q.; Zhou, W. *ACS Appl. Mater. Interfaces* **8,** 26851–26859 (2016).

63. Yu, Y.; He, T.; Guo, L.; Yang, Y.; Guo, L.; Tang, Y.; Cao, Y. *Sci Rep* **5,** 9561 (2015).

64. Zaleska, A. *Recent Patents Eng.* **2,** 157–164 (2008).

65. Falaras, P.; Gratzel, M.; Hugoy-Le Goff, A.; Nazeeruddin, M.; Vrachnou, E. *J. Electrochem. Soc.* **140,** L92–L94 (1993).

66. Tao, P.; Guo, W.; Du, J.; Tao, C.; Qing, S.; Fan, X. *J. Colloid Interface Sci.* **478,** 172–180 (2016).

67. Rajeshwar, K.; Osugi, M. E.; Chanmanee, W.; Chenthamarakshan, C. R.; Zanoni, M. V. B.; Kajitvichyanukul, P.; Krishnan-Ayer, R. *J. Photochem. Photobiol. C Photochem. Rev.* **9,** 171–192 (2008).

68. Chatterjee, D.; Dasgupta, S. *J. Photochem. Photobiol. C Photochem. Rev.* **6,** 186–205 (2005).

69. Zhang, Q.; Li, R.; Li, Z.; Li, A.; Wang, S.; Liang, Z.; Liao, S.; Li, C. *J. Catal.* **337,** 36–44 (2016).

70. Chen, Y.; Xu, Y.; Jiao, S.; Wang, X.; Li, L.; Fang, Z.; Pang, G.; Feng, S. *Dye. Pigment.* **129,** 191–198 (2016).

71. Grabowska, E.; Marchelek, M.; Klimczuk, T.; Trykowski, G.; Zaleska-Medynska, A. *J. Mol. Catal. A Chem.* **423,** 191–206 (2016).

72. Szabó-bárdos, E.; Horváth, O.; Szabó, P.; Horváth, K. **284,** 179–186 (2017).

73. Fakharan, Z.; Naji, L. *J. Alloys Compd.* **708,** 1184–1194 (2017).

74. Liu, L.; Ding, L.; Liu, Y.; An, W.; Lin, S.; Liang, Y.; Cui, W. *Appl. Catal. B Environ.* **201,** 92–104 (2017).

75. Yao, B.; Peng, C.; Zhang, W.; Zhang, Q.; Niu, J.; Zhao, J. *Appl. Catal. B Environ.* **174–175,** 77–84 (2015).

76. Hou, H. J.; Zhang, X. H.; Huang, D. K.; Ding, X.; Wang, S. Y.; Yang, X. L.; Li, S. Q.; Xiang, Y. G.; Chen, H. *Appl. Catal. B Environ.* **203,** 513–517 (2017).

77. Park, J. *J. Ind. Eng. Chem.* (2017). doi:10.1016/j.jiec.2017.03.022

78. Liu, B.; Zhao, X. *Appl. Surf. Sci.* **399,** 654–662 (2017).

79. Parvathi V, P.; Jaiakumar, T.; Umadevi, M.; Mayandi, J.; Sathe, G. V. *Mater. Lett.* **184,** 82–87 (2016).

80. Gao, L.; Li, Y.; Ren, J.; Wang, S.; Wang, R.; Fu, G.; Hu, Y. *Appl. Catal. B Environ.* **202,** 127–133 (2017).

81. Wang, T.; Xu, T. *Ceram. Int.* **43,** 1558–1564 (2017).

82. Zhang, W.; Liu, Y.; Pei, X.; Chen, X. *J. Phys. Chem. Solids* **104,** 45–51 (2017).

83. Silvestre, A. J.; Rout, S.; Dalui, S.; Pereira, L. C. J.; Viana, A. S.; Conde, O. **17,** 174–180 (2017).

84. Saini, M.; Kumar, M.; Som, T. *Appl. Surf. Sci.* 1–6 (2017). doi:10.1016/j.apsusc.2017.01.262

85. Song, J.; Li, S. P.; Zhao, Y. L.; Yuan, J.; Zhu, Y.; Fang, Y.; Zhu, L.; Gu, X. Q.; Qiang, Y. H. *J. Alloys Compd.* **694,** 1232–1238 (2017).

86. Di Valentin, C.; Pacchioni, G. *Catal. Today* **206,** 12–18 (2013).

87. Xu, Z.; Yang, W.; Li, Q.; Gao, S.; Shang, J. K. *Appl. Catal. B Environ.* **144,** 343–352 (2014).

88. Samsudin, E. M.; Hamid, S. B. A.; Juan, J. C.; Basirun, W. J.; Centi, G. *Chem. Eng. J.* **280,** 330–343 (2015).

89. Yang, H.; Wang, Y.; Xue, X. *Colloids Surfaces B Biointerfaces* **122,** 701–708 (2014).

90. Fagan, R.; McCormack, D. E.; Hinder, S.; Pillai, S. C. *Mater. Des.* **96,** 44–53 (2016).

91. Sun, S.; Zhang, J.; Gao, P.; Wang, Y.; Li, X.; Wu, T.; Wang, Y.; Chen, Y.; Yang, P. *Appl. Catal. B Environ.* **206,** 168–174 (2017).

92.Ivanov, S.; Barylyak, A.; Besaha, K.; Dimitrova, A.; Krischok, S.; Bund, A.; Bobitski, J. *J. Power Sources* **326,** 270–278 (2016).

93.Samsudin, E. M.; Abd Hamid, S. B. *Appl. Surf. Sci.* **391,** 326–336 (2017).

94.Uddin, M. N.; Shibly, S. U. A.; Ovali, R.; Saiful Islam; Mazumder, M. M. R.; Islam, M. S.; Uddin, M. J.; Gulseren, O.; Bengu, E. *J. Photochem. Photobiol. A Chem.* **254,** 25–34 (2013).

95.Asahi, R.; Morikawa, T.; Ohwaki, T.; Taga, Y. *Science (80-.).* **293,** 269–271 (2001).

96.Wang, Y.; Feng, C.; Zhang, M.; Yang, J.; Zhang, Z. *Appl. Catal. B Environ.* **100,** 84–90 (2010).

97.Dong, S.; Feng, J.; Fan, M.; Pi, Y.; Hu, L.; Han, X.; Liu, M.; Sun, J.; Sun, J. *RSC Adv.* **5,** 14610–14630 (2015).

98.Chen, Y. J.; Jhan, G. Y.; Cai, G. L.; Lin, C. S.; Wong, M. S.; Ke, S. C.; Lo, H. H.; Cheng, C. L.; Shyue, J. J. *J. Vac. Sci. Technol. A* **28,** 779–782 (2010).

99.AltIn, I.; Sökmen, M.; Biyiklioɫlu, Z. *Mater. Sci. Semicond. Process.* **45,** 36–44 (2016).

100.Gaminian, H.; Montazer, M. *J. Photochem. Photobiol. A Chem.* **332,** 158–166 (2017).

101.Pan, L.; Zou, J. J.; Wang, S.; Huang, Z. F.; Zhang, X.; Wang, L. *Appl. Surf. Sci.* **268,** 252–258 (2013).

102.Yun, E. T.; Yoo, H. Y.; Kim, W.; Kim, H. E.; Kang, G.; Lee, H.; Lee, S.; Park, T.; Lee, C.; Kim, J. H.; *et al. Appl. Catal. B Environ.* **203,** 475–484 (2017).

103.Shang, J.; Zhao, F.; Zhu, T.; Li, J. *Sci. China Chem.* **54,** 167–172 (2011).

104. Diak, M.; Grabowska, E.; Zaleska, A. *Appl. Surf. Sci.* **347,** 275–285 (2015).

105. Halasi, G.; Tóth, A.; Bánsági, T.; Solymosi, F. *Int. J. Hydrogen Energy* **41,** 13485–13492 (2016).

106. Hou, X.-G.; Ma, J.; Liu, A.-D.; Li, D.-J.; Huang, M.-D.; Deng, X.-Y. *Nucl. Instruments Methods Phys. Res. Sect. B Beam Interact. with Mater. Atoms* **268,** 550–554 (2010).

107.Poulios, I.; Tsachpinis, I. *J. Chem. Technol. Biotechnol.* **74,** 349–357 (1999).

108.Khodja, A. A.; Sehili, T.; Pilichowski, J.-F.; Boule, P. *J. Photochem. Photobiol. A Chem.* **141,** 231–239 (2001).

109.Sakthivel, S.; Neppolian, B.; Shankar, M. V; Arabindoo, B.; Palanichamy, M.; Murugesan, V. *Sol. Energy Mater. Sol. Cells* **77,** 65–82 (2003).

110.Chakrabarti, S.; Dutta, B. K. *J. Hazard. Mater.* **112,** 269–278 (2004).

111.Daneshvar, N.; Salari, D.; Khataee, A. R. *J. Photochem. Photobiol. A Chem.* **162,** 317–322 (2004).

112.Chen, X.; Chen, W.; Lin, P.; Yang, Y.; Gao, H.; Yuan, J.; Shangguan, W. *Catal. Commun.* **36,** 104–108 (2013).

113.Qutub, N.; Pirzada, B. M.; Umar, K.; Mehraj, O.; Muneer, M.; Sabir, S. *Phys. E Low-dimensional Syst. Nanostructures* **74,** 74–86 (2015).

114.Yan, J.; Li, X.; Yang, S.; Wang, X.; Zhou, W.; Fang, Y.; Zhang, S.; Peng, F.; Zhang, S. *Int. J. Hydrogen Energy* **42,** 928–937 (2016).

115.Qian, J.; Chen, F.; Wang, F.; Zhao, X.; Chen, Z. *Mater. Res. Bull.* **47,** 1845–1848 (2012).

116.Huang, J.; Ren, H.; Chen, K.; Shim, J. J. *Superlattices Microstruct.* **75,** 843–856 (2014).

117.Zhang, P.; Liu, Y.; Tian, B.; Luo, Y.; Zhang, J. *Catal. Today* **281,** 181–188 (2017).

118.Wen, X.-J.; Zhang, C.; Niu, C.-G.; Zhang, L.; Zeng, G.-M.; Zhang, X.-G. *Catal. Commun.* **90,** 51–55 (2017).

119. Gondal, M. A.; Dastageer, M. A.; Khalil, A. *Catal. Commun.* **11,** 214–219 (2009).

120. Liu, Y.; Xie, C.; Li, H.; Chen, H.; Zou, T.; Zeng, D. *J. Hazard. Mater.* **196,** 52–58 (2011).

121. Selvarajan, S.; Suganthi, A.; Rajarajan, M.; Arunprasath, K. *Powder Technol.* **307,** 203–212 (2017).

122. Oliveira, H. G.; Ferreira, L. H.; Bertazzoli, R.; Longo, C. *Water Res.* **72,** 305–314 (2015).

123. Yin, Q.; Qiao, R.; Zhu, L.; Li, Z.; Li, M.; Wu, W. *Mater. Lett.* **135,** 135–138 (2014).

124. Wang, J. C.; Ren, J.; Yao, H. C.; Zhang, L.; Wang, J. S.; Zang, S. Q.; Han, L. F.; Li, Z. J. *J. Hazard. Mater.* **311,** 11–19 (2016).

125. Sun, T. W.; Zhu, Y. J.; Qi, C.; Ding, G. J.; Chen, F.; Wu, J. *J. Colloid Interface Sci.* **463,** 107–117 (2016).

126. An, S.; Joshi, B. N.; Lee, M. W.; Kim, N. Y.; Yoon, S. S. *Appl. Surf. Sci.* **294,** 24–28 (2014).

127. Kayaci, F.; Vempati, S.; Ozgit-Akgun, C.; Donmez, I.; Biyikli, N.; Uyar, T. *Appl. Catal. B Environ.* **176–177,** 646–653 (2015).

128. Zhao, D.; He, Z.; Wang, G.; Wang, H.; Zhang, Q.; Li, Y. *Sensors Actuators, B Chem.* **229,** 281–287 (2016).

129. Ma, S.; Li, R.; Lv, C.; Xu, W.; Gou, X. *J. Hazard. Mater.* **192,** 730–740 (2011).

130. Li, C.; Ahmed, T.; Ma, M.; Edvinsson, T.; Zhu, J. *Appl. Catal. B Environ.* **138–139,** 175–183 (2013).

131. Kandjani, A. E.; Mohammadtaheri, M.; Thakkar, A.; Bhargava, S. K.; Bansal, V. *J. Colloid Interface Sci.* **436,** 251–257 (2014).

132. Fang, J.; Fan, H.; Ma, Y.; Wang, Z.; Chang, Q. *Appl. Surf. Sci.* **332,** 47–54 (2015).

133. Toubane, M.; Tala-Ighil, R.; Bensouici, F.; Bououdina, M.; Cai, W.; Liu, S.; Souier, M.; Iratni, A. *Ceram. Int.* **42,** 9673–9685 (2016).

134. Sett, D.; Basak, D. *Sensors Actuators B Chem.* **243,** 475–483 (2017).

135. Lam, S. M.; Sin, J. C.; Zuhairi Abdullah, A.; Rahman Mohamed, A. *Mater. Lett.* **93,** 423–426 (2013).

136. Ameen, S.; Shaheer Akhtar, M.; Shin, H. S. *Mater. Lett.* **106,** 254–258 (2013).

137. An, X.; Teng, F.; Zhang, P.; Zhao, C.; Pan, X.; Zhang, Z.; Xie, E. *J. Alloys Compd.* **614,** 373–378 (2014).

138. Bojer, C.; Schöbel, J.; Martin, T.; Ertl, M.; Schmalz, H.; Breu, J. *Appl. Catal. B Environ.* **204,** 561–565 (2017).

139. Kansal, S. K.; Singh, M.; Sud, D. *J. Hazard. Mater.* **141,** 581–590 (2007).

140. Jule, L. T.; Dejene, F. B.; Ali, A. G.; Roro, K. T.; Hegazy, A.; Allam, N. K.; El Shenawy, E. *J. Alloys Compd.* **687,** 920–926 (2016).

141. Mustafa, L.; Anjum, S.; Waseem, S.; Khurshid, H.; Choudhary, R.; Bashir, F. *Materials Today: Proceedings* **2,** (Elsevier Ltd., 2015).

142. Duan, L.; Zhao, X.; Wang, Y.; Shen, H.; Geng, W.; Zhang, F. *J. Alloys Compd.* **645,** 529–534 (2015).

143. Achouri, F.; Corbel, S.; Balan, L.; Mozet, K.; Girot, E.; Medjahdi, G.; Said, M. Ben; Ghrabi, A.; Schneider, R. *Mater. Des.* **101,** 309–316 (2016).

144. Labiadh, H.; Sellami, B.; Khazri, A.; Saidani, W.; Khemais, S. *Opt. Mater. (Amst).* **64,** 179–186 (2017).

145. Sharma, D.; Jha, R. *J. Alloys Compd.* **698,** 532–538 (2017).

146. Zheng, J. H.; Song, J. L.; Zhao, Z.; Jiang, Q.; Lian, J. S. *Cryst. Res. Technol.* **47,** 713–718 (2012).

147. Ashokkumar, M.; Muthukumaran, S. *J. Lumin.* **162,** 97–103 (2015).

148. Guruvammal, D.; Selvaraj, S.; Meenakshi Sundar, S. *J. Alloys Compd.* **682,** 850–855 (2016).

149. Xu, K.; Liu, C.; Chen, R.; Fang, X.; Wu, X.; Liu, J. *Phys. B Condens. Matter* **502,** 155–159 (2016).

150. Pal, B.; Sarkar, D.; Giri, P. K. *Appl. Surf. Sci.* **356,** 804–811 (2015).

151. Maswanganye, M. W.; Rammutla, K. E.; Mosuang, T. E.; Mwakikunga, B. W. *Sensors Actuators B Chem.* (2017). doi:10.1016/j.snb.2017.02.039

152. Garcia, M. A.; Merino, J. M.; Pinel, E. F.; Quesada, A.; De La Venta, J.; González, M. L. R.; Castro, G. R.; Crespo, P.; Llopis, J.; González-Calbet, J. M.; *et al. Nano Lett.* **7,** 1489–1494 (2007).

153. Dai, Z.; Nurbawono, A.; Zhang, A.; Zhou, M.; Feng, Y. P.; Ho, G. W.; Zhang, C. *J. Chem. Phys.* **134,** (2011).

154. Wang, F.; Liang, L.; Shi, L.; Liu, M.; Sun, J. *Dalt. Trans.* **43,** 16441–16449 (2014).

155. Valour, A.; Cheviré, F.; Tessier, F.; Grasset, F.; Dierre, B.; Jiang, T.; Faulques, E.; Cario, L.; Jobic, S. *Solid State Sci.* **54,** 30–36 (2016).

156. Hiragino, Y.; Tanaka, T.; Takeuchi, H.; Takeuchi, A.; Lin, J.; Yoshida, T.; Fujita, Y. *Solid. State. Electron.* **118,** 41–45 (2016).

157. Kumari, R.; Sahai, A.; Goswami, N. *Prog. Nat. Sci. Mater. Int.* **25,** 300–309 (2015).

158. Debbichi, M.; Sakhraoui, T.; Debbichi, L.; Said, M. *J. Alloys Compd.* **578,** 602–608 (2013).

159. Xie, X. Y.; Zhan, P.; Li, L. Y.; Zhou, D. J.; Guo, D. Y.; Meng, J. X.; Bai, Y.; Zheng, W. J. *J. Alloys Compd.* **644,** 383–389 (2015).

160. Crystalimpact. Available at: http://www.crystalimpact.com/match/.

161. Brunauer, S.; Emmett, P. H.; Teller, E. *J. Am. Chem. Soc.* **60,** 309–319 (1938).

162. Thommes, M.; Kaneko, K.; Neimark, A. V.; Olivier, J. P.; Rodriguez-Reinoso, F.; Rouquerol, J.; Sing, K. S. W. *Pure Appl. Chem.* **87,** 1051–1069 (2015).

163. Hapeshi, E.; Fotiou, I.; Fatta-Kassinos, D. *Chem. Eng. J.* **224,** 96–105 (2013).

164. Daughton, C. G. *Sci. Total Environ.* **562,** 391–426 (2016).

165. Ramasundaram, S.; Seid, M. G.; Choe, J. W.; Kim, E. J.; Chung, Y. C.; Cho, K.; Lee, C.; Hong, S. W. *Chem. Eng. J.* **306,** 344–351 (2016).

166. Dávila-Jiménez, M. M.; Elizalde-González, M. P.; García-Díaz, E.; Marín-Cevada, V.; Zequineli-Pérez, J. *Appl. Catal. B Environ.* **166–167,** 241–250 (2015).

167. Fernández, J.; Kiwi, J.; Baeza, J.; Freer, J.; Lizama, C.; Mansilla, H. D. *Appl. Catal. B Environ.* **48,** 205–211 (2004).

168. Kaplan, R.; Erjavec, B.; Drazic, G.; Grdadolnik, J.; Pintar, A. *Appl. Catal. B Environ.* **181,** 465–474 (2016).

169. Ghazi, N. M.; Lastra, A. A.; Watts, M. J. *Water Res.* **56,** 148–155 (2014).

170. Souza, B. S.; Dantas, R. F.; Cruz, A.; Sans, C.; Esplugas, S.; Dezotti, M. *Chem. Eng. J.* **237,** 268–276 (2014).

171. Liao, C. H.; Kang, S. F.; Wu, F. A. *Chemosphere* **44,** 1193–1200 (2001).

~ Chapter 4.

Tandem, high-resolution and ion-mobility mass spectrometry for the detection and characterisation of transformation products generated by TiO_2 photocatalysis.

Today, the identification of unknown compounds contained in complex samples is one of the major challenges in the field of environmental studies [1–4], metabolomics [5–7], proteomics [8–10] and related "-omics" sciences. Most of these detected compounds are sometimes unidentified or difficult to identify due to the small repository of entries in current libraries and/or the unavailability of reference standards [4,11]. Nowadays, all efforts to solve this problem seem to be driven to the creation of extensive libraries [12] with the use of different analytical platforms. These analytical techniques may involve a separation step such as gas chromatography (GC), or liquid chromatography (LC) coupled to mass spectrometry (MS) or nuclear magnetic resonance (NMR) [13–17]. However, with the irruption of such powerful instruments, capable of measuring from hundreds to thousands of signals in one analytical run, data processing plays a critical role in the analytical method and can greatly affect the outcome of the data analysis. Most manufacturers have specific software for their instruments and data processing, which are able to automatically extract signals of interest to facilitate the suspect screening approaches. However, despite the tremendous advances in the development of commercial software capable of performing advanced operations, sometimes, not all required information or operations are available in one platform, leading users to develop independent software, usually written in open-source such as R-code [18–20], C++ [9,21], JAVA [22–24] or MATLAB [25,26].

The present chapter is divided into a general introduction, an experimental section and the discussion of results obtained. In the introduction, the most common analytical platforms addressing environmental studies dealing with the detection and characterisation of unknown compounds will be discussed. Special emphasis will be given to mass spectrometry instruments as well as to their operational modes. Due to the high impact that informatic tools and libraries represent nowadays, a review, dealing with the most promising available tools is included. The experimental section deals with the detection and characterisation of ofloxacin transformation products after titanium (IV) oxide photocatalysis and its discussion, showing the main challenges faced and the strategies adopted for its resolution.

4.1. Introduction

There is an increasing interest in the scientific community to apply the full capabilities of mass spectrometry related techniques for the discovery of new molecules (or macromolecules) related to the environmental, metabolomics, proteomics field. Three different analysis approaches are usually described for the detection and/or identification of compounds: target, suspect and non-target screening [27–30]. Target methods are limited to a number of pre-established lists of compounds for which analytical standards are commercially available. Suspect screening uses a database of "known" compounds that is then correlated to mass spectral data to give potential positive compounds that need to be confirmed by the use of reference standards in a final step. The third, non-target approach, has gained a lot interest from the scientific community, but it is notoriously difficult to face since no previous information and/or knowledge is available [31–33]. In this strategy, data processing plays a crucial role, representing the major challenges that mass spectrometrists have to face. It is for this reason that along with the vast improvements done in instrumentation (hardware), the continuous development of data processing tools have gained an enormous interest by independent researchers, developing custom-made software, and instrument manufacturers, always increasing software capabilities and functionalities.

In order to carry out the mentioned analysis strategies upon sample extraction, pre-concentration and matrix *clean-up*, gas or liquid chromatography separation techniques coupled to high-resolution mass spectrometry are the preferred instrumentation of choice. One limitation of these techniques that could not be solved before, however, was the acquisition of three-dimensional information of the molecules under study (unless carrying out hydrogen−deuterium exchange or NMR, X-ray crystallography, etc.). In this way, ion mobility (IM) hyphenated with mass spectrometry and computational chemistry support has made possible the elucidation of three-dimensional structures even for highly complex samples or for low-concentration analytes.

The present introduction will review the main advances carried out in ionisation techniques, instrumentation and processing tools for the analysis of highly complex samples.

4.1.1 Ionisation techniques and mass analysers

Ionisation is the starting point for the mass spectrometric analyses and determines the scope and utility of the method. On the basis of the energy transferred from the ionisation source to the analyte, ionisation techniques can broadly be grouped into high and low energy (hard and soft respectively) modes. Hard ionisation techniques such as electron impact ionisation (EI) occurs under vacuum and heavily fragments a compound by creating high energy electrons (70 eV) that interact with the analyte by ionising it and transferring an excess of energy, which later results in its fragmentation. On the other side, soft ionisation usually occurs at atmospheric pressure conditions, also called atmospheric pressure ionisation (API) techniques. API source types include electrospray (ESI), atmospheric pressure chemical ionisation (APCI) and atmospheric pressure photoionisation (APPI) are the most representative ionisation sources for the coupling of liquid chromatography to mass spectrometry. Other ionisation techniques based upon desorption phenomena such as fast atom bombardment (FAB) [34–36], matrix assisted laser desorption ionisation (MALDI) [37–41], secondary ion mass spectrometry (SIMS) [42,43] and desorption electrospray (DESI) [44,45] and have exponentially received an increasing interest and the applications have expanded into a wide variety of scientific fields such as environmental studies [34,36,44,45], metabolomics [37,38], proteomics [40,41,43] and all related "*-omics*" sciences. In the present thesis, electrospray has been, by far, the ionisation source mostly employed for the detection and characterisation of transformation products generated after TiO_2 photocatalysis of drugs of abuse. However, since these generated TPs may have different chemical characteristics, APCI was also used to investigate wherever these generated TPs could be better ionisable by APCI than ESI.

4.1.1.1. Ionisation techniques

Electrospray (ESI) is, by far, the API technique most used for the coupling of liquid chromatography to mass spectrometry. It enables the ionisation of non-volatile molecules of different polarities, ranging from mild to high polarity compounds. Moreover, its ionisation mechanism enables the detection of high molecular weight molecules, up to MDa, thanks to the generation of multiple charged species if the molecule (or macromolecule) contains enough active sites prone to be ionisable.

The ionisation in electrospray occurs in the liquid phase where the analyte might be present in its protonated or deprotonated molecular specie via acid/base equilibrium.

After the application of a high electric field by applying a potential difference of 2-6 kV between the capillary and the counter-electrode, droplets are enriched in either positive or negative charge, depending on the polarity mode employed. Two mechanisms have been proposed (still under discussion) to explain the formation of gas-phase ions from charged liquid droplets: the ion evaporation model (IEM) proposed by Iribarne and Thomson [46] and the charged residue model (CRM) proposed by Dole *et al.* [47]. The first model considers that the formation of gas-phase ions is the result of direct ion emission from the droplet after repeated solvent evaporation. This is possible when the radii of the charged droplets decreases up to 10 nm or less, point where the electric field strength at the surface of the droplet becomes great enough (Rayleigh limit) to push ions out of the droplet. The charged residue model assumes that gas-phase ions are formed after continuous droplet evaporation. This solvent evaporation is repeated until the analyte is left with the same charge the droplet initially carried with it.

Regardless, the ESI mechanism produces mass spectra with little or no fragmentation through the ionisation process, mainly generating the $[M+H]^+$ and $[M-H]^-$ ions although *in-source* fragmentation can be observed for more labile compounds. Electrospray is the API source most susceptible to suffer from ion suppression or ion enhancement effects [48–51]. These drawbacks of ion efficacy are usually the result of the addition of additives to the mobile phase, with coeluting compounds or matrix effects which are in constant competition with the analyte of interest to reach the gas-phase. Moreover, these inconveniences can be magnified with the ability of the analyte to form adducts with the ions present in the mobile phase, such as sodium, ammonia, acetate, etc. which would result in the decrease of the quasimolecular ions $[M+H]^+$ or $[M-H]^-$. All these phenomena need to be taken into consideration during the method development process since its underestimation would evoke into quantitation mistakes if it is not adequately corrected. Because of the ESI nature, a well-controlled electrochemical cell, analytes can experiment electrochemical processes during the electrospray ionisation [52,53]. The compounds amenable to experiment such processes typically have redox potentials ranging from -0.8 to 1.0 V. Hence, these compounds can be observed as radical cations and anions in the positive and negative ion modes respectively.

Contrary to electron ionisation, this lack of fragment ions in the ESI mechanism makes it necessary to use of with tandem mass spectrometers to obtain structural evidences of the analytes of interest.

Atmospheric pressure chemical ionisation (APCI) represents an alternative to electrospray ionisation when coupling liquid chromatography to mass spectrometry [54–58]. APCI can generate ions from neutral molecules, thus, being able to achieve the ionisation of relatively mild to low polarity compounds eluting from a liquid chromatograph. In contrast to ESI, the ionisation in APCI occurs in the gas-phase via ion-molecule reactions after the application of a high voltage to a sharp tip of a needle (also called corona discharge) mounted in front of the mass analyser inlet. This corona discharge, by electron ionization, generates primary ions, typically $N_2^{+\bullet}$ or $O_2^{+\bullet}$ which initiates a cascade of gas-phase ion-molecule reactions with the mobile phase species. The interaction of these primary radical ions with the vaporised solvent molecules produces secondary reactant gas ions. These secondary ions latter interact with the analyte (*via* proton transfer, proton abstraction or adduction) causing the final generation of the analyte ions. One advantage of APCI over ESI is that it is less likely to suffer from having drawbacks coming from ion suppression/enhancement due to matrix effects or coeluting compounds. However, in contrast to ESI, APCI is prone to suffer from *in-source* fragmentation due to the higher energy involved in this mechanism. The potential applied to the corona discharge pin and the high temperature applied in the vaporizer chamber can have a significant effect on the *in-source* fragmentation patterns, which makes it crucial for optimal modulation of it. High voltages promote undesirable fragmentation in the source while too low voltages usually lead to poor ion extraction.

4.1.1.2. Mass analysers

In addition to ionisation sources, mass analysers constitute the heart of the mass spectrometer which greatly determines the selectivity and sensibility of the analysis to be performed. Mass analysers can be classified in three main groups: 1) low resolution (unitary resolution) such as quadrupoles (Q) and ion traps (IT); 2) high-resolution mass spectrometers such as time of flight (ToF), magnetic sector (B), ion cyclotron resonance (ICR) and orbitrap and 3) hybrid mass spectrometers, instruments consisting of the combination of different types of mass analysers connected by ion-guiding devices, thus, making possible to unify the strongest characteristics of each individual mass analyser.

The quadrupole (Q) mass analyser is the mostly employed instrument for routine analysis. Quadrupoles consists of four parallel and cylindrical rods to which direct current (DC) and radio frequency (RF) voltages are applied. The modulation of DC and RF voltages permits ions to follow a stable trajectory between these rods (prior to reaching the detector), or strike the rods, resulting in ion losses. The advantages of such instruments are their high ion-transmission, their high-speed mass scan, their relatively inexpensive cost and their robustness. However, the use of single quadrupoles mass analysers coupled to API sources in LC-MS has been gradually decreasing due to the poor structural information that can be obtained. In this sense, triple quadrupoles instruments covered the gap, introducing a second quadrupole acting as the collision chamber and a third quadrupole mass analyser for the analysis of product ions (tandem mass spectrometry in space). Still in low resolution, in ion trap (IT) mass analysers, ions are trapped and can therefore be accumulated over time in a three electrodes device (1 ring electrode and 2 end-cap electrodes). These instruments are characterised for being able to perform multistage fragmentation (MS^n, tandem *in-time*) with unmatched sensitivity and fast data acquisition. Classical ion trap devices have been gradually replaced by linear ion traps (LIT) with higher ion-trapping capacities. This feature has expanded the dynamic range and the overall sensitivity of these instruments. Even though all the advantages ion traps may have, these instruments operate at unitary resolution making difficult to discriminate between coeluting isobaric compounds.

In this way, high-resolution mass spectrometers can measure *m/z* values with a precision up to 0.0001 Da [59], thus, solving the problem above mentioned. In this sense, the ToF mass analyser has been and still is one of the major representatives in the field of high-resolution in LC-MS. Although in its beginnings the resolution offered by these instruments was limited, the performance of ToF analysers, in terms of resolution and mass accuracy, has greatly improved [59–61]. This has been possible by the introduction of orthogonal acceleration [61–63], that is, ions being extracted in the orthogonal direction of the original ion beam, and reflectrons [64,65], correcting the dispersion in kinetic energy of ions and increasing the path ions have to travel. In this way, ToF mass analysers can routinely achieve resolving powers between 10,000 FWHM (*full width half maximum*) and 60,000 FWHM [59]. However, in order to correct the drift mass and acquire the data with an acceptable mass accuracy (<5 ppm) on these instruments, the continuous infusion of a standard during the analysis is still needed (lock mass). Even though the continuous development of mass spectrometers, achieving higher resolution powers, ion cyclotron resonance combined with Fourier transform mass spectrometry (ICR-FTMS) is still the mass spectrometer with highest resolution available in the market, being able to achieve mass resolution of more than 3,000,000 at *m/z* 245 [66]. The ICR-FTMS traps ions in a Penning trap where they are excited at their resonant frequencies. These oscillating charged ions induce a charge on a pair of electrodes which, after performing a Fourier Transform, are finally used to obtain a mass spectrum. Due to its elevated purchase and maintenance prize, the FT-ICR mass spectrometer is generally employed in specific applications usually related to proteomics [67,68] (main application field), metabolomics and petrolomics [69,70].

The development of the Orbitrap mass analyser by Makarov in 2000 [71], has made high-resolution mass spectrometry accessible to a wide number of analytical laboratories working in a wide range of research fields. The Orbitrap is an electrostatic ion trap that uses the Fourier transform to obtain mass spectra. An outer barrel-like electrode, cut in two equal parts with a small interval, is coaxial with the inner spindle-like electrode. Ions are injected tangentially through the interstice between the two parts of the external electrode. An electrostatic voltage of several kV (negative for positive ions) is applied to the central electrode, while the outer electrode is at ground potential. Ions are injected with a kinetic energy and start to oscillate in the trap in intricate spirals around the central electrode under the influence of the electrostatic field. *m/z* values are then measured from the frequency of harmonic ion oscillations along the axis of the electrostatic field. This instrument routinely achieves resolutions of 140,000 FWHM (*m/z* 200) (up to 1,000,000 FWHM [72]) but with a limited acquisition rate. Other important features of this instrument are: large space charge capacity, high mass accuracy (<2–3 ppm), an *m/z* range of at least 6000 and high stability and sensitivity. Even though the Orbitrap is based on the ion trap technology, it does not have MS^n capabilities. This instrument, however, accounts with a dissociation cell, also called HCD (Higher-energy Collisional Dissociation), which permits the fragmentation of all ions arriving to the mass spectrometer (all-ion fragmentation).

4.1.1.2.1. Hybrid mass spectrometers

As mentioned before, the goal of a hybrid instrument is to combine different performance characteristics offered by various types of mass analysers into one mass spectrometer. These performance characteristics may include mass resolving power, the ion kinetic energy for collision-induced dissociation and speed of analysis. Since the use of API gives little or no fragmentation (unless *in-source* fragmentation), it is of special interest to obtain evidences on the structural information of the molecules via tandem mass spectrometry.

Contrary to the IT, which is able to perform the tandem MS *in-time*, two mass analysers are needed to perform tandem mass spectrometry *in-space*. Triple quadrupoles (QqQ) and quadrupole-ion trap (Q-TRAP) are examples of hybrid mass spectrometers operating at unitary resolution. In between the main two quadrupoles or the quadrupole – ion trap, a collision cell is installed to promote the fragmentation of the precursor ion, previously selected in the first mass analyser. The multiple reaction monitoring (MRM) acquisition mode is of special interest for quantitation purposes: the precursor and product ions are continuously monitored in the first and the third quadrupole respectively. These instruments can also be operated in the scanning mode for *non-target* analysis (product ion scan, precursor ion scan and neutral loss) but its sensitivity is dramatically reduced.

Nowadays, the Q-ToF, the Q-Orbitrap and the IT-Orbitrap are the most implemented hybrid instruments. These instruments consist in a low resolution mass analyser, which act either as an ion guide or as a precursor selector, coupled to a high-resolution mass spectrometer (Orbitrap or ToF) which analyses molecular ions (or product ions) with a mass accuracy lower than 5 ppm. The main potential of these instruments is the *non-target* analysis due to their high sensitivity in the full scan mode and their ability to conduct tandem experiments at the same time (further discussed in **section 4.1.1.3**). Moreover, with the continuous development and optimisation of digital detectors, the linearity and sensitivity offered by these instruments is optimal in order to carry out quantitation experiments even at very low concentrations (parts per trillion – parts per billion range), achieving detection and quantification limits which were usually offered by triple quadrupoles instruments in MRM mode.

There is no doubt on the advantages high-resolution mass spectrometry and hybrid mass spectrometers has brought to the scientific community, achieving enhanced detection and identification in such a wide number of research fields, already discussed in the present introduction. However, these techniques offer limited structural evidences, especially when isobaric compounds co-elute and share the same (high-resolution) tandem mass spectra. In this way, ion mobility separation coupled to mass spectrometry has emerged as a new analytical platform to overcome these existing limitations of "conventional" mass spectrometry instruments. The present introduction will review the fundamentals of this technique, applications, collisional cross-section (CCS) theoretical calculations and current instrument configurations under research.

4.1.1.2.2. Ion mobility

Ion mobility (IM) has emerged as a powerful analytical platform for enhanced separation of complex mixtures. This technique is especially valuable when coupled to a hyphenated technique such as liquid or gas chromatography and mass spectrometry, adding an extra separation dimension and increasing peak capacity. In this way, such a wide number of publications have appeared in the field of metabolomics [73–76], proteomics [77–80], environmental analysis [81–84], etc.

The physical basis of this technique is rather simple: once ions enter the drift/mobility chamber, they are accelerated by means of an applied electric field but decelerated by a buffer gas contained in the mobility chamber (typically He or N_2). In this way, ions reach a characteristic velocity and the time they take to pass through the mobility cell is measured, also known as drift time (t_D). This measure depends on the length of the drift tube (l_D), the electric field applied (E) and the mobility of a given ion (K) **(Equation 4.1).**

$$t_D = \frac{l_D}{KE} \qquad \textbf{Eq. 4.1}$$

K is the mobility coefficient, depending on the mass and shape of the ion and the type of gas, its structure, its electric properties and the temperature and the pressure of the system. Since K depends on such experimental parameters described before, reduced mobilities (K_0) are often reported, as illustrated by **Equation 4.2**:

$$K_0 = \frac{l_D}{t_D E}\frac{P}{760}\frac{273.2}{T} \qquad \textbf{Eq. 4.2}$$

where P and T are the pressure (in Torr) and temperature (in Kelvin) of the buffer gas. Reduced mobility can be related to collisional cross-section through **Equation 4.3.**

$$K_0 = \frac{(18\pi)^{1/2}}{16}\frac{ze}{(k_B T)^{1/2}}\left[\frac{1}{m_I}+\frac{1}{m_B}\right]^{1/2}\frac{1}{N}\frac{1}{\Omega} \qquad \textbf{Eq. 4.3}$$

where ze is the charge on the ion, k_b is the Boltzmann constant, T, the temperature, m_I and m_B the reduced masses of the ion and the buffer gas respectively, and N, the neutral number density of the buffer gas. Hence, combining Equations 4.2 and 4.3, the collisional cross section of an ion can be calculated using **Equation 4.4**:

$$\Omega = \frac{(18\pi)^{1/2}}{16}\frac{ze}{(k_B T)^{1/2}}\left[\frac{1}{m_I}+\frac{1}{m_B}\right]^{1/2}\frac{t_D E}{l_D}\frac{760}{P}\frac{T}{273.2}\frac{1}{N} \qquad \textbf{Eq. 4.4}$$

Hence, it can be easily noted that the mobility of an ion is proportional to the inverse of their collision cross section (CCS, Ω) and directly proportional to the charge of it. One of the main drawbacks of this technique is the ability to predict these CCS values from a molecular structure. This experimental CCS is the momentum transfer collision integral Ω_{avg} averaged over all possible ion collision geometries defined by the angles θ, ϕ and γ and the scattering angle χ (the angle by which the gas is deflected after its collision with the ion), all included in **Equation 4.5**.

Eq. 4.5

$$\Omega_{avg} = \frac{1}{8\pi^2}\int_0^{2\pi} d\vartheta \int_0^{\pi} d\vartheta \sin\vartheta \int_0^{2\pi} d\gamma \frac{\pi}{8}\left(\frac{\mu}{k_B T}\right)^3 \int_0^{\infty} dg\, e^{-\frac{\mu g^2}{2k_B T}} g^5$$

$$x \int_0^{\infty} db\, 2b(1-\cos\chi\,(\vartheta,\gamma,\phi,g,b)$$

Hence, different algorithms have been developed and implemented for this purpose: the trajectory method (TM), the exact hard-sphere scattering (EHSS), the projection approximation (PA), the projection superposition approximation [85,86] and scattering on electron density isosurfaces [87]. The first three methods have been implemented in the Mobcal distribution and hence, will be shortly reviewed in the present introduction.

4.1.1.2.2.1. CCS calculation

Trajectory method

The trajectory method (TM) obtains a calculated CCS value by averaging over all possible collision geometries between the buffer gas and the ion. This is achieved evaluating the effective potential of the ion (using a 12-6-4 potential Lennard-Jones potential), **Equation 4.6**.

Eq. 4.6

$$\phi(\vartheta,\gamma,\emptyset,g,b) = 4\epsilon\sum_{i}^{n}\left[\left(\frac{\sigma}{r_i}\right)^{12} - \left(\frac{\sigma}{r_i}\right)^{6}\right] - \frac{\alpha}{2}\left(\frac{ze}{n}\right)^{2}\left[\left(\sum_{i}^{n}\frac{x_i}{{r_i}^3}\right)^{2} + \left(\sum_{i}^{n}\frac{y_i}{{r_i}^3}\right)^{2} + \left(\sum_{i}^{n}\frac{z_i}{{r_i}^3}\right)^{2}\right]$$

where ϵ is the well depth and σ is the distance where the potential becomes positive. α is the polarizability of the drift gas and n is the number of atoms in the ion. The term 12-6 from equation 4.6 represents the Van der Waals interactions between the buffer gas and the ion while the rest of second half of **Equation 4.6** the charge-induced dipole interaction.

Exact hard spheres scattering

The exact hard spheres scattering (EHSS) assumes that both the ion and the buffer gas behave as hard spheres. Hence, this method determines the scattering angles resulting from their interactions, as depicted by **Equation 4.7**.

$$\Omega = \frac{1}{4\pi}\int_{0}^{\pi} d\emptyset \sin\emptyset \int_{0}^{2\pi} d\gamma\Omega_{dir}(\emptyset,\gamma)$$

Eq. 4.7

$\varnothing$, and γ are the spatial angles defining the ion orientation and Ω_{dir} is the corresponding directional cross section, being calculated as **Equation 4.8**.

$$\Omega_{dir} = \int_{-\infty}^{+\infty}\int_{-\infty}^{+\infty} 1 - \cos\chi\ (\varnothing,\gamma,\mathrm{y},\mathrm{z})\ \mathrm{dydz},$$

Eq. 4.8

Projection approximation

The projection approximation (PA) calculates the CCS by rotating the ion through all the possible orientations. The projection onto the y-z plane is calculated as shown in **Equation 4.9**.

$$\Omega_{dir} = \int_{-\infty}^{+\infty}\int_{-\infty}^{+\infty} M\ (\varnothing,\gamma,\mathrm{y},\mathrm{z})\ \mathrm{dydz},$$

Eq. 4.9

where M is equal to 1 when a collision occurs for the configuration defined by $\varnothing,\gamma,y,z$. If not, M is equal to 0.

Amongst the three implemented methods in the Mobcal code, the TM is the most suitable for CCS prediction but is the most computationally expensive whereas the PA is the most computationally simple and serves as a first calculation estimation.

4.1.1.2.2.2. Instrumentation

Different kind of ion mobility instruments can be found described in the literature: drift tube IM (DTIMS) [88–90]; travelling wave IM (TWIMS) [91–94]; trapped IM (TIMS) [95]; high-field asymmetric ion mobility spectrometer (FAIMS) [96–98]; Circular IMS [99,100]; transversal modulation ion mobility (TMIM) [101–103] and overtone mobility spectrometry (OMS) [101–103]. All these ion mobility techniques are based on various and different principles, especially designed and optimised for different applications. It is worth noting that not all these IM devices are coupled to a mass spectrometer, with the exception of TWIMS, which is always coupled to a ToF mass analyser. Due to the fact that the experimental section of the present thesis has been carried out with two instruments based on the travelling wave ion mobility technology (Synapt G2-Si and Vion, both commercialised by Waters Corp.) and a prototype circular ion mobility device (Waters, Corp.), the present introduction will review the advances done in these instruments.

Travelling wave ion mobility

Travelling wave ion mobility mass spectrometers were first commercialised by Waters Corporation with the release of the Synapt G1 in 2006. Since this initial release, Waters Corporation has launched to the market a number of instruments releases including, the Synapt G2-Si High Definition Mass Spectrometer, in 2009. Moreover, in 2015 the Vion™ IMS Q-ToF™ Mass Spectrometer was released at the 63rd conference of the American Society for Mass Spectrometry (ASMS), a completely renewed instrument incorporating new advances done in the ToF technology and ion optics. A representation of both instruments is illustrated in **Figure 4.1 and Figure 4.2.**

In TWIMS, ions are guided through the mobility cell using a stacked ring ion guide (SRIG). Travelling waves are generated by raising the direct current (DC) voltage on selected, periodically spaced electrodes and then moving the potential along the ring electrodes. Moreover, radio frequency (RF) voltages are used through this ion guide to radially confine ions, preventing them from radial diffusion. This kind of ion mobility separation has two key parameters that can significantly improve the instrument performance: the velocity and height of the traveling wave. Due to the fact that ion trajectories through this mobility cell have not been fully elucidated, CCS values cannot be directly measured from the drift time of the analyte, as would be done in conventional drift tube ion mobility cells. Hence, CCS are derived through instrument calibration against molecules whose CCS are well known.

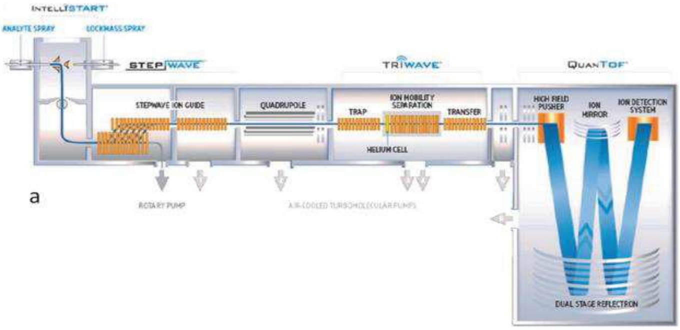
INTELLISTART
ANALYTE SPRAY
LOCKMASS SPRAY
STEPWAVE
TRIWAVE
QUANTOF
STEPWAVE ION GUIDE
QUADRUPOLE
TRAP
ION MOBILITY SEPARATION
TRANSFER
HELIUM CELL
HIGH FIELD PUSHER
ION MIRROR
ION DETECTION SYSTEM
a
ROTARY PUMP
AIR-COOLED TURBOMOLECULAR PUMPS
DUAL STAGE REFLECTRON

Figure 4.1. Scheme of the Synapt G2-Si High Definition Mass Spectrometer. *Reprinted with permission from Waters Corporation*.

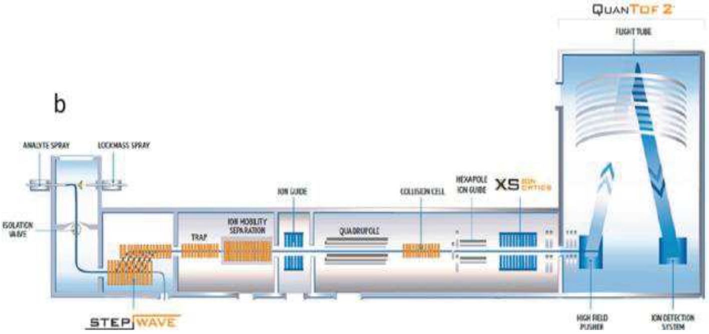
QUANTOF 2
FLIGHT TUBE
b
ANALYTE SPRAY
LOCKMASS SPRAY
ISOLATION VALVE
ION GUIDE
COLLISION CELL
HEXAPOLE ION GUIDE
XS ION OPTICS
TRAP
ION MOBILITY SEPARATION
QUADRUPOLE
STEPWAVE
HIGH FIELD PUSHER
ION DETECTION SYSTEM

Figure 4.2. Scheme of the Synapt G2-Si High Definition Mass Spectrometer. *Reprinted with permission from Waters Corporation*.

An interesting feature implemented in these instruments was the incorporation of short ion guides before and after the TWIM cell enabling ion fragmentation. The fragmentation done before the TWIM cell enables the study of the mobility of productions derived from the parent compound. Fragmentation completed after the cell, shows all the product ions to have the same mobility as the parent compound. This latest acquisition mode is especially useful when acquiring at the same time the full-scan and tandem mass spectra, since it enables the fast correlation (or match) of the parent compound and its fragment ions.

Cyclic ion mobility

Resolution is defined by the length of the TWIM cell in the two devices described above. One of the ways by which resolving power can be improved in an ion mobility device is increasing the length of the mobility chamber. Hence, a solution for not increasing the instrument size is to guide ions through a circular ion chamber **(Figure**

4.3). In order to achieve a stable ion motion trough the cyclic chamber, the electric field applied is varied with the motion of the ions, ensuring different passes or loops of motion. In this way, resolving powers of 200 and 1000 have been reported for some specific applications.

One practical difficulty of cyclic ion mobility comes from the differentiation of overlapping ions after passing through the chamber a different number of times. For instance, if ion X travels through the cyclic chamber two times faster than ion Z, ion X will travel twice the chamber length in the same time it does ion Z, finishing their flight in the same space point.

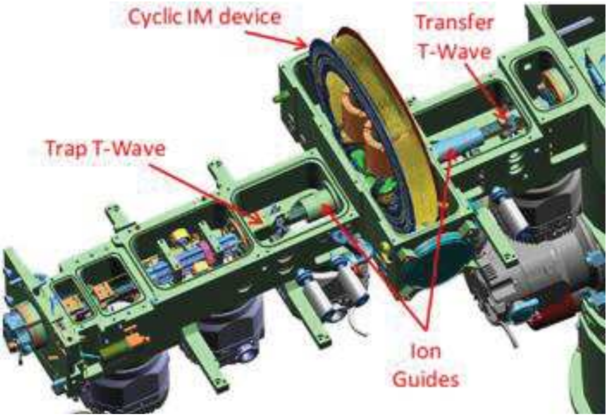

Figure 4.3. IMS-MS with a circular drift tube. Reprinted with permission from *Kevin Giles (Waters Corporation).*

Hardware developments done to instrumentation have been accompanied with new acquisition methods expanding the applicability and versatility of mass spectrometers. Hence, the next section will be devoted to review the acquisition methods the mass spectrometrists have within reach.

4.1.1.3. Targeted *versus* non-targeted analysis

Tandem mass spectrometry has been widely used in different research areas in order to obtain structural information of particular molecules of interest. Depending on prior available information, different MS/MS acquisition modes might be adopted in order to obtain such structural evidences. Nowadays, the acquisition of tandem mass spectra can be divided into targeted and non-targeted modes of operation, depending on the previous knowledge of the analytes under investigation. Targeted acquisition is usually conducted in *Multiple Reaction Monitoring* (MRM) and can also be extended to three *semi-targeted* modes of operation: precursor ion scan, product ion scan and neutral loss scan. These three methods offer limited structural information of the analytes under study but still are not able to resolve isobaric interferences. On the other side, untargeted analysis is usually divided into three modes of operation: full-scan (with or without fragmentation), data-dependant and data-independent analysis (DDA and DIA respectively), which continuously acquires the full scan and tandem mass spectra.

The data-dependent acquisition (DDA) approach is one of the most common strategies adopted for the fast identification of unknown compounds or protein modifications [104–106]. Suspect ions in a full scan spectrum (MS^1) are sequentially selected and isolated, on the basis of a predefined threshold to generate the tandem high-resolution spectra (MS^2), as depicted by **Figure 4.4**. However, DDA technology suffers several limitations [107,108]: not all precursor ions are able to be readily isolated and fragmented in one experiment, and random selection of precursor ions cannot ensure reliable quality of the generated tandem spectra and selected precursor ions may be derived from adducted ions and/or in-source fragments instead of molecular ions.

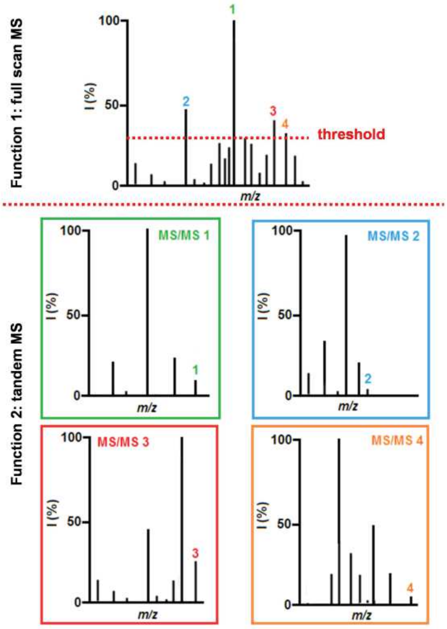

Figure 4.4 Schematic representation of the DDA workflow.

In order to overcome these mentioned limitations, an alternative workflow, data independent acquisition (DIA), has been introduced in commercial instruments such as

MS^E (Waters), SWATH (SCIEX) and has been extensively implemented for proteomics and metabolomics [8,104,109–112].

The DIA approach cycles through the whole mass range in segments of predetermined isolation windows, at each segment producing one multiplexed MS^2 spectrum derived from multiple precursor ions.

Therefore, DIA strategy enables a continuous and unbiased acquisition of both MS^1 and MS^2 ions in time and ion intensity, and increases the dimensionality of data relative to DDA approach, in which MS^2 spectra are recorded only at selected time points **(Figure 4.5).** In addition, the large isolation window in DIA increases transmission efficiency and abundance of the fragment ions, thereby improving the MS^2 spectrum sensitivity. However, compared to the mentioned approaches, the loss of the direct link between a precursor ion and their fragment ions in multiplexed MS/MS spectra makes the subsequent data analysis non-trivial. Despite all the numerous advantages that modern mass spectrometers, especially those with high-resolution capabilities, have brought to our daily routine, instrumentation and the acquisition of the full and tandem mass spectra just represents the tip of the iceberg for the mass spectrometrist. Since tens of thousands of *m/z* signals, defined by their retention time and intensity, can be measured and detected in a single chromatographic run, the key issue in modern mass spectrometry is the analysis of all generated data.

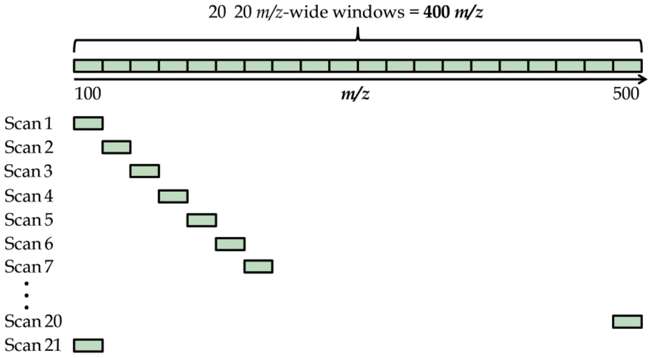

Figure 4.5. Schematic representation of the DIA workflow.

The complexity of generated data sets makes impractical their manual comparison. It is for this reason that the development of informatics tools capable of handling such large amounts of data has driven the attention of a wide number of independent research groups as well as mass spectrometry manufacturer's informatics department.

4.1.1.4. Processing tools

Several freely available software tools have been developed and successfully implemented such as MzMine [23,24], Skyline [10], XCMS [12,113–115], MetaQuant [116] and METIDEA [117]. MS manufacturers have also been developing commercially available tools, such as MetaboLynx, UNIFY and MarkerLynx (Waters), Sieve and Compound Discover 2.0 (Thermo Fischer Scientific) and Masshunter (Agilent). Despite of the fact that most of the available tools to date have been developed towards their implementation to the metabolomics and proteomics fields, they can be easily adapted and used to all kind of studies dealing with mass spectrometry data. All these platforms share several features and data processing steps such as peak picking, chromatogram deconvolution, peak alignment, peak deisotoping, etc. Most of the mentioned software packages have also included different tools to carry out statistical analysis: principal component analysis (PCA), heat maps, cluster analysis, etc. and direct access to reference libraries such as MassBank [118], METLIN [119] and NIST [120]. All published data treatment workflows generally comprise two major steps: data pre-processing and data post-processing. The objective of the first one is to convert the instrumental raw data to an annotated matrix composed of *m/z* ions, retention times and intensities while data post-processing refers to the statistical analysis and chemical interpretation of processed data.

4.1.1.4.1. Data pre-processing

Pre-processing steps are usually composed of several operations by which multiple algorithms have been especially described and further detailed below. In the present thesis, the freely available MzMine 2 software was used to carry out the mentioned pre-processing steps.

1) (Data cleaning) and extraction of m/z features.

Data cleaning removes irrelevant signals and reduces data size. Baseline drift is a common issue in LC-MS analysis since the gradient of the mobile phase causes the chromatographic baseline to be trending up or downwards and also introduces fronting and tailing. Background correction methods have been developed to address this problem [121–124]. These algorithms reduce systematic background drift by subtracting either a reference or an estimated background intensity value from the sample chromatogram. Moreover, background ions can also be directly removed from the mass spectra when extracting the *m/z* features by selecting the ion intensity threshold by which ions are chosen or discarded. Peak detection packages can be divided in those which only use the *m/z* dimension to peak *m/z* features (VIPER [125], Open MS [125], Peplist [125], amongst others) or those which are based on the chromatographic and the *m/z* dimensions (vectorized peak detection [125]; MzMine [23,24], amongst others).

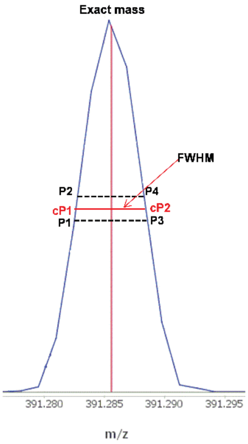

Figure 4.6. Example of the exact mass algorithm implemented in MzMine2 used within the present thesis.

Amongst the algorithms implemented in the MzMine software (centroid, exact mass, local maximum, recursive threshold, and wavelet transform), the exact mass algorithm was the most suitable for peak picking detection since one of the instrument used in this thesis was a QExactive Orbitrap. This algorithm searches for the 4 nearest data points (P1 to P4) to the peak centre at half of the maximum intensity. With these 4 points, the algorithm calculates two additional points (cP1 and cP2) of the *m/z* signal and defines the peak width. The centre of this width is the considered the exacta mass (**Figure 4.6**).

2) Generation and deconvolution of ion chromatograms;

Once the mass detection step has been conducted, the detected *m/z* features detected need to be connected in the LC dimension. MzMine and other available software automatically connect *m/z* peaks (within a mass error) over consecutive scans (minimum predefined time span) which generate, in the LC dimension, mass chromatograms. Since a single extracted chromatogram with multiple peaks can result from a single compound or from multiple compounds, peaks in the same trace need to be distinguished in case they overlap through deconvolution. Even though several algorithms have been developed in order to carry out this operation, MzMine implements 4 in its code: baseline cut-off; noise amplitude; Savitzky-Golay and local minimum search. Their performance relies on the characteristics of the raw data obtained.

The baseline cut-off is the simplest deconvolution algorithm and works by cutting off any point below the baseline level previously defined by the user. The remaining data points are measured against the subsequent LC parameters, also predefined by the user, such as minimum peak duration (minutes) and minimum intensity. The noise amplitude algorithm works similarly to the baseline cut-off, but the baseline level is applied to each chromatogram generated. This is especially useful for chromatograms with significant and variable noise levels. The Savitzky-Golay deconvolution algorithm uses the Savitzky-Golay polynomial to get the second smoothed derivative of the chromatogram intensities. As before, peak intensity and peak duration needs to be predefined by the user. Finally, the last algorithm implemented is suitable for chromatograms with Gaussian peak shapes since it detects peak local minima in order to split between chromatographic peaks. This last algorithm can also be tuned by the user by setting a threshold, retention time range and peak height/intensity.

3) Deisotoping of detected m/z signals

Deisotoping algorithms, in conjunction with the deconvolution step, have been extensively implemented in mass spectrometry experiments without prior chromatographic separation, that is, MALDI-ToF, DESI-MS, DART-MS or even flow injection analysis (FIA). These two operations are of special interest in order to deisotope signals of interest and then perform their deconvolution in order to separate species of different charge. When performing untargeted analysis, this action is not essential but simplifies much more the analysis of data since it removes (or groups) the isotopic cluster of the feature detected, thus significantly reducing the number of signals to be analysed. The deisotoping algorithm implemented in MzMine processes peaks by decreasing intensity and finds the most suitable charge for all of them. Then, considering the same charge for a cluster of peaks, the same retention time and a mass difference of ~1.0033 Da (the exact mass of one neutron is 1.008665 Da but part of this mass is consumed as energy), the software removes all ions considered to be within the isotopic cluster of the molecules of interest. Even though it would be desirable to know the chemical formula of the *m/z* peak before its deisotoping, most of algorithms implemented to date use this default mass to deisotope *m/z* clusters. In most of the cases the chemical formula is still not known at this stage of the data treatment process which, on the other side, would be the best way to calculate the isotopic distribution and proceed to the removal of *m/z* peaks attributed to the isotopic cluster.

4) Alignment of annotated features across samples.

Retention times of compounds can vary from run to run due to matrix effects, altered column conditions, pressure differences and instrumental drifts. These retention time shifts can be up to several seconds and pose a major obstacle for cross-sample comparisons. Algorithms can work on either the raw data or extracted features and group signals/features across samples by correlation, accounting for the non-linear nature of retention time deviations. As usual, both classes of algorithms have their major pros and cons. The first group of algorithms [126,127] working on the raw data search for optimal warping functions to map retention times of one experiment to that of another, thus accounting for global variation in retention times. This group, however, may fail in the alignment of individual molecules or features. The second group [128] of alignment methods use the detected feature lists, and allow some variation in the chromatographic dimension of detected signals. The major drawback of these methods resides in the inaccuracy that may result from the peak detection step. Many software platforms such as msInspect [129], SpecArray [130], and MzMine are included in the last group of aligning methods. Briefly, MzMine implements in its code two aligning methods once the features of interest have been detected: the Join aligner and the RANSAC algorithms. The first one creates a master list of peaks (features detected) by which every detected feature of the sample to be aligned is crossed against it. Then, a score is given between the feature of the master list and the sample. Those pairs of signals with better match score are finally aligned. The RANSAC aligner algorithm is an extension of the previous method described. This algorithm tries to align detected features between two samples and creates a fitted model using a non-linear regression. After its creation, this model can predict the shift in the retention time along the peak list and use the match score function (as the Join aligner method) to match features between samples. One of the key parameters of this algorithm is the number of iterations allowed. Infinite operations usually assure better quality fittings but if the matrix to be aligned is large, large processing times are required, which can result in little improvement in alignment performance.

Now that the mass chromatogram has been converted into a matrix composed of samples analysed, *m/z* values, intensities and retention times, additional operations such as mass defect, isotopic pattern filtering, etc. [131–133], can be performed to discriminate between the signals detected and those relevant for the study in progress. The term mass defect refers to the difference between the exact mass and the nominal mass of a chemical compound. The way on how the mass defect is used strongly depends on prior information available and the information to be extracted from the sample. For instance, if one plots the mass defect of *m/z* signals detected versus their corresponding nominal mass, some authors have been able to reveal homologue patterns in complex samples, for instance, hydrocarbons [132] or halogenated contaminants [134,135], such as petroleum products or environmental samples. However, in order to reveal these series of molecules (-CH_2- repetitions or replacement of hydrogen atoms for chlorine) over the thousands of peaks, it is needed to convert the IUPAC mass and mass scales (C = 12.0000 Da) to the mass scale of interest. For instance, the IUPAC mass scale can be easily converted to the Kendrick mass scale (CH_2 = 14.0000 Da) using **Equations 4.10** and **4.11** [136,137], as depicted below,

$$\text{Kendrich mass} = \text{IUPAC mass x}\frac{14.0000}{14.01565} \qquad \textbf{Eq. 4.10}$$

$$\text{mass defect} = \text{Kendrich mass} - \text{nominal mass (IUPAC)} \qquad \textbf{Eq. 4.11}$$

In a more fashioned way of applying mass defect, Zhang and co-workers [131], implemented an absolute mass defect filter to aid drug metabolite identification. Taking advantage of the observation that most metabolomics modifications to a drug changed the mass defect by less than +/-0.050 Da (relative to the parent compound), their software filter removed all *m/z* values outside of this range, eliminating potentially interfering endogenous compounds from consideration. Since then, other researchers have used mass defect to aid identifications for other compound classes in a wide range of investigations.

4.1.1.4.2. Data post-processing

Once these pre-processing steps have been performed, the chemical annotation and identification of detected signals is the key step of the overall process in non-target analysis. After that, the statistical analysis and the chemical interpretation of processed data is conducted and gives chemical sense to the overall study performed. These actions are included in the so-called post-processing steps.

Once putative *m/z* signals have been successfully extracted from the raw data, the annotation and identification of such features is of major interest. In order to confirm possible hypothesis, spectral evidences are needed by means of tandem (high-resolution) mass spectrometry, as previously described. Once discrete signals (and tandem MS spectra) have been isolated, the identification process starts by queering all data collected against databases such as MassBank [118], covering MS/MS spectra of about 4700 compounds, METLIN [119], comprising high-resolution MS/MS spectra for about 12000 compounds, and the NIST [120] mass spectral databases which includes MS/MS spectra for around 9000 compounds. Together, fewer than 30000 unique compound MS/MS spectra are available through these three major experimental libraries. Even though it is in itself a great achievement in producing these mass spectral libraries, the complete coverage of spectral libraries of all reference chemicals is far from becoming a reality. In addition to this limitation, all spectra acquired of reference compounds suffers limitation from not being obtained under standardized conditions, for example, the same MS parameters and instruments. However, *in-silico* fragmentation software and bottom-up strategies have evolved as a solution to overcome the problem of standardised conditions and spectral libraries coverage. The first one comprises software packages such as Mass Frontier (Thermo) and MetFrag [138]. These platforms help users to understand fragmentation patterns with a *top-down* approach by which the software generates all possible fragment ions from the measured tandem mass spectra. Other software such as SIRIUS [139], LipidInspector [140], LipidXplorer [141,142], mzGroupAnalyzer [143] and MzMine, however, uses the so-called *top-down* approach, which associates molecular structures or molecular formulas to unknown spectra. One major drawback of the mentioned data acquisition and treatment may come from stereoisometry, which shares the same exact mass and, in most of the cases, the same tandem (high-resolution) mass spectra.

4.2. Experimental work

As discussed in Chapter 3, titanium (IV) oxide has been used along this thesis in order to achieve the complete degradation and mineralization of four model drugs: ofloxacin (OFX), clofibric acid (CLOF), diclofenac (DCF) and ibuprofen (IBU). Before achieving complete degradation of these drugs, generation of transformation products (TPs) may occur via direct oxidation and/or reduction on the surface of the catalyst or in solution *via* reactive oxygen species (ROS) generated on the surface of the catalyst.

The present experimental work deals with the detection and characterisation of ofloxacin transformation products (OFX TPs). Since the chemical nature of these transformation products may substantially differ in comparison to the parent drug ofloxacin, different analytical techniques as well as ionisation sources have been employed for the full characterisation of OFX TPs. Moreover, targeted MS/HRMS, data dependant analysis (DDA) and data independent analysis (DIA) were evaluated in order to acquire structural information of the generated TPs. As already mentioned in the introduction of the present chapter, high-resolution mass spectrometry delivers such a vast amount of data that represents one of the limiting steps in the discovery of untargeted molecules. It is for this reason that data mining techniques, such as mass defect filtering, isotopic pattern matching amongst others, have also been adopted for the fast and reliable evaluation of high-resolution data.

Since no standards of these transformation products are commercially available, tandem high-resolution mass spectrometry and the photocatalysis of the labelled ofloxacin were used to provide structural information of these unknowns. Moreover, ion mobility coupled to tandem mass spectrometry experiments were performed in order to achieve a higher degree of confidence on the structures tentatively attributed as well as for investigating isobaric isomers formed along the photocatalytical process. Theoretical CCS calculations were finally carried out in order to confirm the structures hypothesised.

4.2.1. Materials and methods

4.2.1.1. Chemicals and reagents

Ofloxacin (OFX), ofloxacin-d_3 (OFX-d_3) and TiO_2 P25-Degussa were purchased from Sigma-Aldrich (Steinheim, Germany). LC/MS grade acetonitrile and water were obtained from Fluka (Steinheim, Germany), while formic acid (98– 100%) was purchased from Merck (Darmstadt, Germany). Individual OFX and OFX-d_3 stock solutions (1000 mg L^{-1}) were prepared in acetonitrile:water (1:1 *v/v*) and stored at −18° C. Working standards were prepared by dilution in water from the stock solution. In the Q-Orbitrap mass spectrometer, nitrogen (99.995% pure) supplied by Air Liquide (Barcelona, Spain) was used as the sheath and auxiliary gas in the API source and as collision-induced dissociation gas (CID gas) in the MS/HRMS experiments. When performing the same experiments with the IM-QToF instrument, nitrogen was used as desolvation gas whereas argon was employed as CID gas.

4.2.1.2. Photocatalysis experiments

Photocatalytic experiments with artificial irradiation were performed in a 600 mL borosilicate 3.3 photochemical reactor (Trallero&Schlee, Barcelona, Spain). Photocatalytic experiments with suspended and supported TiO_2 P25 nanoparticles (NPs) or home-made TiO_2 nanofibers (NFs), synthetized by electrospinning, were carried out as follows: 350 mL of an aqueous solution containing 10 mg L^{-1} of OFX (or OFX-d_3) and the appropriate amount of TiO_2 NPs (or NFs) was added so as to have the desirable catalyst loading (250 mg L^{-1}). The resulting suspension was loaded into the photochemical reactor and sonicated for 30 min in darkness to ensure the homogenization of the TiO_2 suspension and the complete equilibration of adsorption/desorption of the substrate on the catalyst surface. The solution was then irradiated using 4 UVA lamps of 25W (Radium Ralutec, 9W/78, 315–400 nm, λmax = 365 nm) placed around the reactor, providing a total UV irradiation at the center of the solution in the 0.8-1.1 mW cm^{-2} range. UV irradiation was measured with an UV light meter YK-35UV from Lutron (Barcelona, Spain). In photocatalytic experiments with supported TiO_2 (NPs or NFs), 10 mg of TiO_2 were supported on a glass fiber support and left at the bottom of the photochemical reactor. These experiments were carried out with 50 mL solution containing 10 mg L^{-1} OFX (or OFX-d_3), and one 25W UVA lamp (Radium Ralutec, 9W/78, 315–400 nm, λmax = 365 nm) placed above the reactor providing a total irradiance of 1.6 mW cm^{-2}. Three reference experiments were also carried out in the same experimental conditions: 10 mg L^{-1} OFX solution was maintained for 4 hours without irradiation and without catalyst; 10 mg L^{-1} OFX solution was maintained for 4 hours without irradiation but with catalyst and 10 $mg \cdot L^{-1}$ OFX was irradiated without catalyst (photolysis). Temperature was kept at 25±2ºC and the solution was stirred at 200 rpm in both set-up experiments. To follow the kinetic evolution of photoproducts, 14 samples were periodically withdrawn from the reactor: 0, 5, 10, 15, 20, 25, 30, 60, 90, 120, 150, 180, 210 and 240 min.

4.2.1.3. Sample treatment

Sample aliquots (4 mL in suspended conditions and 400 µL in supported conditions) were stored at -70 ºC until their analysis. Samples were centrifuged at 20,000g (15,000 rpm) for 15 min to remove catalyst particles in the experiments in which TiO_2 was suspended. In supported photocatalysis, no sample pre-treatment was needed, as no catalyst was leeched from the filter to the solution. Prior injection, all samples were filtered through a 0.22 µm PVDF filter (Agilent, PaloAlto, CA, USA) and diluted (1:20) with LC-MS grade water before the HPLC-HRMS analysis.

4.2.1.4. High performance liquid chromatography

High performance liquid chromatography (HPLC) was performed on an Accela HPLC system (Thermo Fisher Scientific, San José, CA, USA) equipped with a quaternary pump, an autosampler and a column oven. A BEH C18 column (100 x 2.1mm and 2.5 µm particle size; Waters, Milford, MA, USA) was used with a flow rate of 400 $\mu L \cdot min^{-1}$ and held at 40 ºC. Solvents used in the gradient elution program were H_2O (solvent A) and CH_3CN (solvent B) both acidified with a 0.1% formic acid (*v/v*) when using positive ESI and H_2O (solvent A) and CH_3CN (solvent B) when applying negative ESI. In both cases, the gradient elution program was as follows: 10% B isocratic for 1 min as initial conditions, then in 5 min solvent B was risen up to a 90% B and this mobile phase composition was held for 1 min; finally the system went back to initial condition in 1 min.

4.2.1.5. High-Resolution Mass Spectrometry

HPLC-HRMS analysis was performed in a Q-Exactive Orbitrap (Thermo Fisher Scientific, San José, CA, USA) equipped with a thermally assisted electrospray ionization source (H-ESI II). The operating parameters in positive mode were as follows: ESI voltage was 3.5 kV; capillary and vaporizer temperatures were 320 ^{o}C;

sheath gas, auxiliary gas and sweep gas flow rate were 40, 10 and 2 au (arbitrary units) respectively, and the tube lens was held at 50 V. In the negative mode, the ESI voltage was set at -2.5 kV and the rest of tune parameters were the same as in positive mode. In order to facilitate the ionisation in negative mode a 5 µL min^{-1} post column addition of NH_3 (0.25 % *v/v*) was used. For targeted tandem MS experiments (MS/HRMS), nitrogen was used as collision gas (1.5 mTorr), and the normalized collision energy (NCE) ranged from 20 to 60 % depending on the compound. The mass spectrometer was operated in profile mode (scan range, *m/z* 100-1,000) with a resolving power of 70,000 FWHM (*full width half maximum*) (at *m/z* 200) and an automatic gain control setting of 3 x 10^6 with a maximum injection time of 200 ms.

4.2.1.6. Ion mobility

Ion mobility experiments were performed in a Waters Synapt HDMS, a Vion IMS and a prototype cyclic ion mobility instrument, all of them from Waters Corporation (Wilmslow, UK). All these instruments were coupled to an UPLC I-Class instrument. The chromatographic method was the same as that described in **section 4.2.1.4**.

All experiments were conducted using electrospray as the ionisation source in the positive ion mode. A spray voltage of 0.5 kV was applied. Source and desolvation temperatures were 130 and 600 ºC respectively. Sample cone voltage was set at 30 V. Desolvation and cone gas flow were set at 1000 and 50 L h^{-1} respectively. Argon was used for collision induced dissociation (CID).

The default IMS screening parameters were: IMS T-Wave velocity ramp: started at 1000 m s^{-1} and ended at 300 m s^{-1}; IMS T-Wave Pulse Height was set at 40 V; the drift gas was nitrogen (N_2) at a flow of 90 mL min^{-1}. Data was recorded in the HDMS (high definition mass spectrometry) and HDMS^E modes. The first function uses default parameters, typically set at 6 eV to enable ion transmission to collect drift time specific precursor ion data. The second function uses an elevated-energy (collision energy ramp from 30 to 70 eV) to generate drift time specific ion mobility product ion data from mobility separated precursors.

Mass spectra were corrected by infusing a Leu-Enk solution, using the *m/z* 556.2771 signal as lock mass.

4.2.1.7. Peak extraction

The generated *raw data files were converted to *mzXML files with the MSConverter software (http://proteowizard.sourceforge.net). These files were processed using MZmine version 2.3, an open source LC–MS derived data processing software (http://mzmine.sourceforge.net/). The accurate LC–HRMS data was imported and a list of ions for each scan was generated using the exact mass algorithm. All *m/z* values under a 10% relative intensity of each full scan spectrum were discarded for further data analysis. This step might be critical if a high threshold is chosen, since low abundance candidates would be missed. For each *m/z* value that could be detected continuously over ten scans, the extracted mass chromatogram was constructed and deconvoluted. To avoid peak duplication due to the isotopic pattern, M+1 and M+2 peaks were fitted into one candidate. Chromatograms were aligned using the RANSAC algorithm implemented in MZmine2. Maximum allowed retention time difference before the alignment was set to 0.3 min. and maximum allowed retention time difference after the alignment process was set to 0.1 minutes. The software automatically calculated the number of iterations performed by the algorithm. Finally, each *m/z* extracted ion chromatogram was integrated across all samples.

4.2.1.8. Data analysis

Untargeted data treatment was processed using MATLAB 2014a (Mathworks, Natick, MA, USA) with home-made scripts. Data analysis was performed in two steps. The first step was the selection of potential TPs based on three criteria: 1) the LC-HRMS peak should be detected in two consecutive points during the kinetic experiments, 2) the peak area should be above a threshold value of 10^5 units, 3) the candidate ion should present a linear response when diluting. To check the response linearity of the different candidates, samples were diluted 10 times and 100 times. If this requirement was not accomplished, the *m/z* value was removed despite having passed the first two filters. The second step in data analysis included the evaluation of a multiple mass defect and isotopic patterns (using 3 isotopes) filters. For the selected candidates, its molecular formulae was estimated with a mass tolerance of 5 ppm within the following elemental composition ranges: $C_{(5-40)}$, $H_{(10-60)}$, $O_{(0-10)}$, $N_{(0-8)}$ and $F_{(0-3)}$.

Structural elucidation was based on the accurate mass of the selected candidates and their product ion scan (MS/HRMS). Identification of degradation products was confirmed when possible by direct comparison to on-line databases of the obtained HRMS and MS/HRMS and in-silico fragmentation prediction.

4.2.1.9. Theoretical CCS calculation

Prior to CCS calculation, all hypothesised structures were first optimised using UFF, MMFF94 and GAFF force fields implemented in the Avogadro 1.2 software package. Gaussian inputs were then generated for energy optimisation.

Structures were optimised (Gaussian 09) using B3LYP DFT function and energy minimised using the 6-31G basis set. The obtained geometry was further optimised using the 6-31G++(d,p) basis set. If the molecules hypothesised did not converge using the mentioned basis, structures were first optimised using the 6-31 G basis set, then further optimised using the 6-31G(d,p) basis and finally refined by the 6-31G++(d,p) basis set.

Partial atomic charges were determined using Mulliken, electrostatic surface potential (ESP) and natural population analysis (NPA) algorithms implemented in Gaussian computational chemistry software.

Theoretical CCS calculations were performed with the original Mobcal code, developed by Jarrold and co-workers (http://www.indiana.edu/~nano/software/) and a revised Mobcal code, gently provided upon request by Dr. Ian Campuzano. The original Mobcal code implements the TM, PA and EHSS algorithms and performs the CCS calculations using He as buffer gas. The revised Mobcal code only implements the TM algorithm but uses N_2 as buffer gas. Theoretical CCS calculations of ofloxacin were performed using both codes. The unknown structures under investigation were only calculated using the revised Mobcal code (Dr. Ian Campuzano).

All these calculations were carried out on a server equipped with two Intel Xeon X5650 processors at 2.66 GHz consisting of 6 cores each. All Gaussian calculations were carried out in parallel using 6 cores whereas Mobcal calculations were done with only one processor, since this code did not permit parallelisation.

4.2.2. Results and discussion

In this Chapter, high performance liquid chromatography coupled to mass spectrometry using both ESI and APCI have been used to identify and characterise the photocatalytic TPs of OFX. The chemical structure information obtained from tandem mass spectrometry, high-resolution mass spectrometry, ion mobility and theoretical CCS have been used for the characterization of the most important TPs to help in the understanding of the degradation pathway of OFX.

4.2.2.1. Chemical analysis of ofloxacin

First of all, the full scan mass spectrum and tandem high-resolution mass spectrum of ofloxacin was obtained using ESI and APCI in both positive and negative polarities. In the positive ion mode, both API sources showed the protonated molecular ion $[M+H]^+$ as the base peak of the mass spectrum but differed in the *in-source* fragmentation observed in the APCI ion mode, showing the loss of a neutral CO_2 molecule. As discussed in **Chapter 3**, ofloxacin shows in its MS/HRMS two main characteristic fragmentation ions: these include an ion at *m/z* 318.1610 due to the loss of neutral CO_2 (loss of *m/z* 43.9898) and the ion at *m/z* 261.1035 due to the consecutive loss of CO_2 and C_3H_7N at the pyperazine moiety, confirmed by means of a low resolution ion trap mass spectrometer. These results are in accordance with the work published by Calza *et al.* [144], which used a LIT-Orbitrap$^{(R)}$. The loss of C_3H_7N occurring at the pyperazine moiety was of special interest for the annotation of the chemical structures of generated TPs sharing the same fragment ion. In the negative ion mode, the deprotonated molecular ion $[M-H]^-$ at *m/z* 360.1365 was observed when a 0.025% NH_3 was added to a mixture of 50% *v/v* $H_2O:CH_3CN$.

4.2.2.2. Chemical analysis of irradiated samples.

In order to simplify both the data analysis process and support the structural identification of ofloxacin transformation products, the photocatalysis of the deuterated homologue, OFX-d_3 (Δm/z 3.0188), was also carried out.

Once the photocatalysis of both ofloxacin and deuterated ofloxacin at a concentration of 10 mg L^{-1}were performed, samples were analysed by LC-HRMS in the full scan mode in ESI (+/-) and APCI (+/-) ionisation modes in replicate injections as described in the experimental section. GC-MS was also carried out using EI as ionisation source. **Figure 4.8** shows the obtained TIC and extracted mass chromatograms of one irradiated sample of ofloxacin photocatalysis under P25 nanoparticles. ESI in the negative ion mode and APCI in both the positive and negative ion modes did not show any relevant chromatographic signals of interest in comparison to that presented in **Figure 4.7**.

Prior to the completion of the analysis using the established analytical method (by LC-HRMS(/MS)) samples collected at 0, 15, 30 and 60 minutes were analysed using the different approaches introduced in **section 4.1.1.3** of the present chapter, that is, full-scan (without fragmentation), all-ion fragmentation (AIF), data dependant scan (DDS) and data independent analysis (DIA). Results obtained are depicted in **Figures 4.8** and **4.9.** All of them clearly showed the vast amount of transformation products generated by the photocatalytical degradation of ofloxacin but some differences were observed in the results obtained via tandem mass spectrometry.

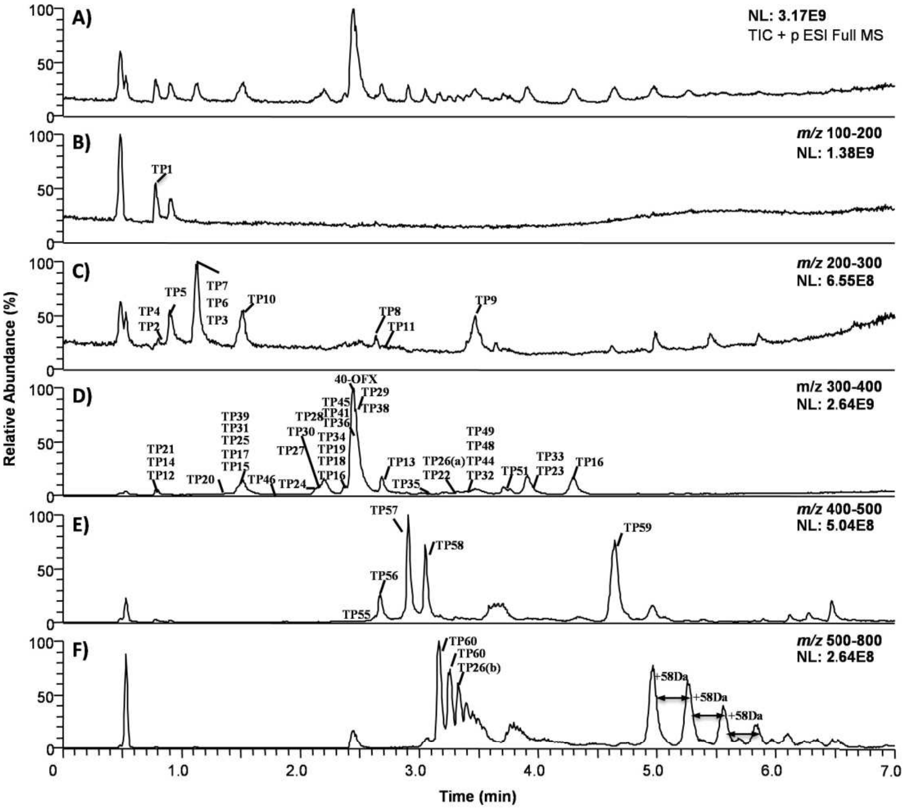

Figure 4.7. A) Total ion chromatogram in the electrospray positive ion mode m/z 100 – 1,000 is shown for a sample collected at 15 min under supported TiO_2 nanofibers; B) *m/z* 100-200; C) *m/z* 200-300; D) *m/z* 300-400; E) *m/z* 400-500 and F) *m/z* 500-800. Characteristic retention time of all TPs detected is shown in the presented chromatograms.

As expected, AIF and DIA acquisition modes did not show remarkable differences in their fragmentation mass spectra. Contrary to those targeted acquisition methods, these offered the advantage of obtaining simultaneously both the full-scan and the fragmentation mass spectra without a significant decrease of sensitivity. However, as illustrated in **Figure 4.8**, no direct link was found between the observed ions in the full scan and product ion scan, as three compounds were coeluting in the same retention time. Alternatively, the resulting tandem mass spectrum, in both acquisition modes, was the sum of the dissociation of all ions reaching the high collision dissociation (HCD) cell without prior selection of the precursor ion. Both acquisition modes clearly required the deconvolution of both full and product ion scans in order to determine a direct relationship between both precursor and product ion scans. Despite having performed these deconvolution operations, coeluting compounds made impractical the establishment of direct relationships between the full and product ion scans, thus not producing definite experimental evidence on the chemical structure of the generated TPs. DDA, however, did provide direct evidence on the preselected ions (**Figure 4.9**) but no more than one scan was found for the tandem MS. where no chromatographic points are shown (These experiments were performed using a DDA setting to select the “top five” most-abundant ions for MS/MS analysis, the threshold chosen was varied from 10 to 50 %.

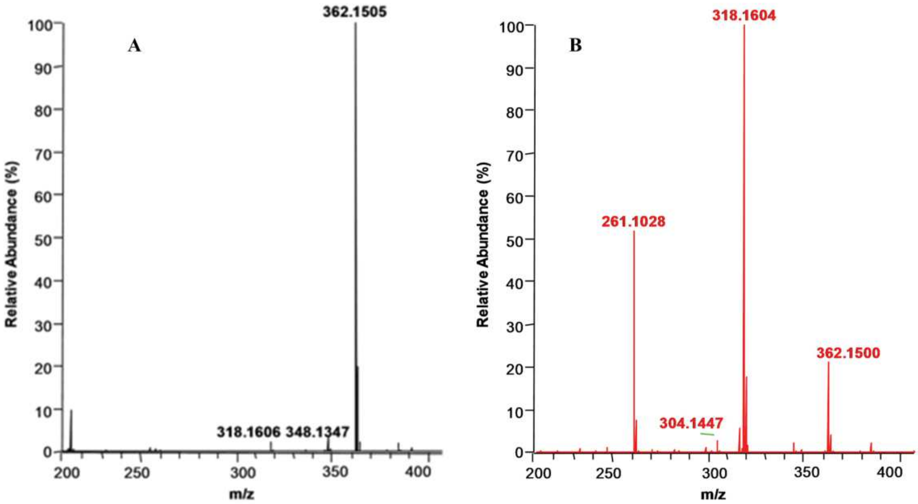

Figure 4.8. Full scan (A) and tandem high-resolution (B) spectra obtained for signal at 2.2 min retention time using AIF acquisition.

For the fragmentation of the generated TPs, the normalized collision energy was set to 25%, and one microscan was acquired for each spectrum.In order to maximise the signal, the maximum injection time was set to 300 ms for MS and to 50 ms for MS/MS. Due to the poor chromatographic resolution and the vast number of ions to fragment simultaneously, a maximum of 5 different MS/MS scans per peak were collected during each run, which negatively affected the MS/MS spectrum quality. By increasing the threshold value and the duration of the chromatographic run (up to 30 minutes), it was possible to increase the number of different MS/MS spectra (up to three times) per second with a significant improve in the quality of the mass spectra.

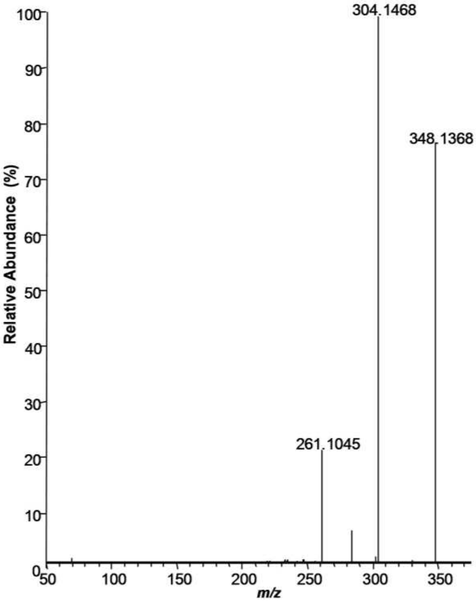

Figure 4.9. Obtained tandem mass spectrum of *m/z* 348.135using data dependant acquisition mode.

However, these changes still did not accomplish the final goal of detecting all generated TPs (previously checked by inspecting the full scan chromatographic run). These limitations observed made us reconsider the analytical workflow chosen for the detection and characterisation of OFX TPs. As described in the introduction of this chapter, the detection of unknowns is a challenging task because the ions of interest may be masked by background noise or are coeluting with other ions of interest. It is for this reason that our analytical method and research, after the injection of the sample(s) in the full scan mode (without fragmentation) started by managing the vast amount of data obtained by high-resolution mass spectrometry.

4.2.2.3. Data processing

A standard of pure ofloxacin was prepared at a concentration of 100 µg L^{-1} and injected into the LC-MS system. The *m/z* signal at 362.1510 (corresponding to the protonated ofloxacin) represented a 15% of the intensity (~10^5 intensity units) of the overall MS spectrum (full-scan) and the area below the extracted chromatogram of this standard was approximately of $5 \cdot 10^6$ area units.

The peak picking process started with the mass detection module, already implemented in the software, which selects individual ions in the mass spectrum. Amongst the algorithms available, the exact mass algorithm was chosen since it is the most suitable for high-resolution data. The critical parameter in this step is the selection of the optimum threshold by which signals are ignored or considered to be signals of interest. It is for this reason that this parameter was selected by considering the signal produced by the standard of ofloxacin and the run-to-run and day-to-day background noise observed in the instrument. Three different noise levels were tested: 10^3 units (as the minimum level); 10^5 units (as the medium level) and 10^7 units (as the upper level). Now that a matrix of *m/z* signals was constructed on the basis of the noise threshold previously selected, only those signals appearing over continuous scans which made possible the construction of chromatographic signals were of our interest. It is for this reason that the chromatogram builder package implemented in MzMine2 was used. This package constructs chromatograms for each *m/z* signal previously detected that can be connected over (at least) a pre-established period of time. This period of time was set to be 0.3 minutes which corresponds to the maximum peak amplitude observed for increasing concentrations of the standard of ofloxacin. The number of MS signals obtained in each case was of 9756; 2933; 1557 respectively for each of the mentioned cases. It is of clear evidence that managing a matrix of approximately 10,000 potential signals would represent a challenging and tedious task, favouring the inclusion of more background signals to the potential list of interest. In the latter case and even though that 1557 ions represented a great amount of signals to handle, it was considered that this scenario could favour the omission of signals that should be taken into account. It is for this reason that the threshold of 10^5 units was considered the optimum threshold to remove ions that are within the background noise of our instrument. Ion chromatograms were finally deconvoluted to ensure having one *m/z* signal per chromatographic peak.

These operations performed, however, took into account isotopes as signals to be considered as potential candidates. Allowing a maximum *m/z* tolerance of 5 mDa or 5 ppm, the algorithm implemented in MzMine searched for signals in the generated peak list that could form an isotope pattern.

The peak picking process ended by aligning all obtained signals across all samples analysed using the RANdom SAmple Consensus (RANSAC) method. This alignment corrected any linear or non-linear retention time deviation that could occur during the analysis by column bleeding, matrix interferences, etc. As explained in **section 4.2.1.7** of the experimental section, the maximum allowed retention time deviation before the alignment was of 0.3 minutes while after the correction was of 0.1 minutes. Even though the photocatalytical reaction was conducted in MilliQ water, and thus, no matrix interferences were expected, this alignment was conducted to correct little deviations caused by the instrument or HPLC column performance.

The final result was an $m \times n$ peak matrix, m was the set of samples analysed (12) and n was the set of ions detected (*m/z* values) in each sample (2497). This matrix also contained all data related to peak area and retention times. This matrix was further improved by treating this data using in-home data scripts.

The conditions imposed in **section 4.2.1.8** reduced the original matrix from 2497 signals to 227, as depicted in **Figure 4.10.A** and **4.10.B**. Even though this reduction was a great achievement, further reduction was needed to handle these 227 ions, especially because obtaining the targeted tandem spectra would be a tedious and time consuming task. In order to overcome these limitations, mass defect filters were applied.

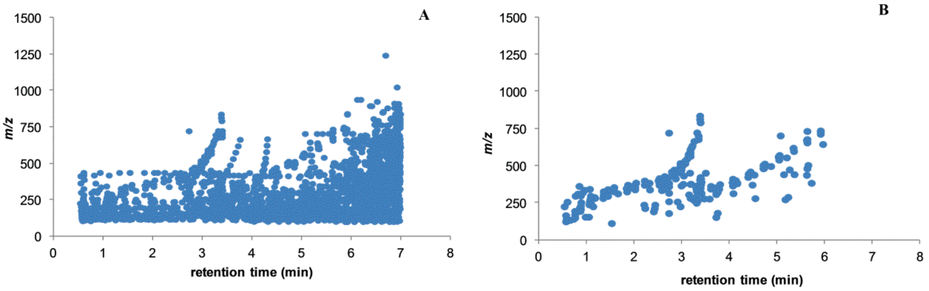

Figure 4.10. Reduction of peak signals after the peak processing step. A) original matrix; B) reduced matrix of signals.

The second step in data evaluation, which was based on the chemical structure, consisted in the application of a single (SMDF) and multiple (MMDF) mass defect filters that were developed, applied and compared using in home-scripts. The SMDF was based on the core structure of ofloxacin and common reactions that can take place during the photocatalytical process: multiple hydroxylation/dehydroxylation ($\pm n \times$ OH; $\pm\ n \times$ 2.7 mDa), CO_2 loss (10.17 mDa), defluorination (-1.6 mDa), C-C oxidations/reductions ($\pm n \times H_2$; $\pm\ n \times$ 15.66 mDa). It is for that reason that SMDF was chosen to be between 100 - 200 mDa over the mass range of 300 – 400 Da. As a result, only 35 candidates with closely related chemical structure to OFX were identified as potential TPs. Moreover, the previous inspection of the raw LC-HRMS data also revealed the presence of ions at *m/z* below 300 and over 500, in agreement to previous works reported by Hapeshi *et al.* [145,146], Michael *et al.* [147,148]. For instance, these authors reported the cleavage of the piperazine ring of OFX yielding the $[M+H]^+$ ion at *m/z* 279 and the dimerisation of the OFX molecule generating the $[M+H]^+$ ion at *m/z* 588. Hence, a MMDF was developed in order to consider TPs over the whole mass range. In addition to the SMDF (Filter #1 of the MMDF), Filter #2 was chosen to be around a mass defect of 50–100 mDa covering a mass range of 200–300 Da; Filter # 3 was chosen to be between 500–700 Da comprising a mass defect between 450–550 mDa in order to output dimers and high molecular weight structures. When the MMDF was applied, 99 OFX TPs were identified in addition to those 35 candidates obtained with the SMDF. For the best filtering performance, the MMDF had to be applied as poor results were obtained by extending the SMDF algorithm (increasing *m/z* and mass defect ranges).

After the whole process of data analysis mentioned before, this 12 × 134 matrix was further reduced by only picking up those signals appearing in OFX and OFX-d_3 photocatalysis. Every MS scan was inspected for pairs of two m/z peaks, M, which corresponded to OFX TPs, and (M + $n \times$ 3.0188 Da, being n the number of $-CD_3$ groups) which denoted OFX-d_3 TPs. The acceptance criteria for each pair of m/z peaks were a maximum mass tolerance (1 ppm) and a maximum allowed retention time of 0.2 minutes. Thus, a comprehensive list of 70 candidate ions was obtained, being reduced to 59 candidates after discarding those ions generated by both *in-source* CID and redox reactions, as it will be described in **Section 4.2.2.4**. **Table 4.1** summarises the final candidate list of OFX and OFX-d_3 photocatalysis, showing the accurate *m/z* value identified, the proposed molecular formula and its associated relative mass error (ppm).

Moreover, this list shows the most characteristic product ions, their experimental *m/z* value, associated mass relative error (ppm) and ion assignment.

4.2.2.4. Discrimination between TPs and *in-source* generated ions

Different operational conditions should be tested when conducting untargeted analysis, especially if the nature of the analytes under study is not known or has not been previously studied. In order to discard those ions originated by in-source fragmentation, adduct formation or redox reactions in the ESI source, the effect of the electrospray working conditions were studied. Two different samples submitted to the photocatalysis process with TiO_2 NPs and TiO_2 NFs were chosen for this purpose.

In-source CID fragmentation and adduct formation

The *S-lens* and *in-source* fragmentation energy are tuneable parameters that can favour *in-source* CID fragmentation. For this reason, these parameters were changed in replicated injections between 40 and 80 V and between 5 and 50 eV respectively. Two coeluting candidates of TPs detected in the positive ESI mode, m/z 360.1356 and *m/z* 378.1463, eluting at 2.50 min, were checked for the *in-source* CID fragmentation. As both candidates differ in 18.0106 *m/z* units, the ion at *m/z* 360.1356 could be attributed to the loss of a water molecule from *m/z* 378.1463 by in-source CID. Nevertheless, the ion at *m/z* 378.1463 did not show any water loss in its product ion spectrum allowing the independent assignment of both ions. Another *in-source* CID fragmentation example was found for *m/z* 318.1610, which showed two chromatographic peaks at 2.48 and 2.68 min, the last one at the same retention time of OFX. Both *m/z* signals were attributed to the carbon dioxide cleavage from ofloxacin.

The first peak (2.48 min) was attributed to a TP generated in the photocatalysis process, while the other, eluting at 2.68 min was thought to be generated by in-source CID from OFX. This hypothesis was in accordance to the MS/HRMS fragmentation pattern of OFX, which yielded a product ion due to the CO_2 loss (*m/z* 318.1610). This fact was further confirmed by increasing the CID energy, which produced simultaneously a decrease in the intensity of protonated OFX $[M+H]^+$ and an increase in the abundance of *m/z* 318.1610. In addition to the mentioned examples, 5 additional suspect ions were found to be generated via *in-source* fragmentation, all being removed from the candidate list.

Table 4.1. Detected OFX and OFX-d_3 transformation products after TiO_2 photocatalysis.

TP	Precursor ion (OFX)	MS/HRMS		Precursor ion (OFX-d_3)	MS/HRMS	Suggested chemical structure
	m/z (ppm) Ion assignment	*m/z* (ppm)	Ion assignment	*m/z* (ppm) Ion assignment	*m/z* (ppm)	
TP1	195.1229 (-1.3) $[M+H]^+$ $[C_8H_{19}O_5]^+$	177.1123 (0.9) 133.0859 (-0.2)	$[M+H-H_2O]^+$ $[M+H-C_2H_6O_2]^+$	195.1231 (2.1) $[M+H]^+$ $[C_8H_{19}O_5]^+$	177.1124 (1.5) 133.0855 (-3.1)	–
TP2	209.1018 (0.6) $[M+H]^+$ $[C_8H_{17}O_6]^+$	191.0915 (0.5) 163.0965 (0.1)	$[M+H-H_2O]^+$ $[M+H-CH_2O_2]^+$	209.1017(-1.3) $[M+H]^+$ $[C_8H_{17}O_6]^+$	191.0913 (-0.5) 163.0965 (0.7)	–
TP5	254.1600 (0.8) $[M+H]^+$ $[C_{10}H_{24}NO_6]^+$	210.1338 (1.0) 209.1387 (1.6) 163.0965 (0.1)	$[M+H-C_2H_4O]^+$ $[M+H-CH_3NO]^+$ $[M+H-C_3H_9NO_2]^+$	254.1603 (1.9) $[M+H]^+$ $[C_{10}H_{24}NO_6]^+$	210.1333 (-1.5) 209.1387 (0.3) 163.0965 (0.7)	–
TP6	261.1035 (0.4) $[M+H]^+$ $[C_{14}H_{14}FN_2O_2]^+$	241.0976 (1.8) 221.0720 (-0.4) 219.0564 (-0.2)	$[M+H-HF]^+$ $[M+H-C_3H_4]^+$ $[M+H-C_3H_6]^+$	261.1034 (0.1) $[M+H]^+$ $[C_{14}H_{14}FN_2O_2]^+$	241.0972 (0.2) 221.0720 (0.1) 219.0564 (0.8)	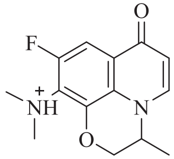
TP9	279.0776 (0.1) $[M+H]^+$ $[C_{13}H_{12}FN_2O_4]^+$	235.0877 (-0.2) 261.0671 (0.3) 153.0546 (-0.1)	$[M+H-CO_2]^+$ $[M+H-H_2O]^+$ $[M+H-C_5H_3FN_2O]^+$	279.0773 (-1.0) $[M+H]^+$ $[C_{13}H_{12}FN_2O_4]^+$	235.0875 (-1.0) 261.0671 (0.3) 153.0545 (-0.8)	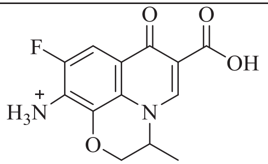
TP10	283.1756 (1.7) $[M+H]^+$ $[C_{12}H_{27}O_7]^+$	239.1492 (1.3) 237.1332 (-0.3) 177.1123 (1.1)	$[M+H-C_2H_4O]^+$ $[M+H-C_2H_6O]^+$ $[M+H-C_4H_{10}O_3]^+$	283.1750 (-0.5) $[M+H]^+$ $[C_{12}H_{27}O_7]^+$	239.1490 (0.4) 237.1332 (-0.28) 177.1120 (-0.8)	–

TP12	305.0943 (3.6) $[M+H]^+$ $[C_{15}H_{14}FN_2O_4]^+$	287.0826 (1.1) 277.0617 (-0.7) 233.0720 (-0.40)	$[M+H-H_2O]^+$ $[M+H-C_2H_4]^+$ $[M+H-C_2H_4-CO_2]^+$	305.0938 (1.9) $[M+H]^+$ $[C_{15}H_{14}FN_2O_4]^+$	287.0825 (-0.5) 277.0620 (0.3) 233.0722 (0.5)	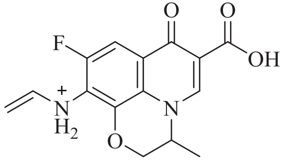
TP13	306.1083 (-0.5) $[M+H]^+$ $[C_{14}H_{16}N_3O_5]^+$	250.0824 (0.7) 248.0670 (1.6) 209.0560 (1.5)	$[M+H-C_3H_4O]^+$ $[M+H-C_3H_6O]^+$ $[M+H-C_5H_7NO]^+$	306.1084 (-0.2) $[M+H]^+$ $[C_{14}H_{16}N_3O_5]^+$	250.0821 (-0.6) 248.0668 (0.8) 209.0562 (2.5)	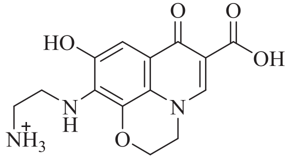
TP14	314.0668 (-0.8) $[M+H]^+$ $[C_{13}H_{13}FNO_7]^+$	296.0565 (1.7) 278.0457 (-0.8) 268.0619 (1.2) 252.0668 (0.5)	$[M+H-H_2O]^+$ $[M+H-2H_2O]^+$ $[M+H-CH_2O_2]^+$ $[M+H-CH_2O_3]^+$	314.0664 (-2.1) $[M+H]^+$ $[C_{13}H_{13}FNO_7]^+$	296.0565 (1.7) 278.0459 (-0.1) 268.0620 (1.6) 252.0668 (0.5)	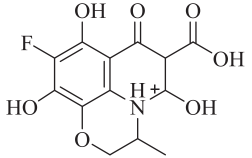
TP16	316.1452 (-1.0) $[M+H]^+$ $[C_{17}H_{19}FN_3O_2]^+$	261.1035 (0.4) 233.0722 (0.5)	$[M+H-C_3H_5N]^+$ $[M+H-C_5H_9N]^+$	319.1648 (1.21) $[M+H]^+$ $[C_{17}H_{16}D_3FN_3O_2]^+$	261.1035 (0.4) 233.0725 (1.8)	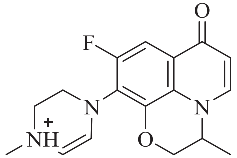
TP17	318.1610 (-0.6) $[M+H]^+$ $[C_{17}H_{21}FN_3O_2]^+$	261.1035 (0.4) 233.0722 (0.5)	$[M+H-C_3H_7N]^+$ $[M+H-C_5H_{11}N]^+$	321.1802 (0.4) $[M+H]^+$ $[C_{17}H_{18}D_3FN_3O_2]^+$	261.1035 (0.4) 233.0720 (-0.4)	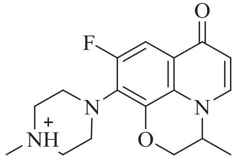
TP19	320.1242 (0.2) $[M+H]^+$ $[C_{15}H_{18}N_3O_5]^+$	276.1342 (-0.2) 277.0821 (0.7) 262.0824 (0.6)	$[M+H-CO_2]^+$ $[M+H-C_2H_5N]^+$ $[M+H-C_3H_6O]^+$	320.1240 (-0.3) $[M+H]^+$ $[C_{15}H_{18}N_3O_5]^+$	276.1342 (-0.2) 277.0821 (0.7) 262.0824 (-0.5)	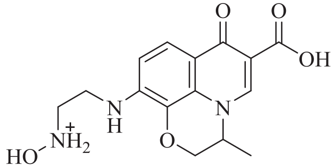

TP22	334.1194 (-1.0) $[M+H]^+$ $[C_{16}H_{17}FN_3O_4]^+$	290.1299 (-0.1) 279.0775 (-0.2) 261.1038 (1.6)	$[M+H-CO_2]^+$ $[M+H-C_3H_5N]^+$ $[M+H-CO_2-CH_3N]^+$	337.1388 (0.6) $[M+H]^+$ $[C_{16}H_{14}D_3FN_3O_4]^+$	293.1488 (0.1) 279.0775 (-0.2) 261.1036 (0.8)	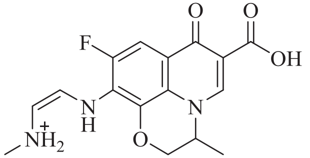
TP24	336.1354 (-0.1) $[M+H]^+$ $[C_{16}H_{19}FN_3O_4]^+$	316.1295 (1.0) 305.0938 (1.9) 292.1455 (-0.3) 279.0775 (-0.2) 261.1038 (1.6)	$[M+H-HF]^+$ $[M+H-CH_5N]^+$ $[M+H-CO_2]^+$ $[M+H-C_3H_7N]^+$ $[M+H-CO_2-CH_5N]^+$	339.1545 (0.8) $[M+H]^+$ $[C_{16}H_{16}D_3FN_3O_4]^+$	319.1484 (1.2) 305.0938 (1.0) 295.1640 (1.0) 279.0777 (0.5) 261.1036 (0.8)	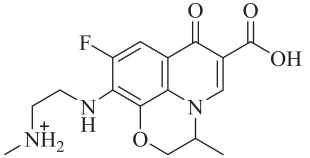
TP25	338.1511 (0.2) $[M+H]^+$ $[C_{16}H_{21}FN_3O_4]^+$	318.1444 (1.0) 307.1085 (-1.2) 294.1612 (-0.1) 279.0775 (-0.2)	$[M+H-HF]^+$ $[M+H-CH_5N]^+$ $[M+H-CO_2]^+$ $[M+H-C_3H_9N]^+$	341.1701 (0.6) $[M+H]^+$ $[C_{16}H_{18}D_3FN_3O_4]^+$	321.1634 (-0.8) 307.1091 (0.8) 297.1801 (0.2) 279.0775 (-0.2)	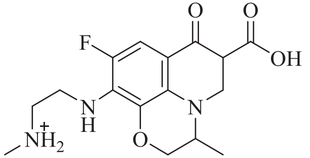
TP26	340.2595 (-0.3) $[M+2H]^{2+}$ $[C_{36}H_{68}N_6O_6]^{2+}$	566.4267 (-1.6) 453.3426 (2.1) 435.3693 (-0.1) 433.3539 (0.5)	$[M+H-C_6H_{11}NO]^+$ $[M+H-C_{11}H_{18}N_2O_3]^+$ $[M+H-C_{11}H_{20}N_2O_4]^+$ $[M+H-C_{11}H_{22}N_2O_4]^+$	340.2595 (-0.3) $[M+2H]^{2+}$ $[C_{36}H_{68}N_6O_6]^{2+}$	566.4267 (-1.6) 453.3423 (1.9) 435.3694 (0.1) 433.3538 (0.2)	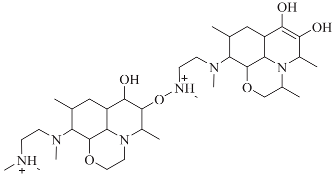
TP27	340.2595 (-0.1) $[M+H]^+$ $[C_{18}H_{34}N_3O_3]^+$	322.2491 (0.6) 227.1755 (-1.1) 209.1648 (-0.2)	$[M+H-H_2O]^+$ $[M+H-C_6H_4NO]^+$ $[M+H-C_6H_{13}NO_2]^+$	340.2595 (-0.1) $[M+H]^+$ $[C_{18}H_{34}N_3O_3]^+$	322.2490 (0.3) 227.1755 (-1.1) 209.1646 (-1.1)	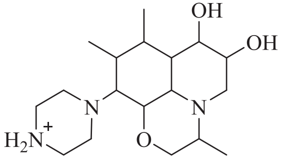
TP30	344.1609 (1.3) $[M+H]^+$ $[C_{18}H_{21}N_3O_4]^+$	330.1447 (-0.4) 261.0869 (-0.3) 245.1284 (-0.2)	$[M+H-CH_2]^+$ $[M+H-C_5H_9N]^+$ $[M+H-CO_2-C_3H_5N]^+$	347.1795 (0.5) $[M+H]^+$ $[C_{18}H_{19}D_3N_3O_4]^+$	330.1450 (0.5) 261.0871 (0.4) 245.1285 (0.2)	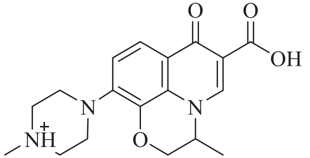

TP32	346.1202 (0.4) $[M+H]^+$ $[C_{17}H_{17}FN_3O_4]^+$	328.1092 (0.1) 302.1302 (0.9) 261.1035 (1.2)	$[M+H-H_2O]^+$ $[M+H-CO_2]^+$ $[M+H-CO_2-C_2H_3N]^+$	346.1203 (1.5) $[M+H]^+$ $[C_{17}H_{17}FN_3O_4]^+$	328.1089 (-0.9) 302.1302 (0.9) 261.1035 (1.2)	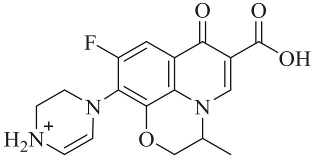
TP34	348.1354 (-0.1) $[M+H]^+$ $[C_{17}H_{19}FN_3O_4]^+$	330.1255 (1.9) 304.1459 (1.0) 261.1035 (0.4)	$[M+H-H_2O]^+$ $[M+H-CO_2]^+$ $[M+H-CO_2-C_2H_5N]^+$	348.1354 (-0.1) $[M+H]^+$ $[C_{17}H_{19}FN_3O_4]^+$	330.1255 (1.9) 304.1459 (1.0) 261.1035 (0.4)	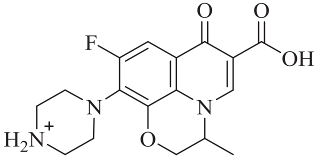
TP36	350.1146 (0.4) $[M+H]^+$ $[C_{16}H_{17}FN_3O_5]^+$	332.1041 (1.2) 306.1249 (0.2) 279.0779 (1.2)	$[M+H-H_2O]^+$ $[M+H-CO_2]^+$ $[M+H-C_3H_5NO]^+$	350.1143 (-1.0) $[M+H]^+$ $[C_{16}H_{17}FN_3O_5]^+$	332.1039 (-0.6) 306.1249 (0.2) 279.0775 (-0.2)	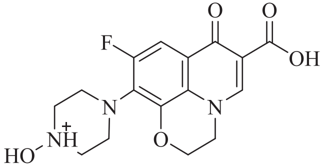
TP39	360.1356 (0.2) $[M+H]^+$ $[C_{18}H_{19}FN_3O_4]^+$	342.1259 (3.0) 316.1458 (0.7) 261.1034 (0.1)	$[M+H-H_2O]^+$ $[M+H-CO_2]^+$ $[M+H-CO_2-C_3H_5N]^+$	363.1544 (0.4) $[M+H]^+$ $[C_{18}H_{16}D_3FN_3O_4]^+$	345.1440 (0.9) 319.1648 (1.2) 261.1034 (0.1)	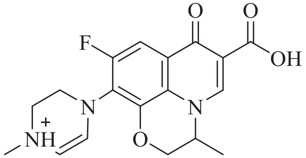
Ofloxacin	362.1510 (-0.1) $[M+H]^+$ $[C_{18}H_{21}FN_3O_4]^+$	344.1410 (1.5) 318.1612 (-0.1) 316.1459 (0.7) 261.1034 (0.1)	$[M+H-H_2O]^+$ $[M+H-CO_2]^+$ $[M+H-H_2CO_2]^+$ $[M+H-CO_2-C_3H_7N]^+$	365.1701 (0.57) $[M+H]^+$ $[C_{18}H_{18}D_3FN_3O_4]^+$	347.1593 (-0.1) 321.1801 (0.2) 319.1644 (-0.1) 261.1035 (0.5)	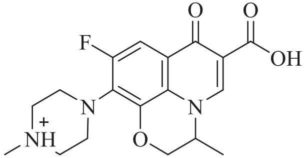
TP42	364.1301 (-0.7) $[M+H]^+$ $[C_{17}H_{19}FN_3O_5]^+$	346.1194 (1.0) 316.1294 (0.7) 284.1393 (-0.2)	$[M+H-H_2O]^+$ $[M+H-CHFO]^+$ $[M+H-CHFO_3]^+$	364.1305 (0.5) $[M+H]^+$ $[C_{17}H_{19}FN_3O_5]^+$	346.1192 (-1.6) 316.1294 (0.7) 284.1393 (-0.5)	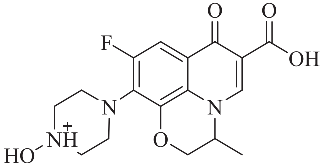

TP43	364.1503 (-0.1) $[M+H]^+$ $[C_{17}H_{22}N_3O_6]^+$	348.1560 (1.7) 320.1604 (-0.2) 307.1280 (-2.7) 261.1034 (0.1)	$[M+H-OH]^+$ $[M+H-CO_2]^+$ $[M+H-C_2H_2NOH]^+$ $[M+H-CO_2-C_2H_4OH]^+$	364.1504 (0.3) $[M+H]^+$ $[C_{17}H_{22}N_3O_6]^+$	348.1556 (0.6) 320.1604 (-0.2) 307.1285 (-1.1) 261.1034 (0.1)	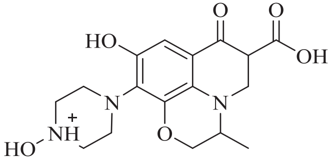
TP44	364.1671 (-1.1) $[M+H]^+$ $[C_{18}H_{23}FN_3O_4]^+$	320.1769 (0.1) 306.1609 (-1.1) 265.1346 (-0.3)	$[M+H-CO_2]^+$ $[M+H-CO_2-CH_2]^+$ $[M+H- CO_2-C_3H_5N]^+$	367.1855 (-0.2) $[M+H]^+$ $[C_{18}H_{20}D_3FN_3O_4]^+$	323.1960 (0.9) 306.1612 (-0.1) 265.1346 (0.1)	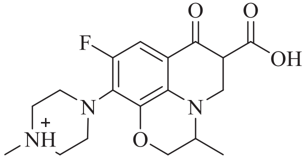
TP46	374.1149 (0.3) $[M+H]^+$ $[C_{18}H_{17}FN_3O_5]^+$	330.1250 (0.5) 312.1142 (-0.9) 261.1032 (-0.7)	$[M+H-CO_2]^+$ $[M+H-CO_2-H_2O]^+$ $[M+H-CO_2-H_2O-C_3HN]^{+\bullet}$	377.1335 (0.5) $[M+H]^+$ $[C_{18}H_{14}D_3FN_3O_5]^+$	333.1436 (-0.2) 315.1330 (-0.3) 261.1034 (0.1)	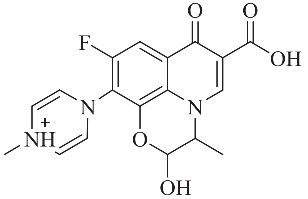
TP47	376.1303 (-0.1) $[M+H]^+$ $[C_{18}H_{19}FN_3O_5]^+$	332.1411 (1.8) 314.1301 (0.5) 261.1035 (0.4)	$[M+H-CO_2]^+$ $[M+H-CO_2-H_2O]^+$ $[M+H-CO_2-H_2O-C_3H_3N]^+$	379.1491 (-0.2) $[M+H]^+$ $[C_{18}H_{16}D_3FN_3O_5]^+$	335.1592 (-0.4) 317.1487 (-0.2) 261.1034 (0.1)	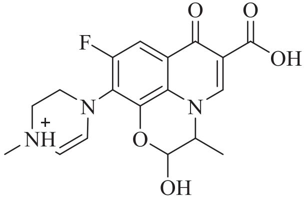
TP48	378.1463 (0.3) $[M+H]^+$ $[C_{18}H_{21}FN_3O_5]^+$	334.1573 (-2.8) 316.1455 (-0.2) 261.1034 (0.1)	$[M+H-CO_2]^+$ $[M+H-CO_2-H_2O]^+$ $[M+H-CO_2-H_2O-C_3H_5N]^+$	381.1648 (0.3) $[M+H]^+$ $[C_{18}H_{18}D_3FN_3O_5]^+$	337.1749 (-0.2) 319.1643 (-0.4) 261.1034 (0.1)	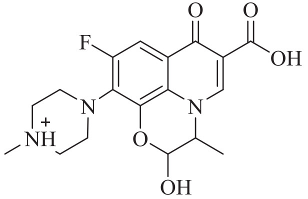

TP49	379.1510 (-0.4) $[M+H]^+$ $C_{15}H_{24}FN_2O_8$	361.1405 (-0.2) 335.1615 (0.6) 319.1664 (-0.8) 317.1508 (0.2)	$[M+H-H_2O]^+$ $[M+H-CO_2]^+$ $[M+H-CHO_3]^+$ $[M+H-CH_2O_3]^+$	379.1510 (-0.4) $[M+H]^+$ $C_{15}H_{24F}N_2O_8$	361.1403 (-0.6) 335.1612 (-0.3) 319.1665 (0.4) 317.1508 (0.2)	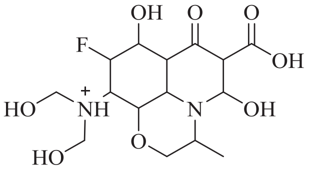
TP51	392.1253 (0.2) $[M+H]^+$ $[C_{18}H_{19}FN_3O_6]^+$	374.1145 (-0.4) 362.1146 (-0.2) 330.1246 (-0.7) 279.1137 (-0.8)	$[M+H-H_2O]^+$ $[M+H-CH_2O]^+$ $[M+H-CO_2-H_2O]^+$ $[M+H-CO_2-H_2O- C_3HN]^+$	395.1441 $[M+H]^+$ $[C_{18}H_{16}D_3FN_3O_6]^+$	377.1332 (-0.8) 365.1335 (1.3) 333.1436 (-0.2) 279.1139 (-0.2)	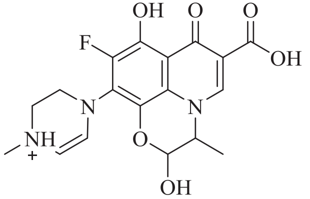
TP52	394.1411 (0.5) $[M+H]^+$ $[C_{18}H_{21}FN_3O_6]^+$	376.1304 (0.2) 364.1303 (-0.2) 332.1406 (0.3) 279.1139 (-0.5)	$[M+H-H_2O]^+$ $[M+H-CH_2O]^+$ $[M+H-CO_2-H_2O]^+$ $[M+H-CO_2-H_2O- C_3H_2N]^+$	397.1597 $[M+H]^+$ $[C_{18}H_{18}D_3FN_3O_6]^+$	379.1493 (0.4) 367.1493 (0.4) 335.1596 (0.8) 279.1141 (0.5)	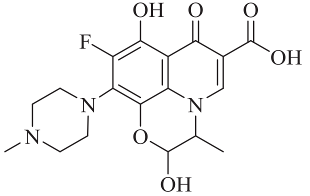
TP53	396.1566 (0.3) $[M+H]^+$ $[C_{18}H_{23}FN_3O_6]^+$	378.1460 (-0.1) 366.1459 (-1.3) 334.1561 (-1.0) 279.1139 (-0.2)	$[M+H-H_2O]^+$ $[M+H-CH_2O]^+$ $[M+H-CO_2-H_2O]^+$ $[M+H-CO_2-H_2O- C_3H_4N]^+$	399.1753 $[M+H]^+$ $[C_{18}H_{20}D_3FN_3O_6]^+$	381.1651 (0.7) 369.1650 (0.5) 337.1749 (-0.3) 279.1139 (-0.2)	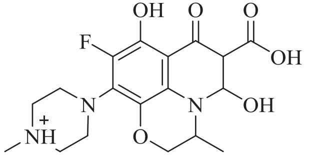
TP54	412.1521 (1.6) $[M+H]^+$ $[C_{18}H_{23}FN_3O_7]^+$	394.1409 (-0.3) 368.1626 (2.6) 348.1565 (3.2) 339.0987 (0.6)	$[M+H-H_2O]^+$ $[M+H-CO_2]^+$ $[M+H-CHFO_2]^+$ $[M+H-C_3H_7NO]^+$	415.1703 $[M+H]^+$ $[C_{18}H_{20}D_3FN_3O_7]^+$	399.1753 (-0.2) 371.1804 (-0.7) 351.1742 (3.2) 339.0987 (0.6)	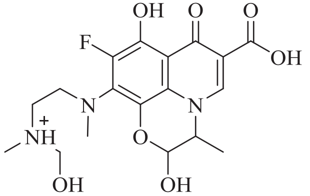
TP55	430.1773 (1.3) $[M+H]^+$ $[C_{22}H_{25}FN_3O_5]^+$	386.1874 (-0.1) 316.1450 (-1.8) 261.1033 (-0.3)	$[M+H-CO_2]^+$ $[M+H-C_5H_6O_3]^+$ $[M+H-C_8H_{11}NO_3]^+$	430.1773 (1.3) $[M+H]^+$ $[C_{22}H_{25}FN_3O_5]^+$	386.1874 (-0.1) 316.1450 (-1.8) 261.1035 (0.4)	–

TP56	434.2087 (0.2) $[M+H]^+$ $[C_{22}H_{29}FN_3O_5]^+$	390.2187 (-0.2) 318.1610 (-0.7) 261.1033 (-0.3)	$[M+H-CO_2]^+$ $[M+H-C_5H_8O_3]^+$ $[M+H-C_8H_{15}NO_3]^+$	434.2087 (0.2) $[M+H]^+$ $[C_{22}H_{29}FN_3O_5]^+$	390.2187 (-0.2) 318.1610 (-0.7) 261.1033 (-0.3)	–
TP57	447.2930 (0.84) $[M+H]^+$ $[C_{19}H_{39}N_6O_6]^+$	429.2817 (-1.1) 232.1659 (1.5) 202.1550 (-0.1)	$[M+H-H_2O]^+$ $[M+H-C_9H_{15}N_3O_2]^+$ $[M+H-C_{10}H_{19}N_3O_3]^+$	447.2930 (0.84) [M+H]+ $[C_{19}H_{39}N_6O_6]^+$	429.2817 (-1.1) 232.1655 (-0.29) 202.1550 (-0.1)	–
TP58	505.3344 (-1.8) $[M+H]^+$ $[C_{22}H_{45}N_6O_7]^+$	456.2453 (0.1) 244.1291 (0.5)	$[M+H-C_2H_{11}N]^+$ $[M+HC_{12}H_{27}N_3O_3]^+$	505.3344 (-1.8) $[M+H]^+$ $[C_{22}H_{45}N_6O_7]^+$	456.2453 (0.1) 244.1291 (0.5)	–
TP59	621.4221 (-0.12) $[M+H]^+$ $[C_{33}H_{57}N_4O_7]^+$	603.4116 (0.6) 526.3275 (-0.1) 313.2121 (-0.3)	$[M+H-H_2O]^+$ $[M+H-C_3H_{13}NO_2]^+$ $[M+H-C_{17}H_{28}N_2O_3]^+$	621.4221 (-0.12) $[M+H]^+$ $[C_{33}H_{57}N_4O_7]^+$	603.4116 (0.6) 526.3277 (0.3) 313.2121 (0.4)	–

Finally, this list was examined with respect to adduct formation (mainly H_2O, CH_3CN, HCOOH) in both positive and negative electrospray polarities. The absence of ions that matched in both retention times and mass shifts indicated that no adducts were present.

In-source oxidation

Redox reactions may occur in the ESI source [149] leading to false data interpretation. In these experiments, the ESI potential was varied between 2 and 4 kV to discriminate between those ions generated during the photocatalysis process from those that could be originated by a redox process in the ionisation source. For instance, the relative intensities of ions at *m/z* 336.1354 (t_R: 1.12 and 1.40 min) and *m/z* 338.1511 (t_R: 1.12 min) were recorded *versus* the ESI voltage in the positive mode (**Figure 4.11 A**). When the ESI voltage was gradually increased, the relative intensity of ion at *m/z* 336.1354 increased while the intensity of *m/z* 338.1511 simultaneously decreased when the ESI voltage was set over 2.5 kV. These results indicated that the first *m/z* peak could came from an oxidation process of *m/z* 338.1511, resulting in the oxidation of one hydroxyl group to carbonyl. In contrast, those ions not suffering redox reactions in the source only showed a slightly increase with the ESI voltage, as shown in **Figure 4.11 B**, with *m/z* 346.1210 and *m/z* 348.1354 respectively. In this study, other examples of redox reactions were found in the positive ionisation mode. Ions corresponding to TP21 and 28 (*m/z* 331.2102 and *m/z* 341.1216 respectively), which were considered to be radical cations ($[M]^{+\bullet}$) generated in the electrospray source, described a convex exponential function when the ESI voltage was gradually changed (**Figure 4.11 C**). Different to the mentioned behaviour, TP34 and OFX (*m/z* 348.13541 and *m/z* 362.15106 respectively, both $[M+H]^+$) showed a concave function when the ESI voltage was increase, represented in **Figure 4.11 D**. A total of eight radical cations (including the mentioned examples) were found to describe the same convex trend when the capillary voltage was changed.

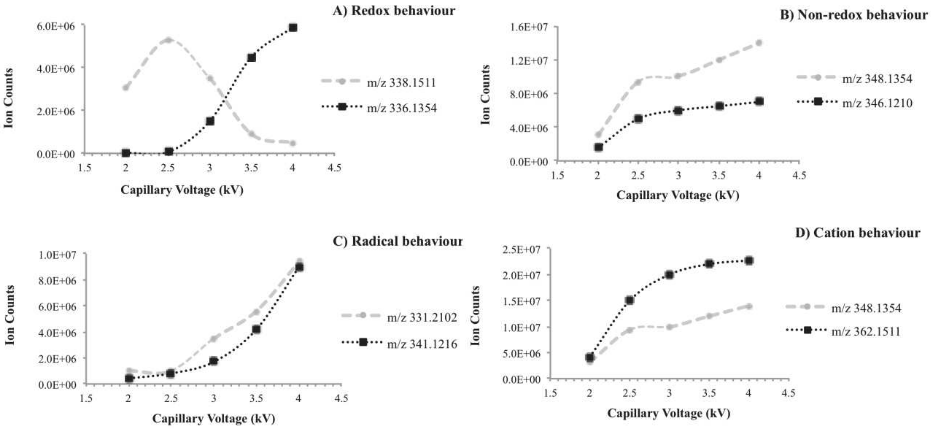

Figure 4.11. Ion intensity behaviour versus the capillary voltage to illustrate: A) redox; B) non-redox; C) radical; D) cation behaviours.

4.2.2.5. Characterisation of ofloxacin transformation products

As mentioned in **Section 4.2.2.2** and as can be seen in **Figure 4.8**, 59 intermediates were identified as OFX TPs generated during the photocatalytical process. The elemental composition was calculated on the basis of the accurate m/z values and the isotopic patterns. For each detected TP (both OFX and OFX-d_3), a chemical structure was proposed taking into account their high-resolution product ion spectrum (MS/HRMS), depicted in Table 4.1.

The first TPs to be characterised were those TPs sharing the same core structure of OFX and showing similar fragmentation patterns. For instance, TP 36, 39, 42, 51, 52, amongst others, showed the loss of H_2O (*m/z* 18.0105) due to one or multiple hydroxyl groups in their structure due to the attack of the radical OH. For instance, TP 48 was attributed to the hydroxylation at position 12, which was previously reported by Calza *et al*. [144]. Amongst the different positional isomers that could be hypothesized for TP48, position 12 is the only one able to show a water loss on TP48 and those TPs derived from it, that is, TP 46, 47, 51 and 52. Since the MS/MS spectrum of TP46, attributed to the hydroxylation at position 12 and oxidation at the pyperazine moiety, showed the same product ions of TP48, made it possible to discard the hydroxylation at position2 or 3. Moreover, the •OH attack at position 14 was also discarded as it would have shown the loss of $C_3H_7NO_2$ on the quinolone moiety, as stated by Calza *et al.* [144] The neutral loss of CO_2 (*m/z* 43.9898) was always observed in the MS/MS spectrum when the generated transformation products still had the quinolone moiety unmodified or with little modifications (TP 22, 23, 24 and 25 as well as TP 30–39).

Additionally, the simultaneous loss of CO_2 and C_3H_7Noccurring at the pyperazine moiety yielding the ion at *m/z* 261.1035was observed in the MS/MS spectra of TPs 32, 34, 43 and 46, as well as in the tandem mass spectrum of OFX. The loss of C3H7N at the pyperazine moiety observed for OFX was of special significance since C-C oxidations of some of the generated TPs could be easily distinguished. For example, TPs 46–48 are a clear example on how this product ion could reveal how many unsaturations showed the piperazine moiety, since the most unsaturated ring (3 unsaturations) showed the loss of C_3HN while the reduced form showed the loss of C_3H_7N (1 unsaturation). That was applicable to all TPs which showed oxidations in the piperazine ring. Despite having obtained relevant data to characterise and attribute chemical structures to the identified TPs, the chemical structure of some of them could not be fully characterised. The information obtained with the accurate mass and the MS/HRMS was not enough relevant to propose a chemical structure with a high degree of confidence. Moreover, the lack of standards or previous literature describing such degradation made more complicated this characterisation. However, these transformation products were attributed to the lasts steps of ofloxacin degradation since they started appearing at the middle-end of the reaction. It is for this reason that TP1 to TP5 and TP10 could be the result of extensive hydroxylation and chemical transformations involving all chemical processes taking place during the photocatalytical treatment.

The comparison of the product ion spectra of TPs generated from the photocatalysis of OFX and OFX-d_3 was useful for the chemical structure assignment. Especially useful was when it was needed to know the tentative position of the different methyl groups present in the suspect molecule. Since the accurate *m/z* value can led to different molecular formulae, and thus, different molecular structures, the use of the deuterated ofloxacin (isotopically labelled in the piperazine methyl group) and target MS/HRMS were crucial to discriminate amongst all possibilities. There are several examples in which the molecular structure was confirmed by means of the deuterated compound, that is, when the piperazine methyl did not suffer any modification. For instance, **Figure 4.12** shows the MS/HRMS spectra obtained for TP 24 (*m/z* 336.1360; *m/z* 339.1549) when studying both OFX and OFX-d_3 photocatalysis. After the opening of the piperazine ring and the likely loss of C_2H_4, the labelled methyl group, at 4’, still remained in this position, fact which led to the proposal of the molecule shown in

Figure 4.12. Having applied the described methodology and reasoning, it was possible to confirm 18 structures generated after the photo-catalysis process. On the other hand, if the same ions were observed in both experiments would indicate the loss of the piperazine methyl group or its substitution in the mentioned position. This was the case found for the rest of molecules presented in **Table 4.1**.

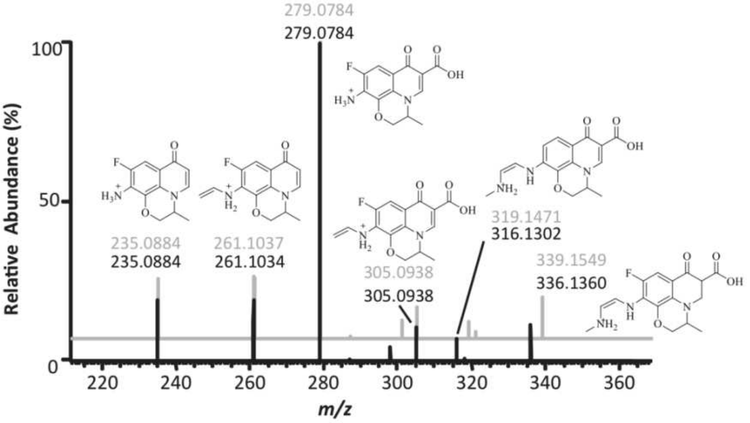

Figure 4.12. MS/MS spectrum of non-deuterated (in black) and deuterated (in grey) of TP 24.

Moreover, multiple potential deuterated molecules (n × 3.0188 Da) were inspected and were not detected. This would indicate that after radical CH_3/CD_3 loss, further methyl additions might not been taking place to the generated TPs. Moreover, the generation of dimers did not led to multiple deuterated molecules, thus indicating that the loss of the piperazine methyl is a previous step to molecule dimerisation or after the dimerisation of OFX or generated TPs, methyl groups are lost. However, despite all efforts made in this study, there is still a need to achieve higher confidence in the proposal of some chemical structures, since some identified isomers were not possible to distinguish on the basis of their accurate mass and their MS/MS pattern. Hence, it is for this reason that ion mobility coupled to high-resolution mass spectrometry was used to achieve a greater understanding of the photocatalytical process.

4.2.2.6. Adding an extra dimension to high-resolution mass spectrometry

As cited in the introduction of the present chapter and **section 4.1.1.2**, high-resolution mass analysers cannot distinguish between those coeluting compounds that have the same retention time, same accurate mass and tandem mass spectrum. In this way, the present research made use of ion mobility (travelling wave and cyclic IMS) coupled to high-resolution mass spectrometry in order to assess the investigation of possible positional isomers that could not have been detected by "conventional" (tandem) high-resolution mass spectrometry. As described in the experimental section of the present chapter, the LC method used was described in **section 4.2.1.4**.

First of all, a standard of 100 μg L^{-1} of ofloxacin was injected into the LC-IM-MS system (Synapt G2-Si) in order to acquire its mobiligram and CCS values. Results derived from this injection are presented in **Figure 4.13** (ofloxacin mobiligram) and **Table 4.2**, showing the observed drift time (ms) and the CCS values derived from it.

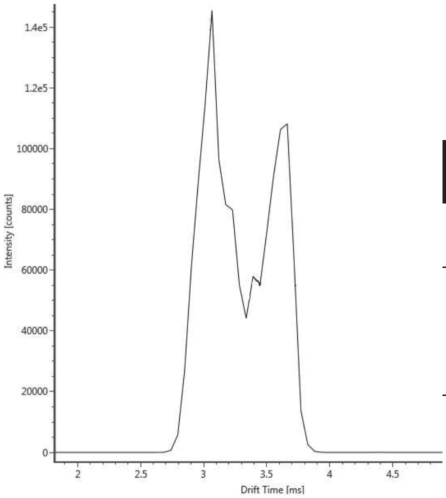

Figure 4.13. Mobility separation obtained in the Synapt G2-Si.

Table 4.2. Mobility drifts and experimental CCS values for OFX.

Drift time (ms)	**Observed CCS (Å^2)**
3.05	178.2
3.62	195.9

It can be easily seen that two species were separated by ion mobility under the studied instrumental conditions in the positive ion mode. Ofloxacin has five protonation sites (**Figure 4.14**): N at positions 1', 4' and 1 and the resonant carboxylic acid, positions 16 and 18. Moreover, the standard injected and used in the photocatalytic reaction was a racemic mixture of R-(+) and S-(-) of ofloxacin (position 13). Hence, in order to attribute one chemical structure to one of the observed signals, theoretical CCS values were derived using the original Mobcal code developed by Jarrod and co-workers [86,150] and that revised and modified by Campuzano *et al.* [151].

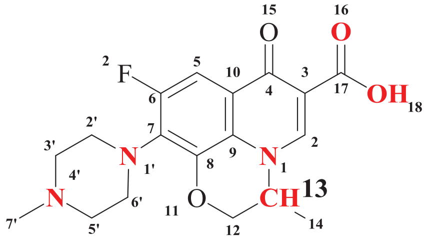

Figure 4.14. Chemical structure of ofloxacin.

Initially, these chemical structures were optimised using the MMFF94 level of theory (Avogadro 1.2). Structures were optimised using the B3LYP DFT function (Gaussian 09) and energy minimised using the 6-31G++(d,p) basis set. Partial atomic charges were determined using Mulliken, electrostatic surface potential (ESP) and natural population analysis (NPA) algorithms. In the Mulliken method, charges are assigned to an atomic center on the basis of the total electron density in basis functions located on that center. The NPA algorithm involves partitioning the charge into atomic orbitals on each center, constructed by dividing the electron density matrix into sub-blocks with the appropriate symmetry. The ESP calculation method uses the electrostatic potential of the molecule to compute charges on its nuclei. The Mulliken method is the simplest one from those used in the present thesis, as it is basis set sensitive. Whereas NPA and ESP methods require significant larger amounts of CPU time, these methods offer much better results than the Mulliken method.

All the hypothesised protomers and racemic structures (8 structures) were energy optimised and the partial atomic charges (Mulliken, NPA and ESP) were calculated as described in the experimental section. Hence, 24 input Mobcal files were generated and used to estimate the theoretical CCS values. Even though the present manuscript will only show the derived results from the revised Mobcal code (**Table 4.3** to **4.5**, using N_2 as buffer gas), theoretical CCS results using He as buffer gas will briefly discussed.

Original Mobcal code (He as buffer gas).

As expected, the obtained collision cross section values using He as buffer gas led to significant deviations from the experimental derived values. Even though not presented in the present text, these theoretical results constitute the next step of the present research, as the same measurements will be carried out using He as buffer gas.

Table 4.3. Calculated CCS values for OFX using N$_2$ as buffer gas and the ESP charge calculation method.

Molecule	**(S)-(-)_OFX_N4'**	**Deviation (%)***	**(R)-(+)_OFX_N4'**	**Deviation (%)***
Optimised energy (Ha)	-1263.40948		-1186.013268	
TM (Å^2)	198.45	1.28	182.67	2.44
Molecule	**(S)-(-)_OFX_N1**	**Deviation (%)**	**(R)-(+)_OFX_N1**	**Deviation (%)**
Optimised energy (Ha)	-1263.32872		-1263.32826	
TM (Å^2)	187.26	-4.61	190.25	2.96
Molecule	**(S)-(-)_OFX_N1'**	**Deviation (%)**	**(R)-(+)_OFX_N1'**	
Optimised energy (Ha)	-1263.39106		-1263.39106	
TM (Å^2)	192.01	-2.02	192.05	-2.00
Molecule	**(S)-(-)_OFX_COOH**	**Deviation (%)**	**(R)-(+)_OFX_COOH**	**Deviation (%)**
Optimised energy (Ha)	-1263.41561		-1263.41545	
TM (Å^2)	186.72	4.56	185.69	4.03

* *versus* the nearest experimental value

Table 4.4. Calculated CCS values for OFX using N_2 as buffer gas and the Mulliken charge calculation method.

Molecule	**(S)-(-)_OFX_N4'**	**Deviation (%)**	**(R)-(+)_OFX_N4'**	**Deviation (%)**
TM (Å^2)	207.67	5.66	182.67	2.44
Molecule	**(S)-(-)_OFX_N1**	**Deviation (%)**	**(R)-(+)_OFX_N1**	**Deviation (%)**
TM (Å^2)	194.88	-0.52	188.53	-3.90
Molecule	**(S)-(-)_OFX_N1'**	**Deviation (%)**	**(R)-(+)_OFX_N1'**	**Deviation (%)**
TM (Å^2)	207.06	5.38	207.19	5.44
Molecule	**(S)-(-)_OFX_COOH**	**Deviation (%)**	**(R)-(+)_OFX_COOH**	**Deviation (%)**
TM (Å^2)	200.92	2.49	198.51	1.31

* *versus* the nearest experimental value

Table 4.5. Calculated CCS values for OFX using N_2 as buffer gas and the NPA charge calculation method.

Molecule	**(S)-(-)_OFX_N4'**	**Deviation (%)**	**(R)-(+)_OFX_N4'**	**Deviation (%)**
TM (Å^2)	203.56	3.76	186.48	-5.05
Molecule	**(S)-(-)_OFX_N1**		**(R)-(+)_OFX_N1**	
TM (Å^2)	192.55	-1.73	195.72	-0.092
Molecule	**(S)-(-)_OFX_N1'**		**(R)-(+)_OFX_N1'**	
TM (Å^2)	196.03	0.066	196.17	0.14
Molecule	**(S)-(-)_OFX_COOH**		**(R)-(+)_OFX_COOH**	
TM (Å^2)	190.78	-2.68	189.70	-3.26

* *versus* the nearest experimental value

On the basis of the theoretical results obtained (not shown in the text), the best calculation approximation was found to be the Exact Hard Spheres Scattering (EHSS), with an average value of 133 Å^2. The charge calculation method did not significantly affect (max 0.1%) to the final result obtained. This could be attributed to the simplicity of helium as buffer gas, that is, interacting as a hard-sphere with the generated ions.

Revised Mobcal code (N_2 as buffer gas).

According **to Table 4.3** to **Table 4.5,** it was possible to correlate the experimental results with the predicted CCS values. With a maximum error allowance of 2% between the experimental and calculated values (ESP method), the signal at 3.05 msec (178.2 Å^2) could be attributed to the R form of ofloxacin, localising the positive charge at position 4' whereas the signal at 3.62 msec (195.9 Å^2) could correspond to: R or S form of ofloxacin localising the positive charge at position N1' and N1. Additionally, this could also be attributed to the S form localising the positive charge at N4'. As suggested by the theoretical calculations, no separation would be observed between these forms.

Contrary to what was observed using helium as buffer gas, the charge calculation method influenced the final theoretical result (up to a 5%), as illustrated in the mentioned tables. On the basis of the obtained results, the ESP method offered the best correlation between the predicted and observed CCS values. This fact could be directly linked to the partial atomic charges derived from the ESP algorithm, which were the ones that fitted best according to the chemical intuition, as depicted in **Table 4.6.** This table shows the partial atomic charges obtained for the hypothesised structure (S)-(-) OFX protonated at position N4'.

Table 4.6. Calculated partial atomic charges for (S)-(-)_OFX_N4'.

Position	ESP	Mulliken	NPA
N4'	0.3067	-0.1696	-0.4712
N1'	-0.2050	0.2327	-0.5346
N1	0.08500	0.0731	-0.3956
O16	-0.3874	-0.3410	-0.5355
O18	-0.1679	0.01241	-0.7000

Since positions at N4', N1', N1 and O16-18 were the atoms at which the positive charge was located to hypothesise the different isomers possible, the obtained partial atomic charges and their chemical interpretation was of some importance to explain and decide which method offered the best calculation performance, especially for the structural elucidation of the generated transformation products. Hence, in the illustrated example, N4' presented negative charge values when it was employed the Mulliken and NPA calculation algorithms. Even though localising the positive charge at position N4', this was immediately distributed through the pyperazine and quinolone ring, according to the partial atomic charges observed for the most relevant atoms studied. Even though the ESP method offered the best fit, the Mulliken and natural population analysis algorithms were still under consideration when modelling ofloxacin transformation products. Since the predicted values derived from the revised Mobcal code (using N_2 as drift gas) completely correlated the experimental results, this program was further used to calculate the theoretical CCS values of the generated transformation products under investigation. Although not shown in the present manuscript, the original code first developed by Jarrod and co-workers still was used for future works using He as buffer gas in the mobility cell.

Once optimised the instrumental conditions for the parent drug ofloxacin, irradiated samples were injected to the LC-IM-MS systems (Synapt G2-Si and Vion), as depicted in **Figures 4.15** and **4.16**. Both figures show the total ion chromatogram *versus* drift time obtained for one of the samples injected (30 min irradiation with P25 nanoparticles). Rather than concentrating on the same ions as previously detected and characterised by (tandem) high-resolution mass spectrometry (**Table 4.1**), data treatment and analysis was focused on the discovery of those transformation products with the same retention time, accurate mass but different drift time.

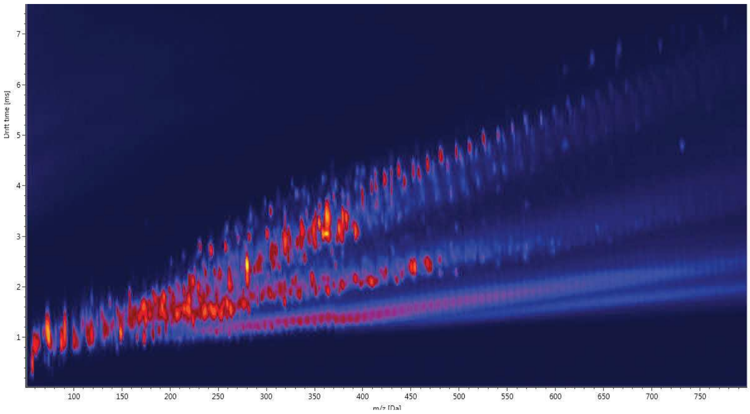

Figure 4.15. Total ion current and mobility separation. *m/z* (x-axis) and drift time (y-axis) obtained on the Synapt G2-Si instrument.

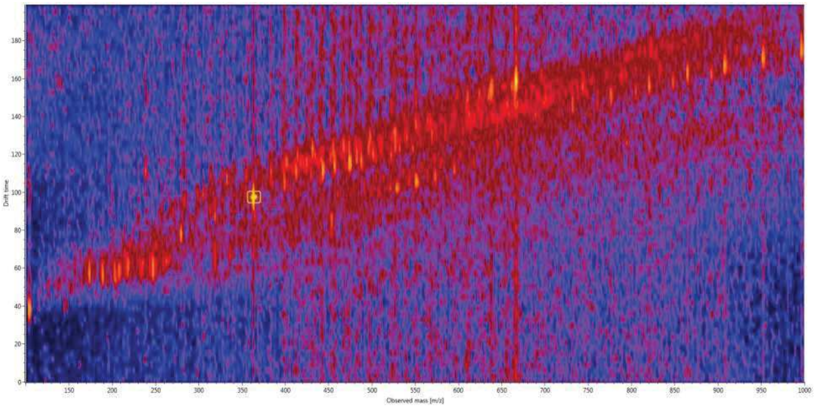

Figure 4.16. Total ion current and mobility separation. *m/z* (x-axis) and drift time (y-axis) obtained on the Vion QToF instrument.

Hence, 7 examples satisfying these requirements were found, as listed in **Table 4.7**. Some examples on the separation obtained in the Synapt G2-Si and Vion instruments for these transformation products can be seen in **Figure 4.17** to **Figure 4.20**.

Table 4.7. Detected transformation products with the same retention time and accurate mass but different mobility drifts.

TP	*m/z* observed	Mobility drift (ms)	Experimental CCS (Å ^{2})	Mobility drift (ms)	Experimental CCS (Å ^{2})
*	305.0936	2.43	159.53	2.71	168.42
17	318.1618	2.85	172.64	3.06	179.38
*	322.1204	2.68	167.26	3.09	180.22
24	336.1359	2.85	172.23	3.14	181.47
48	378.1469	3.25	183.24	3.45	189.56
52	394.1403	3.19	181.94	3.60	194.76

* Not previously identified with the QExactive Orbitrap platform.

It can be observed that, not all these mobility signals were completely resolved. For instance, the trace at *m/z* 318.1618 (**Figure 4.17**) showed a broad tailing peak that made it difficult to distinguish if this signal was attributed to the high concentration injected or was the cause of different peaks overlapping in the same signal. Alternatively, the trace at *m/z* 336.1256 (**Figure 4.18)** presented two well differentiated peaks, although they were not completely resolved. Additionally, the traces at *m/z* 394.1403 and *m/z* 322.1204, **Figures 4.19** and **4.20** respectively, presented two well resolved mobiligram traces. It is for this reason that, in order to achieve an enhanced and better resolved mobility separation of those poorly resolved traces, ofloxacin and irradiated samples were injected into a mobility prototype instrument from Waters Corp. based on a cyclic ion mobility instrument.

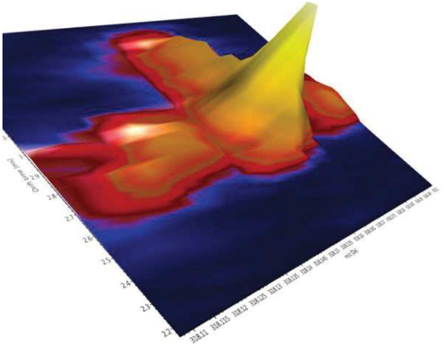

Figure 4.17. IM separation of *m/z* 318.1618

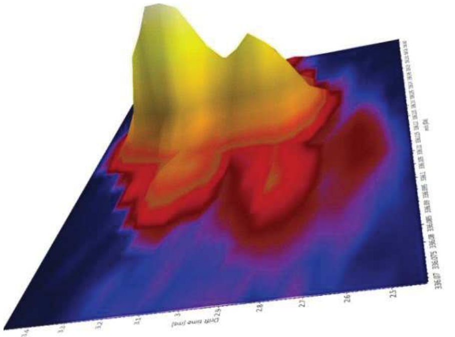

Figure 4.18. IM separation of *m/z* 336.1256

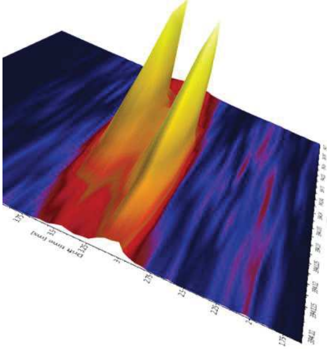

Figure 4.19. IM separation of *m/z* 394.1403

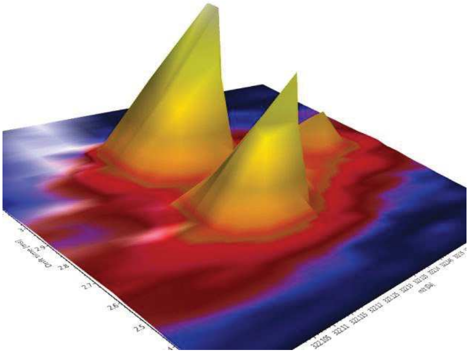

Figure 4.20. IM separation of *m/z* 322.1204

Prior the injection of the irradiated samples, the ion mobility separation was first performed on a standard of ofloxacin (**Figure 4.21**). This figure clearly shows that by increasing the number of cyclic passes (increasing the separation time, that is, the flight time through the cyclic chamber), both signals were gradually separated, making it possible at the same time, to validate those results derived from both Synapt G2-Si and Vion instruments. Once we had studied the mobility separation of ofloxacin, different LC runs were performed by changing the separation time (number of passes through the cyclic mobility tube), to separate the compounds that were not initially resolved. **Figure 4.22** shows the separation of **TP17**, *m/z* 318.1618, **Figure 4.23** for the separation of **TP 24** (*m/z* 336.1359) and **Figure 4.24** the mobility separation of **TP 48**, *m/z* 378.1469.

As observed with ofloxacin, increasing the number of cyclic passes led to a resolution increase of the detected TPs, in comparison to those separations observed using either the Synapt or Vion instruments. For instance, the separation of TP17, *m/z*

318.1618, is shown in **Figure 4.22**. Two mobility peaks can be poorly resolved under one cyclic pass (sep time of 20 – purple trace). By increasing it up to 125 and 150 sep time (green and red traces respectively), both signals were completely resolved, achieving in this way, enhanced resolution in comparison to Synapt or Vion instruments. As expected, the traces at *m/z* 336.1256 and *m/z* 378.1469 (**Figures 4.24 and 4.25 respectively**) were much better resolved when the cyclic ion mobility instrument was used. The trace at *m/z* 336.1256, however, was not completely separated to baseline level. Especially interesting was TP 48 (*m/z* 378.1469), which, with only one cyclic loop, were completely be separated to baseline level.

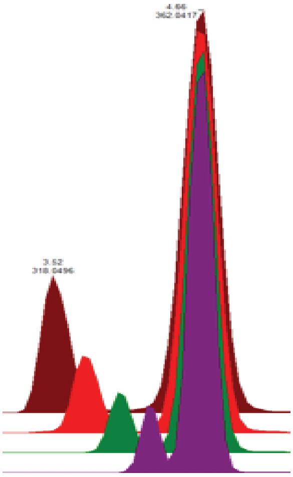

Figure 4.21. Cyclic IM separation of ofloxacin. Purple: sep time 20; green: sep time 150; red: sep. time 225; brown: sep. time 315

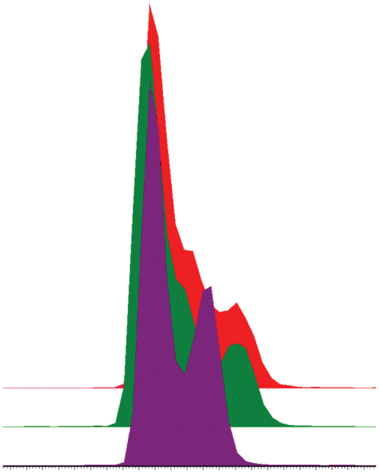

Figure 4.22. Cyclic IM separation of *m/z* 318.1618. purple sep time 20; green sep time 125: red sep time 150

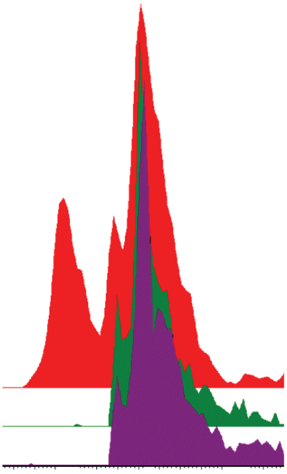

Figure 4.23. Cyclic IM separation of *m/z* 336.1256 purple sep time 20; green sep time 50; red sep. time 100

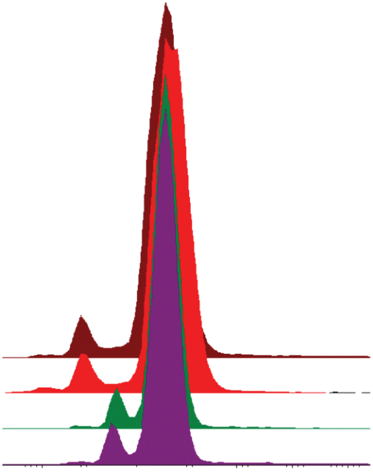

Figure 4.24. Cyclic IM separation of *m/z* 378.1469 purple sep time 50; green sep time 75; red sep. time 125; brown sep. time 150;

As performed before with ofloxacin, in order to validate the experimental results observed for these transformation products, theoretical cross sections were calculated for two of the detected transformation products: TP 17, *m/z* 318.1618 and TP 24, *m/z* 336.1256. Results derived from these calculations are presented in **Tables 4.8 to 4.10** for TP 17 and **Table 4.11** to **Table 4.13** for TP 24.

For TP17, *m/z* 318.1618, the calculated theoretical results were in agreement with the experimental results using the electrostatic surface potential charge calculation method. As observed with ofloxacin, this method produced the best chemical interpretation for the proposed modelled structure. Hence, the signal observed at 3.06 ms drift (179.38 Å^2) was attributed to (S)-(-)_318.1618_N4', that is, "localising" the positive charge on the N at position 4'of the piperazine moiety (ESP charge calculation method). Meanwhile, the signal observed at 2.85 ms drift (172.64 Å^2) could be attributed to the localised charge at the N at position 1 of the quinolone moiety or 1' of the piperazine moiety. Interestingly, the low deviation between the experimental and theoretical CCS values were found for both structures using the NPA analysis (<2%). As occurred with the parent drug, CCS values derived from Mulliken led to high deviations from the experimental value.

In respect to TP 24, *m/z* 336.1356, only one of the eight hypothesised structures, (S)-(-)_336.1359_COOH, using the ESP charge calculation method, was in accordance to the experimental results (3.14 ms drift, 181.47 Å^2) as depicted in **Table 4.11**. The rest of the obtained values of the optimised R and S forms presented high deviations from the signal at 2.85 ms drift (172.23 Å^2).

As stated in the beginning of this section, ion mobility measurements using He as buffer gas and He theoretical calculations are now under investigation and will improve the understanding and comprehension on the chemical nature of the generated transformation products. Up to this point, the combination of ion mobility and theoretical calculations has been evaluated by studying some of the observed TPs.The results have permitted (on the basis of the observed and calculated CCS) the confirmation of the mentioned TPs, which were previously detected by high-resolution mass spectrometry. Hence, our future investigation will be devoted to calculate the theoretical CCS values for those structures hypothesised in **Table 4.1** and correlate them with the acquired mobility data.

Table 4.8. Calculated CCS values for *m/z* 318.1618_N4' using N_2 as buffer gas.

Molecule	**(S)-(-)_318.1618_N4'**	
Optimised energy (Ha)	-1074.82075	**Deviation (%)**
TM ($Å^2$) – ESP method	184.00	2.51
TM ($Å^2$) – Mulliken method	214.53	16.38
TM ($Å^2$) – NPA method	189.43	5.30

Table 4.9. Calculated CCS values for *m/z* 318.1618_N1' using N_2 as buffer gas.

Molecule	**(S)-(-)_318.1618_N1'**	
Optimised energy (Ha)	-1074.80660	**Deviation (%)**
TM ($Å^2$) – ESP method	175.75	1.77
TM ($Å^2$) – Mulliken method	199.64	10.14
TM ($Å^2$) – NPA method	179.44	0.033

Table 4.10. Calculated CCS values for *m/z* 318.1618_N1 using N_2 as buffer gas.

Molecule	**(S)-(-)_318.1618_N1**	
Optimised energy (Ha)	-1074.75185	**Deviation (%)**
TM ($Å^2$) – ESP method	175.73	1.76
TM ($Å^2$) – Mulliken method	186.27	3.69
TM ($Å^2$) – NPA method	181.41	1.12

Table 4.11. Calculated CCS values for *m/z* 336.1359 using N_2 as buffer gas and the ESP charge calculation method.

Molecule	**(S)-(-)_336.1359_N4'**	**Deviation (%)***	**(R)-(+)_336.1359_N4'**	**Deviation (%)***
Optimised energy (Ha)	-1186.00293		-1186.00347	
TM (Å^2)	191.40	5.18	190.66	4.82
Molecule	**(S)-(-)_336.1359_N1**	**Deviation (%)***	**(R)-(+)_336.1359_N1**	**Deviation (%)***
Optimised energy (Ha)	-1185.92673		-1185.92607	
TM (Å^2)	190.34	4.66	186.41	2.65
Molecule	**(S)-(-)_336.1359_N1'**	**Deviation (%)***	**(R)-(+)_336.1359_N1'**	**Deviation (%)***
Optimised energy (Ha)	-1185.98109		-1185.98006	
TM (Å^2)	191.86	5.41	190.23	4.60
Molecule	**(S)-(-)_336.1359_COOH**	**Deviation (%)***	**(R)-(+)_336.1359_COOH**	**Deviation (%)***
Optimised energy (Ha)	-1186.01471		-1263.40968	
TM (Å^2)	183.80	1.26	198.08	8.38

* *versus* the nearest experimental value

Table 4.12. Calculated CCS values for *m/z* 336.1359 using N_2 as buffer gas and the Mulliken charge calculation method.

Molecule	**(S)-(-)_336.1359_N4'**	**Deviation (%)***	**(R)-(+)_336.1359_N4'**	**Deviation (%)***
TM (Å^2)	193.39	6.16	193.03	5.98
Molecule	**(S)-(-)_336.1359_N1**	**Deviation (%)***	**(R)-(+)_336.1359_N1**	**Deviation (%)***
TM (Å^2)	193.14	6.04	188.02	3.48
Molecule	**(S)-(-)_336.1359_N1'**	**Deviation (%)***	**(R)-(+)_336.1359_N1'**	**Deviation (%)***
TM (Å^2)	192.35	5.65	192.16	5.56
Molecule	**(S)-(-)_336.1359_COOH**	**Deviation (%)***	**(R)-(+)_336.1359_COOH**	**Deviation (%)***
TM (Å^2)	193.12	6.03	207.54	12.56

* *versus* the nearest experimental value

Table 4.13. Calculated CCS values for *m/z* 336.1359 using N_2 as buffer gas and the NPA charge calculation method.

Molecule	**(S)-(-)_336.1359_N4'**	**Deviation (%)***	**(R)-(+)_336.1359_N4'**	**Deviation (%)***
TM (Å^2)	194.83	6.85	194.04	6.47
Molecule	**(S)-(-)_336.1359_N1**	**Deviation (%)***	**(R)-(+)_336.1359_N1**	**Deviation (%)***
TM (Å^2)	196.36	7.58	191.80	5.38
Molecule	**(S)-(-)_336.1359_N1'**	**Deviation (%)***	**(R)-(+)_336.1359_N1'**	**Deviation (%)***
TM (Å^2)	195.19	7.02	194.04	6.47
Molecule	**(S)-(-)_336.1359_COOH**	**Deviation (%)***	**(R)-(+)_336.1359_COOH**	**Deviation (%)***
TM (Å^2)	187.71	3.32	202.91	10.56

* *versus* the nearest experimental value

4.2.2.1.Ofloxacin degradation pathway

After annotation of the candidate structures, two approximations were taken into account in order to suggest the path by which OFX is degraded: time evolution and mass comparison of all TPs generated from both OFX and OFX-d_3 photocatalysis in the different conditions tested.

As no standards were available, peak area evolution has been considered, as in previous publications [144–147], as a quantitative approximation in order to follow the evolution of the generated TPs.

The degradation pathway was built up looking for first-generation TPs, that is, small transformation changes to OFX structure. Then, consecutive degradation was investigated looking for small modifications to first-generation TPs. Most of these found TPs were characterised by maintaining the quinolone moiety, which is the main responsible for the antibacterial activity, thus, the drug is not inactivated [144–147]. A tentative degradation pathway is shown in **Figure 4.25**. For instance, it was considered to be first generation TPs demethylation of the piperazine ring (TP 34) yielding the ion at *m/z* 348.1354, hydroxyl attack and consecutive demethylation generating a hydroxylamine at the N-pyperazine position giving raise to TP 42 (*m/z* 364.1503), defluorination (TP 30) yielding the ion at *m/z* 344.1609, decarboxylation generating TP 17 (*m/z* 318.1610) and C_2H_4 loss at the 5'–6' positions of the pyperazine ring yielding TP 24 (*m/z* 336.1354).

Additionally, hydroxyl attack to the OFX quinolone moiety led to TP 48 (*m/z* 378.1463). The results from the extracted-ion chromatograms were handled to build plots of the TPs peak area evolution (% relative to their maximum) *versus* reaction time **(Figure 4.26)**. These TPs showed a fast concentration increase after 5 min of photocatalytical treatment, which agrees to the assumption of being first-generation TPs.

On the basis of time evolution and chemical reactions taking place during the photocatalytic process, consecutive degradation of these TPs occurred, and thus, next generation TPs were tentatively proposed.

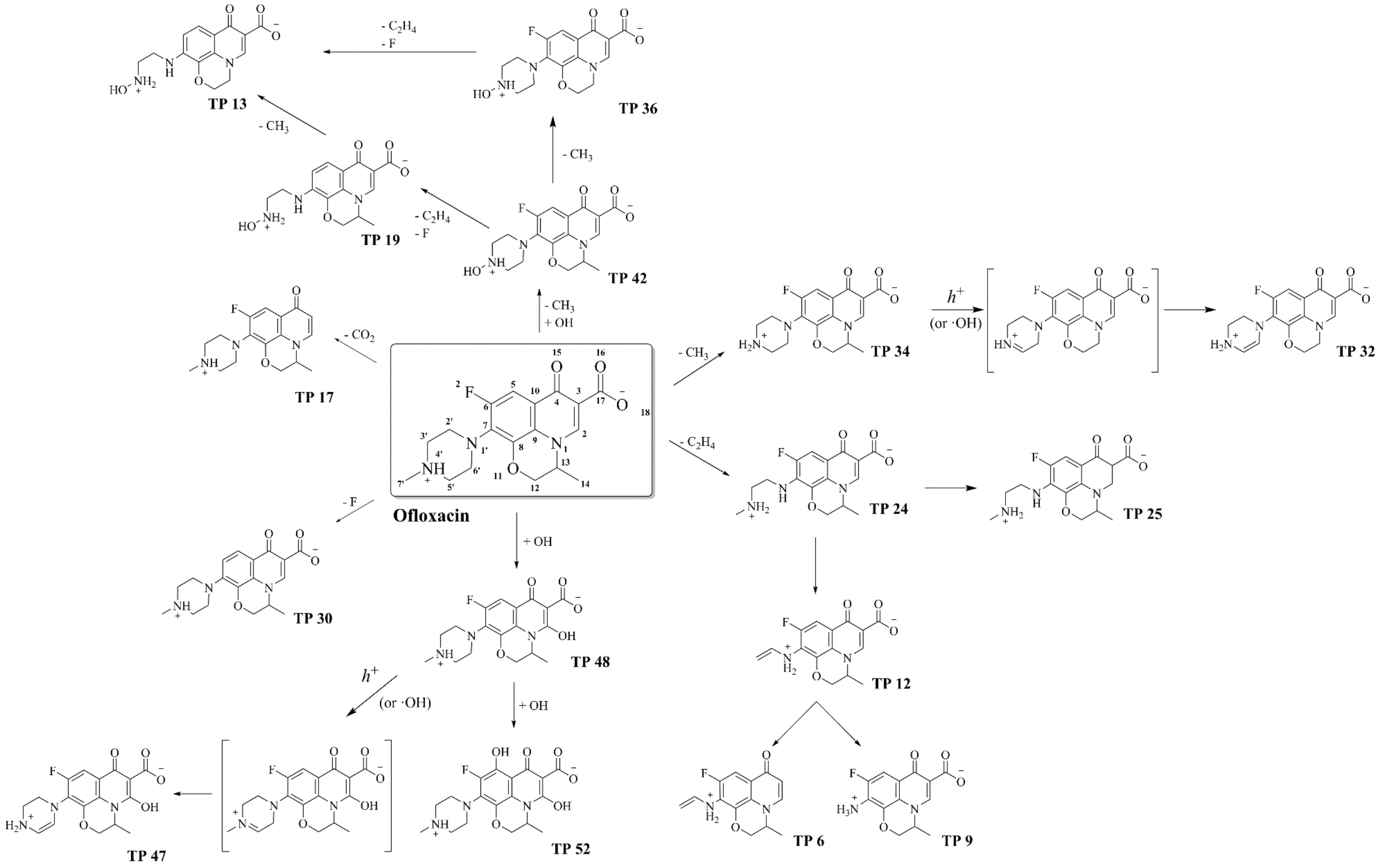
TP 13
- C$_2$H$_4$
- F
TP 36
- CH$_3$
- CH$_3$
TP 19
- C$_2$H$_4$
- F
TP 42
TP 17
- CO$_2$
- CH$_3$
+ OH
Ofloxacin
- CH$_3$
TP 34
h^+
(or ·OH)
TP 32
- C$_2$H$_4$
TP 24
TP 25
- F
TP 30
+ OH
TP 48
TP 12
h^+
(or ·OH)
+ OH
TP 47
TP 52
TP 6
TP 9

Figure 4.25. Tentative degradation pathway of ofloxacin. Not all TPs detected and listed in **Table 1** are shown.

For instance, TP 24 could presumably lead to TP12 after the cleavage of the N-CH_2 bond between the 3'– 4'positions. Finally, TP 12 would tentatively lead to TP 6 (*m/z* 261.1035) and TP 9 (*m/z* 279.0776) after CO_2 and C_2H_4 loss respectively. TP48 has been reported [144] to lead to TP 52 (*m/z* 394.1411) after the consecutive addition of a hydroxyl group to the quinolone moiety.TP 42 could presumably lead to TP 36 (*m/z* 350.1146) and TP 19 (*m/z* 320.1242) after the loss of the methyl group and the simultaneous loss of −F and C_2H_4 (5' – 6') respectively. These last two mentioned TPs could explain the generation of TP 13 (*m/z* 306.1083) via two different reaction mechanisms.

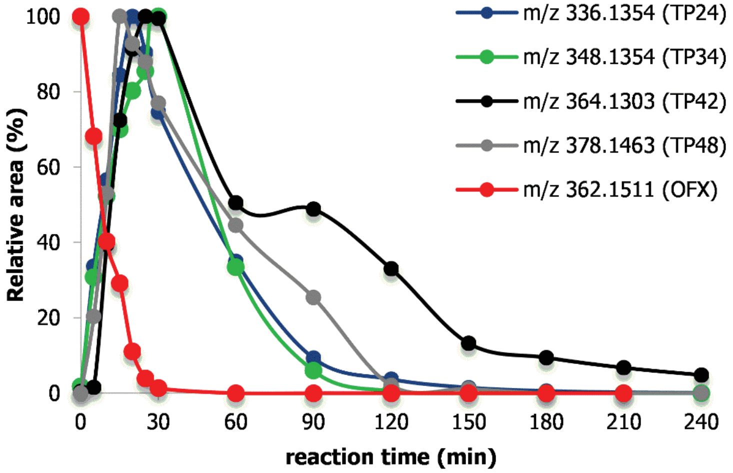

Figure 4.26. Degradation kinetics of OFX (*m/z* 362.1511 in red), TP 24 (*m/z* 336.1354 in blue), TP 34 (*m/z* 348.1354 in green), TP42 (*m/z* 364.1303 in black) and TP 48 (*m/z* 378.1463 in grey).

In regard to the faster concentration increase of TP 36 **(Figure 4.27)**, the loss of the methyl group at position 13 seems to be favoured in comparison to the loss of C_2H_4 in the pyperazine ring. Also this was confirmed by knowing at which kinetic point both TPs started to appear, thus, being 10 min for TP36 and 20 min for TP 19. However, parallel reaction pathways leading to the same TP may also be considered, as for example, TP 19 showed a concentration increase after 120 min of treatment.

Apart from oxidation due to reactive oxidative species (ROS), the generated holes (h^+) on the TiO_2 surface (Fujishima *et al.* and Salvador [152,153]) can also oxidise organic species if they are adsorbed on the surface of the catalyst. A tentative explanation rationalising its presence has been reported in previous literature [154] and the mechanism for this particular case is shown in **Figure 4.28.**

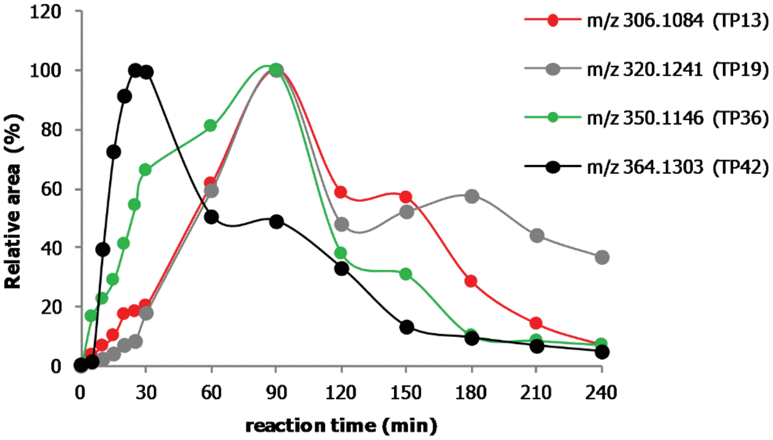

Figure 4.27. Appearance and degradation kinetics found for TP42 (black dots), TP36 (green dots), TP19 (in grey) and TP13 (red dots).

After an electron capture by the N atom at the 1’ or 4’ and consecutive electron rearrangement, a new N - C bond might be formed leading to an imine or an iminium ion. These compounds might immediately be transformed to their respective enamines after losing the H at position 6’ thus appearing TPs 16, 22, 32, 39, 47 and 51 or the piperazine ring might be opened leading to different reactions.

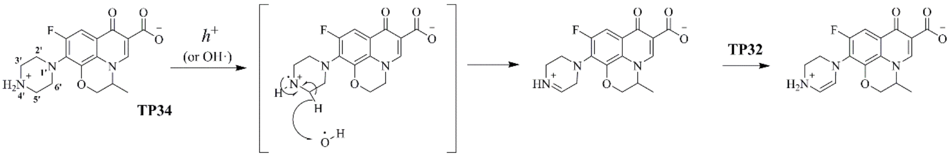

Figure 4.28. Reaction mechanism involved in the oxidation of the piperazine ring of OFX and its homologues. These steps explain such transformations if the mechanism is via the generated holes originated in the photocatalyst or via the radical hydroxyl.

Although not being the most common reactions in TiO_2 photocatalysis, reduction processes occurring at the quinolone moiety were also observed on some of the identified TPs, for instance TP24 to TP25 or OFX to TP44. These reduction processes have been previously reported in literature [155,156]. The interaction of H^+ ions with the excited electrons, generated after the emission of one electron from the valence band to the conduction band, leads to the formation of H• radicals and molecular hydrogen at the photocatalyst’s surface, thus being plausible these reduction processes on the mentioned molecules.

High molecular weight molecules (*m/z* 500–1000) were separated on the C18 LC column as shown in **Figure 4.8**. The presence of such molecules has been extensively reported [145,157]. The stabilized organic radicals can be subject to dimerization reactions via carbon–carbon or carbon-oxygen couplings or via addition of such radicals onto neutral molecules [155]. Structure annotation of some of these signals was not possible due to the fact that tandem MS was not obtained despite having performed different LC runs increasing the collision energy. However, it was noticed a mass difference of +58 Da between consecutive chromatographic peaks, as indicated in **Figure 4.8**, which could be attributed to consecutive additions of butyl groups. There were some exceptions, as TP 26 (*m/z* 679.5181, (*m/z* 340.2591 due to $[M+2H]^{2+}$)) shown in **Figure 4.29**, which tentatively resulted from the condensation of two core structures of ofloxacin and consecutive group cleavage and oxidation/reductions reactions, as it was observed in previous examples shown in Figure. 4.8.

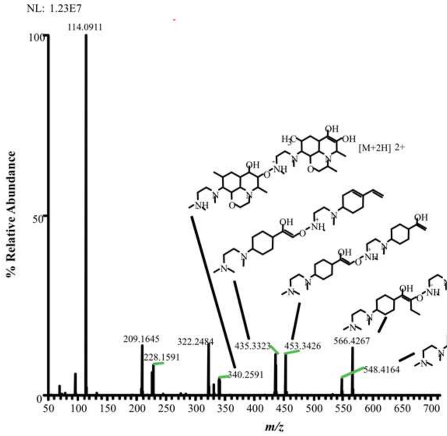

Figure 4.29. MS/MS spectrum and structure annotation of TP 26 ($[C_{36}H_{68}N_6O_6]^{2+}$). The same MS/MS spectra was obtained when the TP 26 ($[C_{36}H_{67}N_6O_6]^{+}$) was selected for target MS^2.

4.3. Conclusions

Liquid chromatography coupled to high-resolution mass spectrometry and ion-mobility have vastly demonstrated its applicability and the advantages they offers to environmental analysis over conventional analysis techniques, especially when dealing with the removal of organic compounds and the generation of by-products

- The peak picking process and structure identification still remain the most significant challenging tasks in untargeted analytics. The application of the *in-home* data scripts can significantly reduce data processing time and allowed the automated detection of candidate TPs, even if some of them were coeluting or masked by the background noise.
- Even though that these filtering parameters used in the present thesis can be easily defined and modified for instant results update, the mass spectrometrist's critical point of view was found to be crucial to identify *in-source* reactions (oxidation or fragmentation) that might be taking place in the electrospray source, since it can induce to false data interpretation.
- In addition to classical structural elucidation techniques based on HRMS and MS/HRMS, the study of the isotope labelled ofloxacin OFX(-d_3) has proven to be of significant support for the correct structure assignment. Moreover, its use has also provided a deeper understanding on the mechanism involved in the photocatalytical process since it was possible to compare OFX(-d_3) kinetics.
- Ion mobility mass spectrometry has demonstrated its applicability to the untargeted analysis of OFX TPs making possible the separation of protomers and isomers that could not be resolved before. Better mobility resolution was then achieved by using a prototype instrument based on a cyclic ion mobility spectrometer, being possible to completely separate signals that were observed as tailing peaks in the Synapt and Vion instruments. Additionally to those mentioned advantages, the calculation of theoretical CCS made possible the correlation of experimental evidences with the hypothesised chemical structures of these detected TPs.
- On the basis of the identified TPs and their observed kinetics, it was proposed a general scheme of degradation which started with little modifications of OFX structure such as reduction, oxidations, hydroxylations and ended with low molecular weight structures. High molecular weight structures were also detected, presumably corresponding to OFX dimers generated in the termination step of the

radical processes. Furthermore, it has been possible to discriminate between first generation TPs and their consecutive transformation pattern.

4.4. References

1. Paul, T.; Dodd, M. C.; Strathmann, T. J. *Water Res.* **44,** 3121–3132 (2010).
2. Van Doorslaer, X.; Haylamicheal, I. D.; Dewulf, J.; Van Langenhove, H.; Janssen, C. R.; Demeestere, K. *Chemosphere* **119,** 75–80 (2015).
3. Tay, K. S.; Madehi, N. *Sci. Total Environ.* **520,** 23–31 (2015).
4. Bade, R.; Causanilles, A.; Emke, E.; Bijlsma, L.; Sancho, J. V.; Hernandez, F.; de Voogt, P. *Sci. Total Environ.* **569–570,** 434–441 (2016).
5. De Vos, R. C. H.; Moco, S.; Lommen, A.; Keurentjes, J. J. B.; Bino, R. J.; Hall, R. D. *Nat. Protoc.* **2,** 778–791 (2007).
6. Neumann, N. K. N.; Lehner, S. M.; Kluger, B.; Bueschl, C.; Sedelmaier, K.; Lemmens, M.; Krska, R.; Schuhmacher, R. *Anal. Chem.* **86,** 7320–7327 (2014).
7. Katajamaa, M.; Orešič, M. *J. Chromatogr. A* **1158,** 318–328 (2007).
8. Doerr, A. *Nat. Publ. Gr.* **12,** 35 (2015).
9. Teo, G.; Kim, S.; Tsou, C. C.; Collins, B.; Gingras, A. C.; Nesvizhskii, A. I.; Choi, H. *J Proteomics* **129,** 108–120 (2015).
10. Egertson, J. D.; MacLean, B.; Johnson, R.; Xuan, Y.; MacCoss, M. J. *Nat. Protoc.* **10,** 887–903 (2015).
11. Kumari, S.; Stevens, D.; Kind, T.; Denkert, C.; Fiehn, O. *Anal. Chem.* **83,** 5895–5902 (2011).
12. Smith, C. A.; Want, E. J.; Maille, G. O.; Abagyan, R.; Siuzdak, G. **78,** 779–787 (2006).
13. Kolmonen, M.; Leinonen, A.; Pelander, A.; Ojanperä, I. *Anal. Chim. Acta* **585,** 94–102 (2007).
14. Pelander, A.; Ojanperä, I.; Laks, S.; Rasanen, I.; Vuori, E. *Anal. Chem.* **75,** 5710–5718 (2003).
15. Kolmonen, M.; Leinonen, A.; Kuuranne, T.; Pelander, A.; Ojanperä, I. *Drug Test. Anal.* **1,** 250–266 (2009).
16. Akira, K.; Hichiya, H.; Shuden, M.; Morita, M.; Mitome, H. *J. Pharm. Biomed. Anal.* **66,** 339–344 (2012).
17. Halket, J. M.; Waterman, D.; Przyborowska, A. M.; Patel, R. K. P.; Fraser, P. D.; Bramley, P. M. *J. Exp. Bot.* **56,** 219–243 (2005).
18. Li, H.; Cai, Y.; Guo, Y.; Chen, F.; Zhu, Z. J. *Anal. Chem.* **88,** 8757–8764 (2016).
19. Tautenhahn, R.; Patti, G. J.; Kalisiak, E.; Miyamoto, T.; Schmidt, M.; Lo, F. Y.; Mcbee, J.; Baliga, N. S.; Siuzdak, G. 696–700 (2011).
20. Cho, K.; Mahieu, N.; Ivanisevic, J.; Uritboonthai, W.; Chen, Y.; Siuzdak, G.; Patti, G. J. *Anal. Chem.* **86,** 9358–9361 (2014).
21. Lommen, A. *Anal. Chem.* **81,** 3079–3086 (2009).
22. Ma, Y.; Kind, T.; Yang, D.; Leon, C.; Fiehn, O. *Anal. Chem.* **86,** 10724–10731 (2014).
23. Katajamaa, M.; Miettinen, J.; Orešič, M. *Bioinformatics* **22,** 634–636 (2006).
24. Pluskal, T.; Castillo, S.; Villar-Briones, A.; Oresic, M. *BMC Bioinformatics* **11,** 395 (2010).
25. Wei, X.; Sun, W.; Shi, X.; Koo, I.; Wang, B.; Zhang, J.; Yin, X.; Tang, Y.; Bogdanov, B.; Kim, S.; *et al. Anal. Chem.* **83,** 7668–7675 (2011).

26. Worley, B.; Powers, R. *ACS Chem. Biol.* **9,** 1138–1144 (2014).

27. Hernández, F.; Ibáñez, M.; Portolés, T.; Cervera, M. I.; Sancho, J. V.; López, F. J. *J. Hazard. Mater.* **282,** 86–95 (2015).

28. Hernández, F.; Ibáñez, M.; Botero-Coy, A. M.; Bade, R.; Bustos-López, M. C.; Rincón, J.; Moncayo, A.; Bijlsma, L. *Anal. Bioanal. Chem.* **407,** 6405–6416 (2015).

29. Gago-Ferrero, P.; Schymanski, E. L.; Bletsou, A. A.; Aalizadeh, R.; Hollender, J.; Thomaidis, N. S. *Environ. Sci. Technol.* **49,** 12333–12341 (2015).

30. Aceña, J.; Stampachiacchiere, S.; Pérez, S.; Barceló, D. *Anal. Bioanal. Chem.* **407,** 6289–6299 (2015).

31. Schymanski, E. L.; Singer, H. P.; Longrée, P.; Loos, M.; Ruff, M.; Stravs, M. A.; Ripollés Vidal, C.; Hollender, J. *Environ. Sci. Technol.* **48,** 1811–1818 (2014).

32. Krauss, M.; Singer, H.; Hollender, J. *Anal. Bioanal. Chem.* **397,** 943–951 (2010).

33. Zedda, M.; Zwiener, C. *Anal. Bioanal. Chem.* **403,** 2493–2502 (2012).

34. Mizuno, Y.; Sato, K.; Sano, T.; Kurihara, R.; Kojima, T.; Yamakawa, Y.; Ishii, A.; Katsumata, Y. *Leg. Med.* **4,** 207–216 (2002).

35. Sano, T.; Sato, K.; Kurihara, R.; Mizuno, Y.; Kojima, T. **3,** 149–156 (2001).

36. Luo, J.; Lamb, J. H.; Lim, C. K. **15,** 1289–1294 (1997).

37. Nozawa, H.; Minakata, K.; Yamagishi, I.; Hasegawa, K.; Wurita, A.; Gonmori, K.; Suzuki, O.; Watanabe, K. *Leg. Med.* **17,** 150–156 (2014).

38. Sturtevant, D.; Lee, Y. J.; Chapman, K. D. *Curr. Opin. Biotechnol.* **37,** 53–60 (2016).

39. Lagarrigue, M.; Caprioli, R. M.; Pineau, C. *J. Proteomics* **144,** 133–139 (2016).

40. Hunt, N. J.; Phillips, L.; Waters, K. A.; Machaalani, R. *J. Proteomics* **138,** 48–60 (2016).

41. Singhal, R.; Carrigan, J. B.; Wei, W.; Taniere, P.; Hejmadi, R. K.; Forde, C.; Ludwig, C.; Bunch, J.; Griffiths, R. L.; Johnson, P. J.; *et al. J. Proteomics* **80,** 207–215 (2013).

42. Aoyagi, S.; Kawashima, Y.; Kudo, M. *Nucl. Instruments Methods Phys. Res. Sect. B Beam Interact. with Mater. Atoms* **232,** 146–152 (2005).

43. Aoyagi, S.; Oiw, Y.; Kudo, M. *Appl. Surf. Sci.* **231–232,** 432–436 (2004).

44. Yong, W.; Guo, T.; Fang, P.; Liu, J.; Dong, Y.; Zhang, F. *Int. J. Mass Spectrom.* (2017). doi:10.1016/j.ijms.2017.03.005

45. Suni, N. M.; Lindfors, P.; Laine, O.; Östman, P.; Ojanperä, I.; Kotiaho, T.; Kauppila, T. J.; Kostiainen, R. *Anal. Chim. Acta* **699,** 73–80 (2011).

46. Iribarne, J. V.; Thomson, B. A. *J. Chem. Phys.* **64,** 2287–2294 (1976).

47. Dole, M; Mack, L.; Hines, R. L. *J. Chem. Phys.* **49,** 2240–2249 (1968).

48. Colizza, K.; Mahoney, K. E.; Yevdokimov, A. V.; Smith, J. L.; Oxley, J. C. *J. Am. Soc. Mass Spectrom.* **27,** 1796–1804 (2016).

49. Gosetti, F.; Mazzucco, E.; Zampieri, D.; Gennaro, M. C. *J. Chromatogr. A* **1217,** 3929–3937 (2010).

50. Annesley, T. M. *Clin. Chem.* **49,** 1041–1044 (2003).

51. Liang, H. R.; Foltz, R. L.; Meng, M.; Bennett, P. *Rapid Commun. Mass Spectrom.* **17,** 2815–21 (2003).

52. Dupont, A.; Gisselbrecht, J.-P.; Leize, E.; Wagner, L.; Dorsselaer, A. Van. *Tetrahedron Lett.* **35,** 6083–6086 (1994).

53. Berkel, G. J. V.; Zhout, F. *Anal. Chem.* **67,** 3958–3964 (1995).

54. Wick, A.; Fink, G.; Ternes, T. A. *J. Chromatogr. A* **1217,** 2088–2103 (2010).

55. Robb, D. B.; Covey, T. R.; Bruins, a. P. *Anal. Chem.* **72,** 3653–3659 (2000).

56. Itoh, H.; Kawasaki, S.; Tadano, J. *J. Chromatogr. A* **754,** 61–76 (1996).

57. Rosenberg, E. *J. Chromatogr. A* **1000,** 841–889 (2003).

58. Portolés, T.; Sales, C.; Abalos, M.; Sauló, J.; Abad, E. *Anal. Chim. Acta* **937,** 96–105 (2016).

59. Casares, A.; Kholomeev, A.; Wollnik, H. *Int. J. Mass Spectrom.* **206,** 267–273 (2001).

60. Wollnik, H.; Casares, A.; Radford, D.; Yavor, M. *Nucl. Instruments Methods Phys. Res. Sect. A Accel. Spectrometers, Detect. Assoc. Equip.* **519,** 373–379 (2004).

61. Richardson, K.; Hoyes, J. *Int. J. Mass Spectrom.* **377,** 309–315 (2015).

62. Poteshin, S. S.; Zarakovsky, A. *J. Chromatogr. B* **1047,** 39–44 (2016).

63. Poteshin, S. S.; Chernyshev, D. M.; Sysoev, A. A.; Sysoev, A. A. *Phys. Procedia* **72,** 266–273 (2015).

64. Vlasak, P. R.; Beussman, D. J.; Ji, Q.; Enke, C. G. *J. Am. Soc. Mass Spectrom.* **7,** 1002–1008 (1996).

65. Manoravi, P.; Joseph, M.; Sivakumar, N. *Int. J. Mass Spectrom.* **276,** 9–16 (2008).

66. Smith, D. F.; Kiss, A.; Leach, F. E.; Robinson, E. W.; Paša-Tolić, L.; Heeren, R. M. A. *Anal. Bioanal. Chem.* **405,** 6069–6076 (2013).

67. Smith, R. D. *Int. J. Mass Spectrom.* **200,** 509–544 (2000).

68. Liu, G.; Tu, Z.; Wang, H.; Zhang, L.; Huang, T.; Ma, D. *Food Chem.* **227,** 413–421 (2017).

69. Palacio Lozano, D. C.; Orrego-Ruiz, J. A.; Cabanzo Hernández, R.; Guerrero, J. E.; Mejía-Ospino, E. *Fuel* **193,** 39–44 (2017).

70. Giraldo-Dávila, D.; Chacón-Patiño, M. L.; Orrego-Ruiz, J. A.; Blanco-Tirado, C.; Combariza, M. Y. *Fuel* **185,** 45–58 (2016).

71. Makarov, A. **72,** 1156–1162 (2000).

72. Denisov, E.; Damoc, E.; Lange, O.; Makarov, A. *Int. J. Mass Spectrom.* **325–327,** 80–85 (2012).

73. Tebani, A.; Schmitz-Afonso, I.; Rutledge, D. N.; Gonzalez, B. J.; Bekri, S.; Afonso, C. *Anal. Chim. Acta* **913,** 55–62 (2016).

74. Ruzsanyi, V.; Baumbach, J. I.; Sielemann, S.; Litterst, P.; Westhoff, M.; Freitag, L. *J. Chromatogr. A* **1084,** 145–151 (2005).

75. Gallegos, J.; Arce, C.; Jordano, R.; Arce, L.; Medina, L. M. *Food Chem.* **220,** 362–370 (2017).

76. Burnum-Johnson, K. E.; Baker, E. S.; Metz, T. O. *Placenta* 6–11 (2017). doi:10.1016/j.placenta.2017.03.016

77. Boschmans, J.; Lemière, F.; Sobott, F. *J. Chromatogr. A* **1490,** 80–88 (2017).

78. Berezovskaya, Y.; Porrini, M.; Barran, P. E. *Int. J. Mass Spectrom.* **345–347,** 8–18 (2013).

79. Shepherd, D. A.; Marty, M. T.; Giles, K.; Baldwin, A. J.; Benesch, J. L. P. *Int. J. Mass Spectrom.* **377,** 663–671 (2014).

80. Zhang, H.; Liu, H.; Lu, Y.; Wolf, N. R.; Gross, M. L.; Blankenship, R. E. *Biochim. Biophys. Acta - Bioenerg.* **1857,** 734–739 (2016).

81. Fan, R.-J.; Zhang, F.; Chen, X.-P.; Qi, W.-S.; Guan, Q.; Sun, T.-Q.; Guo, Y.-L. *Anal. Chim. Acta* **961,** 82–90 (2017).

82. Negreira, N.; Regueiro, J.; Valdersnes, S.; Berntssen, M. H. G.; Ørnsrud, R. *Anal. Chim. Acta* **965,** 72–82 (2017).

83. Márquez-Sillero, I.; Aguilera-Herrador, E.; Cárdenas, S.; Valcárcel, M. *TrAC - Trends Anal. Chem.* **30,** 677–690 (2011).

84. Criado García, L.; Almofti, N.; Arce, L. *Sensors Actuators, B Chem.* **235,** 370–377 (2016).

85. Shvartsburg, A. A.; Jarrold, M. F. *Chem. Phys. Lett.* **261,** 86–91 (1996).

86. Hudgins, R. R.; Woenckhaus, J.; Jarrold, M. F. *Int. J. Mass Spectrom. Ion Process.* **165–166,** 497–507 (1997).

87. Shvartsburg, A. A.; Liu, B.; Jarrold, M. F.; Ho, K.-M. *J. Chem. Phys.* **112,** 4517 (2000).

88. Causon, T. J.; Hann, S. *J. Chromatogr. A* **1416,** 47–56 (2015).

89. Heptner, A.; Reinecke, T.; Langejuergen, J.; Zimmermann, S. *J. Chromatogr. A* **1356,** 241–248 (2014).

90. Samotaev, N.; Pershenkov, V.; Belyakov, V.; Vasilyev, V.; Golovin, A.; Ivanov, I.; Malkin, E.; Gromov, E. *Procedia Eng.* **87,** 436–439 (2014).

91. Giles, K.; Wildgoose, J. L.; Langridge, D. J.; Campuzano, I. *Int. J. Mass Spectrom.* **298,** 10–16 (2010).

92. Goscinny, S.; Joly, L.; De Pauw, E.; Hanot, V.; Eppe, G. *J. Chromatogr. A* **1405,** 85–93 (2015).

93. Sivalingam, G. N.; Yan, J.; Sahota, H.; Thalassinos, K. *Int. J. Mass Spectrom.* **345–347,** 54–62 (2013).

94. Gonzales, G. B.; Smagghe, G.; Coelus, S.; Adriaenssens, D.; De Winter, K.; Desmet, T.; Raes, K.; Van Camp, J. *Anal. Chim. Acta* **924,** 68–76 (2016).

95. Silveira, J. A.; Ridgeway, M. E.; Laukien, F. H.; Mann, M.; Park, M. A. *Int. J. Mass Spectrom.* **413,** 168–175 (2017).

96. Guevremont, R. *J. Chromatogr. A* **1058,** 3–19 (2004).

97. Zhang, J.; Li, L. F.; Guo, D. P.; Zhang, Y.; Wang, Q.; Li, P.; Wang, X. Z. *Fenxi Huaxue/ Chinese J. Anal. Chem.* **41,** 986–992 (2013).

98. Ruan, Z.; Chen, C.; Chen, R.; Liu, Y.; Wang, X.; Li, S.; Yu, J. *Int. J. Mass Spectrom.* **414,** 8–12 (2017).

99. Glaskin, R. S.; Valentine, S. J.; Clemmer, D. E. *Anal. Chem.* **82,** 8266–8271 (2010).

100. Trimpin, S.; Clemmer, D. E.; Trimpin, S.; Clemmer, D. E. *Anal. Chem.* **80,** 9073–9083 (2008).

101. Barrios-Collado, C.; Vidal-De-Miguel, G. *Int. J. Mass Spectrom.* **376,** 97–105 (2015).

102. Puton, J.; Namiesnik, J. *TrAC - Trends Anal. Chem.* **85,** 10–20 (2016).

103. Ewing, M. A.; Glover, M. S.; Clemmer, D. E. *J. Chromatogr. A* **1439,** 3–25 (2016).

104. Bauer, M.; Ahrné, E.; Baron, A. P.; Glatter, T.; Fava, L. L.; Santamaria, A.; Nigg, E. A.; Schmidt, A. *J. Proteome Res.* **13,** 5973–5988 (2014).

105. Michael A Gillette, and S. A. C. *Nat Methods* **10,** 28–34 (2013).

106. Li, Austin; Gohdes, Mark; Shouy, W. *Rapid Commun. Mass Spectrom.* **24,** 3567–3577 (2010).

107. Montesano, C.; Vannutelli, G.; Gregori, A.; Ripani, L.; Compagnone, D.; Curini, R.; Sergi, M. *J. Anal. Toxicol.* **40,** 519–528 (2016).

108. Decaestecker, T. U.; Vande Casteele, S. R.; Wallemacq, P. E.; Van Peteghem, C. H.; Defore, D. L.; Van Bocxlaer, J. F. *Anal. Chem.* **76,** 6365–6373 (2004).

109. Geromanos, S. J.; Vissers, J. P. C.; Silva, J. C.; Dorschel, C. A.; Li, G. Z.; Gorenstein, M. V.; Bateman, R. H.; Langridge, J. I. *Proteomics* **9,** 1683–1695 (2009).

110. Gillet, L. C.; Navarro, P.; Tate, S.; Rost, H.; Selevsek, N.; Reiter, L.; Bonner, R.; Aebersold, R. *Mol. Cell. Proteomics* **11,** O111.016717-O111.016717 (2012).

111. Johnson, C. H.; Ivanisevic, J.; Benton, H. P.; Siuzdak, G. *Anal. Chem.* **87,** 147–156 (2015).

112. Röst, H. L.; Rosenberger, G.; Navarro, P.; Gillet, L.; Miladinović, S. M.; Schubert, O. T.; Wolski, W.; Collins, B. C.; Malmström, J.; Malmström, L.; *et al. Nat. Biotechnol.* **32,** 219–23 (2014).

113. Tautenhahn, R.; Patti, G. J.; Rinehart, D.; Siuzdak, G. *Anal. Chem.* **84,** 5035–5039 (2012).

114. Benton, H. P.; Wong, D. M.; Trauger, S. A.; Siuzdak, G. *Anal. Chem.* **80,** 6382–6389 (2008).

115. Patti, G. J. *Anal. Chem.* **86,** 1632–1639 (2014).

116. Bunk, B.; Kucklick, M.; Jonas, R.; Münch, R.; Schobert, M.; Jahn, D.; Hiller, K. *Bioinformatics* **22,** 2962–2965 (2006).

117. Broeckling, C. D.; Reddy, I. R.; Duran, A. L.; Zhao, X.; Sumner, L. W.; Division, P. B.; Roberts, S.; Foundation, N.; Box, P. O. *Anal. Chem.* **78,** 4334–4341 (2006).

118. https://www.massbank.jp; April 2017.

119. https://metlin.scripps.edu/index.php; April 2017.

120. https://www.nist.gov; April 2017.

121. Xu, Z.; Sun, X.; Harrington, P. D. B. *Anal. Chem.* **83,** 7464–7471 (2011).

122. Krishnan, S.; Vogels, J. T. W. E.; Coulier, L.; Bas, R. C.; Hendriks, M. W. B.; Hankemeier, T.; Thissen, U. *Anal. Chim. Acta* **740,** 12–19 (2012).

123. Cawley, A. T.; Flenker, U. *J. Mass Spectrom.* **43,** 854–864 (2008).

124. Jackson, P.; Attalla, M. I. *Rapid Commun. Mass Spectrom.* **24,** 3567–3577 (2010).

125. Monroe, M. E.; Tolić, N.; Jaitly, N.; Shaw, J. L.; Adkins, J. N.; Smith, R. D. *Bioinformatics* **23,** 2021–2023 (2007).

126. Nielsen, N. P. V; Carstensen, J. M.; Smedsgaard, J. *J. Chromatogr. A* **805,** 17–35 (1998).

127. Wang, W.; Becker, C. H.; Zhou, H.; Lin, H.; Roy, S.; Shaler, T. A.; Hill, L. R.; Norton, S.; Kumar, P.; Anderle, M. *Anal. Chem.* **75,** 4818–4826 (2003).

128. Radulovic, D.; Jelveh, S.; Ryu, S.; Hamilton, T. G.; Foss, E.; Mao, Y.; Emili, A. *Mol. Cell. Proteomics* **3,** 984–997 (2004).

129. Bellew, M.; Coram, M.; Fitzgibbon, M.; Igra, M.; Randolph, T.; Wang, P.; May, D.; Eng, J.; Fang, R.; Lin, C.; *et al. Bioinformatics* **22,** 1902–1909 (2006).

130. Xiao-jun Li, Eugene C. Yi, Christopher J. Kemp, Hui Zhang, R. A. *Mol. Cell. Proteomics* **4,** 1328–1340 (2005).

131. Zhang, H.; Zhang, D.; Ray, K.; Zhu, M. *J. Mass Spectrom.* **44,** 999–1016 (2009).

132. Dier, T. K. F.; Egele, K.; Fossog, V.; Hempelmann, R.; Volmer, D. A. *Anal. Chem.* **88,** 1328–1335 (2016).

133. Zhu, P.; Tong, W.; Alton, K.; Chowdhury, S. *Anal. Chem.* **81,** 5910–5917 (2009).

134. Myers, A. L.; Jobst, K. J.; Mabury, S. a.; Reiner, E. J. *J. Mass Spectrom.* **49,** 291–6 (2014).

135. Jobst, K. J.; Shen, L.; Reiner, E. J.; Taguchi, V. Y.; Helm, P. A.; McCrindle, R.; Backus, S. *Anal. Bioanal. Chem.* **405,** 3289–3297 (2013).

136. C.Hughey; C.Hendrickson; Rodgers, R.; Marshall, A. *Anal. Chem.* **71,** 4676–4681 (2001).

137. Wu, Z.; Rodgers, R. P.; Marshall, A. G. *Anal. Chem.* **76,** 2511–2516 (2004).

138. Wolf, S.; Schmidt, S.; Müller-Hannemann, M.; Neumann, S. *BMC Bioinformatics* **11,** 148 (2010).

139. Böcker, S.; Letzel, M. C.; Lipták, Z.; Pervukhin, A. *Bioinformatics* **25,** 218–224 (2009).

140. Schwudke, D.; Oegema, J.; Burton, L.; Entchev, E.; Hannich, J. T.; Ejsing, C. S.; Kurzchalia, T.; Shevchenko, A. *Anal. Chem.* **78,** 585–595 (2006).

141. Herzog, R.; Schuhmann, K.; Schwudke, D.; Sampaio, J. L.; Bornstein, S. R.; Schroeder, M.; Shevchenko, A. *PLoS One* **7,** 15–20 (2012).

142. Ronny Herzog, Dominik Schwudke, A. S. *Curr. Protoc. Bioinforma.* **14,** 11–30 (2013).

143. Doerfler, H.; Sun, X.; Wang, L.; Engelmeier, D.; Lyon, D.; Weckwerth, W. *PLoS One* **9,** (2014).

144. Calza, P.; Medana, C.; Carbone, F.; Giancotti, V.; Baiocchi, C. *Rapid Commun. Mass Spectrom.* **22,** 1533–1552 (2008).

145. Hapeshi, E.; Fotiou, I.; Fatta-Kassinos, D. *Chem. Eng. J.* **224,** 96–105 (2013).

146. Hapeshi, E.; Achilleos, A.; Vasquez, M. I.; Michael, C.; Xekoukoulotakis, N. P.; Mantzavinos, D.; Kassinos, D. *Water Res.* **44,** 1737–1746 (2010).

147. Michael, I.; Hapeshi, E.; Michael, C.; Fatta-Kassinos, D. *Water Res.* **44,** 5450–5462 (2010).

148. Michael, I.; Hapeshi, E.; Aceña, J.; Perez, S.; Petrović, M.; Zapata, A.; Barceló, D.; Malato, S.; Fatta-Kassinos, D. *Sci. Total Environ.* **461–462,** 39–48 (2013).

149. Vessecchi, R.; Crotti, A. E. M.; Guaratini, T.; Colepicolo, P.; Galembeck, S. E.; Lopes, N. *Mini-Rev. Org. Chem.* **4,** 75–87 (2007).

150. Mesleh, M. F.; Hunter, J. M.; Shvartsburg, A. A.; Schatz, G. C.; Jarrold, M. F. *J. Phys. Chem.* **100,** 16082–16086 (1996).

151. Campuzano, I.; Bush, M. F.; Robinson, C. V.; Beaumont, C.; Richardson, K.; Kim, H.; Kim, H. I. *Anal. Chem.* **84,** 1026–1033 (2012).

152. Salvador, P. *J. Phys. Chem. C* **111,** 17038–17043 (2007).

153. Fujishima, A.; Zhang, X.; Tryk, D. A. *Surf. Sci. Rep.* **63,** 515–582 (2008).

154. Lee, J.; Choi, W. *Environ. Sci. Technol.* **38,** 4026–4033 (2004).

155. Souissi, Y.; Bourcier, S.; Ait-Aissa, S.; Maillot-Maréchal, E.; Bouchonnet, S.; Genty, C.; Sablier, M. *J. Chromatogr. A* **1310,** 98–112 (2013).

156. Kočí, K.; Obalová, L.; Matějová, L.; Plachá, D.; Lacný, Z.; Jirkovský, J.; Šolcová, O. *Appl. Catal. B Environ.* **89,** 494–502 (2009).

157. Poerschmann, J.; Trommler, U.; Górecki, T. *Chemosphere* **79,** 975–986 (2010).

~ Chapter 5.

Toxicity evaluation of generated transformation products after oxidative treatments.

Since Hignite and Azarnoff [1] first reported in 1977 the presence of clofibrate, salicylic acid and their related metabolites in surface and ground water in sewage treatment plants in the United States, hundreds to thousands of research papers have appeared dealing with their presence and their concentration levels [2–6]. Scientific concern arises from their potential to promote antimicrobial resistance or hazard to the aquatic environment.

It is for this reason that in recent years, as discussed in **Chapter 1** and **Chapter 3** of the present thesis, such a wide variety of removal techniques, most of them employing the hydroxyl radical as the driving removal force, have been developed and optimised in order to efficiently remove these chemicals from the aquatic systems. However, it has been vastly demonstrated, as discussed in **Chapter 4** of this work, the appearance and disappearance kinetics of new chemical entities, also called transformation products (TPs), originated along the application of such water treatment processes. Little is known about the potential toxicity effects of these transformation products. Some investigations carried out to date have demonstrated that these TPs may lead to a toxicity increase [7–12], others have proven that these TPs may not pose an additional hazard to the environment [13–15] while some literature can be found describing opposite results [9,16,17]

It is for this reason that the continuous development of oxidative techniques for the removal of emerging pollutants and related drugs requires efficient bioassays in order to assure the complete decontamination and detoxification of the sample. The present chapter is composed into one general introduction, an experimental section and the discussion of results obtained. In the introduction section will be presented the main biological techniques carried out to date for the toxicity evaluation of environmentally relevant chemicals, as well as a general discussion of previous investigations and main results dealing with the present topic. The experimental deals with the toxicity evaluation of ofloxacin (OFX) transformation products. This work is closely linked to the experimental section presented and discussed in **Chapter 3** and **Chapter 4**, which dealt with the degradation and detection of OFX TPs respectively.

5.1. Introduction

As it has been widely discussed throughout the present thesis manuscript, the use of advanced oxidation processes (AOPs) for the removal of organic and inorganic compounds from water and wastewater matrices lead to the formation of non-desired *by-products* [14,17–20] if the process is not operated during the minimum time required for its complete depletion. The formation and presence of such chemicals may unfortunately render more toxicity than the parent compound(s), thus, needing to assure during the whole process that toxification of the treated water is not taking place. Past researches used to monitor toxicity on the bases of biodegradability**.** However, this parameter has demonstrated to lead to misinterpretations to what toxicity is refereed. Today, scientists have, within reach, a wide battery of bioassays and cytotoxicity tests that can be performed using different organisms: invertebrates, microorganisms, cell lines, whole animals and such a wide variety of end-points. All of them constitute a valuable and non-confusing tool to estimate the potential hazard of these new chemical entities. Even though none of them, apart from animal testing, would reliable predict *in-vivo* toxicity, these tests are completely accepted to constitute an useful tool to monitor toxicity changes in treated solutions and rank compounds on the basis of the toxicity response.

Bioassays and *in-vitro* assays rely on measuring the response (luminescence, oxygen consumption, viability, etc.) of the organisms of study to a control sample. Bioassays can be classified on the basis of the organism that has been incorporated to the assay: invertebrates, plants and algae, microorganisms and fishes. Cytotoxicity tests, however, depend on the cell line used and the end-point to be measured, for instance, cell lines can be tumoral and/or primary and the end-points, amongst others, can be the 3-[4,5-dimethylthiazol-2-yl]-3,5-diphenylformazan test (MTT test) or the neutral red assays.

5.1.1. Factors affecting toxicity

Independently of which toxicity screening technique is selected, there are several factors, for instance, concentration, duration and frequency, synergism and metabolism that should be noted and introduced before going forward on the development of the present chapter.

Duration and frequency

On the basis of the duration and the frequency of exposure, four different categories can be distinguished [21]:

- *Acute toxicity*: This term refers to short term exposure (normally for less than 24 hours).

- *Sub-acute toxicity*: This term refers to the experimental conditions by which (a) chemical(s) has been administrated in repeated times but for less than one month.

- *Sub-chronic and chronic toxicity*: These terms refer to the experimental conditions tested for repeated exposure of the substance(s) tested for less than three months (sub-chronic) and more than three months (chronic) respectively.

It is clear, then, that short-term toxicity may result in quite different results than those experiments carried out after repeated exposures [22–27]. It is for this reason that results have always to be accompanied with the exposure time to which the substance(s) have been in contact with the organism of interest.

Synergism

The combination of different substances to the same test may influence the results obtained, for instance, potentiation occurs when one substance, given alone, does not have a toxicity effect, but when given in combination with another substance, the first makes the second agent much more toxic. On the other side, antagonism occurs when a number of chemicals, administered together, interfere with the action of one another and results in an overall toxicity decrease than if the agents were given alone. As what occurred with administration frequency, it is of sum importance to know, as much as possible, the composition of the sample. Both effects have well been demonstrated with bioassays such as *Vibrio fischeri* or *Daphnia magna* [28–32] or cytotoxicity tests employing animal or human derived cell lines [33–39].

Presence of a metabolising system

The presence of a metabolising system can deeply influence the toxicity results obtained. Although biotransformation reactions are generally linked to a detoxification processes, it has been widely demonstrated that some chemicals are non-toxic by themselves but, when modified by the metabolising system [40–42], the generated metabolites render more toxicity than the parent compound. This is the case, for example, of acetaminophen [43,44], halothane [45,46], isoniazid [47,48] and diclofenac [49–51]. Two types of reactions are involved, described as phase I and phase II reactions [52–54]. Phase I reactions involve oxidation, reduction and hydrolysis. Their main function is to make the substance more water-soluble and thus, more suitable for excretion. Phase II are conjugation reactions which involve the substitution of functional groups of the substance to make them more lipophobic (water soluble). Phase I reactions are carried out by the enzyme system of mono-oxygenases containing the cytochrome P-450 (CYP450). This group of enzymes insert one atom from molecular oxygen to the drug while the remaining atom, in combination with two protons, is reduced to water. Other reactions taken by the same group of mono-oxygenases containing the CYP450 to be considered too are: -N, -S, O-dealkylation, aromatic and aliphatic oxidation. The most important phase II reactions are: the addition of a glucuronide and glutathione group by glucoronyl transferase and glutathione S-transferases respectively. The first group of enzymes attaches the glucoronide to aliphatic and aromatic alcohols, mercaptans, acids, primary and secondary aliphatic and aromatic amines. The last group, attaches a molecule of glutathione (a tripeptide) to the substrate by a thioether bond. Then, two aminoacids are lost from the peptide, finally adding an acetyl group from a mercapturic acid derivative.

5.1.2. Bioassays

Once considered some of the critical facts affecting the toxicity of xenobiotics, a summary, depicted in **Table 5.1**, shows the most updated research dealing with the (eco)toxicological evaluation of the most representative fluoroquinolones, the group of antibiotics of concern of the research carried out. **Table 5.2**, in addition to **Table 5.1**, tries to emphasise the importance of the toxicity evaluation of water samples (both synthetic and raw wastewater) submitted to advanced oxidation processes: Fenton, photolysis, photocatalysis, etc. In the following pages, both bioassays and cytotoxic effects will be reviewed.

As it can be easily seen from both tables, bioassays are, by far, the most widely used tests to carry out the toxicity evaluation of both the parent drug and the generated transformation products. Going deeply into both tables, it is quite clear that most of these studies rely on invertebrates, mainly *Daphnia,* and on microorganisms, being always *Vibrio fischeri* the main focus of attention.

Table 5.1. Toxicity tests carried out on fluoroquinolones.

Organism	**Target**	**Method**	**Comments**	**Ref.**
Daphnia magna	Ciprofloxacin Enrofloxacin	ISO1996	EC_{50}: 87.14 mg L^{-1} for ciprofloxacin and 16.34 for enrofloxacin. Binary mixtures of both fluoroquinolones diminished the obtained EC_{50} value up to a 50%.	[55]
Daphnia magna	Enrofloxacin	ISO1996	Mortality of later generations (up to 4) of *D. Magna* exposed to 2 mg L^{-1} of enrofloxacin increased up to 100%.	[56]
Daphnia magna	Ciprofloxacin	ISO1996	Acute toxicity; 24 h EC_{50} > 192 mg L^{-1}; Precipitation of ciprofloxacin before reaching the half-maximum inhibitory effect on the tested conditions.	[57]
- *Vibrio fischeri* - *P. putida* - *P. subcapitata* - *T. thermophila*	Ofloxacin	- ISO 11348-3 - ISO 10712 - European Guideline OECD TG - Operational Procedure Guidelines of Protoxkit FTM	The sensitivity order found for the exposure of ofloxacin was as follows: *P.putida*>*P. subcapitata*>*T. thermophila*>*V.fischeri*. *P.putida* presented an EC_{50} of 0.11 mg L^{-1}, *P.subcapitata* 1.9 mg L^{-1} whereas *T. thermophila* and *V.fischeri* presented EC_{50} values over 100 mg L^{-1}.	[9]
Vibrio fischeri	Ciprofloxacin	ISO 11348-3 (Microtox)	Prior the toxicity assays, *Vibrio fischeri* was incubated for 16-22 hours. The IC_{50} found was 5600 mg L^{-1}.	[58]
Vibrio fischeri HepG2 cells	Ciprofloxacin	ISO 11348-3 (Microtox) Comet assay	The concentrations tested on HepG2 cells using the comet assay ranged from 10 ng $L^{-1}$to 100 µg L^{-1}. These concentrations did not induce DNA damage. On Vibrio fischeri, 100 µg·L^{-1} caused. 40% inhibition.	[59]
Vibrio fischeri	Ciprofloxacin	Modified ISO/CD 11348-3 and Lumistox LCK 482	Ciprofloxacin showed no effects against the target point in a concentration up to 0.3 mg L^{-1}.	[60]

Table 5.2. Toxicity tests carried out in evaluating the degradation of fluoroquinolones.

Organism	Target	Degradation method	Comments	Ref.
Daphnia magna	Ofloxacin	**Sonolysis, photocatalysis, sonocatalysis, sonophotocatalysis** 300 mL; light source (9 W/78, UV-A lamp, 3.16 W m^{-2}); power density: 130–640 W L^{-1}; sonolysis power and frequency: 400W and 20 Hz; [ofloxacin]= 10 mg L^{-1}	20 transformation products were tentatively identified after the degradation of ofloxacin. Slightly higher toxicity (10-20%) after 24 h of exposure compared to the untreated solution was observed for the sonophotocatalytically treated samples. After 48 h exposure, the toxicity dramatically increased (up to 60%).	[16]
Daphnia magna	Ofloxacin	**Solar fenton and solar TiO_2** [ofloxacin]= 10 mg L^{-1} 1 kW Xenon lamp; 272 W m^{-2} **Solar Fenton** pH 3; 35% *w/w* H_2O_2; **Solar TiO_2** pH 8; [TiO_2] = 0.25 - 4 g L^{-1}	The spiked solution of ofloxacin at a concentration tested showed no toxicity to the *end-point* chosen in this study. Treated solutions shows slight toxicity (24h) compared to the parent drug (up to 20%) and high toxicity in solutions treated for 48 h (up to 90%). Solar TiO_2 treatment has a maximum toxicity (25%) after 48 h exposure.	[18]
QSAR prediction	Ofloxacin	**Solar fenton and solar TiO_2** [ofloxacin]= 10 mg L^{-1} 1 kW Xenon lamp; 272 W m^{-2} **Solar Fenton** pH 3; 35% *w/w* H_2O_2; **Solar TiO_2** pH 8; [TiO_2] = 0.25 - 4 g L^{-1}	Fourteen transformation products were detected. However, this number varied as a function of the pH used to carry out the degradation treatment. The QSAR prediction depicted that these TPs were not harmful (>100 mg L^{-1}) with the exception of 2 by-products which appeared to be harmful (chronic toxicity) to fish, daphnid and algae.	[18]

Table 5.2 ***(continued).*** Toxicity tests carried out in evaluating the degradation of fluoroquinolones.

Organism	**Target**	**Degradation method**	**Comments**	**Ref.**
- *Vibrio fischeri* - *P. putida* - *P. subcapitata* - *T. thermophila*	Ofloxacin	**Ozone** Water flow rate: 142 mL min^{-1} gas flow was 390 mL min^{-1}. Ozone dosage was 145 mg O_3 L^{-1} of wastewater (mgL^{-1}).	Twelve transformation products were found during the ozonation of ofloxacin. The toxicity for *P. Putida* and *P. Subcapitata* was reduced with the increasing ozone dosage. *T. thermophila* showed no inhibition before and after the water treatment. *V.fischeri* showed up to a 50% inhibition until its complete depletion at the end of the photocatalytical treatment.	[57]
Vibrio fischeri Closed bottle test (biodegradability)	Ciproloxacin	**Photolysis** 2.5 L solution; pH 9; 6 mg L^{-1} ciprofloxacin ; 30ºC ; 150W mercury lamp	Ciprofloxacin TPs were not biodegradable and toxic for the bacteria present. No differences were observed respect to the parent drug and irradiated samples did not cause more luminescence inhibition than the parent drug.	[59]
Escherichia Coli	Cirpofloxacin	**Photolysis** 200 mL solution; pH 6; 100 µM ciprofloxacin, 25ºC ; 450 W O_3 free xenon arc lamp **Photocatalysis** Equal to photolysis + 500 mg L^{-1} TiO_2 nanoparticles	8 TPs were identified after the treatments. The depletion of ciprofloxacin results in a decrease of the antibacterial efficacy suggesting that ciprofloxacin TPs do not retain the same antibacterial efficacy than ciprofloxacin.	[60]

Table 5.2 *(continued).* Toxicity tests carried out in evaluating the degradation of fluoroquinolones.

Organism	Target	Degradation method	Comments	Ref.
Vibrio fischeri	Enrofloxacin	**Catalytic wet air oxidation (CWAO)** 25 mL solution containing 2 mg L^{-1} enrofloxacin; 0.5 MPa O_2; 120 min treatment **Ozonation** 7.3 L h^{-1} ozone 1.4 L reactor; 2 mg L^{-1} enrofloxacin 60 min treatment.	11 enrofloxacin TPs were proposed. For CWAO treatment, after 120min reaction time the BOD_5/COD relationship showed that enrofloxacin TPs were more biodegradable than the parent drug. Moreover, *V. fischeri* showed 43% inhibition at the beginning of the process and it was reduced to 12% after 120 min treatment. The ozonation clearly showed a clear toxicity increase as a function of ozonation time (from 8% to 50% inhibition).	[61]
Vibrio fischeri	Ciprofloxacin Enrofloxacin Danofloxacin Marbofloxacin Levofloxacin	**Photolysis under solar light** 500 mL of urban WWTP secondary effluent; pH 6.9; Solar simulator set at a power factor 250W m^{-2} 50 µg L^{-1} of each fluoroquinolone 20 µg L^{-1} danofloxacin	After the degradation of individual fluoroquinolones, the presence of transformation products lead to a toxicity increase of the overall solution (up to a 15%) with the exception of levofloxacin and marbofloxacin which lead to a toxicity increase of 60 and 40% respectively. *Vibrio fischeri* appeared to overcome the toxic stress to what was submitted after 24 hour incubation time.	[62]
Pseudomonas putida *Vibrio fischeri* HepG2 cells	Ofloxacin	**Photolysis; TiO_2 photocatalysis** 750 mL solution [OFX] = 20 mg L^{-1} Mercury vapour lamp 150W [TiO_2] = 1 g L^{-1}	Untreated solutions (20 mg L^{-1} ofloxacin) caused high inhibition to both *P. putida* and *V, fischeri* (94 % and 90% respectively). After irradiation of the solution, toxicity decreased up to approximate 20 % inhibition for both toxicity tests. Cytostasis to the HepG2 cell line did not show remarkable effects before and after the irradiation of the ofloxacin solution.	[63]

Contrary to cytotoxic assays, these tests are well established and standardised by ISO and OECD guidelines, which make them very attractive to the scientific community in order to compare results assay to assay and laboratory to laboratory. Moreover, bioassays pose different advantages in respect to *in-vitro* tests: more suitable for routine toxicity testing, lesser susceptible to contaminations, more sensitive to toxicants and usually faster, being possible to acquire toxicity data in a day or less.

5.1.2.1. Invertebrates

By far, *Daphnia magna* is the most used invertebrate organism for the toxicity evaluation of water and wastewater treatment effluents. *Daphnia magna* is a planktonic invertebrate belonging to the phylum of Arthropods. They can be easily found in freshwater like ponds and lakes, but they can also inhabit flowing water. They prefer the warm and eutroph littoral zones. *Daphnids* are easy to culture, they have a quick reproduction circle (parthenogenic reproduction), and are very sensitive to pollutants, making them very attractive to toxicity testing. The toxicity testing procedure is well established and standardised (USEPA 2002; ISO 1996a). *Daphnids* are exposed to the contaminants under controlled conditions and living *daphnias* are counted after the testing period: 24 and 48 hours for acute toxicity and 21 days for chronic toxicity.

5.1.2.2. Microbial techniques

Several microbial techniques can be found and divided in the basis of the mechanism of response: 1) capacity of microorganisms to transform carbon, sulphur and nitrogen [64,65]; 2) enzymatic activity [66,67]; 3) growth inhibition (reduced ability to grow or multiply in an specific zone) [68,69]; 4) radiolabelled substrates uptake activity [70–72]; 5) oxygen consumption [73–75] and 6) luminescence inhibition [76–90]. Amongst these six categories, the capability of transforming micronutrients, the respiration inhibition test and the luminescence inhibition are the most representative and most used techniques in ecotoxicological studies.

The first category of microbial techniques mainly relies in the assimilation and transformation of carbon and nitrogen. It describes the possibility for bacteria to growth once they have been inoculated with the water or wastewater to which the potential hazard wants to be studied. If the rate of carbon and nitrogen transformation decreases in the treated samples in respect to the control, the study implies adverse effects for the studied chemicals (OECD guidelines no.216 and 217 (OECD 2000a; OECD 2000b).

The respiration inhibition test is of high interest to study the toxicity of chemicals to activated sludge. This test consists in measuring the respiration (carbon and/or ammonium oxidation) of microorganisms (mainly bacteria) after the incubation of the test compound. The respiration rate of microorganisms is measured with an oxygen electrode (3h exposure following the OECD guideline) after having incubated the test chemicals. Different exposure times may be tested in order to study the effect of incubation time on the toxicity observed or if the concentration of the tested chemicals cannot be maintained and guaranteed over time (*e.g.* the molecule is rapidly transformed or degraded under the studied conditions) [73–75].

Even though these bioassays have been widely employed, the luminescence inhibition test has been the method of choice in the past years (**Table 5.2**), being the target of choice due to the numerous advantages it poses [79]. For instance, several instruments are commercially available in the market (Microtox [80,81], LumisTox [82,83], BioTox [84,85]). These tests are easy to use, requiring very short exposure times (an indicative toxicity value can be obtained within 5 minutes and being 30 minutes the maximum exposure time), they are highly reproducible and offer great sensitivity to the exposure of toxicants.

Vibrio fischeri is a marine luminescent bacterium that can be found in small amounts in the ocean and in big populations in symbiosis with different marine animals such as the squid, *Euprymna scolopes* [86–88]. Young squids allow in *Vibrio fischeri* into its light organs where they are provided with all of the nutrients needed to survive. This animal has the ability to control its light emittance by releasing or admitting *Vibrio fischeri* in its light organs: it generally reduces its concentration during the day while at night, as the squid is a night-feeder, it may allow in the luminescent bacterium and increase its light emittance [86–88].

The principle of operation of those luminescent assays relies on the light output of the used microorganisms which emit light as a consequence of their respiration [88–90]. In *Vibrio fischeri*, luminescence is produced when the protein luciferase converts the reduced flavin mononucleotide ($FMNH_2$), O_2 and an aliphatic aldehyde (RCHO) to flavin mononucleotide (FMN), water and an aliphatic acid (RCOOH), as depicted by **Equation 5.1**. When exposed to chemicals (or mixtures of chemicals) which are toxic to bacteria, the electron transport system or the cell membrane integrity can be drastically damaged and, as a consequence, result in the reduction of the light output.

$$O_2 + FMNH_2 + RCHO \xrightarrow{luciferase} H_2O + FMN + RCOOH + \text{light (490 nm)}$$

Equation 5.1. *Vibrio fischeri* luminescence mechanism

Despite all the advantages it may pose, the bioluminescence inhibition assay is controversial in ecotoxicology since its ecotoxicological relevance is still under question since *Vibrio fischeri*, a marine bacterium, cannot be used to emulate the behaviour of higher terrestrial organisms [76–78].

Hence, in order to overcome the mentioned limitations *Vibrio fischeri* may have, ecotoxicological studies carried out in the past few years have started to include *in-vitro* cytotoxicity tests performed using animal or human cell lines and measuring their viability using different end-points.

5.1.3. Cytotoxicity tests

Cell lines and primary cell lines are widely used for toxicity testing of any chemical of interest and, as a consequence of the mentioned limitations of conventional ecotoxicity tests, they have been increasingly used in environmental studies, especially those dealing with the transformation of xenobiotics or drugs of abuse via oxidative or biological treatments [91–94].

Many types of cells are commercially available and can be grown from a wide variety of tissues and organisms. The American Type Culture Collection (A.T.C.C) has, by far, the most extensive collection of cell lines, any of which, may be relevant for a concrete cytotoxic evaluation. Even though the ATCC repository consists of over 3600 cell lines from over 150 different species, two main categories of cells can be found: primary cells and cell lines (or stem cells).

Primary cultures consist of cells that have been derived from a living organism and are maintained for growth *in vitro* [95,96]. Primary cells are believed to be more biologically relevant than cell lines in order to study human and animal biology (closer to an *in vivo* model), as demonstrated by Rodríguez-Antona *et al.*, Alge *et al.* and Pan *et al.* [97–99] on the concentration of proteins responsible of metabolism. Primary cells can be divided in two types: adherent or suspension. Adherent cells are derived from tissues of organs and are attachment-dependant to grow. On the other side, suspension cells are derived from blood and are anchorage-independent cells (not requiring attachment for their growth). Once adapted to *in vitro* culture conditions, primary cells undergo a limited number of cell passages before entering senescence.

Cell lines that have been immortalized by tumorigenic transformation can undergo unlimited cell division and have an infinite lifespan. It is because their ability to proliferate indefinitely that they have been used as a cost-effective tool in basic research. These cells offer several advantages over primary cells in addition to those already mentioned (cost effective, easy to use): they avoid ethical concerns associated with the use of animal and human tissue and provide more reproducible results in comparison to primary cells [95,96,100,101]**.**

Depending on the side-effect that it is desired to be found or demonstrated, tests on a particular tissue or specific animal can be performed, using either cell lines or primary cells. The present thesis has focused its research on human cytotoxicity, concretely hepatoxicity (liver, using HepG2 cells), nephrotoxicity (kidney, using HK-2 cells) and skin (fibroblasts, primary cells).

Hepatoxicity

The liver is the major site of biotransformation of xenobiotics. It is the first organ receiving the blood containing the chemical(s) of study. In studying hepatotoxicity, it is of sum importance to know the normal liver functions to detect liver injuries. Amongst the most common human liver cell lines, hepatocytes retain most of the metabolic capabilities of the intact liver [102] and thus allow ADME studies on metabolism of drugs and other new chemicals. Even though the human epithelial hepatoblastoma cell line HepG2 has been found to be less sensitive than human hepatocyte primary cultures when studying cytotoxic and genotoxicicity, it constitutes a first great tool to study the possible adverse effects of chemicals in this organ [103–106]. Several studies have compared the metabolic capabilities of primary hepatocytes and HepG2 cells, showing that even at low CYP levels, they are able to uptake and transform the chemicals under investigation [103–106].

Nephrotoxicity

The structure and function of the kidneys make them particularly interesting for toxicity screening, since they are susceptible to induced injuries after their exposure to xenobiotics. Perhaps, the most commonly used cell lines for such studies are MDCK and LLC-PK1, dog and pig kidney lines respectively. In humans, the renal proximal tubular cell line HK-2 was firstly derived by Ryan *et al.* [107] from an adult male. This cell line retains most of the morphological and biochemical characteristics of an adult male, their ability to gluconeogenesis, etc. [107]. These facts, in addition to their ease of culturing and sub-culturing, these cells are the most suitable and the most used for carrying out *in-vitro* toxicity studies on human kidneys [108–110]. Since then, several studies have appeared dealing with the comparison of HK-2 cells with primary kidney cells from different organisms to compare nephrotoxicity responses, as well as metabolism capabilities, as stated by Guness *et al.*, [111].

Fibroblasts

Fibroblasts are heterogeneous multifunctional cells which play an important regulatory role in wound healing and developmental processes. These cells are dispersed throughout the body where they secrete a non-rigid extracellular matrix rich in collagen and are responsible for the architectural framework of the body. These cells belong to the family of connective-tissue cells which play a key role in the support and repair of almost every tissue and organ. When a tissue is injured, the fibroblasts nearby proliferate, migrate into the wound, and produce large amounts of collagenous matrix, which helps to isolate and repair the damaged tissue. Their ability to face injuries may explain why fibroblasts are one of the easiest cells to grow in lab cultures, a fact that has made them to be one of the most used cells in toxicological studies. Hence, it might be for this reason that Melo *et al.* [112] studied the cytotoxicity of river effluents using V79 fibroblasts (hamster) and the Algae *Selenastrum capricornutum*. Their investigation found hamster V79 fibroblast cells to be a valuable tool for acute toxicity assessment since they appeared to be more sensitive than *S. capricornutum*. Moreover, this research also highlighted the need of using several organisms and assays for the monitoring the detoxification process, since the reduction of TOC and the chronic toxicity towards *S. capricornutum* did not result in the reduction of cytotoxicity.

5.1.4. Toxicological end-points

Cell-based assays are being used every day in culture labs for the screening of hundreds to thousands of chemicals in order to determine if the test molecules have effects on cell proliferation or show direct cytotoxic effects that eventually lead to cell death. Hence, several end-points can serve to estimate *in-vitro* toxicity. The most important and representative tests are: colony formation, dye inclusion/exclusion, membrane integrity, enzyme leakage, respiration and glycolysis, intracellular enzyme activity, colorimetric, and fluorometric tests.

In the present thesis, the colorimetric assay MTT [3,(4,5-dimethyl-thiazol-2-yl)-2,5-diphenyltetrazolium bromide] was the main point of toxicity estimation *in-vitro*. It is for this reason that, in the following lines, a brief revision on the available colorimetric assays will be discussed, giving special emphasis to the method of choice for the present thesis (the MTT assay). These are the neutral red, the cristal violet and the MTT assay.

The Neutral Red (NR) method developed by Borenfreund and Puerner in 1984, [113] quantifies surviving cells by incubating them with the neutral red dye (**Figure 5.1**). This cationic dye penetrates cell membrane by non-ionic passive diffusion and concentrates in the lysosomes, where it binds by electrostatic hydrophobic bonds to phosphate groups of the lysosomal matrix.

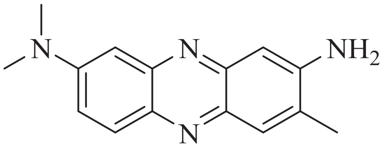

Figure 5.1. Chemical structure of neutral red dye.

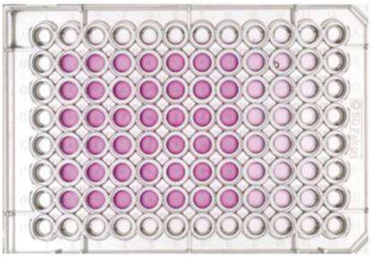

Figure 5.2. Plate after NR incubation. From left to right, toxicity increases.

The dye is then extracted from the viable cells using acidified ethanol, and the absorbance of the solubilised dye (**Figure 5.2**) is quantified using a spectrophotometer. This method has been used for a such wide variety of *in-vitro* toxicity screening of chemicals, such as heavy metals, environmentally relevant compounds, etc.

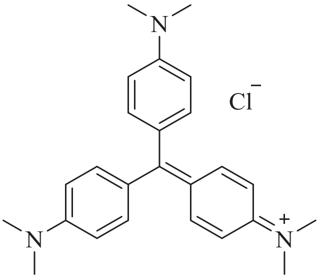

Figure 5.3. Triphenylmethane dye used for the CV assay

The Crystal Violet (CV) assay is based in the triphenylmethane dye (4-[(4-dimethylaminophenyl)-phenyl-methyl]-N,N-dimethyl-aniline), shown in **Figure 5.3**.

Even though this assay was developed to quantify the cell number in a monolayer, as a function of the absorbance taken up by cells, this assay has been now used for estimating cytotoxicity or cell death produced by chemicals, drugs, etc. This dye stains

DNA and the colour of the dye depends on the pH of the solution. Once solubilised, the amount of dye taken-up by cells and the intensity of the colour produced is proportional to cell number.

Finally, the most extensively validated and used of the available colorimetric assays is the MTT assay. Mossman [114], in 1983, used this semi-automated, colorimetric assay to measure cytotoxicity in lymphocytes. The assay was reported to detect living cells and the signal observed had a direct relationship to the number of living cells. One of the main advantages of this assay is that plates where cells are grown can be easily read on a multiwell scanning spectrophotometer with a high degree of precision.

The basis of this assay is that MTT [3,(4,5-dimethyl-thiazol-2-yl)-2,5-diphenyltetrazolium bromide]' a soluble yellow dye, is metabolized by the enzyme succinate dehydrogenase in the mitochondria of living cells, to generate a dark blue insoluble formazan product **(Equation 5.2)**. The precipitate formed can then be solubilised with a variety of methods: acidified isopropanol, DMSO, dimethylformamide, sodium dodecyl sulphate (SDS), and combinations of detergent and organic solvents. Once solubilised, plates (**Figure 5.4**) can be easily read on an automatic plate reader.

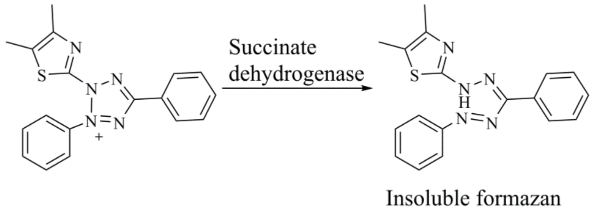

Equation 5.2. Formation of insoluble formazan by succinate dehydrogenase.

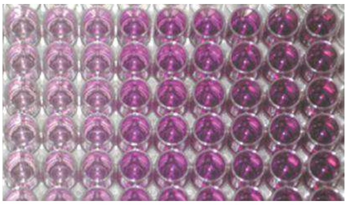

Figure 5.4. Plate after MTT incubation. From left to right, toxicity decreases.

The incubation of the MTT salt with cells usually lasts between 1 to 2 hours before the solubilisation of the formazan precipitate. Some studies have used longer incubation times of the tetrazolium salt resulting in an increased accumulation of colour and an increased sensitivity. However, this strategy for increased sensitivity works up to a point where the cytotoxic nature of the tetrazolium salt slows down the metabolism of viable cells [115–117]. The assay has been successfully tested on an extensive range of cell lines, human and animals, showing linear relationships between cell number and the production of the metabolite formazan.

5.2. Experimental work

As it has been widely discussed along the present thesis, titanium (IV) oxide photocatalysis was used to conduct the photocatalytical degradation of four pharmaceuticals drugs (**Chapter 3**) and ofloxacin transformation products were exhaustively evaluated by means of liquid chromatography coupled to (tandem)-high resolution mass spectrometry (**Chapter 4**). Having characterised these transformation products, the present chapter wants to explore their environmentally and human potential hazard if these were introduced into the aquatic environment.

It is for this reason that, the present work made use of two end-points: *Vibrio-fischeri*, a marine algae extensively used in environmental applications and the MTT assay using three human cell lines. The selected cell lines were: HepG2 and HK-2 (tumoral cells) and fibroblasts (normal cells). The criteria to select these cell lines rather than others will be discussed along the text.

The main experimental work, after having carried out OFX photocatalysis, was divided in four subtasks: (I) estimation of ofloxacin's half maximum inhibitory effect (IC_{50}) under the studied conditions; (II) toxicity kinetics of OFX photocatalysis. Withdrawn samples were submitted to toxicity testing in order to study the toxicity evolution of the photocatalytical process; (III) separation of the generated TPs by preparative HPLC; (IV) individual testing of isolated transformation products. In order to conclude the experimental section, samples separated by preparative HPLC and incubated with the selected cells were analysed by UHPLC-(/MS)HRMS in order to know whatever these cells had metabolism or not against the incubated chemicals.

5.2.1 Experimental section

5.2.1.1 Chemicals and reagents

Ofloxacin (OFX), deuterated ofloxacin (OFX-d_3) and TiO_2 P25-Degussa were purchased from Sigma-Aldrich (Steinheim, Germany). LC/MS grade acetonitrile and water were obtained from Fluka (Steinheim, Germany), while formic acid (98 – 100%) was purchased from Merck (Darmstadt, Germany). TiO_2 was Aeroxide® TiO_2 P25 (anatase:rutile 80:20, particle size 21 nm and 50 m^2 g^{-1} BET area). Nitrogen (99.995% pure) supplied by Air Liquide (Barcelona, Spain) was used as the API gas and as collision-induced dissociation gas (CID gas) in the MS/HRMS experiments. DMEM and DMEM:F12 were purchased at Thermo Scientific (Thermo Fisher Scientific, USA). Fetal bovine serum, l-glutamine, penicillin, streptomycin, EFG (epidermal growth factor), hydrocortisone, insulin and sodium selenite were purchased from Sigma-Aldrich (Steinheim, Germany).

5.2.1.2. Photocatalysis experiments

Photocatalytic experiments with artificial irradiation were performed in a 600 mL borosilicate 3.3 photochemical reactor (Trallero&Schlee, Barcelona, Spain). Photocatalytic experiments with suspended and supported TiO_2 P25 nanoparticles were carried out as follows: 350 mL of an aqueous solution containing 10, 62.5 or 500 mg L^{-1} of OFX and the appropriate amount of TiO_2 NPs was added so as to have the desirable catalyst loading of 250 mg L^{-1}. The resulting suspension was loaded into the photochemical reactor and sonicated for 30 min in darkness to ensure the homogeneous dispersion of the TiO_2 NPs and the complete equilibration of adsorption/desorption of the substrate on the catalyst surface. The solution was then irradiated using 4 UVA lamps of 25W (Radium Ralutec, 9W/78, 315–400 nm, λ_{max} = 365 nm) placed around the reactor, providing a total UV irradiation at the center of the solution in the 0.8-1.1 mW cm^{-2} range. UV irradiation was measured with an UV light meter YK-35UV (Lutron, Barcelona, Spain). Temperature and pH were maintained at 25±2ºC and 7 repectively and the solution was stirred at 200 rpm. To follow the kinetic evolution of photoproducts, 14 samples were withdrawn from the reactor: 0, 5, 10, 15, 20, 25, 30, 60, 90, 120, 150, 180, 210 and 240 min.

5.2.1.3 LC-MS/HRMS conditions

Ultra-high performance liquid chromatography (UHPLC) was performed on an Accela HPLC system (Thermo Fisher Scientific, USA) equipped with a quaternary pump, an autosampler and a column oven. A BEH C18 column (100 × 2.1mm and 1.7 µm particle size; Waters, USA) was used with a flow rate of 400 µL min^{-1} and held at 40 ºC. Solvents were H_2O (solvent A) and CH_3CN (solvent B) both acidified with 0.1% formic acid (*v/v*). The gradient elution program was: 10% B isocratic for 1 min, then in 5 min solvent B was risen up to a 90% and held for 1 min; finally the system went back to initial condition in 1 min. The HRMS analysis was performed in a Q-Exactive Orbitrap (Thermo Fisher Scientific, USA) equipped with a thermally assisted electrospray ionization source (H-ESI II). The operating parameters were as follows: ESI voltage was 3.5 kV; capillary and vaporizer temperatures were 320^{o} C; sheath gas, auxiliary gas and sweep gas flow rate were 40, 10 and 2 au (arbitrary units) respectively, and the tube lens was held at 50 V. For targeted tandem MS experiments (MS/HRMS), nitrogen was used as collision gas (1.5mTorr), and the normalized collision energy (NCE) ranged from 20 to 60%. The mass spectrometer was operated in profile mode (scan range, *m/z* 100-1000) with a resolving power of 70000 FWHM (*full width half maximum*) (at *m/z* 200) and an automatic gain control setting of 3×10^6 with a maximum injection time of 200 ms.

5.2.1.4. Sample fractionation

Sample fractionation was carried out with a semi-preparative HPLC consisting on a binary pump (Binary Gradient Module 2545, Waters, USA) and an autosampler. An X-Bridge preparative C18 OBD column (100×19 mm and 5 µm particle size; Waters, USA) was used with a flow rate of 20 mL min^{-1} and held at room temperature. Solvents used in the gradient elution program were H_2O (solvent A) and CH_3CN (solvent B) both acidified with 0.1% formic acid (*v/v*). The gradient elution program was as follows: started at 5% A, then in 14 min, solvent A was risen up to a 95 % and held for 0.5 min; finally, the percentage of solvent A was reduced to a 5% in 0.5 min and was held for 4 minutes until reequilibarion of the system. The instrument was coupled to the Sample Manager 2767 (Waters, USA), with an UV-Vis detection (UV/Visible Detector 2489; Waters, USA) monitoring two wavelengths (220 and 260 nm) and a single quadrupole mass spectrometer (Micromass ZQ2000; Waters, USA) operated in the positive ESI ion mode and scanning in full scan mode (*m/z* 150 - 600). For each collected fraction, the organic solvent was removed under vacuum, and water was removed by freeze-drying. Individual fractions were then divided in two fractions for different purposes: the first part was devoted to in vitro assay while the second one was used to evaluate its concentration in the solution submitted to toxicity testing. Since standards of photoproducts were not available, quantitation was performed using OFX-d_3 as internal standard (10 mg L^{-1}). When possible, it was assumed that the protonation site of the generated photoproduct was the same as OFX-d_3, thus, assuming equivalent response factors.

5.2.1.5. Bioluminescence inhibition test of *Vibrio fischeri*

In vitro tests were carried out using *V. fischeri* commercial test kits. The freeze-dried luminescent bacteria and the luminometer (Microtox® M500) were purchased from Modern Water (Guildford, UK). A working solution of luminescent bacteria was prepared by reconstituting a vial of frozen lyophilized *V. fischeri* cells using 10 mL of the reagent diluent provided by the manufacturer. The reconstituted solution was equilibrated for 30 minutes at 4 ºC. The analysis was carried out with all dilution and reagents maintained at 15 ºC. The osmolality was adjusted to 2% *w/v* NaCl in each solution or sample. The sample pH values ranged 6.8 - 7.2 units. A fixed amount of bacteria (100 µL of the reconstituted cell suspension) was added to the dilution vials. Luminescence was measured at time zero (before addition of test solution) and then after 15 and 30 min and compared to the measured value of a bacterial control. The inhibition percentage (I %) was determined by comparing the relative responses of the control and test samples.

5.2.1.6. Cell culture

Human eukariotyc cell lines were obtained from the European collection of cell cultures. HepG2 cells were grown in DMEM supplemented with a 20% fetal bovine serum (FBS), 100 units mL^{-1} penicillin and 100 $\mu L \cdot mL^{-1}$ streptomycin while HK2 were cultured in DMEM:F12 supplemented with a 10% FBS, 1% l-glutamine, 100 units mL^{-1} penicillin and 100 µL mL^{-1} streptomycin, 1 µL mL^{-1} EFG (epidermal growth factor), 1 µL mL^{-1} hydrocortisone, 1 µL mL^{-1} insulin and 1 % sodium selenite. Fibroblasts were grown in DMEM supplemented with a 10% FBS, 1% l-glutamine, 100 units mL^{-1} penicillin and 100 µL mL^{-1} streptomycin. All cell lines were maintained and grown in an humidified atmosphere of 5% CO_2, 95% air at 37 ºC and cultured in 75 cm^2 cell culture flasks. The passage number range for all cell lines studied were maintained between 10 and 30 with the exception of fibroblasts which were maintained between 4 and 12. Confluent cells (60–80%) in T-75 flasks were detached using a trypsin–EDTA solution followed by the addition of propagation medium to neutralize trypsin. After centrifugation, supernatants were removed and cell pellets were resuspended in assay medium. The trypan blue exclusion method was used to discriminate between viable and non-viable cells.

For experimental purposes, cells were cultured in 96-well plates at a density of 10^5cells per well. Cells were allowed to attach for 24 h prior incubation of the selected compounds. Thereafter, the three cell lines were incubated, in different experiments, with: 1) pure OFX at different concentration levels for the estimation of the half maximum inhibitory effect (IC_{50}); 2) sample aliquotes withdrawn from the photochemical reactor after being freeze-dried and reconstituted in neat culture medium; 3) OFX TPs after being fractionated by preparative HPLC. Neat culture medium and sodium dodecylsulfate (SDS) (1% *v/v* in culture medium) were used as the negative and positive controls respectively.

5.2.1.7. MTT assay

After cell incubation with the tested compounds, medium was removed and the 96 well/plates were subsequently washed with phosphate-buffered saline (PBS). Thereafter, a 0.5 mg mL^{-1} of the 3-[4,5-dimethylthiazol-2-yl]-3,5-diphenylformazan (MTT) solution was added to the wells and incubated at 37 ºC during 2 h. After incubation, MTT was discharged and the formazan precipitated inside the wells redissolved in DMSO. Blue-formazan produced by metabolically active cells was quantified by measuring the absorbance at 550 nm in the microplate reader Safire2 TM (Tecan Trading AG, Switzerland). Results were analyzed with the Magellan™ version 2.2.1 (Tecan Trading AG, Switzerland) and are represented as the percentage of control (untreated cells) viability.

5.2.1.8. Statistics

Three independent experiments (photocatalysis and toxicity tests) were performed and mean values ± SD are presented. Regression analysis (linear and non-linear models) were implemented for correlating the concentration of inhibition of growth of bacteria with concentration of OFX. P-values 0.05 were considered to be significant.

5.2.2. Results and discussions

This section will show and discuss the main obtained results during the toxicological evaluation of ofloxacin transformation products, giving special emphasis on the criteria used to select the human cell lines and the experimental conditions (cell density, target concentration, etc.) used along the present chapter. In order to correlate the obtained biological results with the presence and concentration of ofloxacin transformation products, liquid chromatography coupled to high resolution mass spectrometry was used for the analysis of solutions dosed to *Vibrio fischer*i and human cells (before and after sample incubation).

As it has been widely presented in **Chapter 2** and **Chapter 3** of the present thesis, OFX TPs appeared shortly after the application of UV light irradiation in the presence of TiO_2. As discussed in the introduction of the chapter, there are some studies dealing with the toxicity of ofloxacin transformation products after being treated with TiO_2 [118,119] and ozonation [9]. These investigations found the same TPs by LC-HRMS, their toxicological evaluation and conclusions lead to the unequivocal conclusion that OFX TPs were more toxic than the parent compound. As expected, their obtained results strongly depended on the test organism and endpoint used in each case. Vasquez *et al.* [118] found a time-dependent toxicity reducing the inhibition of both *P. putida* and *V. fischeri* as well as an increase in the genotoxicity to HepG2 cells. Calza *et al.* [119] observed an increase in the luminescence inhibition during the photocatalytic treatment of OFX which was not due to the initial TPs generated but attributed to secondary generated transformation products. Finally, the study lead by Carbajo *et al.* [9] found interesting but confusing results for the toxicity evaluation of ofloxacin TPs (generated by ozonation) after their administration to *Vibrio fischeri*, *Pseudomonas putida*, *Pseudokirchneriella subcapitata* and *Tetrahymena thermophila*. While *P. putida*, *P. subcapitata* and *T. thermophila* showed no toxic response to ofloxacin neither for its transformation products in two water matrices (synthetic and effluent), the luminescent inhibition found for *V.fischeri* only increased when the ozonation of OFX was done in the synthetic water matrix while no toxic evidences were found when performed in the effluent water matrix.

It is for this reason that the main objective of this study was to evaluate the toxicity of ofloxacin and its transformation products using two different endpoints: 1) luminescence inhibition using *Vibrio-fischeri*, a standardised method widely employed in ecotoxicological studies and 2) cytotoxicity (production of the precipitate formazan employing the MTT assay) using three human cell lines. Since the luminescent endpoint is a well-known and standardised method which does not require optimisation, in the following pages will be discussed all the criteria used to select the experimental conditions to what human cell lines is refereed: selection of cells, seeding requirements, cell counting, etc. Once these sections are discussed, the effects of drug exposure and the toxicological effects of ofloxacin photocatalysis will be discussed with both mentioned endpoints.

5.2.2.1. Selection of human cell lines of choice

The selection of a cell line over another is a critical step in the study of drug toxicity. The use of primary cell lines supposes a clear advantage for the evaluation of human toxicity and Adsorption Desorption Metabolism and Excretion (ADME) phenomena. These cells are the most widely used for the understanding of molecular mechanisms involved in the biotransformation and toxic responses of new drugs. Despite these advantages, some limitations arise with their use over time: they tend to differentiate and can lose drug-metabolising capabilities, thus, not obtaining comparable results from one cell passage to another. Moreover, their isolation represents both technical and financial difficulties. It is for this reason that the scientific community widely accepts the inclusion of tumoral cell lines in toxicological studies at the *in-vitro* level. These cells do not suffer from differentiation over time, hence, being the best choice for long-term studies. That means that the obtained results are more reproducible than those obtained with primary cells, that is, passage to passage and lab to lab. These cells possess a particular characteristic that can be particularly taken as an advantage in the study of individual molecules without taking care to ADME phenomena. They express lower levels of major phase I/II enzymes involved in the biotransformation of drugs as reported by Rodríguez-Antona *et al.* [97], thus, mainly attributing the toxic response to the drug(s) under study.

In the present thesis, three human cell lines were used to study the potential toxicity of ofloxacin transformation products under the studied removal conditions: 1) the epithelial hepatoblastoma cell line HepG2, 2) the human renal proximal tubular cell line HK-2, both tumoral cells, and 3) fibroblasts, normal epidermal cells.

HepG2 were selected as they have been accepted as a system of choice for liver-like responses at the in vitro level. The low basal levels of cytochromes make them of particular interest for toxicology and ADME studies. These cells, as cited before, have been previously used in past publications [118] for the study of ofloxacin transformation products. HK-2 cells have been found to show quite a similar behaviour in toxicity and metabolic responses when compared to different primary cells as stated by Gunness *et al*. This study compared their behaviour with the porcine renal proximal tubular cell line (LLC-PK1) which is routinely used to study the nephrotoxic effects of drugs in humans, thus, making HK-2 cells of particular interest for the present study. Since both of these mentioned cells were tumoral cells, it was of special interest in this study to compare the *in-vitro* toxicity results obtained carrying out the same experiments in the same conditions with human primary cells. Since fibroblasts had already demonstrated in previous references (Melo *et al.* [112]) to constitute a great tool for toxicity evaluation of different effluents submitted to different water treatment techniques, human fibroblasts were used as the toxicity evaluation tool in the present study.

5.2.2.2. Seeding requirements

Several factors need to be taken in consideration prior starting the *in-vitro* toxicity evaluation of ofloxacin and its transformation products, such as special requirements of cell cultures, seeding conditions and cell counting, amongst others.

General seeding requirements

- Stem cell lines were maintained between passages 15 and 45 for experimental purposes. Fibroblasts primary cultures were maintained between passages 2 and 11. Especial emphasis was given to this passage number since it could drastically influence on the obtained results.

- Cells were passed when confluence reached the 75-80 % approximately (for example, as seen in **Figures 5.5** to **5.8**. A solution containing 0.025% of trypsin was used to detach cells from the culture flasks and were incubated for 3 minutes to allow complete cell detachment. Trypsin was neutralised by growth medium and the solution was centrifuged for 5 min at 1000 rpm. The supernatant was removed and the resulting pellet was reconstituted in 10 mL of fresh growth medium.

Special seeding requirements and cell counting

On the basis of the morphology and growth characteristics of each cell line, some considerations were taken into account before cell counting:

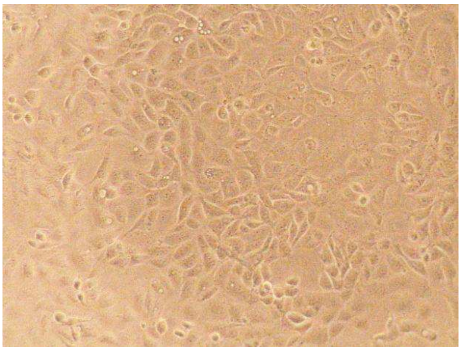

Figure 5.5. Microscopy image of HK-2 cells.

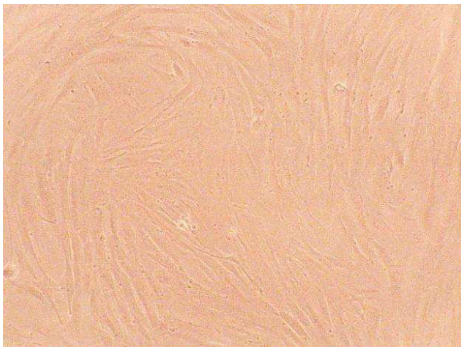

Figure 5.6. Microscopy image of fibroblasts cells.

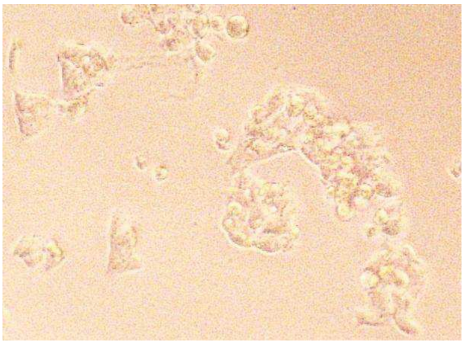

Figure 5.7. Microscopy image of HepG2 cells.

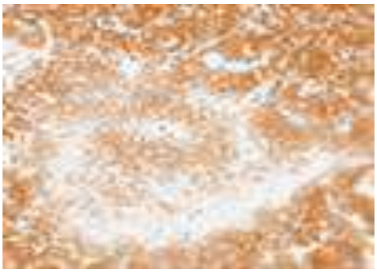

Figure 5.8. Microscopy image of agglomerations formed by HepG2 cells.

- HepG2 cells grow in single monolayer and 3D agglomerates (**Figure 5.7** and **Figure 5.8** respectively). Hence, after reconstituting the pellet with growth medium, cells were forced to pass through an 18 gauge needle to break these agglomerations. If these agglomerations persisted before cell counting, the same procedure was repeated once again. Once counted and seeded, cells were allowed to attach to the flask for six hours and the media was changed in order to get rid of dead cells (consequence of having forced cells to pass though the needle).

- Fibroblasts also tended to form aggregates, but easier to break than HepG2 cells. Hence, after having obtained the cells pellet and reconstituted in growth medium, the solution was pipetted several times (3 to 6) in order to break these agglomerations.

- HepG2 and HK-2 cells were counted by an automatic cell counter using the trypan blue exclusion method. If cells take up the trypan blue (**Figure 5.9**), they are considered non-viable. Then, in order to obtain the percentage and number of cells contained in the culture, **Equations 5.3** and **5.4** were employed

$$\% \text{ viable cells} = \left(1 - \frac{\text{number of blue cells}}{\text{number of total cells}}\right) \times 100 \qquad \textbf{Eq. 5.3}$$

$$\frac{\text{number of cells}}{\text{mL}} = \text{number of viable cells } \times \text{dilution } \times 10^4 \times 1.1 \qquad \textbf{Eq. 5.4}$$

Cell counting was performed per duplicate. For log phase cultures, cell viability was about 95. However, this cell viability appeared to range between 88 to 95% when dealing with fibroblasts and HepG2 cell cultures. This fact was consequence of such an "aggressive" cell treatment, routinely used in culture laboratories.

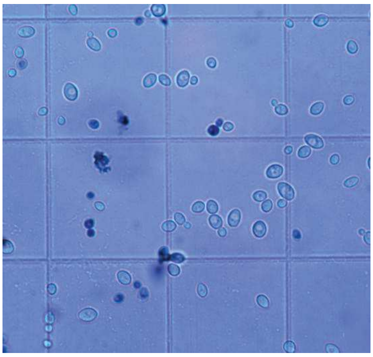

Figure 5.9. Microscopy image of the trypan blue method

- Contrary to HK-2 and HepG2 cells, fibroblasts were counted manually making use of a Nebauer chamber (**Figure 5.10**) and an inverse microscope. That was because previous studies carried out in the culture laboratory determined high inaccuracies in the automatic cell counting with this cell line. The number of cells contained in the literature can be depicted from **Equation 5.5**:

$$\frac{\text{number of cells}}{\text{mL}} = \text{number of counted cells (4 squares)} \times \text{dilution} \qquad \textbf{Eq. 5.5}$$

In all the studied cells, the sub-cultivation ratio for cell proliferation was of 1:4, which resulted, more or less, a million cells in the 75 cm^2 flask.

5.2.2.3. Selection of cell density

After the selection of the cell lines by which test compounds were to be studied, cell density is a critical parameter to be optimised, since the dose of compound per cell has a remarkable effect on the final results obtained. Bearing in hand three different human cells, thus, expecting different responses to the exposure of the tested compounds, a compromise on cell density selection was reached in order to statistically compare the results to be obtained.

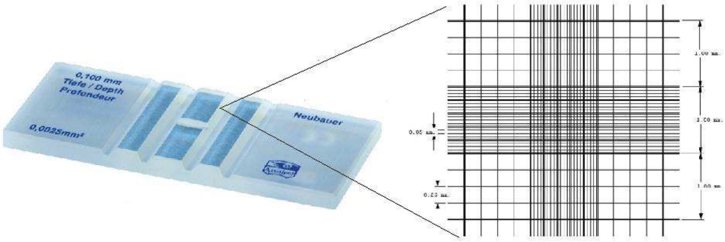

Figure 5.10. Nebauer chamber.

24 and 96 wells plates were used to carry out the optimisation of cell density by which the tests compounds would be studied. Apart from the number of wells, both plates are characterised by their surface area per well, 1.9 cm^2 and 0.32 cm^2 respectively. After seeding cells in wells, a layer of confluent cells is desired in order to achieve a homogeneous distribution and administration of the chemicals to the cells. It is for this reason that different cell densities were tested in both kinds of plates, as summarised in **Table 5.3**.

In all cases, all cells achieved confluence the day after being seeded. However, direct observation of cells seeded in the medium and upper level started to present cell death due to the elevated number of cells incubated per well. Especially remarkable were HepG2 cells which started growing in the third dimension, a phenomenon that needs to be avoided at all circumstances. It is for this reason that a cell density of 50,000 and 10,000 cells per well was selected for the 24 and 96 well plates respectively.

Table 5.3. Seeding conditions used to optimise the toxicity study.

Density level	24 well plate (1.9 cm^2)	96 well plate (0.32 cm^2)
Lower	50,000	10,000
Medium	100,000	20,000
Upper	200,000	40,000

5.2.2.4. Ofloxacin IC_{50}

It is well known by the scientific community that drug exposure regime is a determining factor in the observed response of the cells to the drug. In order to design a good exposure regime with high relevance when studying transformation products, the IC_{50} of ofloxacin was evaluated using both experimental conditions mentioned above and *Vibrio fischeri*. In order to determine the half maximum inhibitory concentration, luminescence inhibition was measured at two exposure times (15 and 30 min) while cytotoxicity was evaluated at 24 and 48 hours. Cell viability was not measured before 24 hours of cell exposure to the drug. Direct microscope observations at 4 and 8 hours did not reveal significant cell mortality neither cell detachment which meant that ofloxacin did not cause cytotoxic short-term effects. The lower and maximum concentration tested ranged between 7.8 and 1000 μg mL^{-1} respectively for both assays.

The response – concentration curve obtained for increasing concentrations of ofloxacin on *Vibrio fischeri* is presented in **Figure 5.11**. **Figures 5.12 A to F** depict the cytotoxic results for human cells under the seeding presented in **Table 5.4**.

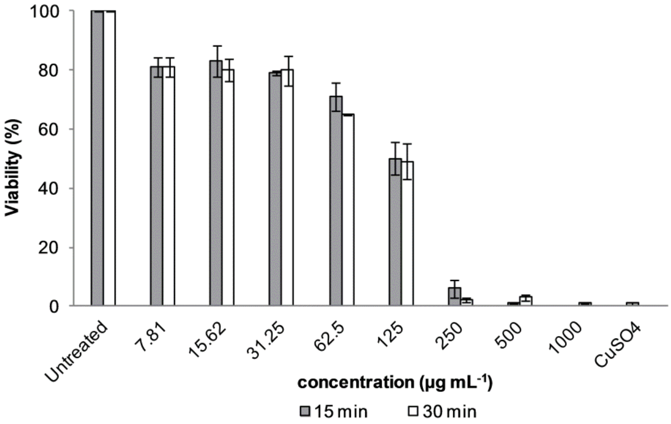

Figure 5.11. Viability-dose responses increasing concentrations of OFX on *Vibrio fischeri*.

The IC$_{50}$ value was found to be significantly different for each bioassay, being 132 μg mL^{-1} and 110 μg mL^{-1} for the *Vibrio fischeri* commercial kit (15 and 30 min incubation respectively) to approximately 1000 μg mL^{-1} for the three human cell lines tested. These differences might be attributed to the fact that *Vibrio fischeri*, in its lyophilised form, must face the stress caused by the toxicant administration as well as freeze injury, whereas lab cultures, collected during the growing curve, are in a more physiological state to overcome the toxic stress. These differences observed between the values of IC$_{50}$ constituted a great tool with different sensitivity for the evaluation of the acute toxicity of the reactant solution containing OFX and its related TPs.

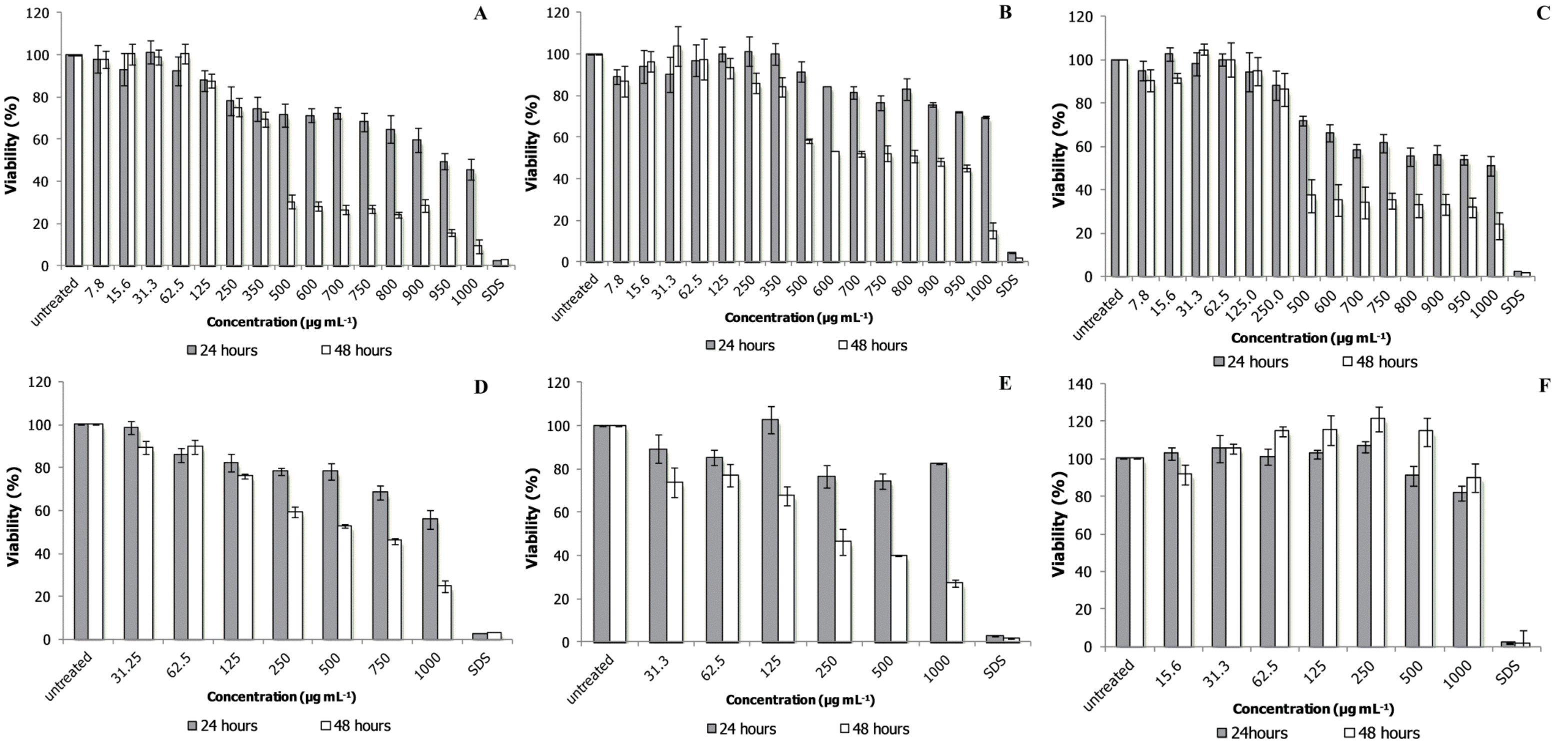

Figure 5. 12. Viability-dose responses for human cells tested: A) HK-2; B) HepG2; C) fibroblasts (96 wells, 10,000 cells/well) and D) HK-2; E) HepG2; F) fibroblasts (24 wells, 50,000 cells/well).

In contrast to the eukaryotic cell lines, the toxicity of ofloxacin for *Vibrio fischeri* was concentration-dependent. Among the cell lines studied, HK-2 and fibroblasts were found more sensitive to OFX incubation after 24 h exposure, having an IC_{50} of 950 and 1000 µg mL^{-1} respectively. This toxicity was even more evident for HK-2 cells and fibroblasts after 48 h incubation. At this time, cell viability went down to 40% at all tested concentrations. HepG2 did not show an inhibitory response at 24 hours incubation while at 48 hours was found to be at a concentration of 805 µg mL^{-1}.

Even though having used the same density of cells per cm^2, the IC_{50} value clearly differed between both experimental conditions in all cells used in this study. As expected, wells incubated with 50,000 cells appeared to be more resistant to the exposure of equal doses of ofloxacin. Even though having used the same cell density, the dose of ofloxacin administrated per cell was one fifth than wells incubated with 10,000 cells. As noted in **Figures 5.12 A** to **F**, the maximum dose tested on HepG2 and fibroblasts cells was found to have a maximum 45% mortality, thus, never reaching the IC_{50} value, which, by extrapolation, would range between 1000 and 1500 µg mL^{-1}. These concentrations, however, could not be tested due to the fact that ofloxacin becomes complete insoluble in the growth medium and would have little relevance on ecotoxicological studies.

Table 5.4. Ofloxacin IC_{50} (µg mL^{-1}) found under the studied conditions and end-points.

Luminescence inhibition	**IC_{50} (15min)**		**IC_{50} (30min)**	
V.fischeri	132		110	
Formazan production (MTT test)	**IC_{50} (24h)**		**IC_{50} (48h)**	
	96w	**24w**	**96w**	**24w**
HepG2	>1000	>1000	805	>1000
HK-2	961	>1000	<500	550
Fibroblasts	1000	>1000	<500	>1000

Since the final objective of the present study was to observe toxicological differences between the parent drug ofloxacin and its transformation products after having it submitted to TiO_2 photocatalysis, the experimental conditions selected was to seed cells at a concentration of 10,000 cells/well in 96 well plates. These experimental conditions were found to be the most favourable to observe toxicological effects of the administrated transformation products even if they were present at very low concentrations.

In order to conclude this section of effect of drug exposure, once incubated and before carrying out the MTT test, the basal medium containing the test drug was removed in order to perform the chemical analysis by liquid chromatography coupled to (tandem) high-resolution mass spectrometry. Acidified acetonitrile was added to precipitate the protein content, the sample was then centrifuged and finally, the supernatant was diluted with water and injected to the MS system.

Even though that Antona *et al.* [97] clearly demonstrated that enzymes responsible of metabolism were down-regulated, especially that of the cytochrome family, some phase I metabolites of ofloxacin were found in both HK-2 and HepG2 cells, as depicted in **Figure 5.13**. These results are in accordance with previous publications [111] which used these cell lines and also investigated the metabolites coming from both kind of cells. Hence, these experimental evidences clearly show that these cells can uptake ofloxacin and metabolise it even though the enzymes responsible of it are in very low concentrations in comparison to normal cells. In addition to synergic effects that may exist once exposed cells to the reaction crude, the presence of these phase I/II metabolites can also play a critical role on the toxicity results obtained.

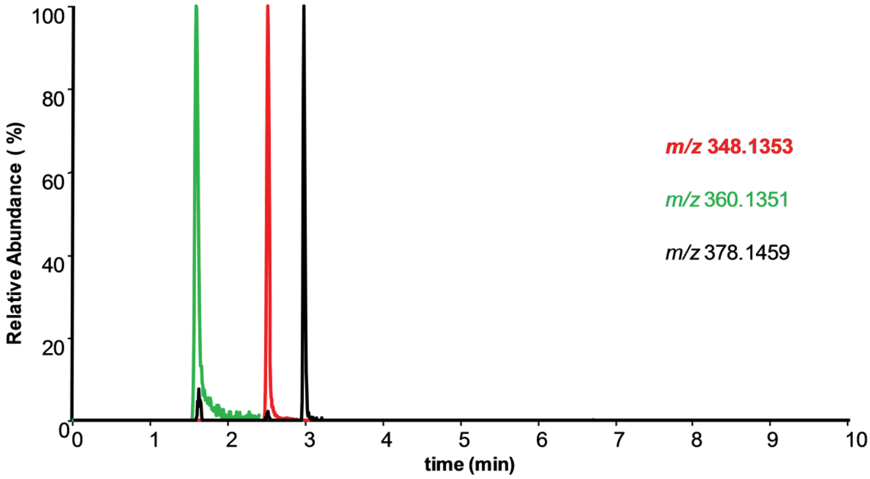

Figure 5.13. Extracted ion chromatograms of some of the identified metabolites. Red, *m/z* 348.1353 TP 34; green. *m/z* 360.1351 (TP39) and black, *m/z* 378.1459 (TP 48).

Since more toxic compounds may be formed during the treatment process, the toxicity evaluation of the reaction solution was performed at different reactant times of the applied photocatalytic processes. Prior incubation of the reactant solution, the catalyst was centrifuged, samples were lyophilized and reconstituted in the specific growth medium for *Vibrio fischeri* and each particular cell line (as described in the experimental section). Evaluation of the toxicity of the reactant solution was performed at two initial ofloxacin concentrations: 10 µg mL^{-1} (*V.fischeri* and human cell lines) as the lowest dose administrated and half of the obtained IC$_{50}$ for each conducted bioassay (62.5 µg mL^{-1} for *V.fischeri* and 500 µg mL^{-1} for the tested human cell lines) as the highest administration dose.

Quality assurance

All mediums, reactants and materials used for carrying out the MTT on the tested conditions were sterilised and under bacterial growth control. The presence of such bacteria could result in non-desired cell death, thus, obtaining false positive results. Since there was no way to sterilise samples coming from the photochemical reaction, quality assurance was focused on controlling bacterial growth by two methods: direct microscope observations on the seeded wells and incubation of the LB (Lysogeny broth) medium on the tested samples. Since direct observation could lead to confusion between cell death and bacterial growth, the latest method, a colorimetric method, was used to assure that there was not bacterial growth on the incubated samples. If this was observed, the experiment would be not valid. The LB (Lysogeny broth) medium is a nutritionally rich medium which is commonly used for the growth of bacteria. Its formulation contains tryptone, yeast extract and sodium chloride. Tryptone provides peptides and peptones, the yeast extract provides vitamins and trace elements while the function of sodium chloride is to provide sodium ions for the osmotic balance.

Aliquots of 50 µL of the tested compounds for 24 and 48 hours were collected and incubated for 24 hours at 40ºC under atmospheric conditions with 100 µL of the LB medium. This incubator, however, was outside of the culture laboratory in order to prevent cross-contaminations. Fresh cell growth medium was used as the negative control whereas saliva was used as the positive control. The determination of contamination of the sample(s) could be easily done by visual inspection: if sediments were present in the well, samples were contaminated, whether not, samples were free of bacteria.

5.2.2.5. Toxicity kinetics on *Vibrio fischeri*

While the initial solution of ofloxacin at both initial concentrations showed no inhibition, luminescent inhibition increased up to 50% after 5 min of photocatalytical treatment and was maintained for 60 minutes, before achieving its minimum inhibition (<1 %) at the end of the photocatalytical process. These data clearly pointed out the efficiency of the photocatalytical process in the detoxification of the irradiated solution. **Figure 5.14 A** shows the time evolution of the luminescence inhibition at a $[OFX]_0$ of 62.5 µg mL^{-1}. Since *V.fischeri* showed a concentration and dose-response dependency for OFX, as stated in **section 5.2.2.4**, it could be also noted the same behaviour for the mixture involving generated TPs and OFX. Even though toxicity data related to the photocatalysis of ofloxacin at a starting concentration of 10 µg mL^{-1} is not presented, the maximum luminescent inhibition reached the 60%. The inhibition caused for OFX TPs at a starting concentration of 62.5 µg mL^{-1} reached the 80% and was maintained for 60 minutes, reaction point when the generated TPs and OFX were completely degraded (no detectable by LC-HRMS). All these observations clearly demonstrate that during the photocatalytical treatment, even at very low TPs concentrations (<1 µg·mL^{-1}), generated TPs appear to be more toxic than ofloxacin. These results are in agreement with previous results reported [9, 35], which reported a toxicity increase in the irradiated solutions with the same toxicology test. However, these authors attributed this toxic effect to secondary TPs, mainly piperazine and its derivatives, which resulted from the consecutive degradation of first-generation TPs. However, **Figure 5.14 A** clearly shows that first-generation TPs may also induce a toxicity response on the luminescent bacteria, appearing to remain constant before the complete mineralisation of OFX and its TPs.

5.2.2.6. Toxicity kinetics on human cell lines

In the same line of proceeding as described in **section 5.2.2.5**, the photocatalytical reaction was also conducted at an initial concentration of 10 µg mL^{-1} and half of the IC_{50} found. Human cell lines also appeared to be less sensitive to the addition of the reaction mixture, thus, being less sensitive to the low amount of generated TPs. Although toxicity data related to the photocatalysis of ofloxacin at a starting concentration of 10 µg mL^{-1} is not shown, at 24 hours after the incubation of samples collected, cell viability was not found to be significant, while after their incubation for 48 hours, a significant toxicity increase ($p<0.5$) was found in samples collected between

15 – 30 min. At the end of the photocatalytical reaction, irradiated solutions appeared to be completely detoxified. As expected, the photocatalytical reaction conducted at 500 μg mL^{-1} promoted a higher toxic stress on the studied cell lines. Direct cell observations with the treated solutions showed significant cellular mortality in comparison to control cells. **Figures 5.14 B to D** show the relation between OFX TPs appearance and the evolution of the inhibition of the response of the three cell lines tested.

Although all results obtained led to the conclusion that OFX transformation promotes more toxic compounds, significant differences were observed between HK-2/fibroblasts and HepG2 cell lines. Cell viability decreased from 80% (initial concentration) to 50 – 60% (24 hours incubation) and 5 - 30% (48 hours incubation), for HK-2 and fibroblasts respectively, after 10 minutes of photocatalytical treatment which was maintained for the whole photocatalytical process. HepG2 cell viability was maintained over the whole process (24 hours incubation) and decreased from 68% to a maximum of 40% (48 hours incubation). In an analogous way as observed in **section 5.2.2.4**, HepG2 cell lines were less sensitive in comparison to HK-2 or fibroblasts, thus showing a different response to overcome the toxic stress. Although differences observed between these cell lines, these results are in agreement with those observed in **section 5.2.2.5**, indicating that first-generation TPs may lead to an increase of the overall toxicity, as well as later generation TPs, being the responsible of not achieving higher viability values at longer reaction times. From these obtained results, it is of unequivocal evidence that generated TPs lead to a toxicity increase of the overall solution.

Summing up, the evolution of toxicological data related to the kinetics of ofloxacin under TiO_2 photocatalysis has clearly showed with both end-points, the MTT assay and luminescence, that the generated transformation products are more toxic than the parent compound ofloxacin. As expected, photocatalytical reactions conducted at higher initial concentrations of the parent drug caused more mortality than those conducted at lower initial concentrations. Both bioassays conducted in this study were completely in agreement ones with others and with previous literature conducted to date. However, there were some points that differed from the published literature and needs to be further discussed:

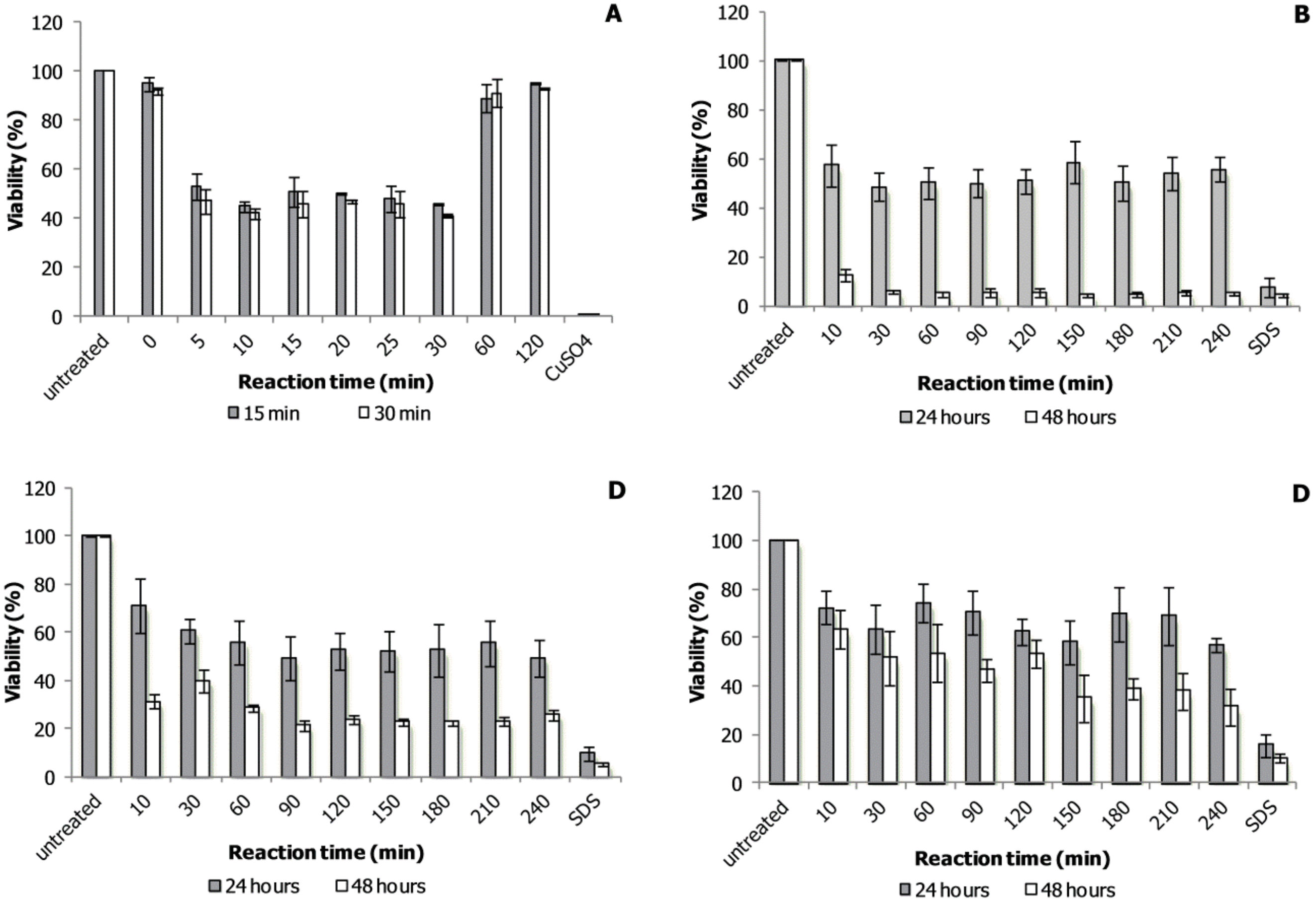

Figure 5.14. Viability evolution found for the tested human cell lines and Vibrio along the photocatalysis of ofloxacin. A) *Vibrio-fischeri* $[OFX]_0 = 62.5$ µg L^{-1}; B) HK-2; C) Fibroblasts; D) HepG2; $[OFX]_0 = 500$ µg L^{-1}

- Reactions conducted at 500 mg L^{-1} needed to be prolonged up to 8 hours in order to achieve complete detoxification. That was the moment were all of the detected transformation products were also degraded as a consequence of the photocatalytical treatment. Even though this concentration tested was poorly environmentally realistic, these conditions permitted obtaining higher concentrations of generated TPs, which further helped their isolation by chromatographic techniques.

- Data acquired with all tests and previously presented in this work clearly suggest that first-generation ofloxacin transformation products lead to a mortality increase. That was clear from the 25% mortality observed in cells and 50% on *V.fischeri* only after 5 minutes of photocatalytical treatment. This fact is not in complete agreement with the experimental evidences found by Calza *et al.* [119] and Carbajo *et al.* [9] which attributed the observed toxicity to second-generation transformation products, that is, chemical compounds derived from the degradation of first-generation transformation products. They attributed this toxicity to piperazine and its derivatives and other degradation products present in the tested samples. Since our research also considered *Vibrio fischeri* as a toxicity endpoint, these disagreements found can only be attributed to the photocatalytical treatment conditions, hence, not having the same sample composition in the different studies.

As conducted before by exposing ofloxacin to cells, the solution in contact with these in-vitro systems was submitted to the chemical analysis by high-resolution mass spectrometry. As before, some ofloxacin metabolites were still identified in the culture mediums. Moreover, some transformation products, well characterised in the previous chapter, could have been metabolised by cells as depicted by the peak area evolution of samples collected at 0, 24 and 48 hours of incubation. However, direct relationships could not be established because some of the identified TPs coming from the photocatalytical treatment were the same as the metabolites generated by cells.

Bearing in hand all data collected, it was unequivocally clear that ofloxacin transformation products were more toxic than ofloxacin. It is for this reason that the next step of this study was to conduct the separation and fractionation of the reaction crude in order to study individual toxicity of the generated compounds. This study was conducted using a liquid chromatograph coupled to a sample fractionator, which collected compounds eluting from the chromatographic column. Details on the chromatographic conditions used have been extensively described in the experimental section of the present chapter. All toxicity results obtained with the MTT test appeared to lead to similar results, that is, HK-2 cells were the most sensitive to drug exposure. It is for this reason that only HK-2 cells and *Vibrio fischeri* were used to conduct the toxicity investigation of the reaction crude.

As expected, direct well observations and the microbiology test carried out showed negative bacteria growth on the tested samples. Since samples were not sterilised, these results could be attributed to the fact that ofloxacin itself and its transformation products served as antibiotic for the cells tested in this study, thus, preventing bacterial growth. Previously discussed, the antibacterial activity of (fluoro)quinolones is mainly attributed to the quinolone ring. In **Chapter 4**, it was widely demonstrated that most of the detected transformation products maintained the quinolone moiety, thus, preserving the antibacterial activity.

5.2.2.7. Fractionation

In order to investigate the toxic impact of each individual photoproduct (or overall solution), the photocatalytical process was conducted at 500 µg mL^{-1} OFX and fractionated (**section 5.2.1.4**). After quenching (6 hours) and centrifuging the reaction, water was removed and reconstituted in MilliQ water at an approximate mixture concentration of 50 mg mL^{-1}. The sample was divided in 17 fractions as shown in **Figure 5.15**. Unreacted OFX eluted at 3.5 min, appearing in F9 with other TPs. The identification and purity of each fraction was evaluated by UHPLC-MS/HRMS. The concentration (µg g^{-1}) of each photoproduct (before and after cell incubation) was estimated according to **section 5.2.1.4**. Since estimating the IC$_{50}$ of 17 fractions could be time consuming, a screening test was conducted to discard between toxic and non-toxic photoproducts. Bearing in mind the IC$_{50}$ of OFX for end-point tested, individual fractions were finally reconstituted in the proper volume of medium so as to have a final concentration of 50 µg mL^{-1} (*V.fischeri*) and 500 µg mL^{-1} (HK-2 cells), concentrations at which the unreacted OFX should not have a significant impact on sample toxicity. Toxicity blanks results for *V.fischeri* and HK-2 cells are presented in **Figures 5.16 A** and **5.16 B** respectively while solutions containing TPs are presented in **Figures 5.17 A** and **5.17 B.**

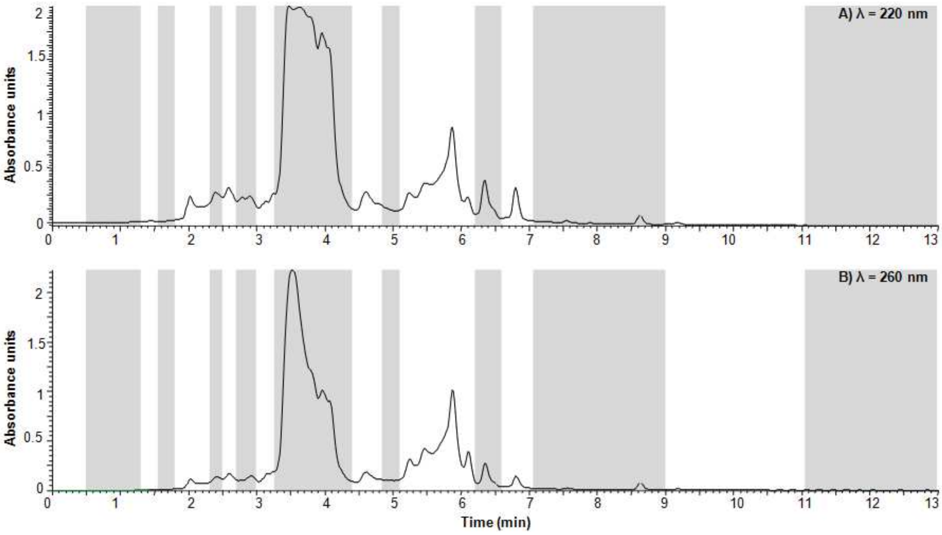

Figure 5.15. UV-Vis chromatogram obtained for the fractionation of the crude reaction.

Toxicological data of blank fractions did not render toxic effects (Figure 5.21 A and B). Both bioassays show significant differences for the toxicity response on those fractions eluting before F9. While *V.fischeri* appeared to overcome the toxic stress, even at higher concentrations than those presented in **Figure 5.17 A** (maximum concentration tested 500 µg mL^{-1}), HK-2 cells showed a remarkable effect on samples incubated for 48 hours (**Figure 5.17 B**). Bearing in mind the results obtained for the IC$_{50}$ of the parent drug, these experimental evidences on individual fractions are poorly understood and are the main point of investigation of our new study.

Four fractions were chosen for their IC$_{50}$ evaluation: F4, 7, 8 and 9. All these fractions presented a high decrease at 48 hours incubation. The IC$_{50}$ values of overall fraction obtained from the MTT test with the HK-2 cell line and *V.fischeri* are presented in **Table 5.5**. F4, F7 and F8 did not show a concentration-dependence relationship for the HK-2 cell line neither for *Vibrio fischeri*, not being possible to calculate their IC$_{50}$. Meanwhile, F9 showed a dose - dependant response, thus, it was possible to calculate the IC$_{50}$ values for the overall solution in both bioassays (**Table 5.5**). The chemical analysis of fraction 9 revealed the presence of 9 TPs and OFX itself (**Table 5.5** and **Table 5.6**).

Since the approximate concentration of OFX was 200 µg g^{-1}, the formation of these compounds and/or their synergic effect might be the responsible of the toxicity increase of the overall solution.

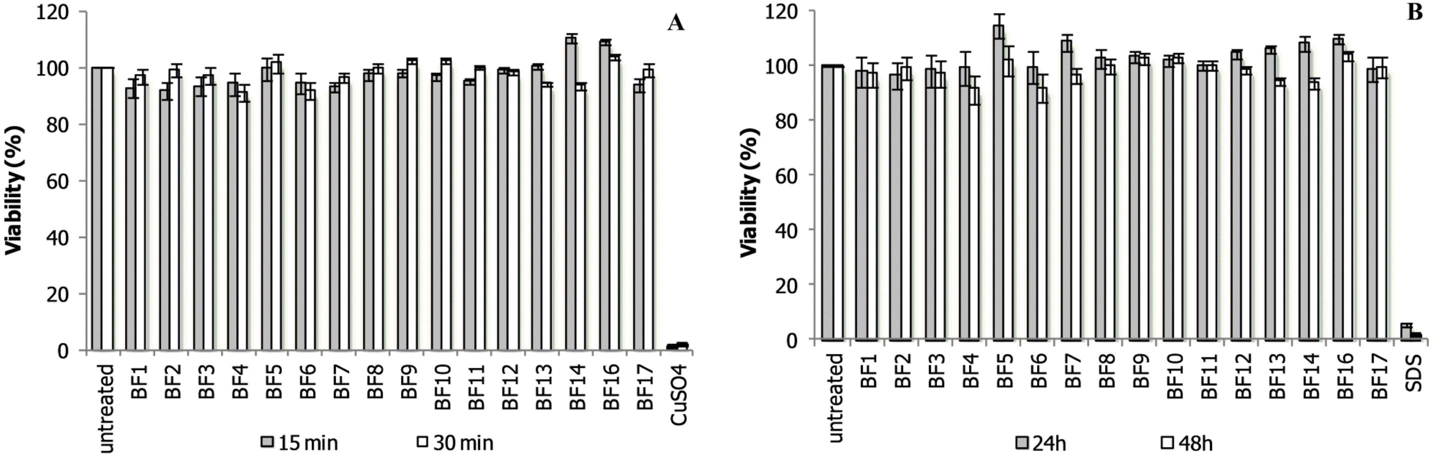

Figure 5.16. Toxicity results obtained for the blank fractions after its incubation on *V.fischeri* (A) and HK-2 cells (B).

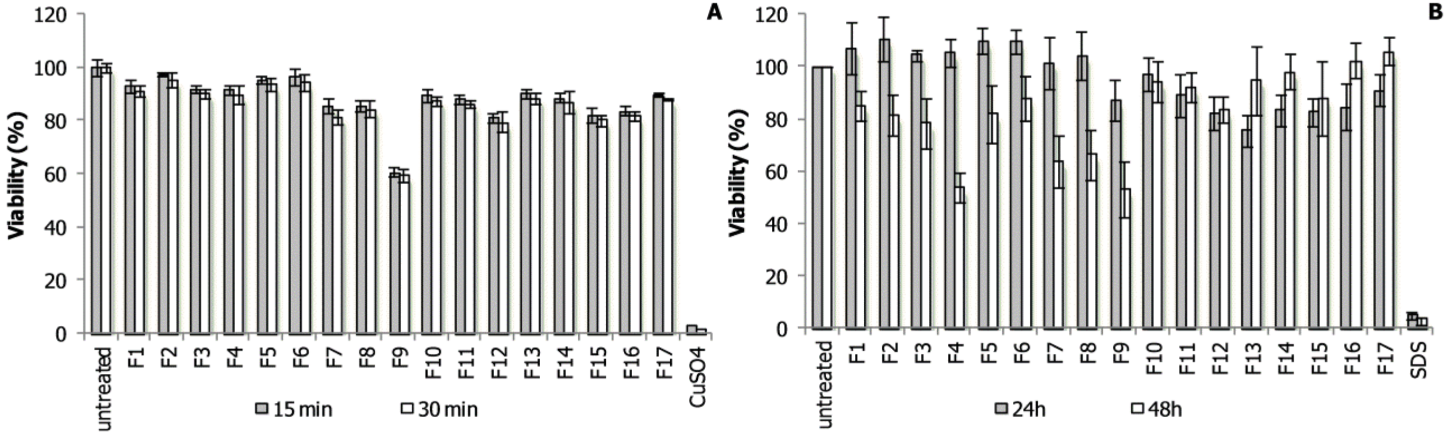

Figure 5.17. Toxicity results obtained for the tested fractions after its incubation on *V.fischeri* (A) and HK-2 cells (B).

In respect to OFX, the overall toxicity of F9 was increased up to 1.5 and 27 times (24 and 48 hours for HK-2 cells) while the IC_{50} tested on *V. fischeri* (OFX = 132 µg mL^{-1}) appeared to be significantly higher than OFX itself. A feasible reason explaining such differences is still poorly understood, but all data collected to date seem to point to a strong synergic effect on *V.fischeri* or may be related to HK-2 metabolism, since the concentrations of detected TPs varied along the incubation time, also reported by Guness *et al.* [111].

Table 5.5. IC_{50} (µg·g^{-1}) and chemical analysis of fractions tested.

Fraction	**measured *m/z*; mass error (ppm)**	**IC_{50} *V.fischeri***		**IC_{50} HK-2**	
		15 min	**30 min**	**24 h**	**48 h**
F9	362.1510; (-0.1)* 335.1056; (-1.2) 309.1261; (-1.7) 353.1163-A; (5.4) 353.1163-B; (5.4) 348.1354; (-0.1) 331.1076; (-0.2) 336.1353; (0.3) 378.1459-A; (0.6) 378.1459-B; (0.6)	191	187	685	35.5

* Ofloxacin

Having reached this point of the study, it would be of special interest to fractionate F9 and study the individual toxicity of the present photoproducts. However, due to the structural similarity between species, it was only possible to separate certain photoproducts under UHPLC conditions and columns. New chromatographic conditions, based on ultra-high performance liquid chromatography, were studied such as solvent gradient, column chemistry, column length, etc. None of these parameters helped to achieve better separations, only achieving unitary resolution to some of the compounds present in the sample (**Figure 5.18**).

When importing these conditions to the preparative HPLC, chromatographic separation was not accomplished and even worse than UHPLC, thus, not achieving satisfactory conditions for individual toxicity testing.

Table 5.6. Precursor and product ions measured and estimated concentrations of generated TPs identified in fraction 9.

Precursor ion measured *m/z*; (ppm)	Product ion measured *m/z*; (ppm)	Tentative chemical structure assigned	Estimated conc. (µg g^{-1})		
			0h	24 h	48 h
309.1261; (-1.7)	289.1183; (-0.3) 263.1212; (8.3)	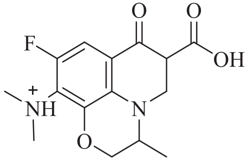	95.6	121.4	138.4
331.1076; (-0.2)	253.1313; (-8.8) 231.1493; ( )	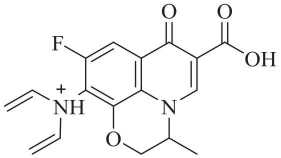	3	4.2	6
335.1056; (-1.2)	301.1184; (0.4) 299.1026; ( ) 289.1005; (7.1)	*	186.5	160.5	121.3
336.1353; (0.3)	316.1292; (0.02) 279.0776; (-0.04) 261.1034; (-0.1)	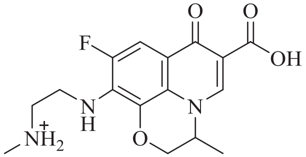	35	17.4	9.3
348.1354; (-0.1)	330.1255; (1.9) 304.1459; (1.0) 261.1035; (0.4)	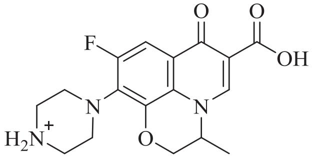	20.2	20.3	20.3

Table 5.6 (*Continued*). Precursor and product ions measured and estimated concentrations of generated TPs identified in F9.

Precursor ion measured *m/z*; (ppm)	Product ion measured *m/z*; (ppm)	Tentative chemical structure assigned	Estimated conc. (µg g^{-1})		
			0h	24 h	48 h
353.1163-B; (5.4)	335.1057; (5.6) 309.1265; (6.3) 263.1211; (7.7)	*	0.6	0.6	0.7
362.1510; (-0.1)**	344.1410 (1.5) 318.1612 (-0.1) 316.1459 (0.7) 261.1034 (0.1)	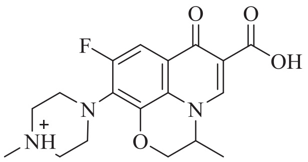	197.4	193.8	193.6
378.1459; (0.6)	360.1355; (0.3) 334.1562; (0.1) 316.1457; (0.4)	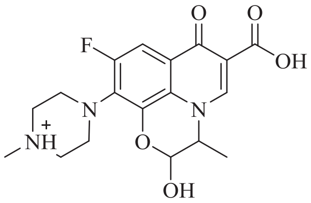	0.8	0.8	0.8
378.1459; (0.6)	361.1432; (-0.2) 317.1535; (0.2)	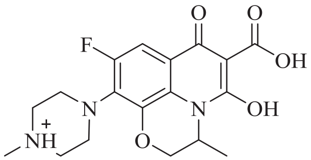	1.1	1.1	1.1

* Tandem mass spectrum did not provide enough structural information to tentatively attribute a chemical structure.

** Ofloxacin

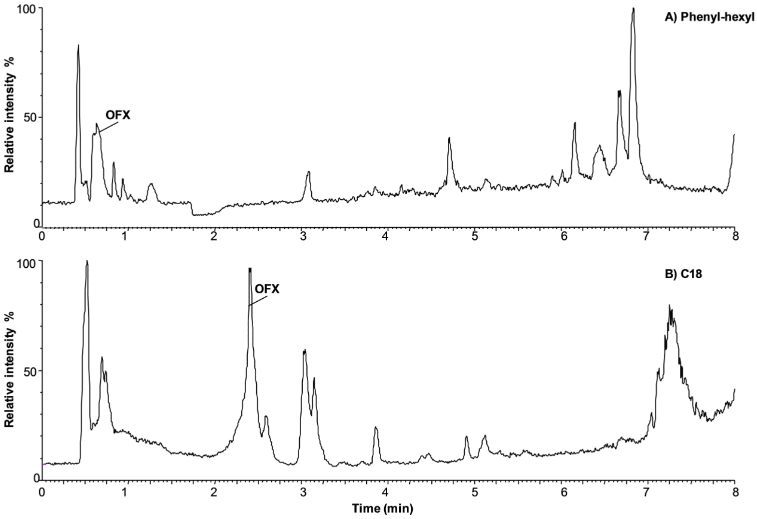

Figure 5.18. Obtained chromatograms for F9: A) Phenyl-Hexyl column; B) C18 column;

Thus, the only option to date, after having characterised these transformation products by (tandem) high-resolution mass spectrometry, is the chemical synthesis of all detected TPs in the reaction crude and the latter toxicity screening. Due to time and resources limitations, this action could not be done. However, some chemical routes, adapted from the investigation carried out by Dinakaran *et al.* [120,121] are proposed for future investigations in the same line of research (Figures 5.19 to 5.23).

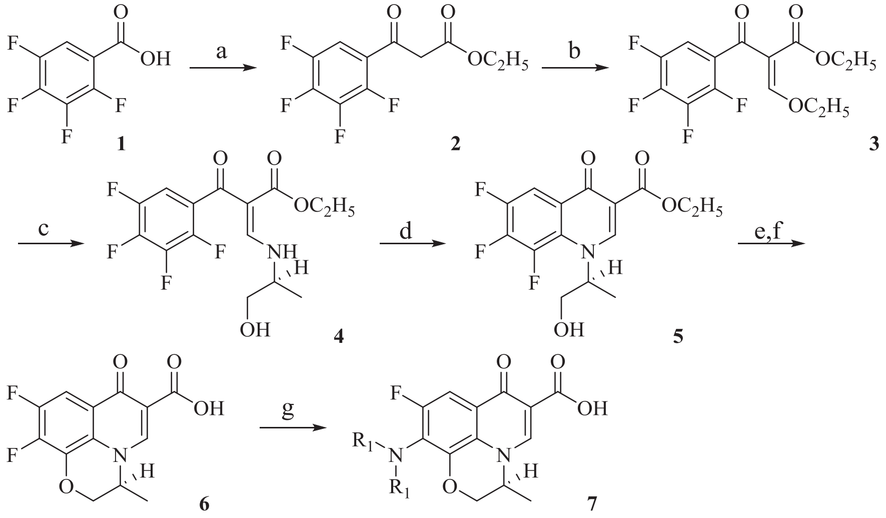

Figure 5.19. Synthetic route proposed by Dinakaran *et al.* to synthesise ofloxacin and derivatives. Reagents and conditions of every step: (a) CDI, $EtOCOCH_2CO_2K$, $MgCl_2$, Et_3N; (b) $(EtO)_3CH$, AC_2O; (c) (+)-2-amino-1-propanol, $EtOH/Et_2O$ (50:50); (d) DMSO, K_2CO_3; (e) THF, 10% KOH; (f) H_2SO_4, KNO_3; (g) various secondary amines, DMSO, MW;

Hence, TP 34 can be obtained by the nucleophilic aromatic substitution reaction of the intermediate product 6 with piperazine in DMSO and microwave irradiation (MW), as depicted by **Figure 5.20**.

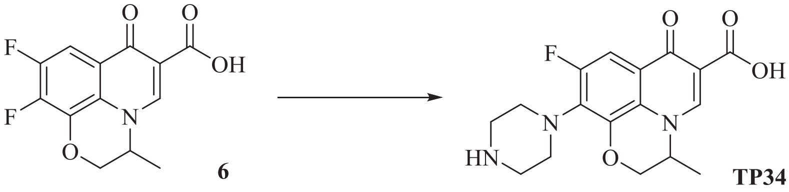

Figure 5. 20. Proposed synthetic route for the synthesis of TP34. Reagents and conditions: pyperazine in DMSO and MWI.

TP 17 could be obtained by two equivalent synthetic routes from intermediate product 8. For instance, this could be promoted by increasing temperature (reaction a), thus decarboxyling the intermediate product 6, giving rise to the intermediate product 8. Then, TP17 could be obtained by a nucleophilic aromatic substitution (reaction b) promoted by methylpiperazine in an appropriate solvent such as DMSO and the application of microwave irradiation (MWI), as depicted by **Figure 5.21**. The same product would be obtained by performing step b in the first instance followed by step a.

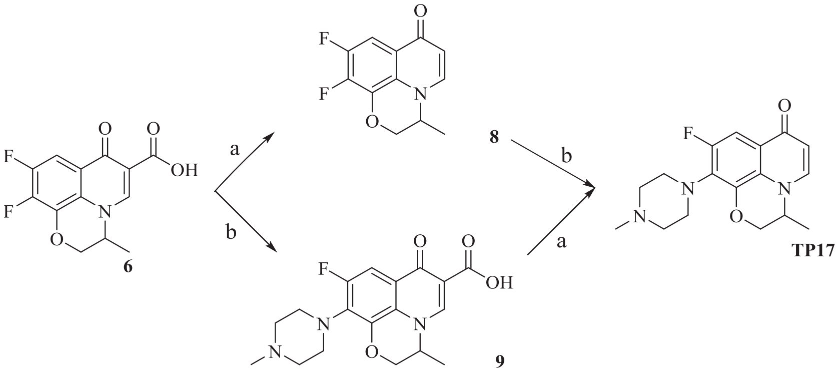

Figure 5.21. Alternative synthetic route to synthesise TP17. Reagents and conditions: a) temperature; b) methylpyperazine in DMSO and MWI.

TP36 could be obtained by the Michael and retro-Michael addition of ethanolamine to the intermediate product 3 (*step a* from **Figure 5.22**) yielding the intermediate product 10. Then, this would be converted to the intermediate product 12 using the same steps proposed by Dinakaran *et al.* Finally, TP36 would be the result of the nucleophilic aromatic substitution of the intermediate product 12 using 1-hydroxypiperazine (step e).

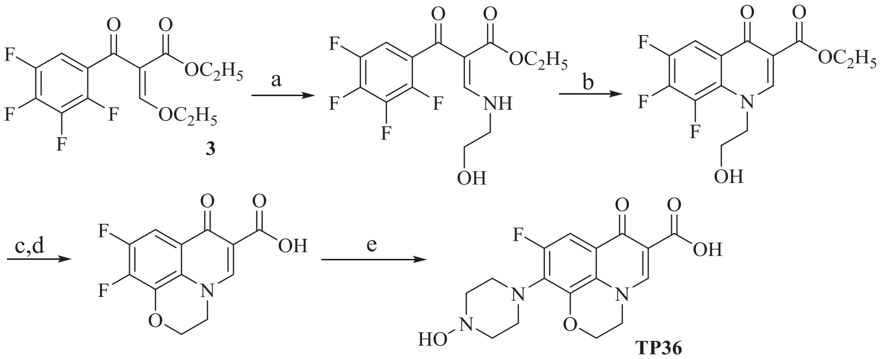

Figure 5.22. Proposed synthetic route to synthesise TP36. Reagents and conditions: a) aminoethanol, EtOH/Et_2O (50:50); (b) DMSO, K_2CO_3; (c) THF, 10% KOH; (d) H_2SO_4, KNO_3; (e) 1-hydroxypiperazine in DMSO and MWI.

The last synthetic route proposed is that to obtain TP42 from the intermediate product 6 of the synthetic route proposed by Dinakaran *et al.* [120,121]. Hence, this TP would be the result of the one-step reaction of this intermediate with 1-hydroxypiperazine in DMSO assisted with microwave irradiation.

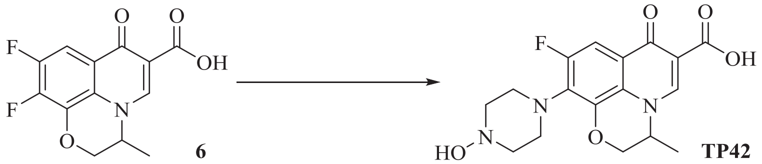

Figure 5.23. Proposed synthetic route to synthesise TP42. Reagents and conditions: 1-hydroxypiperazine in DMSO and MWI.

5.3. Conclusions

Current studies on treatment processes for pharmaceuticals removal from the environment have shown that particular attention should be paid not only to parent compounds toxicity but also to their TPs due to their potential contribution to the overall toxicity.

- The present research has driven a special attention to the use of human eukaryotic cell lines for the estimation of the hazard of OFX TPs. As already demonstrated in past publications, the present study has shown the importance of choosing different type of bioassays for the same target compound.
- As expected, *V. fischeri* suspensions from lyophilised commercial kits showed an intense sensitivity to OFX (IC_{50} = 132 μg μL^{-1}) while cultured cells presented an IC_{50} from 5 to 10 times higher (IC_{50} = 500 – 1000 μg μL^{-1}) than the lyophilised bacteria.
- The toxicity analysis of the irradiated solutions was tested at two initial OFX concentrations. In all cases, the results obtained led to a toxicity increase in the first minutes of the photocatalytical process and maintained until the complete degradation of OFX and its generated TPs. In all cases, the complete detoxification was achieved by ensuring enough irradiation time.
- The HPLC analysis method was scaled to a preparative HPLC instrument in order to fractionate the reaction crude obtained at the end of the photocatalytical process. As expected, due to the high number of generated TPs, the complete separation of all TPs was not possible.
- The toxicity analysis of the generated fractions permitted to enclose which chemicals were the responsible of the observed toxicity increase. Additionally, this analysis showed significant differences between the behaviour of *V. fischeri* and cultured cells (HK-2 cells). These differences were mainly attributed to synergic effects or to cells metabolism (still under study).

In order to overcome these limitations encountered along the experimental work and to explain the different behaviour observed between human cells and *V. fischeri*, the synthesis of these chemicals seems to be the only way to study individual toxicity. This is the reason why several synthesis routes are currently under investigation which will be presented in future works.

5.4. References

1. Hignite., C.; Azarnoff., D. L. *Life Sci.* **20,** 337–341 (1977).

2. Verlicchi, P.; Zambello, E. *Sci. Total Environ.* **565,** 82–94 (2016).

3. Paíga, P.; Santos, L. H. M. L. M.; Ramos, S.; Jorge, S.; Silva, J. G.; Delerue-Matos, C. *Sci. Total Environ.* **573,** 164–177 (2016).

4. Moreira, F. C.; Soler, J.; Alpendurada, M. F.; Boaventura, R. A. R.; Brillas, E.; Vilar, V. J. P. *Water Res.* **105,** 251–263 (2016).

5. Cunha, V.; Burkhardt-Medicke, K.; Wellner, P.; Santos, M. M.; Moradas-Ferreira, P.; Luckenbach, T.; Ferreira, M. *Ecotoxicol. Environ. Saf.* **136,** 14–23 (2017).

6. Bing, J.; Hu, C.; Zhang, L. *Appl. Catal. B Environ.* **202,** 118–126 (2017).

7. Zhu, X.; Wu, G.; Lu, N.; Yuan, X.; Li, B. *J. Hazard. Mater.* **324,** 272–280 (2017).

8. Lambropoulou, D.; Evgenidou, E.; Saliverou, V.; Kosma, C.; Konstantinou, I. *J. Hazard. Mater.* **323,** 513–526 (2017).

9. Carbajo, J. B.; Petre, A. L.; Rosal, R.; Herrera, S.; Letón, P.; García-Calvo, E.; Fernández-Alba, A. R.; Perdigón-Melón, J. A. *J. Hazard. Mater.* **292,** 34–43 (2015).

10. Hamdi El Najjar, N.; Touffet, A.; Deborde, M.; Journel, R.; Leitner, N. K. V. *Chemosphere* **93,** 604–611 (2013).

11. Yang, B.; Kookana, R. S.; Williams, M.; Ying, G.-G.; Du, J.; Doan, H.; Kumar, A. *J. Hazard. Mater.* **320,** 296–303 (2016).

12. El Najjar, N. H.; Deborde, M.; Journel, R.; Vel Leitner, N. K. *Water Res.* **47,** 121–129 (2013).

13. García-Galán, M. J.; Anfruns, A.; Gonzalez-Olmos, R.; Rodriguez-Mozaz, S.; Comas, J. *Chemosphere* **147,** 451–459 (2016).

14. Gong, H.; Chu, W. *J. Hazard. Mater.* **314,** 197–203 (2016).

15. Lutterbeck, C. A.; Wilde, M. L.; Baginska, E.; Leder, C.; Machado, Ê. L.; Kümmerer, K. *Sci. Total Environ.* **527,** 232–245 (2015).

16. Hapeshi, E.; Fotiou, I.; Fatta-Kassinos, D. *Chem. Eng. J.* **224,** 96–105 (2013).

17. Michael, I.; Hapeshi, E.; Aceña, J.; Perez, S.; Petrović, M.; Zapata, A.; Barceló, D.; Malato, S.; Fatta-Kassinos, D. *Sci. Total Environ.* **461–462,** 39–48 (2013).

18. Tay, K. S.; Madehi, N. *Sci. Total Environ.* **520,** 23–31 (2015).

19. Salgado, R.; Pereira, V. J.; Carvalho, G.; Soeiro, R.; Gaffney, V.; Almeida, C.; Cardoso, V. V.; Ferreira, E.; Benoliel, M. J.; Ternes, T. A.; *et al. J. Hazard. Mater.* **244–245,** 516–527 (2013).

20. Lassalle, Y.; Jellouli, H.; Ballerini, L.; Souissi, Y.; Nicol, É.; Bourcier, S.; Bouchonnet, S. *J. Chromatogr. A* **1371,** 146–153 (2014).

21. Klaassen, C. D. in *The Basic Science of Poisons* (ed. Curtis D. Klaassen) (1980).

22. Lombardo, A.; Roncaglioni, A.; Benfenati, E.; Nendza, M.; Segner, H.; Jeram, S.; Pauné, E.; Schüürmann, G. *Environ. Res.* **135,** 156–164 (2014).

23. Verma, V.; Yu, Q. J.; Connell, D. W. *Chemosphere* **89,** 1026–1033 (2012).

24. de Boissel, P. G. J.; Gonzalez, P.; Buleté, A.; Daffe, G.; Clérandeau, C.; Vulliet, E.; Cachot, J. *Chemosphere* **181,** 468–477 (2017).

25. Schreiber, B.; Petrenz, M.; Monka, J.; Drozd, B.; Hollert, H.; Schulz, R. *Aquat. Toxicol.* **183,** 46–53 (2017).

26. Libralato, G.; Prato, E.; Migliore, L.; Cicero, A. M.; Manfra, L. *Ecol. Indic.* **69,** 35–49 (2016).

27. DeSesso, J. M. *Curr. Opin. Toxicol.* **3,** 1–5 (2017).

28. Wang, T.; Liu, Y.; Wang, D.; Lin, Z.; An, Q.; Yin, C.; Liu, Y. *J. Hazard. Mater.* **310,** 56–67 (2016).

29. Villa, S.; Migliorati, S.; Monti, G. S.; Vighi, M. *Ecotoxicol. Environ. Saf.* **86,** 93–100 (2012).

30. Dawson, D. A.; Pöch, G.; Wayne Schultz, T. *Ecotoxicol. Environ. Saf.* **65,** 171–180 (2006).

31. Zou, X.; Lin, Z.; Deng, Z.; Yin, D. *Chemosphere* **90,** 2070–2076 (2013).

32. Hernando, M. D.; Ejerhoon, M.; Fernández-Alba, A. R.; Chisti, Y. *Water Res.* **37,** 4091–4098 (2003).

33. Jiang, R.; Cabras, G.; Sheng, W.; Zeng, Y.; Ooka, T. *Neoplasia* **11,** 964–973 (2009).

34. Šantak, G.; Šantak, M.; Forčić, D. *Cytokine* **64,** 494–496 (2013).

35. Kumar, A.; Shalmanova, L.; Hammad, A.; Christmas, S. E. *Transpl. Immunol.* **35,** 40–46 (2016).

36. Juan-García, A.; Juan, C.; Manyes, L.; Ruiz, M. J. *Toxicol. Vitr.* **34,** 264–273 (2016).

37. Zhou, H.; George, S.; Hay, C.; Lee, J.; Qian, H.; Sun, X. *Food Chem. Toxicol.* **103,** 18–27 (2017).

38. Rudzok, S.; Schlink, U.; Herbarth, O.; Bauer, M. *Toxicol. Appl. Pharmacol.* **244,** 336–343 (2010).

39. Chicu, S. A.; Schannen, L.; Putz, M. V.; Simu, G. M. *Ecotoxicol. Environ. Saf.* **134,** 80–85 (2016).

40. Castell, J. V.; Gómez-Lechón, M. J.; Ponsoda, X.; Bort, R. *Cell Biol. Toxicol.* **13,**

331–338 (1997).

41. Park, B. K.; Kitteringham, N. R.; Maggs, J. L.; Pirmohamed, M.; Williams, D. P. *Annu. Rev. Pharmacol. Toxicol* **45,** 177–202 (2005).

42. Leung, L.; Kalgutkar, A. S.; Obach, R. S. *Drug Metab. Rev.* **44,** 18–33 (2012).

43. Dahlin, D. C.; Miwa, G. T.; Lu, A. Y. H.; Nelson, S. D. *Proc. Natl. Acad. Sci. U. S. A.* **81,** 1327–1331 (1984).

44. Thomas, S. *Pharmacol. Ther.* **60,** 91–120 (1993).

45. Gut., J.; Christen, U.; Huwyler, J. *Pharmacol. Ther.* **58,** 133–155 (1993).

46. MJ, C.; JH, S.; GK, G.; JF, A.; WD, H.; R, W. *Anaesth. Intensive Care* **7,** 9–24 (1979).

47. Steele, M. A.; Raymond F, B.; Roger, M. D. *Chest* **99,** 465–471 (1991).

48. Nelson, S. D.; Mitchell, J. R.; Timbrell, J. A.; Snodgrass, W. R.; Corcoran, G. B. *Science (80-.).* **193,** 901–903 (1976).

49. Boelsterli, U. A. *Toxicol. Appl. Pharmacol.* **192,** 307–322 (2003).

50. Bort, R.; MacÉ, K.; Boobis, A.; Gómez-Lechón, M. J.; Pfeifer, A.; Castell, J. *Biochem. Pharmacol.* **58,** 787–796 (1999).

51. Ponsoda, X.; Bort, R.; Jover, R.; Gómez-lechón, M. J.; Castell, J. V. *Toxicol. Vitr.* **9,** 439–444 (1995).

52. Guengerich, F. P. *Arch. Biochem. Biophys.* **409,** 59–71 (2003).

53. Guengerich, F. P. *Chem. Res. Toxicol.* **14,** 611–650 (2001).

54. Isin, E. M.; Guengerich, F. P. *Biochim. Biophys. Acta* **1770,** 314–29 (2007).

55. Dalla Bona, M.; Di Leva, V.; De Liguoro, M. *Chemosphere* **115,** 67–74 (2014).

56. Dalla Bona, M.; Lizzi, F.; Borgato, A.; De Liguoro, M. *Ecotoxicol. Environ. Saf.* **132,** 397–402 (2016).

57. Dave, G.; Herger, G. *Chemosphere* **8,** 459–466 (2012).

58. Ji, J. Y.; Xing, Y. J.; Ma, Z. T.; Zhang, M.; Zheng, P. *Chemosphere* **91,** 1094–1098 (2013).

59. Mater, N.; Geret, F.; Castillo, L.; Faucet-Marquis, V.; Albasi, C.; Pfohl-Leszkowicz, A. *Environ. Int.* **63,** 191–200 (2014).

60. Vasconcelos, T. G.; Henriques, D. M.; König, A.; Martins, A. F.; Kümmerer, K. *Chemosphere* **76,** 487–493 (2009).

61. Li, Y.; Zhang, F.; Liang, X.; Yediler, A. *Chemosphere* **90,** 284–291 (2013).

62. Sturini, M.; Speltini, A.; Maraschi, F.; Pretali, L.; Ferri, E. N.; Profumo, A. *Chemosphere* **134,** 313–318 (2015).

63. Michael, I.; Hapeshi, E.; Michael, C.; Fatta-Kassinos, D. *Water Res.* **44,** 5450–5462 (2010).

64. Soil Microorganisms: Nitrogen Transformation Test, O. *OECD Guidel. Test. Chem.* 1–10 (2000).

65. Soil microorganisms: Carbon transformation test, O. *OECD Guidel. Test. Chem.* 1–10 (2000).

66. NM, F.; JL, S.; RP, L. *Env. Toxicol Chem.* **20,** 160–170 (2001).

67. Gilbert, F.; Galgani, F.; Cadiou, Y. *Mar. Biol.* **112,** 199–205 (1992).

68. Strotmann, U. J.; Eglsäer, H.; Pagga, U. *Chemosphere* **28,** 755–766 (1994).

69. Alsop, G. M.; Waggy, G. T.; Conway, R. A. *Water Pollut. Control Fed.* **52,** 2452–2456 (1980).

70. Gillespie, P. A.; Vaccaro, R. F. *Limnol. Oceanogr.* **23,** 543–548 (1978).

71. Albright, L. J.; Wentworth, J. W.; Wilson, E. . *Water Res.* **6,** 589–1596. (1972).

72. Karl, D. *Appl. Environ. Microbiol.* **38,** 850–860 (1979).

73. OECD. *OECD Guidel. Test. Chem. Sect. 2 Eff. Biot. Syst.* **209,** 1–18 (2010).

74. Gendig, C.; Domogala, G.; Agnoli, F.; Pagga, U.; Strotmann, U. J. *Chemosphere* **52,** 143–149 (2003).

75. Klečka, G. M.; Landi, L. P.; Bodner, K. M. *Chemosphere* **14,** 1239–1251 (1985).

76. Marugán, J.; Bru, D.; Pablos, C.; Catalá, M. *J. Hazard. Mater.* **213–214,** 117–122 (2012).

77. Froehner, K.; Backhaus, T.; Grimme, L. H. *Chemosphere* **40,** 821–828 (2000).

78. Backhaus, T.; Grimme, L. H. *Chemosphere* **38,** 3291–3301 (1999).

79. Parvez, S.; Venkataraman, C.; Mukherji, S. *Environ. Int.* **32,** 265–268 (2006).

80. Alba, P.; Sánchez-Fortún, S.; Alvarez-Perez, S.; Blanco, J. L.; García, M. E. *Toxicon* **53,** 729–733 (2009).

81. Baran, A.; Tarnawski, M. *Ecotoxicol. Environ. Saf.* **98,** 19–27 (2013).

82. Somensi, C. A.; Simionatto, E. L.; Bertoli, S. L.; Wisniewski, A.; Radetski, C. M. *J. Hazard. Mater.* **175,** 235–240 (2010).

83. Dzyadevych, S. V.; Chovelon, J. M. *Mater. Sci. Eng. C* **21,** 55–60 (2002).

84. Costa, S. P. F.; Pinto, P. C. A. G.; Lapa, R. A. S.; Saraiva, M. L. M. F. S. *J. Hazard. Mater.* **284,** 136–142 (2014).

85. Farré, M. J.; Franch, M. I.; Ayllón, J. A.; Peral, J.; Domènech, X. *Desalination* **211,** 22–33 (2007).

86. Ruby, E. G.; McFall-Ngai, M. J. *Trends Microbiol.* **7,** 414–420 (1999).

87. McFall-Ngai, M.; Nyholm, S. V.; Castillo, M. G. *Semin. Immunol.* **22,** 48–53 (2010).

88. Visick, K. L.; Ruby, E. G. *Curr. Opin. Microbiol.* **9,** 632–638 (2006).

89. Dunn, A. K. *Advances in Microbial Physiology* **61,** (Elsevier Ltd., 2012).

90. Kimura, Y.; Tashiro, Y.; Saito, K.; Kawai-Noma, S.; Umeno, D. *J. Biosci. Bioeng.* **122,** 533–538 (2016).

91. Spina, F.; Cordero, C.; Schilirò, T.; Sgorbini, B.; Pignata, C.; Gilli, G.; Bicchi, C.; Varese, G. C. *J. Clean. Prod.* **100,** 185–194 (2015).

92. García-Galán, M. J.; Silvia Díaz-Cruz, M.; Barceló, D.; Barceló, D. *TrAC - Trends Anal. Chem.* **28,** 804–819 (2009).

93. Zeng, C.; Gonzalez-Alvarez, A.; Orenstein, E.; Field, J. A.; Shadman, F.; Sierra-Alvarez, R. *Ecotoxicol. Environ. Saf.* **140,** 30–36 (2017).

94. Miller, M. A.; Bankier, C.; Al-Shaeri, M. A. M.; Hartl, M. G. J. *Mar. Pollut. Bull.* **101,** 903–907 (2015).

95. Eglen, R.; Reisine, T. *Assay Drug Dev Technol* **9,** 108–124 (2011).

96. Möller, C.; Slack, M. *Drug Discov. Today* **15,** 384–390 (2010).

97. Rodríguez-Antona, C.; Donato, M. T.; Boobis, A.; Edwards, R. J.; Watts, P. S.; Castell, J. V.; Gómez-Lechón, M.-J. *Xenobiotica* **32,** 505–520 (2002).

98. Alge, C. S.; Hauck, S. M.; Priglinger, S. G.; Kampik, A.; Ueffing, M. *J. Proteome Res.* **5,** 862–878 (2006).

99. Pan, C.; Kumar, C.; Bohl, S.; Klingmueller, U.; Mann, M. *Mol. Cell. Proteomics* **8,** 443–450 (2009).

100. McGivern, J. V.; Ebert, A. D. *Adv. Drug Deliv. Rev.* **69–70,** 170–178 (2014).

101. Furue, M. K.; Tateyama, D.; Kinehara, M.; Na, J.; Okamoto, T.; Sato, J. D. *Vitr. Cell. Dev. Biol. - Anim.* **46,** 573–576 (2010).

102. Abraham, R. T.; Sauers, M. E.; Zemaitis., M. A.; Alvin, J. *Anal. Biochem.* **129,** 235–244 (1983).

103. Pires, A. do R. A.; Ruthes, A. C.; Cadena, S. M. S. C.; Acco, A.; Gorin, P. A. J.; Iacomini, M. *Int. J. Biol. Macromol.* **58,** 95–103 (2013).

104. Li, X.; Ma, J.; Wang, J. *Ecotoxicol. Environ. Saf.* **120,** 342–348 (2015).

105. Yang, X.; Lv, Y.; Huang, K.; Luo, Y.; Xu, W. *Food Chem. Toxicol.* **92,** 17–25 (2016).

106. Liu, Y.; Jiang, W.; Chen, Y.; Liu, Y.; Zeng, P.; Xue, F.; Wang, Q. *Mutat. Res. - Genet. Toxicol. Environ. Mutagen.* **797,** 36–45 (2016).

107. Ryan, M. J.; Johnson, G.; Kirk, J.; Fuerstenberg, S. M.; Zager, R. A.; Torok-Storb, B. *Kidney Int.* **45,** 48–57 (1994).

108. Tian, T.; Li, J.; Wang, M. Y.; Xie, X. F.; Li, Q. X. *Eur. J. Pharmacol.* **683,** 246–251 (2012).

109. Sohn, S. J.; Kim, S. Y.; Kim, H. S.; Chun, Y. J.; Han, S. Y.; Kim, S. H.; Moon, A. *Toxicol. Lett.* **217,** 235–242 (2013).

110. Wu, Y.; Connors, D.; Barber, L.; Jayachandra, S.; Hanumegowda, U. M.; Adams, S. P. *Toxicol. Vitr.* **23,** 1170–1178 (2009).

111. Gunness, P.; Aleksa, K.; Kosuge, K.; Ito, S.; Koren, G. *Can. J. Physiol. Pharmacol. 88* **88,** 448–455 (2010).

112. Melo, P. S.; Fabrin-Neto, J. B.; De Moraes, S. G.; Assalin, M. R.; Durán, N.; Haun, M. *Chemosphere* **62,** 1207–1213 (2006).

113. Borenfreund, E.; Puerner, J. A. *J. tissue Cult. methods* **9,** 7–9 (1985).

114. Mosmann, T. *J. Immunol. Methods* **65,** 55–63 (1983).

115. Stockert, J. C.; Blázquez-Castro, A.; Cañete, M.; Horobin, R. W.; Villanueva, Á. *Acta Histochem.* **114,** 785–796 (2012).

116. Lü, L.; Zhang, L.; Wai, M. S. M.; Yew, D. T. W.; Xu, J. *Toxicol. Vitr.* **26,** 636–644 (2012).

117. Takahashi, S.; Abe, T.; Gotoh, J.; Fukuuchi, Y. *Neurochem. Int.* **40,** 441–448 (2002).

118. Vasquez, M. I.; Garcia-Käufer, M.; Hapeshi, E.; Menz, J.; Kostarelos, K.; Fatta-Kassinos, D.; Kümmerer, K. *Sci. Total Environ.* **450–451,** 356–365 (2013).

119. Calza, P.; Medana, C.; Carbone, F.; Giancotti, V.; Baiocchi, C. *Rapid Commun. Mass Spectrom.* **22,** 1533–1552 (2008).

120. Dinakaran, M.; Senthilkumar, P.; Yogeeswari, P.; China, A.; Nagaraja, V.; Sriram, D. *Bioorganic Med. Chem. Lett.* **18,** 1229–1236 (2008).

121. Hayakawa, I.; Atarashi, S.; Yokohama, S.; Imamura, M.; Sakano, K.; Furukawa, M. *Antimicrob. Agents Chemother.* **29,** 163–164 (1986).

~ General conclusions

The continuous concern and awareness of the general public and scientific community about the presence of environmentally relevant pollutants in the water cycle have forced local governments and bigger institutions to legislate on their presence and invest large amounts of money in new technologies for their control and removal. These changes have been possible, in part, due to the enormous advances achieved in analytical methodologies and instruments over the past 50 years, which have permitted the detection and quantification of these compounds at trace concentrations levels. Even though these concentrations are much lower than those used in medicine, their toxicological impact and that of their related compounds (metabolites and transformation products) cannot be discarded and have to be studied.

As it has been discussed and shown through the present manuscript, this PhD thesis has focussed in the degradation of environmentally relevant pollutants the identification of their transformation products and their toxicity assessment. Hence, the conclusions derived from this PhD thesis are:

In relation to the development and the application of TiO_2 nanofibers,

- The electrospinning technique has permitted the easy fabrication of TiO_2 nanofibers. Moreover, the tuning of both synthesis and electrospinning operating parameters has allowed the obtention of nanofibers with different surface characteristics.
- Two methodologies have been developed and fully optimised for the fixation of the studied materials onto an inner support for their latter use in industrial applications. The surface analysis of the fixed materials showed that cracks can be formed, which can later lead to TiO_2 leaching and have drastic consequences in their photocatalytical applications.
- The physic analysis of the material synthesised (SEM, XRD and BET) has demonstrated that multiple factors affect to the final degradation performance of the TiO_2 material. Even though the prepared material had less surface area and less anatase content, its adsorption capacity and degradation performance was better in laboratory batch experiments to that of the reference material (TiO_2 P25 nanoparticles).
- None of the tested materials, however, could effectively remove the pharmaceuticals under study when a real water matrix was used, mainly attributed to the *scavenger* effect caused by dissolved salts, surfactants and other organic matter. Due to this limitation, the implementation of TiO_2 photocatalysis in the industrial scale should be addressed after conventional wastewater treatments, once the organic content

in water is significantly lower than the receiving effluents. TiO_2 photocatalysis could be implemented in the water potabilisation process, for example, before the coloration process.

In relation to the analytical techniques used in this PhD thesis,

- Liquid chromatography coupled to high-resolution mass spectrometry has permitted the quantification of the drugs under study and their transformation products at low concentration levels (ng L^{-1} – μg L^{-1}) without prior sample treatment. This fact has been of special merit due to the low amount of sample available of some lab-scale experiments conducted
- Tandem mass spectrometry combined with high-resolution mass spectrometry have made possible the identification and characterization of OFX transformation products, required for the proposal of its photocatalytic degradation pathway. Additionaaly, especial care has been taken to identify in-source fragments and redox in-source fragments in order to prevent false TPs identifications.
- Although novel acquisition methods, such as data-dependant and data-independent analysis were evaluated in the present thesis, they led to the acquisition of a low number of mass scans, and the loss of direct link between the precursor and product ions respectively, fact that led to the reconsideration of the screening method chosen for non-targeted analysis.
- Due to the high number of transformation products derived from ofloxacin photocatalysis, the combination of high-resolution mass spectrometry (in the full scan mode) with data treatment techniques permitted the fast detection and identification of its transformation products.
- Ion mobility mass spectrometry combined with theoretical CCS calculations represents, today, one of the main tools for the acquisition of 3D information of unknown chemicals and the confirmation of their chemical structures. In this PhD thesis ion mobility allowed the individual identification of isobaric TPs that coeluted at the same retention time and that could not been resolved neither high-resolution nor tandem mass spectrometry.

In relation to the toxicity analysis of ofloxacin transformation products,

- Two endpoints were used to assess the toxicity of ofloxacin transformation products, a well standardised method (*Vibrio fischeri*) and cytotoxicity (using 3 human cell lines), showing different sensitivity to the exposure of ofloxacin and its transformation products. These differences observed clearly constituted a valuable tool for the toxicity screening of these TPs, as no prior information was available.

- Both endpoints clearly demonstrated that ofloxacin transformation products rendered higher toxicity than the parent drug. Nevertheless, the complete detoxification was finally achieved at the end of the photocatalytical process, ensuring that the final solution was less toxic that the parent compound ofloxacin.
- The LC fractionation of the reaction crude before the toxicological study made possible the evaluation of smaller and simpler fractions. This strategy permitted to enclose which chemicals were the responsible of the toxicity increase and the study of synergism between them. Interestingly, while *V. fischeri* was more sensitive to ofloxacin, human cell lines were more sensitive to the exposure of individual fractions, fact, that can be linked to synergism or cell metabolism.
- Finally, although the toxicity observed for the different TPs was higher than that of ofloxacin and because the concentration used in this experimental research (100 – 500 times) than those found in the environment, it can be concluded that the generation of these TPs do not pose a hazard to the environment, but, its monitoring and control is specially recommended.